

## **Localisation Super-resolution Imaging Using Germanium Quantum Dots.**

Song, Mingying

The copyright of this thesis rests with the author and no quotation from it or information derived from it may be published without the prior written consent of the author

For additional information about this publication click this link.

<http://qmro.qmul.ac.uk/xmlui/handle/123456789/12916>

Information about this research object was correct at the time of download; we occasionally make corrections to records, please therefore check the published record when citing. For more information contact [scholarlycommunications@qmul.ac.uk](mailto:scholarlycommunications@qmul.ac.uk)

Localisation Super-resolution Imaging Using  
Germanium Quantum Dots

---

Author: Mingying SONG

Supervisors:  
Dr. Andrei V. SAPELKIN  
Dr. Ann P. WHEELER

Submitted in partial fulfilment of the requirements  
of the degree of Doctor of Philosophy  
in the  
Centre for Condensed Matter and Materials Physics  
Department of Physics

October 2015

---

## Statement of Originality

I, MINGYING SONG, confirm that the research included within this thesis is my own work or that where it has been carried out in collaboration with, or supported by others, that this is duly acknowledged below and my contribution indicated. Previously published material is also acknowledged below.

I attest that I have exercised reasonable care to ensure that the work is original, and does not to the best of my knowledge break any UK law, infringe any third party's copyright or other Intellectual Property Right, or contain any confidential material.

I accept that the College has the right to use plagiarism detection software to check the electronic version of the thesis.

I confirm that this thesis has not been previously submitted for the award of a degree by this or any other university.

The copyright of this thesis rests with the author and no quotation from it or information derived from it may be published without the prior written consent of the author.

Signature:

*Mingying Song*

Date: 25/09/2015

---

## Publications

1. A. Karatutlu, M. Song, A. P. Wheeler, O. Ersoy, W. Little, Y. Zhang, P. Puech, F. Boi, Z. Luklinska, A. V. Sapelkin, Synthesis and structure of free-standing germanium quantum dots and their application in live cell imaging, *RSC Advances*, 5, 20566, 2015.
2. N. Hosny, M. Song, John. Commelly, S. Ameer-Beg, M. Knight, A. P. Wheeler, Super-resolution imaging strategies for cell biologists using a spinning disk microscope *PloS one*, 8(10), 2013.
3. M. Song, A. Karatutlu, O. Ersoy, Y. Zhou, Y. Yang, Y. Zhang, W. Little, A. P. Wheeler, A. V. Sapelkin, Spectroscopic super-resolution fluorescence cell imaging using ultra-small Ge quantum dots, *To be submitted to Optics Express*.

## Conferences

1. Poster: Spectroscopy super-resolution fluorescence imaging using ultra-small quantum dots, 4th Single Molecule Localisation Microscopy Symposium, London, UK (August, 2014)
2. Oral Presentation: Spectroscopy super-resolution fluorescence imaging using ultra-small quantum dots, 2014 Focus on Microscopy, Sydney, Australia (April 2014)
3. Poster: Live cell fluorescence super-resolution imaging with bio-friendly quantum dots, 2013 Frontiers in BioImaging, London, UK (July 2013)
4. Hands-On Light Microscopy Workshop, Luxembourg (January 2013)
5. Oral Presentation: Fluorescence Super-resolution imaging with quantum-dots, 1st International Workshop ‘Smart nanocomposite scaffold for tissue engineering’, London, UK (September, 2012)

---

## Acknowledgements

I am extremely grateful for having the opportunity being a member of the CCMMP group in Queen Mary University of London in UK for 4 years. I have had a lot pleasure of working on a fascinating project with many nice people here, without whom completion of this thesis would not have been possible.

Firstly, my supervisor, Dr. Andrei Sapelkin, has been a wonderful guide for me to enter the world of frontier scientific research. I can not thank him enough for providing a positive and stimulating research environment that has enabled me to work in my own way. Thanks to Andrei's constant guidance, I have gained many skills such as logical and critical thinking, academic presenting and timing. Extend sincere gratitude also goes to Dr. Ann Wheeler, my secondary supervisor, who has provided a lot of practical guidance in the imaging lab as well as how to carry out biological scientific experiments efficiently by good planning and pre-thinking. In addition to all the opportunities and support that Andrei and Ann have provided over the years, their willingness to send me to many conferences have been greatly motivating and helpful to my research. I strive to learn their approach and attitude on scientific research, which I am sure will also benefit to my future career when I leave QMUL.

I am grateful to Prof. Christian Soeller and Dr. Dylan Owen for agreeing to be my PhD examination committees.

The research work presented in this thesis would never have been completed without the support and encouragement of my colleagues. Dr. Ali Karatutlu, Osman Ersoy and Kemal Keseroglu are sincerely thanked for their supporting in synthesising and characterising quantum dots. Yuanpeng Zhang and Dr. William Little are helpful in discussion of quantum dots structure and features. During my experiments period in the biological imaging, Isma Ali was very patient and helpful in introducing me to the cell culture protocols and microscopes operations. I also thank Dr. Zofia

---

Luklinska for the help in electron microscope measurements. The algorithm development part of the projects has been a collaborative effort and would not be possible without contributions from Yun Zhou and Yongxin Yang. I am also grateful to have the chances to interact and with many other CCMMP group members, including Prof. Marting Dove, Haizhou Lu and Yiwei Sun.

My utmost gratefulness goes to my parents for supporting my decision of being away for so many years to fulfil my self-development. I also thank Kelly Hu who has been giving a lot of moral encouragement when I meet challenges. In addition, extended thanks are going to my close friends Yaming Chen, Huihui Sun, Wenqing Tao, Chen Chen and Jian Wang who have been very supportive. Special thanks must be expressed to my BSc supervisor, Prof. Xiangai Cheng, who gave me a lot constructive advices both academically and personally.

Finally, I would like to thank the cooperation between China Scholarship Council and Queen Mary, University of London for funding my PhD project.

# Abstract

Novel fluorescent quantum dots of small size, tunable light emission wavelength and high compatibility with biological systems are of great significance to light microscopy super-resolution imaging. In this thesis, colloidal germanium quantum dots of  $\sim 3.8$  nm size have been investigated as a novel fluorescent probe for cell imaging.

Two single molecule localisation super-resolution methods were explored: one utilised QDs blinking statistics and the other one was based on intrinsic QDs size dispersion. We found that the blinking super-resolution strategy which combined the usage of blinking QDs and spinning disk confocal imaging has led to less than seven minutes collection time for 2000 image frames. High precision temporal separation of single molecules has been achieved on Ge QDs and CdSe QDs labelled fixed HeLa cell. The spectroscopic super-resolution strategy that combined the usage of size dependent light emission QDs and spectra imaging, resulted in a 1.6 seconds data acquisition time. Spectroscopic separation and high precision single molecule localisation has been demonstrated using Ge QDs and CdSe QDs labelled fixed HeLa cell samples.

We compared various localisation algorithms when applied to the two super-resolution methods we studied. We found that they did not work well with our data. Consequently, we developed two MATLAB-based localisation algorithms. The first algorithm used the independent component analysis (ICA) model to analyse the blinking stochastic imaging data, whilst the other used the Gaussian mixed model (GMM) to analyse the spectroscopic separation imaging data.

We also conducted comparative toxicity tests of these novel Ge QDs with a typical off-the-shelf system. The cell toxicity of Ge QDs was found to be less than that of CdSe/ZnS QDs. For instance, 25 nM Ge QDs in 1 mL Hela cell solution did not cause observable cells apoptosis in 24 hours. It caused 15% cells apoptosis after 3 days, rather than 35% for CdSe QDs at the same concentration. In addition, long term live cell imaging with QDs revealed that Ge QDs had not significantly changed cellular morphology within a 90 hour period.



# Contents

Statement of Originality . . . . .	2
<b>Contents</b>	<b>7</b>
<b>List of Figures</b>	<b>12</b>
<b>List of Tables</b>	<b>15</b>
<b>Abbreviations</b>	<b>16</b>
<b>Symbols</b>	<b>17</b>
<b>1 Introduction</b>	<b>18</b>
1.1 Thesis content and structure . . . . .	18
1.2 History and developments in light microscopy . . . . .	18
1.3 Microscope optics, magnification . . . . .	25
1.4 Limits of resolution . . . . .	27
1.5 Super-resolution imaging . . . . .	33
1.5.1 Developments in super-resolution imaging strategies . . . . .	33
1.5.2 Single molecule localisation super-resolution imaging . . . . .	38
1.6 Fluorescent probes . . . . .	44
1.6.1 Types of probes . . . . .	44
1.6.2 Fluorescence mechanism . . . . .	49
1.6.3 Quantum dots and bioimaging . . . . .	51
1.6.3.1 Quantum confinement in semiconductor nanostructures	54
1.6.3.2 Optical properties of QDs, blinking . . . . .	59
1.6.3.3 Germanium quantum dots . . . . .	61
1.7 Microscopes: fluorescence and confocal microscopes . . . . .	63
1.7.1 Fluorescence microscopy . . . . .	64
1.7.2 Confocal microscopy . . . . .	66
1.7.2.1 Confocal principles . . . . .	66
1.7.2.2 Types of confocal microscope . . . . .	69
1.7.2.3 Usage and limits of confocal microscopes . . . . .	72

<b>2</b>	<b>Materials and methods</b>	<b>74</b>
2.1	Tissue culture . . . . .	74
2.1.1	Cell culture . . . . .	74
2.1.2	Cell fixation, permeabilisation and staining . . . . .	75
2.1.3	Cell viability assay . . . . .	76
2.1.3.1	Trypan blue qualitative test method . . . . .	76
2.1.3.2	Muse quantitative method . . . . .	77
2.1.4	Medium-term observation of live cells . . . . .	79
2.2	Ge and Invitrogen quantum dots . . . . .	80
2.3	Characterisation methods . . . . .	82
2.4	Microscopy . . . . .	82
2.4.1	Fluorescence microscopes . . . . .	82
2.4.2	Spinning disk confocal microscopy . . . . .	84
2.4.3	Spectroscopic confocal microscopy . . . . .	87
2.4.4	Electron microscopy . . . . .	89
2.5	Computational processing . . . . .	91
2.5.1	Particle size measurements . . . . .	91
2.5.2	Statistical analysis . . . . .	92
2.5.3	Point spread function Gaussian fitting . . . . .	93
2.5.4	Localisation algorithms . . . . .	93
<b>3</b>	<b>Results and discussion</b>	<b>95</b>
3.1	Germanium quantum dots as bioimaging probes . . . . .	95
3.1.1	Ge quantum dots characterisation . . . . .	95
3.1.1.1	Optical characterisation . . . . .	95
3.1.1.2	TEM characterisation . . . . .	97
3.1.2	Biocompatibility tests . . . . .	99
3.1.2.1	Cell viability tests . . . . .	99
3.1.2.2	Medium-term live cell imaging . . . . .	103
3.1.3	Fluorescence imaging . . . . .	108
3.1.3.1	QDs test imaging . . . . .	108
3.1.3.2	Cell imaging with Ge QDs . . . . .	110
3.1.4	Conclusion . . . . .	111
3.2	Stochastic super-resolution cell imaging using spinning disk confocal microscopy and blinking Ge QDs . . . . .	112
3.2.1	Principles of stochastic super-resolution imaging using blinking QDs . . . . .	112
3.2.2	Microscope system characterisation . . . . .	114
3.2.2.1	Localisation precision . . . . .	114
3.2.2.2	PSF dependence on excitation wavelength . . . . .	117
3.2.2.3	Sample drift . . . . .	119

3.2.3	Ge QDs as SDSI probes . . . . .	120
3.2.3.1	Ge QDs blinking measurements . . . . .	120
3.2.3.2	Photo-bleaching . . . . .	123
3.2.4	Stochastic cell imaging with QDs . . . . .	125
3.2.5	Super-resolution reconstruction . . . . .	128
3.2.5.1	Existing stochastic reconstruction algorithms and comparison . . . . .	128
3.2.5.2	BSA description . . . . .	133
3.2.5.3	BSA reconstruction . . . . .	138
3.2.6	Conclusion . . . . .	141
3.3	Spectroscopic super-resolution fluorescence cell imaging using Ge quantum dots . . . . .	143
3.3.1	Spectroscopic super-resolution imaging strategy using quantum dots . . . . .	143
3.3.2	Microscope PSF characterisation . . . . .	146
3.3.3	QDs size dependent emission spectra . . . . .	148
3.3.4	Spectroscopic cell imaging using QDs . . . . .	151
3.3.5	Super-resolution reconstruction . . . . .	154
3.3.5.1	SSA description . . . . .	155
3.3.5.2	SSA reconstruction . . . . .	158
3.3.6	Conclusion . . . . .	161
<b>4</b>	<b>Conclusion and future work</b>	<b>163</b>
4.1	Conclusion . . . . .	163
4.2	Outstanding questions and future work . . . . .	166
4.2.1	Ge QDs quantum yield study and functionalisation . . . . .	166
4.2.2	Improving the super-resolution imaging methods . . . . .	167
4.2.3	Algorithm tests and improvements . . . . .	168
<b>A</b>	<b>Supplementary Muse test data</b>	<b>170</b>
<b>B</b>	<b>Calculation of molar concentration of Ge QDs</b>	<b>171</b>
<b>C</b>	<b>iXon3 photon number calculation</b>	<b>172</b>
<b>D</b>	<b>Supplementary <math>\lambda</math>-stack data in SSRM</b>	<b>173</b>
D.1	Supplementary data 1: 6-Qdots . . . . .	173
D.2	Supplementary data 2: Ge QDs . . . . .	175
<b>E</b>	<b>Correlative imaging</b>	<b>176</b>
E.1	Confocal and SEM correlative imaging . . . . .	178

*Contents*

---

E.2 Confocal and TEM correlative imaging . . . . .	181
<b>F BSA codes</b>	<b>183</b>
<b>G SSA codes</b>	<b>187</b>
<b>Bibliography</b>	<b>204</b>

# List of Figures

1.1	Historical compound microscopes developments from 16 <sup>th</sup> century . . .	20
1.2	Schematic digram of the light path in an infinity corrected microscope and fluorescence microscope . . . . .	21
1.3	Optical paths of Critical and Köhler illumination . . . . .	22
1.4	Key developments of microscopies in the history . . . . .	24
1.5	Example images of several advanced optical microscopies . . . . .	24
1.6	Basic components of modern microscopies . . . . .	25
1.7	Magnification and resolution of optical microscopy images . . . . .	27
1.8	Propagating of light through a small aperture . . . . .	28
1.9	Image formation of microscope in the view of signal processing . . . . .	29
1.10	Normalised microscope PSF and OTF . . . . .	29
1.11	Point spread function and diffraction limit . . . . .	30
1.12	The principle of stimulated emission depletion (STED) microscopy . . .	35
1.13	The principle of structured illumination microscopy (SIM) . . . . .	36
1.14	Spatial and temporal resolutions of some main super-resolution techniques . . . . .	37
1.15	Temporal separation single molecule localisation super-resolution imaging strategy . . . . .	39
1.16	The principle of TIRF illumination . . . . .	41
1.17	Fluorescent probes and fluorescence emission mechanism . . . . .	45
1.18	Excitation and emission spectrum of QDs and dyes . . . . .	47
1.19	Photo-stability comparison between QDs and Alexa 488 dyes . . . . .	48
1.20	Jablonski diagram for fluorescent QDs . . . . .	50
1.21	Current applications of quantum dots as fluorescent probes . . . . .	51
1.22	A typical core-shell type bioimaging quantum dot structure . . . . .	52
1.23	Energy level diagram of a bulk semiconductor and quantum dots . . . .	55
1.24	1-D ‘particle in a box’ model. . . . .	57
1.25	Correlation diagram relating bulk crystal states to quantum dots . . . .	58
1.26	Size-dependent excitation and emission spectra of QDs . . . . .	59
1.27	Direct band gap and indirect band gap in semiconductor materials . . .	62
1.28	Germanium and Silicon QDs band gap energy changes as a function of particle size . . . . .	63
1.29	Schematic diagram of the optical path of an epi-fluorescence microscope	65

1.30	Principle of out-of-focus light rejection in confocal microscopy . . . . .	67
1.31	Optic path of fluorescence microscope and confocal fluorescence microscope . . . . .	68
1.32	Conventional wide-field fluorescence image versus confocal fluorescence image . . . . .	69
1.33	Optical path of single beam scanning confocal microscopes . . . . .	70
1.34	The optical path of a spinning disk imaging system . . . . .	71
2.1	Observation of cell suspension after Trypan blue staining . . . . .	77
2.2	The Muse for quantitative cell viability test . . . . .	78
2.3	Principles of judging cell viability by cell fluorescence . . . . .	78
2.4	An Incucyte system in a cell culture incubator . . . . .	79
2.5	Chemical reactions in colloidal synthesis of our ultra-small Ge QDs . . . . .	81
2.6	Outlook of our spinning disk confocal microscopy system. . . . .	85
2.7	Components of our spinning disk confocal microscopy system . . . . .	85
2.8	Outlook of LSM 710 confocal spectra imaging system . . . . .	87
2.9	Optical path and spectroscopic separation principles of a QUASAR detector . . . . .	88
2.10	QE of the PMT unit in the spectral array detector . . . . .	88
2.11	SEM and TEM systems . . . . .	90
3.1	Ge QDs product in original reaction chemical solution and in ethanol, and bulk Ge powder . . . . .	96
3.2	The optical characterisations of Ge QDs . . . . .	97
3.3	Ge QDs TEM image and size characterisation . . . . .	98
3.4	Phase contrast images of Hela cells after Trypan blue staining . . . . .	100
3.5	Hela cells viability calculated from Trypan Blue images . . . . .	100
3.6	Comparison of cell viability between Ge QDs and Qdot625 . . . . .	103
3.7	Merged phase contrast and fluorescence Incucyte images of Hela cells cultivated with Ge and Qdot625 QDs. . . . .	104
3.8	Hela cells proliferation curve under different QDs treatments . . . . .	105
3.9	Cell and nucleus shape under different QDs treatments . . . . .	106
3.10	Summary of cell nucleus size and shape changes under QDs treatments . . . . .	107
3.11	Ge QDs fluorescence images on a spinning disk microscopy . . . . .	108
3.12	Qdot625 fluorescence images on spinning disk confocal microscopy . . . . .	109
3.13	Hela cells labelled with Ge QDs fluorescence images . . . . .	110
3.14	Position error variations for different imaging frames . . . . .	117
3.15	Multiple views of a PSF image in three directions, collected from standard beads . . . . .	118
3.16	Qdot625 position drifts in X and Y directions on the spinning disk confocal microscope within 40 minutes. . . . .	120
3.17	A few captures of single Ge QD fluorescence intensity changes . . . . .	121

3.18	A few selections of the fluorescence intermittency durations of a single Ge QD . . . . .	122
3.19	Inverse power law distribution of Ge QDs blinking ‘off’ event durations . . . . .	122
3.20	Probes photo-bleaching comparison. . . . .	125
3.21	Fluorescence images of Ge QDs in Hela cells, imaged on the spinning disk confocal microscopy . . . . .	126
3.22	Fluorescence images of CdSe QDs in Hela cells, imaged on the spinning disk confocal microscopy . . . . .	127
3.23	Plot of BSA registered QDs number changes along with the initial guess for maximum number of QDs . . . . .	135
3.24	Super-resolution reconstruction using BSA, QuickPALM and SOFI . . . . .	139
3.25	Schematic sketch of spectroscopic imaging and the super-resolution strategy. . . . .	144
3.26	Principle of spectroscopic super-resolution reconstruction . . . . .	145
3.27	PSF characterisation on Zeiss LSM 710 . . . . .	147
3.28	Gaussian fitted PSF sizes variation with wavelength . . . . .	147
3.29	TEM images of Qdot525, 605, 705 samples . . . . .	148
3.30	An example of Qdots size calculation based on TEM images . . . . .	149
3.31	Calibration of emission spectra of 3 Qdot samples . . . . .	150
3.32	Emission-size analysis for CdSe/ZnS Qdots and Ge QDs . . . . .	150
3.33	Fluorescence spectra channels of the mixed CdSe Qdots sample . . . . .	152
3.34	Spectroscopic super-resolution microscopy images . . . . .	153
3.35	Spectroscopic super-resolution localisation and reconstruction . . . . .	159
D.1	Fluorescence spectra channels of Ge QDs sample . . . . .	175
E.1	Correlative imaging experimental steps . . . . .	177
E.2	SEM images of CdSe QDs . . . . .	179
E.3	Correlative imaging of QDs via confocal light microscopy and SEM at low magnification . . . . .	179
E.4	Correlative imaging of QDs via confocal light microscopy and SEM at high magnification . . . . .	180
E.5	Correlative imaging of QDs via confocal light microscopy and TEM . . . . .	181
G.1	GUI of SSA algorithm . . . . .	188

# List of Tables

1.1	Optical properties comparison between proteins/dyes and QDs . . . . .	48
1.2	Timescales of the basic radiative and non-radiative transitions involved in the Jablonski diagram. . . . .	50
1.3	Band gap energy and the corresponding wavelength of some bulk semiconductor materials that are commonly used for making quantum dots. . . . .	61
1.4	Advantages and disadvantages of fluorescence imaging. . . . .	66
2.1	Cell preparation for Incucyte medium-term imaging . . . . .	80
2.2	Different QDs or materials were added to the cells so that different growth conditions were generated for the cells . . . . .	80
2.3	Light microscopes used in the experiments. . . . .	83
2.4	iXon3 885 key parameters . . . . .	86
2.5	Comparison of SEM and TEM . . . . .	90
2.6	Used algorithms . . . . .	94
3.1	Cells viability with Ge QDs at different time points . . . . .	102
3.2	Comparison of cell viability between Ge QDs and Qdot625. $\diamond$ stands for significant statistical difference ( $p < 0.05$ ) of the cell viabilities between the QDs treated cells and the control cells at the same time point. . . . .	102
3.3	Position error for different imaging frames . . . . .	116
3.4	PSF fitting results for four situations of excitation laser wavelength . . . . .	118
3.5	Description of several existing stochastic super-resolution reconstruction algorithms . . . . .	131
3.6	Performance of several available public algorithms testing on our spinning disk microscopy based blinking QDs in Hela cells dataset . . . . .	132
3.7	Flow chart of ICA based BSA algorithm . . . . .	137
3.8	Quantum dots size calculation summarisation . . . . .	149
3.9	Flow chart of SSA algorithm . . . . .	157
A.1	Comparison of cell viability with Ge QDs and Qdot625 on Muse test . . . . .	170
D.1	Individual Invitrogen QDs $\lambda$ -stack images from LSM710 microscope . . . . .	174



# Abbreviations

<b>QD</b>	Quantum Dot
<b>GFP/RFP</b>	Green/red fluorescent protein
<b>Ge</b>	Germanium
<b>QY</b>	Quantum yield
<b>PBS</b>	Phosphate buffered saline
<b>UV</b>	Ultraviolet
<b>PMT</b>	Photonmultiplier tube
<b>EMCCD</b>	Electron multiplying charged coupled device
<b>NA</b>	Numerical aperture
<b>PSF</b>	Point spread function
<b>OTF</b>	Optical transfer function
<b>FWHM</b>	Full width at half maximum
<b>LSM</b>	Laser scanning confocal microscope
<b>TIRF</b>	Total internal reflection fluorescence microscopes
<b>SEM/TEM</b>	Scanning/transmission electron microscope
<b>STED</b>	Stimulated emission depletion
<b>SIM</b>	Structured illumination microscopy
<b>STORM</b>	Stochastic optical reconstruction microscopy
<b>PALM</b>	Photo-activated localisation microscopy
<b>SDSI</b>	Spinning disk statistical imaging
<b>SPDM</b>	Spectral precision distance determination microscopy
<b>CLEM</b>	Correlative and electron microscopy
<b>SSRM</b>	Spectroscopic super-resolution microscopy
<b>QCE</b>	Quantum confinement effect
<b>CB/VB</b>	Conduction/valence band
<b>ROI</b>	Regions of interest
<b>ICA</b>	Independent component analysis
<b>BSA</b>	Blinking analysis super-resolution algorithm
<b>SSA</b>	Spectroscopic super-resolution algorithm
<b>SOFI</b>	Super-resolution optical fluctuation imaging
<b>CSSTORM</b>	STORM using compressed sensing
<b>MLE</b>	Maximum likelihood estimation
<b>GMM</b>	Gaussian mixture model

# Symbols

$\text{\AA}$	Distance	0.1 nm
$e$	Electron charge	C
eV	Energy	Electron volt ( $1 \text{ eV} = 1.6 \times 10^{-19} \text{ J}$ )
$c$	light speed in vacuum space	$c = 3 \times 10^8 \text{ m/s}$
P	probability density	probability $\cdot\text{s}^{-1}$
$\hbar$	Reduced Planck constant	J $\cdot\text{s}$
$\lambda$	Wavelength	nm
$\omega$	Angular frequency	rads $^{-1}$
$\eta$	Quantum yield	Percentage
$\epsilon$	Dielectric constant	F/m
$\delta$	Position error	nm
$\Delta$	Size	nm
$I$	Luminous intensity	cd

# Chapter 1

## Introduction

### 1.1 Thesis content and structure

In this thesis, we investigate the application of germanium (Ge) quantum dots (QDs) in localisation super-resolution bioimaging. To begin with, a general introduction to the study will outline the challenges in optical imaging, especially the resolution limit. QDs will then be introduced into the fluorescence biological imaging application. Following this, their advantages and disadvantages in super-resolution imaging will be discussed. The application of germanium QDs for cell imaging and their cell toxicity will then be assessed. The central focus of this thesis will be on the super-resolution imaging experimental methods, taking advantage of the blinking phenomenon of Ge QDs, and the spectroscopic super-resolution method utilising size-dependent light emission of Ge QDs.

### 1.2 History and developments in light microscopy

Most of the live activities and biological processes at or below cellular level have been understood through direct visualisation. Microscopes have played an irreplaceable

role in connecting the cellular and sub-cellular level with the human world. Generally speaking, light microscopy is an imaging solution to produce magnified visual images of objects that are too small to be seen by naked human eyes, as well as providing greater detail of the objects to observe. Besides magnification, microscopies require contrast and resolution, and in the history of light microscopy there have been substantial developments in these areas.

The first microscope can be traced back to the 1590s, when two Dutch spectacle makers, Hans Jansen and his son Zacharias Jansen invented a hand-held microscope which achieved focus by sliding a draw tube in or out (Figure 1.1) [1]. This has been regarded as the first compound microscope. An early application of just such a compound microscope to life science was made by Gallieo Galilei, who observed a bee using a modified microscope combining a convex lens and a concave lens, which became a guide for optical path design to other researchers in the seventeenth-century [2]. However, the first printed research devoted to biological samples using microscopy was - *Micrographia*, published in 1665, a work by the English physicist Robert Hooke, who discovered small structures - “cells” in plant tissues [3]. More importantly, in his descriptions of microscopes, focusing mechanisms, illumination system and sample stage were also demonstrated. Contemporaneously, a Dutch microscopist Antonie van Leeuwenhoek used his knowledge of grinding lenses to achieve magnification, as large as  $300\times$ , in compound microscopes [4, 5]. Leeuwenhoek used his single lens microscope with short focal length achieving a resolution down to  $\mu\text{m}$ . As a result, bacteria were introduced to human science. By the early 19<sup>th</sup> century, microscopes were better-made and easier to handle. Lens chromatic aberration<sup>1</sup> and spherical aberration<sup>2</sup> problems were solved during the 1830s by using additional lenses of different shapes and light bending properties into the optical path. Microscope resolution was  $\sim 1 \mu\text{m}$  at that time. Although this was not much of an improvement compared

---

<sup>1</sup>Refers to the halos that results from the lens’s different refractions to different wavelengths light.

<sup>2</sup>Refers to the effect that occurs when all incident light end up focusing at different points after passing through a spherical surface. This results from the less refraction of near axis light than the edge light.

to Leeuwenhoek's microscopes, optimised illumination system and stable mechanical supports were introduced [6].

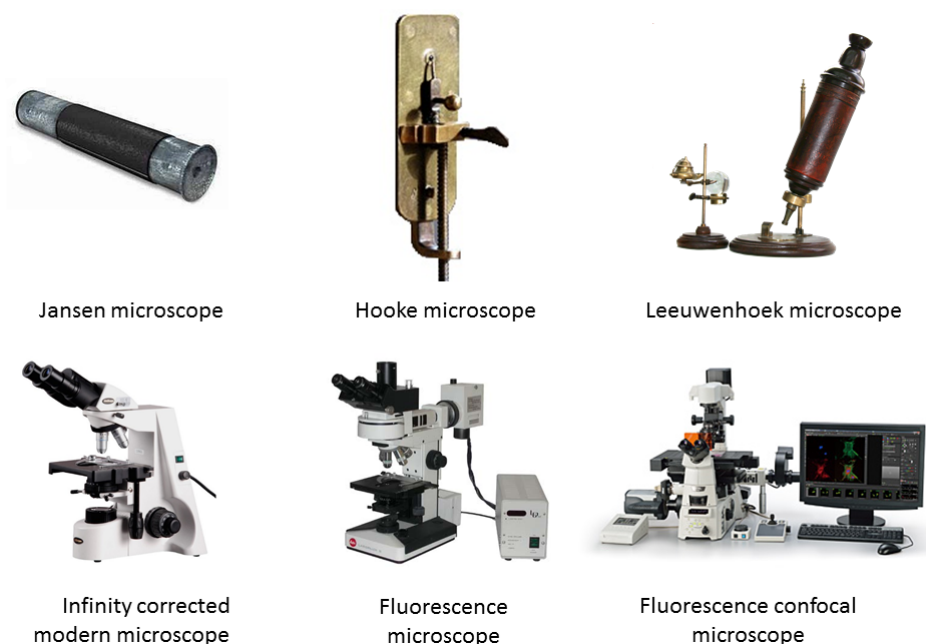


**Figure 1.1:** Historical compound microscopes developments from 16<sup>th</sup> century. Images reprinted from references [5, 7, 8].

A break through in microscope design and its applications came as a result of work by Ernst Abbe in the 1860s [9] who for the first time, provided rigorous mathematical formulation of microscope design and defined the limit of resolution<sup>3</sup>. A microscope manufacturer, Carl Zeiss was the first to realise the importance of optical theory for the manufacturing of high-power microscopes. Zeiss collaborated with Ernst Abbe and produced the leading microscopes in the world with an optical resolution down to  $0.2 \mu\text{m}$  in the 1880s [11]. Since the 20<sup>th</sup> century, as optical principles became better understood, microscopes have been developed into a number of powerful and specific branches. In the 1930s, a Austrian microscope manufacturer Reichert introduced infinity corrected optics, in which an additional tube lens was used to produce an intermediate image (Figure 1.2). The region between the objective lens and tube lens (infinity space) provides a path of parallel light beams, in which additional

<sup>3</sup>See also Rayleigh work [10] on the subject.

optical elements can be placed without the introduction of any aberrations or modification of the objective working distance. The infinity corrected microscopes were further developed by Zeiss and Leica and became common place by the 1980s.

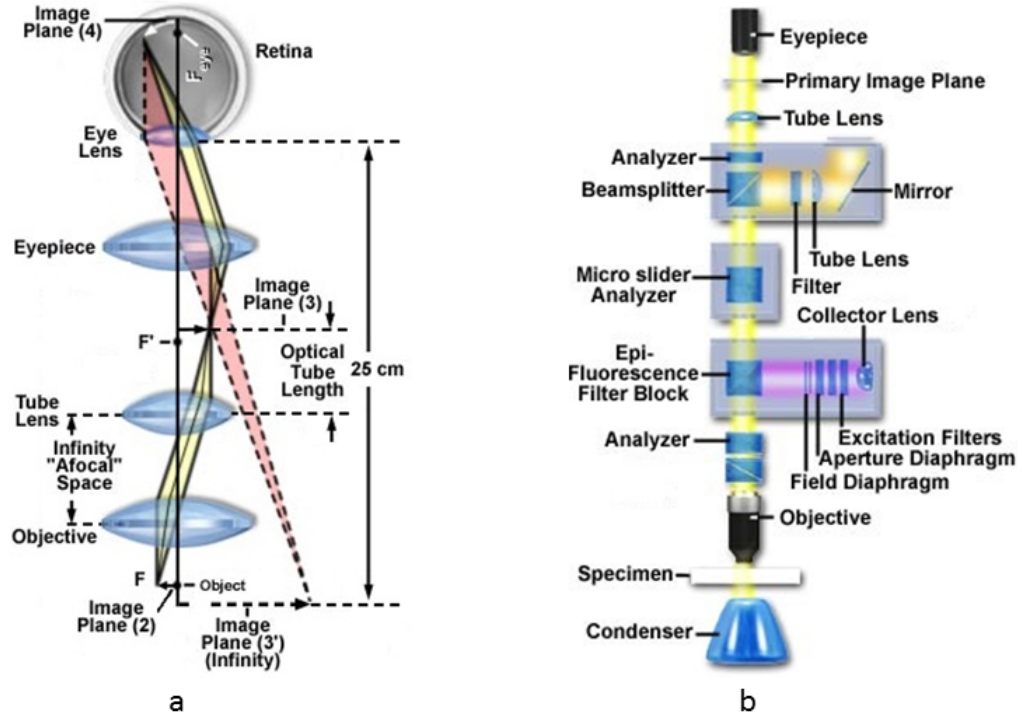


**Figure 1.2:** Schematic diagram of the light path in an infinity corrected microscope (a) and fluorescence microscope (b). Infinity corrected optical system consists of an objective and a tube lens to produce an image. Other optical elements can be placed in the parallel optical path between the objective and tube lens. In a modern fluorescence microscope, excitation light and filters are the key additional elements, which will be further demonstrated in section 1.7.1. [12]

Along with the development of microscopes, microscope illuminators and illumination methods have been developed from the use of simple natural sun light to contemporary laser scanning methods. In terms of sample illumination and light collection methods, there are transmitted light and reflected light microscopes [13, 14]. Ideally, a bright, glare-free and evenly dispersed illumination in the field of view is expected in optimised microscopy. Early microscopes in the 17<sup>th</sup> century relied on natural sun light, candles and oil lamps to provide illumination. These simple unfocused light sources suffered from uneven illumination, glare and were even a potential

fire hazard. At the beginning of 19<sup>th</sup> century, microscope scientists started to realise the importance of illumination aperture. British microscopist Edward Nelson first introduced the Nelson illumination condition (also known as critical illumination) by using a substage condenser to produce a focused image of the flame from an oil lamp on the sample plane to achieve a somewhat even illumination condition over the view field. This illumination condition was then superseded by a far more efficient method - the Köhler illumination, which was developed by August Köhler of the Carl Zeiss corporation in 1893 [15]. As illustrated in figure 1.3, in the Köhler illumination condition, the collector lens, field diaphragm and condenser were used and arranged in an appropriate configuration in order to generate an extremely even illumination. The image of the illumination source was focused on the back focal plane of the objective, instead of the sample plane, in which case the illumination source (flame) was visible in the final image. It has become the predominant illumination condition for modern advanced light microscopy.

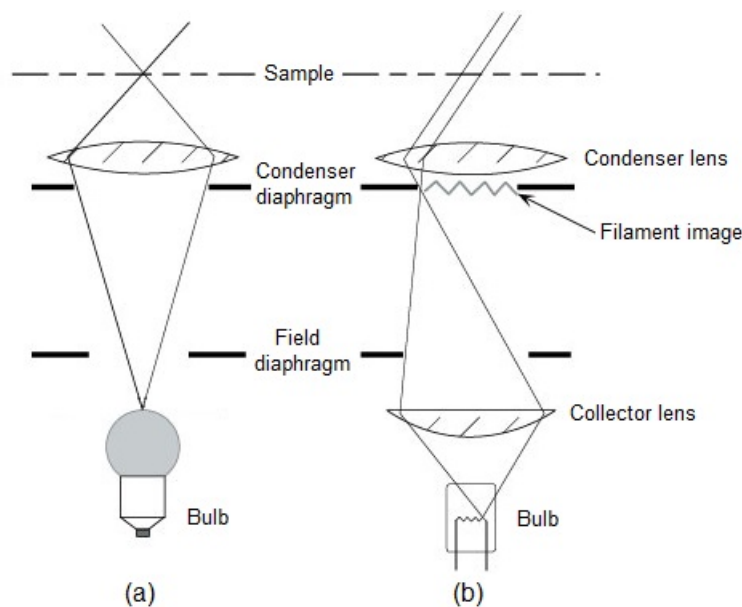


**Figure 1.3:** Optical paths of Critical (a) and Köhler illumination (b). Figure modified from reference [16].

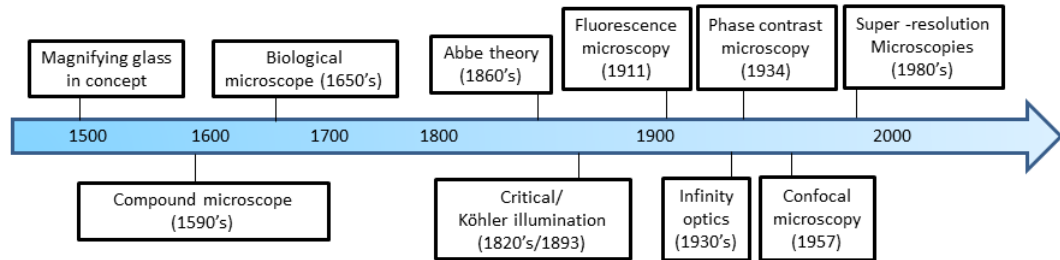
Illumination methods have gained many developments under the guidance of optical principles and inventions of new illumination sources, such as tungsten-halogen

lamps, light-emitting diodes (LEDs) and lasers. Bright and dark field microscopy have been two of the basic classical illumination methods, in which sample contrasts come from the absorbance or scattering of light in the sample. In 1934, phase-contrast microscopy was invented by Dutch physicist Frits Zernike. The phase-contrast technique is a contrast enhancing method that relies on wave nature of light to convert the light variations in the phase into corresponding changes in amplitude [17]. It provides the ability to improve contrast, particularly for transparent and unstained biological samples. Soon after phase-contrast microscopy, another contrast enhancement technique - differential interference contrast (DIC) microscopy (also known as Normarski microscopy) was invented on the principle of gaining optical path length by the interference of two polarised light beams [18].

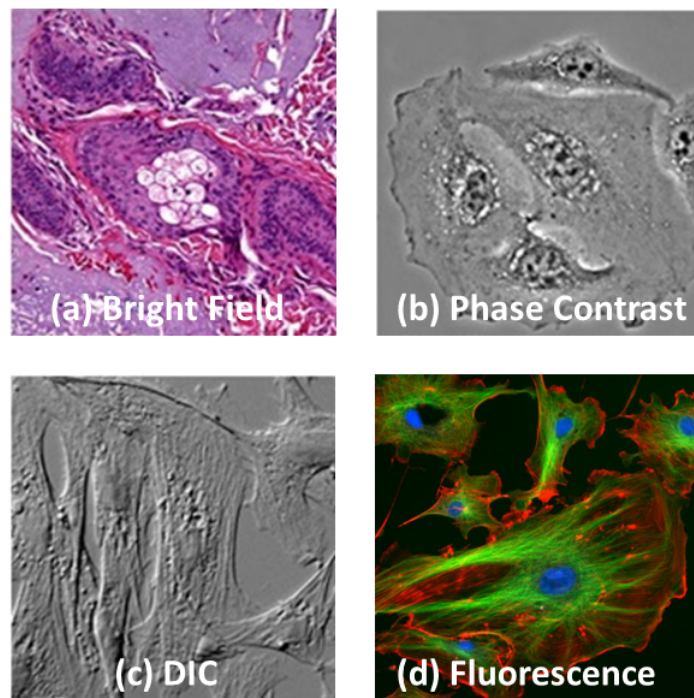
Fluorescence microscopy is another contrast enhancement technique that utilises fluorescent probes based on the principle that fluorescent probe molecules emit light when they are irradiated with a specific light source (Figure 1.2) [19]. Apart from the contrast enhancement, fluorescence microscopy also provides multi-colour imaging. It extends the modern biological imaging to numerous applications, including cell structure staining, immunofluorescence, sensitive and quantitative experimental cell research and quality control [20]. However, it has been observed in fluorescence microscopy that the majority of the fluorescence was affected by strong background signal no matter how well the focus was adjusted. This was later improved by the technique called confocal imaging which was firstly proposed by Nipkow and Minsky in 1957 [21]. A confocal microscope is able to filter out the “out-of-focus” light from above and below the focal plane on the sample. As a result, it provides both high resolution and contrast [22]. Developments in confocal microscopies have paralleled the rapid advances in fluorescence microscopies. The combination of fluorescence and confocal microscopy has been widely accepted as a powerful solution for biological imaging, and evolved into advanced microscopes such as laser scanning confocal fluorescence microscopy (LSCM) and, total internal reflection fluorescence (TIRF) microscopes. Figure 1.4 summarises the milestones in the development of microscopy.



Figure 1.5 presents some example images of four modern microscopy methods.



**Figure 1.4:** Key developments of microscopies in the history.



**Figure 1.5:** Example images of several advanced optical microscopies. (a) Bright field image of a human basal cell carcinoma stained with eosin and haematoxylin, (b) Phase contrast image of living HeLa cells in a plastic tissue culture vessel, (c) Differential interference contrast image of fixed Indian Mugjac cells, (d) Fluorescence image of endothelial cells of which nuclei, microtubules and filaments are blue, green and red stained. Images reprinted from Zeiss-campus [23].

Besides the microscope structure and illumination methods, imaging detection has also evolved, along with the development of optical detectors. Imaging detection and recording techniques have been utilised to replace the human observation

of samples, as well as storing and distributing images. Digital devices that convert photons into electrons to build up image pixels are most popularly used, for example photonmultiplier tube (PMT) and avalanche photodiode point detectors (APD), electron multiplying charged coupled device (EMCCD) and complementary metal oxide semiconductor array detectors (CMOS).

In the next section, microscope optics and the concept of magnification and resolution will be described.

### 1.3 Microscope optics, magnification

All modern microscopes rely on three functionally distinct elements, as shown in Figure 1.6: a light source, microscope optics and a detector. Illumination can be either simple natural light or an advanced artificial illumination system. Very basic microscope optics consist of an objective lens and a tube lens that provide image magnification. Detection can be completed using optical-electron devices for recording images.

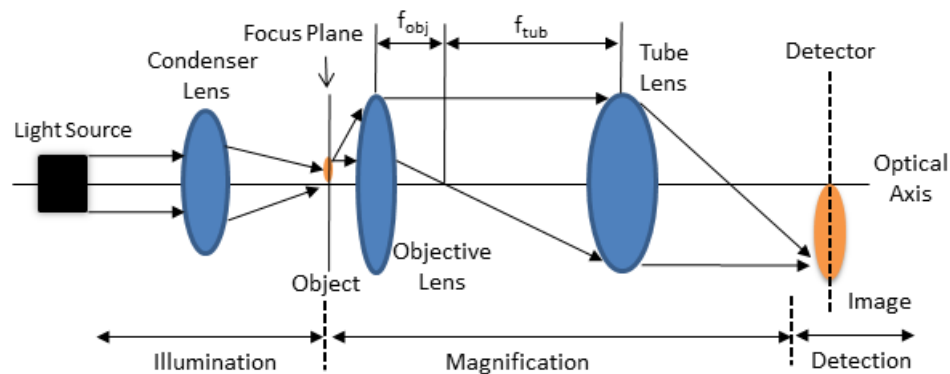


**Figure 1.6:** Basic components of modern microscopies

Microscope magnification is defined as the ratio of the image size to the real object size. To form a magnified image, the light from the sample through an objective lens is further made convergent again by a tube lens. Images are formed in the focal

plane of the tube lens. In this way, the objective lens and tube lens play a key role in achieving magnification. The magnification is physically determined by the focus length of objective and tube lens, which can be expressed as:

$$M_o = \frac{f_{tub}}{f_{obj}} \quad (1.1)$$

where  $f_{tub}$  and  $f_{obj}$  refer to the focal length of the tube lens and objective lens respectively. This indicates a theoretical unlimited large number of magnifications as long as an infinite large ratio of  $f_{tub}$  and  $f_{obj}$  is accounted for. However, it is limited by practical considerations, such as working distance and the microscope size, as well as the fundamental resolution limits of light microscope which will be further discussed. High magnification power of objective lens requires short focal length, which reduces the working distance (distance from the front of the lens to the object). For example, a Nikon oil 100 $\times$  lens has a focus length of around 0.15 mm. Longer working distance high magnification objective lenses are also achievable with higher cost. To date, the current widely used highest magnification of bioimaging microscope objective lens are 100 $\times$  or 150 $\times$ .

Resolution is also an essential parameter of microscopes, apart from just the magnification. It can be regarded as the ability to distinguish two objects, or the ability to provide details of the imaged object. A microscope might have a large magnification (strong ability to make the object appear bigger), however it does not necessarily mean that it provides a good resolution, owing to the different determinants. It is not difficult to magnify an object into a very large image, for example 100 $\times$ , 400 $\times$  or even 1000 $\times$  magnification. However, larger magnification does not make any sense without seeing more details. For instance, enlarging Figure 1.7c by 10 $\times$  wouldn't give great detail of the object than the image Figure 1.7b. A high resolution 100 $\times$  microscopy will show more detailed information than a 1000 $\times$  microscopy with low resolution. A suitable combination of magnification and resolution determines how much useful information a microscope can provide.

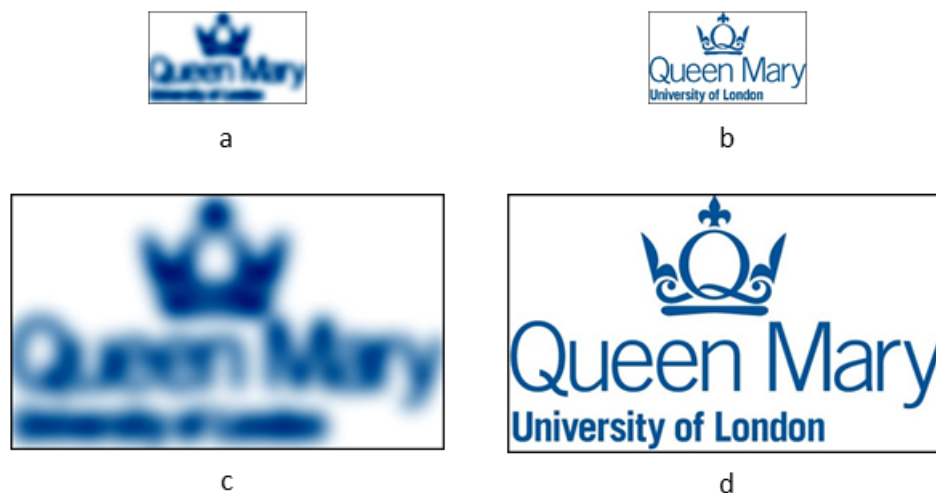


**Figure 1.7:** Magnification and resolution of optical microscopy images. (a) Low magnification, low resolution. (b) Low magnification, high resolution. (c) High magnification, low resolution. (d) High magnification, high resolution.

In order to understand the resolution limit, one must go beyond geometrical optics and consider the wave nature of light. This will be discussed in the next section.

## 1.4 Limits of resolution

Fundamentally, optical resolution is limited by optical diffraction due to the wave nature of light. Diffraction is the bending of light as it passes by objects or through an aperture. It naturally exists in our daily life and becomes noticeable when the object or aperture size is comparable to or smaller than the wavelength of the light. Diffraction has been explained by the Huygens-Fresnel wave theory (proposed by Christiaan Huygens and expanded upon by Augustin Jean Fresnel) which was developed between the 17<sup>th</sup> century to the mid-18<sup>th</sup> century. It stated that every unobstructed point on a wave front acts as a source of secondary spherical waves and the new wave front is the envelope surface to all secondary spherical waves (Figure 1.8). In a situation when either the light source or observation screen is located at a finite distance (comparable

to the light wavelength) to the aperture, it is called near-field diffraction (also known as the Fresnel diffraction condition). When both light source and observation screen are at a much greater distance or infinitely far from the aperture, it is called far-field diffraction (known as the Fraunhofer diffraction). In this case, all incident light rays into the aperture are approximately parallel to each other. Consider the Fraunhofer diffraction in a single slit of size  $a$  (Figure 1.8) for example. If light was not a wave and propagates as straight rays, there would be no diffraction pattern, just as that of geometrical optics (Figure 1.8a). However, according to the Huygens-Fresnel wave theory, all the light points reaching the slit will act as a source of spherical waves (orange, green, blue lines are sketched out as examples in Figure 1.8b). A diffraction pattern (Figure 1.8b) occurs as a consequence of the interference of these spherical waves.

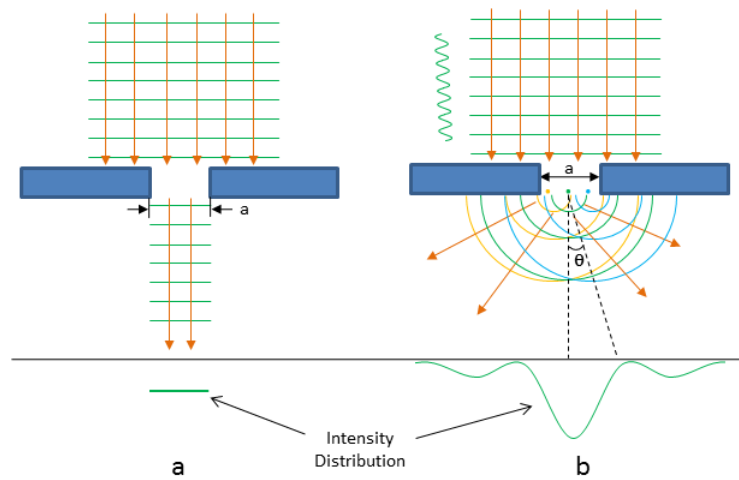


**Figure 1.8:** Propagating of light through a small aperture of size  $a$ . (a) Absence of diffraction pattern. (b) Spreading of light wave leading to a diffraction pattern when the wave nature of light is considered and Huygens principle is used. The diffraction pattern depends on the slit or aperture shape and size.

In far-field microscopes, Fraunhofer diffraction on the aperture of a lens system is the reason for the resolution limit. In most cases round lenses and apertures are used. This causes a ring-like diffraction pattern on the image to any point-like source (Figure 1.11), which is commonly referred to the Point Spread Function (PSF) in the spatial domain. The PSF describes what the microscope does to the object to produce

an image. The image formation can be seen as a signal processing of the microscope to the object function  $A(x, y)$  (Figure 1.9).



**Figure 1.9:** Image formation of microscope in the view of signal processing.

In the real space, the relationship between the image and object is described by a convolution operation<sup>4</sup> of the object function  $A(x, y)$  and the system PSF:

$$A'(x, y) = A(x, y) \otimes PSF \quad (1.2)$$

In frequency space, this is simplified to a multiplication of the Fourier transform of the object function  $F\{A\}$  and optical transfer function (OTF =  $F\{PSF\}$ ) [26]:

$$F\{A'\} = F\{A\} \cdot OTF \quad (1.3)$$

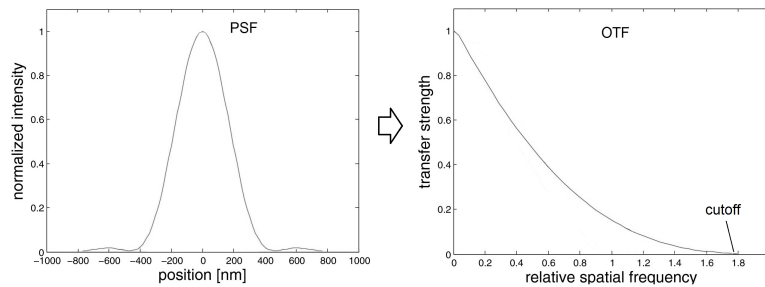


**Figure 1.10:** Normalised microscope point spread function (PSF) and optical transfer function (OTF). Figure modified from reference [27].

A typical PSF and OTF is shown in figure 1.10. The multiplication of  $F\{A\}$  and OTF results in a cutoff of high frequencies in the Fourier spectrum of the object.

---

<sup>4</sup>A mathematical operation normally expressed as  $\otimes$ , for more explanation see reference [24, 25].

For that reason, the imaging process can be seen as a low-pass filtering to the object, which blurs the fine structure of the object, thus reducing the resolution.

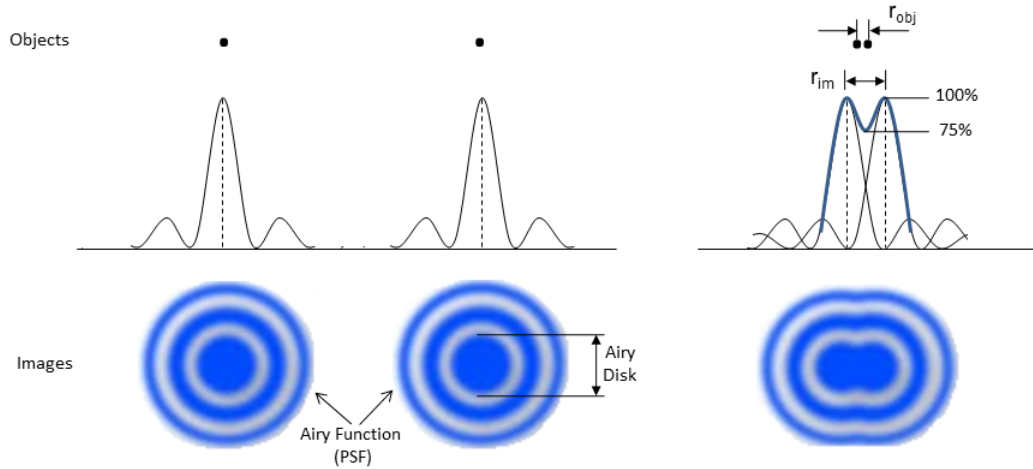


**Figure 1.11:** Points sources PSF and 1D light intensity function, (**Left**) two points are far away from each other, (**Right**) two points are overlapping on the image

In real microscope systems, the limit of resolution is related to the wave nature of light and the aperture size. The theoretical resolution limit of microscopes was established by Ernst Abbe in 1873 [28, 29] and Lord Rayleigh in 1874 [10, 30]. They realised the importance of the light wavelength and objective numerical aperture to the resolution. The term, “numerical aperture”, or NA of a microscope objective, was coined and defined by Abbe:

$$NA = n \sin \theta \quad (1.4)$$

where  $n$  is the refractive index in the objective space and  $\theta$  is half of the cone of light that can enter the objective.

In order to obtain the accurate expressions of resolution limit, there exist several mathematical models to describe the realistic PSF, for examples the Richards-Wolf model [31] that accounts for the wave nature of light, and the Gibson-Lanni model that take cover slips’ effect into consideration [32]. However, the formulas in these models are complicated and have brought too much computational complexity. Thus,

the Airy function, which is simpler for mathematical calculation while still providing good approximations to experimental data, has been used (Figure 1.11):

$$I(r) \sim \frac{\sin \beta}{\lambda} \quad (1.5)$$

in which  $\beta$ ,  $\lambda$  designates half of the opening angle of tube lens and the light wavelength [33, 34]. In the Airy pattern, the centre circle area with a radius defined by the distance between the centre maximum point of  $I(r)$  ( $r = 0$ ) to its first zero is named Airy disk. The Airy disk in the image plane can be calculated as:

$$r_{im} \approx \frac{0.61\lambda}{\sin \beta} \quad (1.6)$$

giving 84% of the total light of the complete distribution within this area. In order to find out the corresponding distance  $r_{obj}$  in the object plane, equation 1.6 must be divided by the corresponding microscope magnification  $M_o$ . Taking the Abbe sine condition of the objective and tube lens system into consideration that  $M_o \sin \beta = \sin \alpha$  where  $\alpha$  denotes half of the opening angle of objective lens, and the effective light wavelength in the immersion medium of index in  $n$  in object space,  $r_{obj}$  is calculated:

$$r_{obj} \approx \frac{0.61\lambda}{n \sin \alpha} = \frac{0.61\lambda}{NA} \quad (1.7)$$

where  $NA = n \sin \alpha$  is the numerical aperture of the objective lens.

Now we can look at an image produced by two neighbour point objects at distance  $r_{obj}$  (Figure 1.11). Their Airy disks are partially overlapping, and the centre maximum point of one reaches the first minimum of the other. In this case, the intensity in the middle between two maxima reaches about 75% of the maximum intensity (Figure 1.11). Although this value may be affected by lens quality, individual Airy disk intensity, detector sensitivity and signal-noise ratio, Lord Rayleigh suggested this distance  $d = r_{obj}$  should correspond to the lateral resolution limit because the human eye and many electronic optical detectors can still distinguish two separate



image points in this case. This has been named the “Rayleigh criterion” [10, 35]. Similarly, axial resolution is described by:

$$r_{axi} = \frac{2n\lambda}{NA^2} \quad (1.8)$$

In practice, however, the Airy function is still too complicated for biological imaging analysis. Consequently, simplified PSF - Gaussian functions have been employed because of their conceptual simplicity and computational efficiency, despite the lack of physical foundation [36, 37]. However, it has been pointed out [38] that use of Gaussian function to approximate a PSF may not always be adequate. For example, it has been argued that for emitters with a fixed dipole orientation Localization errors can reach up to 40 nm for typical optical system parameters and for aberration levels at the diffraction limit. Still, in case of the small (few nm) spherical (or nearly spherical) QDs the random dipole approximation is most appropriate and thus Gaussian function can be used. In terms of a description of the size of PSF, full width at half maximum (FWHM) of the fitting Gaussian function has been extensively used, especially in single molecule fluorescence microscopies.

As indicated in equation 1.7, the highest resolution that a traditional microscopy can achieve is obtained by assuming a high numerical aperture (typically  $\sim 1.4$ ) and visible light ( $\sim 550$  nm) and is around 200 nm. Nevertheless, this resolution cannot satisfy the majority of modern cellular scale biological problems, for example the observation of ribosomes ( $\sim 25$  nm), microtubules ( $\sim 25$  nm) and cellular protein transportation activities (less than 100 nm).

To address the resolution limit problem in biological imaging, super-resolution microscopy methods, which have broken the diffraction limit and brought the light microscopy resolution ability down to several nm, have been developed since the late 1980s. This will be described in the next section.

## 1.5 Super-resolution imaging

Microscopes already achieved  $\sim 1\mu\text{m}$  resolution by the early 1800s, even before the diffraction limit theory was established. Since then, it hasn't been significantly improved, until the late 20th century, when super-resolution light microscopy techniques were developed and achieved to a resolution below  $\sim 200$  nm or even down to the scale of a few nm. Super-resolution imaging techniques make it possible for optical observation for cellular structures and cell activities below the diffraction limit ( $\sim 200$  nm). A brief review of the super-resolution strategies is given in this section. Resolution levels and limitations for each method are described. Then single molecule localisation based super-resolution imaging method is explained. Current limitations and frontiers of the single molecule localisation super-resolution microscopies are described.

### 1.5.1 Developments in super-resolution imaging strategies

It is clear that a short wavelength light source is able to produce a high resolution (as indicated in equation 1.7). Consequently, many short wavelength microscopes were developed, for example ultraviolet fluorescence microscope was invented by August Köhler in 1904. It hasn't been widely accepted in biological imaging due to the great harm of ultraviolet to biosamples and limited improvement in resolution. Another technique achievable through - electron microscope (EM), invented by M. Knoll and E.A.F. Ruska in 1931, who constructed a microscope using electron beams, has been used to visualise cellular structures smaller than 200 nm [39]. The electron beam plays a role of forming images of the specimen objects just similar to the light beams in light microscopy [40, 41]. It provides a resolution as high as 0.1 Å because of the short wavelength of the electron beam [42]. EM has several practical issues that limit its usage in biological imaging. The issues come from the electron beam that carries electron charges, which as a result, requires a fixed, dehydrated and thin section sample to be imaged in a vacuum. Therefore, it is not suitable for live cell imaging

and multi-colour imaging. Besides the method of shortening the wavelength, near-field scanning microscopy (NSOM) has also been demonstrated to address the diffraction problem by placing the imaging aperture close (within one wavelength of light) to the object, to obtain the sub-diffraction resolution before light spatially diverges [43]. However, this method is limited to the very surface of a sample.

On the other hand, far-field optical super-resolution microscopies have also been rapidly developed since the first inventions occurred in the 1980s. These innovations can be divided into three types. One of the strategies is based on increasing the effective NA of an optical system to enhance the resolution. For instance, 4Pi-Microscopy proposed by Stefan Hell who used two opposing objective lenses for sample illumination by two coherent laser beams, and achieved remarkable improvement in axial resolution by a factor of seven [44]. A similar approach, but with an additional illumination path named I<sup>5</sup>M microscopy was later reported with five to seven fold improvement in axial resolution compared to conventional microscopy [45, 46]. However, these axial interferometric techniques provided very little improvement in the lateral resolution (as also can be seen from equations 1.7 and 1.8), because improving the effective NA will improve axial resolution more significantly than lateral resolution.

Another type of resolution enhancement is based on modifying sample illumination. This type of methods either directly shrinks the PSF size thus making equation 1.7 not applicable any more, or modulate the illumination so that the object information below the diffraction limit can be interpreted through modulation patterns. For example, in 1994 Stimulated Emission Depletion (STED) method was developed by Stefan W. Hell and Jan Wichmann (Figure 1.12), which suppresses the fluorescence emission from the probes located off the centre of the excitation by illuminating them with an extra annular laser beam after a normal excitation laser beam. In this method, only probes at the null (centre) of the donut-shaped STED beam remain fluorescence excited, resulting in an extremely small fluorescence area (Figure 1.12)

[47]. With STED depletion, a smaller effective PSF size is obtained in the expression:

$$\Delta_{eff} \approx \frac{\Delta}{\sqrt{1 + I/I_s}} \quad (1.9)$$

where  $\Delta$  refers to the diffraction-limit size of PSF,  $I$  is the crest intensity of the donut-shape beam, and  $I_s$  is the STED intensity used to reduce the fluorescence intensity by one-half [48, 49]. Even though there is no theoretical resolution limit according to this formula, in practise photodamage of the sample restricts the depletion light intensity at a safe value, particularly for biosamples. Typical resolution in biosamples using STED is  $\sim 70$  nm.

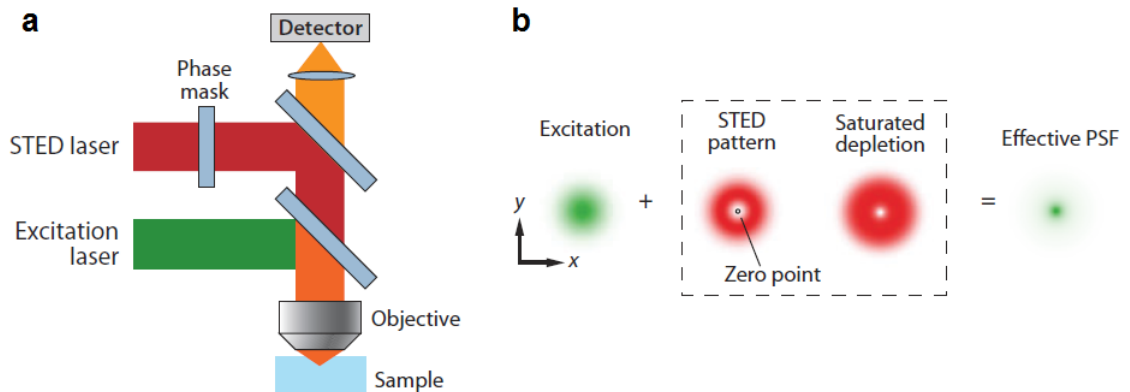


**Figure 1.12:** The principle of stimulated emission depletion (STED) microscopy. (a) Schematic of a STED microscope. An excitation laser and a STED laser are combined and illuminated on the sample through the objective. A phase mask is put in the optical path of STED laser to generate a donut-shape STED pattern. (b) Laterally on the sample, the STED beam is applied with the centre zero-point overlapping with the centre maximum of the excitation laser beam. With saturated depletion of the STED beam to the fluorescent probes, only fluorescence from regions near the zero point is suppressed, resulting in a decreased size of effective point spread function (PSF). Figure reprint from reference [50].

In 1997 and subsequent years, Structured Illumination Microscopy (SIM) was invented, making use of a known spatially structured illumination light and nonlinear dependence of the fluorescence emission rate on the illumination intensity (Figure 1.13) [51].

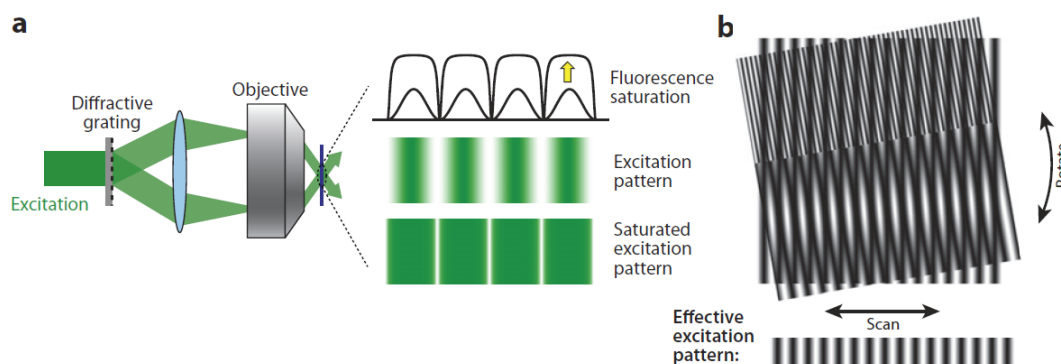
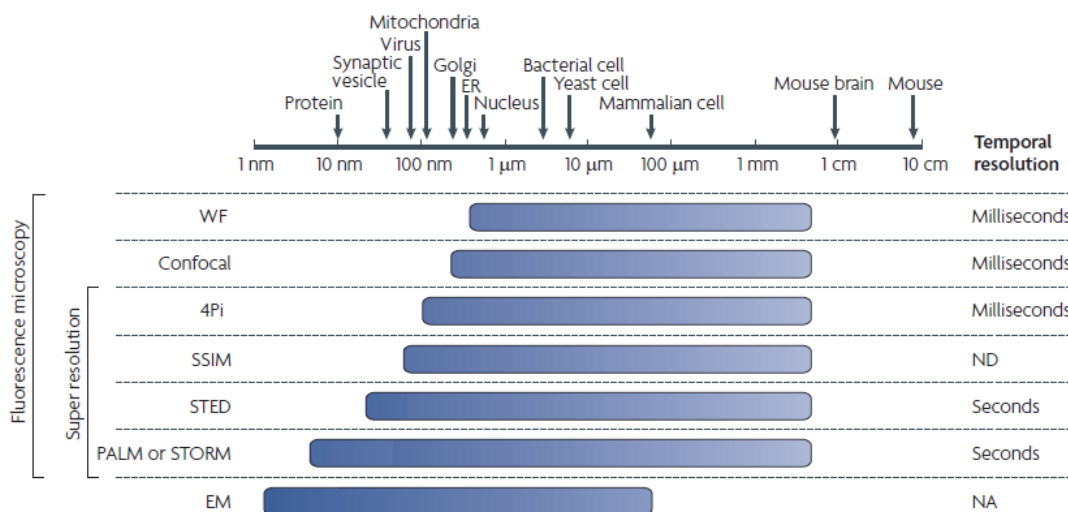


**Figure 1.13:** The principle of structured illumination microscopy (SIM). **(a)** Generation of the illumination pattern. A diffraction grating is placed in the excitation optical path splitting the light into two beams. Their interference after emerging from the objective reaches the sample and creates a sinusoidal illumination pattern with alternating peaks and zero stripes. Strong excitation light saturates the fluorescent probes at the peaks without exciting the ones at zero points, resulting in sharp dark regions as an excitation pattern. **(b)** Resolving sub-diffraction structures with SIM. When a sinusoidal illumination pattern is applied on a sample, a moiré pattern at a significantly lower spatial frequency than that of the sample will appear. Multiple images are generated by scanning and rotating the excitation pattern, which are then used to reconstruct a high resolution image of the sample structure. In this way, sample structures with higher spatial frequency than the illumination pattern still remain unsolvable due to the mixing of moiré patterns. Figure reprint from reference [50]

SIM has been reported to have a good capability for 3D imaging and has also been extended to multi-colour imaging [52, 53]. This makes SIM a well-accepted technique in 3D super-resolution imaging. With regards to resolution, a factor of two improvements in lateral resolution was achieved with SIM in 2000 [54]. In 2005, Gustafsson improved the resolution to 50 nm using non-linear structured illumination [55]. This has been the highest resolution achieved in biological imaging with SIM to date.

Finally, the last type of strategies is single molecule localisation microscopy, which relies on the separation of emission signals of fluorescent probes, followed by precise localisation of single probes with subsequent image reconstruction, thus achieving

higher resolution [56, 57]. This family includes Stochastic Optical Reconstruction Microscopy (STORM) reported in 2006, which uses fluorescent dyes as a stochastic fluorescent probe to obtain a small portion of fluorescent molecules during an image frame capturing, so that molecules are well-separated and can be reconstructed through a computational process [58]; Photo-activated Localisation Microscopy (PALM) reported in 2006 is similar to STORM but proposes fluorescent proteins as the probes [59]; Spectral Precision Distance/Position Determination Microscopy (SPDM) published in 2008 [60], introduced spectral separation of the overlapping diffraction spots instead of temporal separation as has been accomplished in STORM and PALM methods; Spinning Disk microscopy for Super-resolution Imaging (SDSI) proposed in 2013, which is a combination of STORM/PALM and spinning disk confocal microscopy [61]. In these methods, accurate positions of the fluorophores are localised by computational processes on each diffraction spot. Repetition of imaging cycles stops when the majority of the fluorophores' positions are expected to be localised. Super-resolution image is then obtained by addition of all the high accuracy localisations. Super-resolution strategies based on similar localisation such as STORM, PALM, SPDM, SDSI are therefore termed "localisation super-resolution microscopies". Lateral resolutions of 20 nm and even below 10 nm have been reported on biological samples [58, 62].



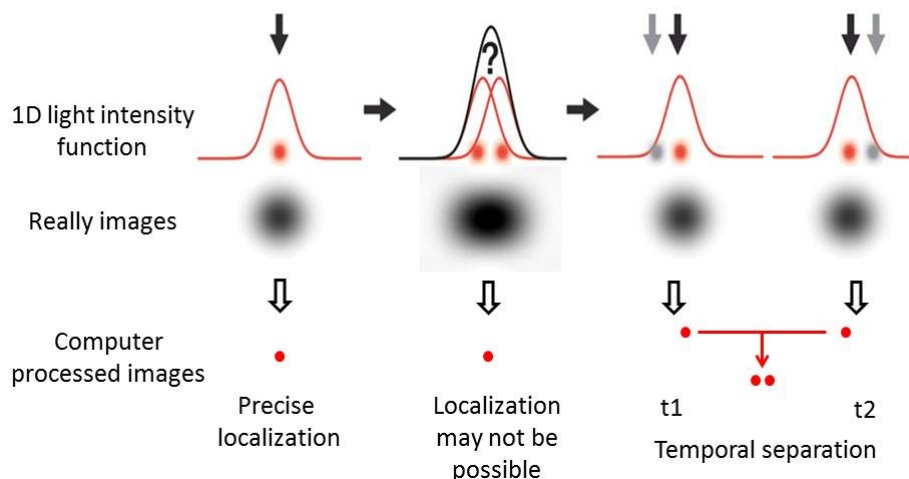
**Figure 1.14:** Spatial and temporal resolutions of some main super-resolution techniques. Figure modified from reference [63].

Figure 1.14 shows a summary of the spatial and temporal resolution of various super-resolution techniques. Optical modulation methods are reliable but still with limited resolution ( $\sim 50 - 70$  nm). Localisation super-resolution imaging methods are able to achieve super high resolution (several nm), and are easy to be carried on conventional fluorescence confocal microscopes. This great significance of far-field super-resolution imaging techniques mainly comes from the biological applications which link the subcellular world with the human world. This great significance could also be seen from the fact that the 2014 Nobel Prize for Chemistry has gone to Eric Betzig, Stefan Hell and William Moerner for developing super-resolution microscopy techniques based on the fluorescent molecules.

In this thesis, single molecule localisation based super-resolution microscopy is investigated with the usage of QDs, using commercially available fluorescence confocal microscopes. Localisation super-resolution strategy is described in more details in the next subsection.

### **1.5.2 Single molecule localisation super-resolution imaging**

The basic principle of single-molecule-based super-resolution microscopy is that the position of a fluorescent probe can be determined with a precision much higher than the width of the PSF when its individual fluorescence image is obtained. Single-molecule detection is the first step in locating the molecule beyond the diffraction limit. This concept was initially demonstrated in 1989 at liquid-helium temperatures [64, 65]. Figure 1.15 presents the basic idea of single molecule localisation super-resolution imaging strategy.



**Figure 1.15:** Temporal separation single molecule localisation super-resolution imaging strategy. **(Left)** Only a single molecule image is captured. The molecule can be localised at a high precision by computational process. **(Middle)** Two molecules are physically too close so that their images are too much overlapping to be identified. This leads to the resolution limit in light microscopy. **(Right)** Two molecules are physically too close, but their images are temporally separated and captured at different time so that each of them can be localised precisely. In this way, the molecules are resolved beyond the diffraction limit.

As seen in Figure 1.15, the top row shows fluorescent probe molecules (size of  $\sim 10$  nm or even less) and their fluorescent emission intensity distribution in 1D and 2D (middle row) which is the diffraction spot usually at the size of  $\sim 200$  nm in a typical confocal microscope. From left to the right as shown, following the array, the figure presents three situations. In the left situation where only a single molecule is being imaged, its diffraction spot image can be characterised and the actual position of the molecule can be precisely localised by computational processing. In the middle situation of two molecules that are too close to each other (distance less than  $\sim 200$  nm), their diffraction spots will overlap on the image, resulting in not being resolvable any more because the Rayleigh criterion will not be met. In the right situation of super-resolution approach, two molecules are close with each other, but only one molecule is imaged at time ( $t_1$ ), so that only one diffraction spot is obtained which allows high accuracy localisation of this molecule. Then the other molecule is imaged



at another time ( $t_2$ ) and being localised precisely as well. In the case of more than two molecules within a diffraction limited region, the imaging procedures are repeated again and again in order to collect as many single molecules as possible. Typically with thousands of images, a super-resolution image which resolves the molecules within a given area is reconstructed by putting all the localisations together into one image. Thus this approach can be regarded as a temporal super-resolution method. It is important to ensure imaging no more than one molecule within a diffraction limited region at any given instant. This becomes a fundamental criterion of single molecule assumption in this super-resolution imaging strategy.

As to the experimental realisations, this approach was independently reported by three research groups in 2006 with the names of STORM or (f)PALM [58, 66, 67] and a resolution of 20 nm was demonstrated for RecA-coated circular plasmid DNA [58]. In practise, STORM/(f)PALM similar methods require only a standard light microscope. To ensure a sufficient number of fluorescent emission events being collected for super-resolution reconstruction, images must be acquired at fast frame rates with good signal-to-noise ratio. This can be challenging to biological samples in widefield illumination due to the photo-bleaching of the probes and the effects arising from the fluorescence light above and below the focal plane. Total Internal Reflection Fluorescence (TIRF) overcomes these problems by using an evanescent wave that only illuminates a thin ( $< 100$  nm) optical section at the immersion oil and cover slip interface (Figure 1.16) [68]. The physics underlining TIRF illumination is that when a light beam is propagating from one medium of high index of refraction  $n_2$  into another medium of low index of refraction  $n_1$  and if the incidence angle ( $\theta$ ) is equal or greater than the critical angle  $\theta_c$ , the beam undergoes total internal reflection. This can be derived from Snell's law [69] and expressed in an equation:

$$\theta_c = \arcsin \frac{n_1}{n_2} \quad (1.10)$$

Some of the energy of in the incident light creates an evanescent field at the interface.

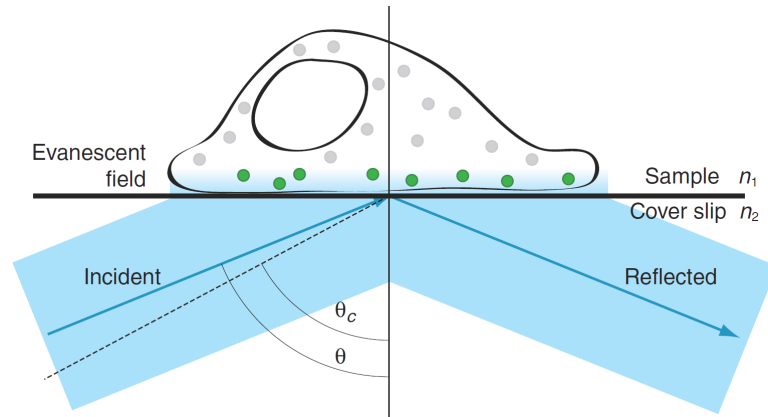


**Figure 1.16:** The principle of TIRF illumination. The excitation beam enters from the left angle  $\theta$  which is greater than the critical angle  $\theta_c$ . Angles are measured from normal. The excitation beam is reflected off the cover slip-sample interface and an evanescent field is generated on the opposite side of the interface. As a result, only fluorophores in the evanescent field are excited. Figure reprinted from reference [68].

This electro-magnetic wave has the same wavelength with the reflected light and its intensity decays exponentially perpendicular to the surface. Due to this decay, the fluorescence excitation of the evanescent field is limited on the very surface of the interface typically below 100 nm. The excellent signal-to-noise ratio this achieves makes TIRF a standard method for SOTRM/(f)PALM type imaging. However, TIRF is not appropriate for all biological sample due to the limited imaging depth. The structures further away from the surface of the cover slip than 100 nm, such as the cell nucleus and mitochondria, can not be imaged using TIRF. Recent research has tried to reduce this problem by introducing a ‘near TIRF’ illumination method called highly inclined laminated optical light sheet (HILO) which use an intense laser, angled through a high numeric aperture objective [70]. Unfortunately, HILO only increases the light penetration depth to 500 nm, so cellular structure that are 2 – 3  $\mu\text{m}$  inside the cells such as the nucleus and Endoplasmic reticulum still can not be imaged. In our research we used confocal microscopy approach to be able to control penetration depth and to be able to utilise flexibility in using fixed cells (since using TIRF places very specific requirements on refraction index of the mounting medium, see Equation 1.10). Confocal microscopy will be described in details in section 1.7.2.

In single molecule localisation super-resolution imaging methods, the key component is the fluorescent probes which can be optically turned ‘on’ and ‘off’ so that they can be selected to image at different temporal points. Furthermore, at any instant, there should be no more than one probe within a diffracted region. Otherwise, false localisations may arise. However, in real biological applications, the single molecule imaging essentially relies on the stochastic process (for example photo-switching, photo-activating and blinking) of the molecules. Some closely located molecules may emit light at the same time. Some molecules may be imaged more than once, while some may be never imaged. All these will increase the uncertainty of the molecule localisations, which as a result will affect the final resolution.

The final resolution in this method is mainly determined by three factors: (i) the probe size; (ii) localisation precision; (iii) labelling density. The probe size is important as one cannot expect the resolution of better than 20 nm if 20 nm size probes are used for fluorescence labelling. Localisation precision limits the resolution by determining how well each probe can be localised. There have been several models to calculate the exact expression, such as the maximum likelihood estimation [71], and the Monte Carlo simulations [72]. One widely accepted formula is given by:

$$\delta \approx \frac{s}{\sqrt{N_p}} \quad (1.11)$$

where  $\delta$  is the single molecule localisation precision,  $s$  is full width at half maximum of PSF, and  $N_p$  is the photon number. According to this, microscopes with small PSF and bright probes (more photons from each probe) and are expected to deliver a high resolution. Nevertheless, this equation is too optimistic as it does not take into account of noise. A full formula is given in section 3.2.2.1 which does include the effect of the background and noise onto the single molecule localisation precision. In many cases, the localisation precisions also varies depending on the use of different detectors (for example CMOS, CCD, EMCCD) and the noise model for each detectors have to be taken into consideration in order to obtain a better understanding of the

localisation capability and limitations [73].

The effect of labelling density on resolution has been quantified by the Nyquist sampling criterion, which states that structures smaller than twice that of the probe-to-probe distance cannot be reliably resolved [74–76]. The smallest resolvable feature size on an image is determined by:

$$\Delta_{Ny} = \frac{2}{N^{1/D}} \quad (1.12)$$

where  $N$  is the density of labelling,  $D$  is the dimension of the structure that is to be imaged. According to this formula, to achieve a 20 nm resolution on a 2D image, a labelling density of  $10^4$  per  $\mu\text{m}^2$  is required. In the laboratory however, a lower density may be sufficient considering the geometry of the sample. This will also be crucially affected by the availability of the biological epitope for labelling and the number of the fluorophores on the probes.

There are a number of challenges in single molecular localisation super-resolution microscopy. These include, among other things, long data acquisition time. In order to obtain a sufficient number of localised probes, photo-switching and imaging procedures are repeated in many cycles, which is typically more than 10000 times. These repetition procedures are time-consuming which means that the data acquisition can take too long (i.e. seconds to minutes). The sample drift problem may become significant on such timescales in biological applications, which will be further discussed in the results section 3.2.2.3. This means the methodologies are suitable only for imaging of fixed cells, as many biological processes occur faster than the time taken to acquire a super-resolution image [61].

Suitable fluorescence probes are one of the key elements of single molecular localisation super-resolution methods. In the next section, fluorescent probes in cell imaging are introduced and compared. Then we will focus on QDs because of their unique optical properties in application of fluorescence imaging.

## 1.6 Fluorescent probes

In this section, current major fluorescent probes - fluorescent protein, dyes and quantum dots - will be introduced and compared, from the light emission mechanism underlying the fluorescence, to the optical performance in the use of fluorescence imaging.

### 1.6.1 Types of probes

Fluorescent probes can be broadly subdivided into several categories depending on the nature of the light emission and sample structure: fluorescent proteins, chemical dyes and QDs. In fluorescent proteins and chemical dyes the mechanism of the light emission is related to the conformational changes (changes in molecular shape) [77, 78]. In QDs, it is the pure electron transitions between different energy states. Figure 1.17d-e indicates the differences between proteins, dyes and QDs. Another important aspect is the quantum yield (QY,  $\eta$ ). Quantum yield refers to the ratio of photons absorbed to photons emitted through fluorescence. For example, a value of 50% means half the number of the excitation light photons result in fluorescence emission. Obviously, high QY corresponds to a high probability of the fluorescence transition, which means strong fluorescence.

Fluorescent proteins are cell proteins that can emit fluorescence light. They are large biological molecules consisting of long chain of polypeptides (Figure 1.17a), which results in a total size of 5 - 200 nm [82]. The revolution that fluorescent proteins have brought to cellular labelling and fluorescence imaging can be seen from the countless break-through publications since the discovery and wide spread use of Green Fluorescent Protein (GFP) in 1962 [83]. The importance of this innovation has also been evidenced by being awarded of Nobel Prize in Chemistry in 2008.

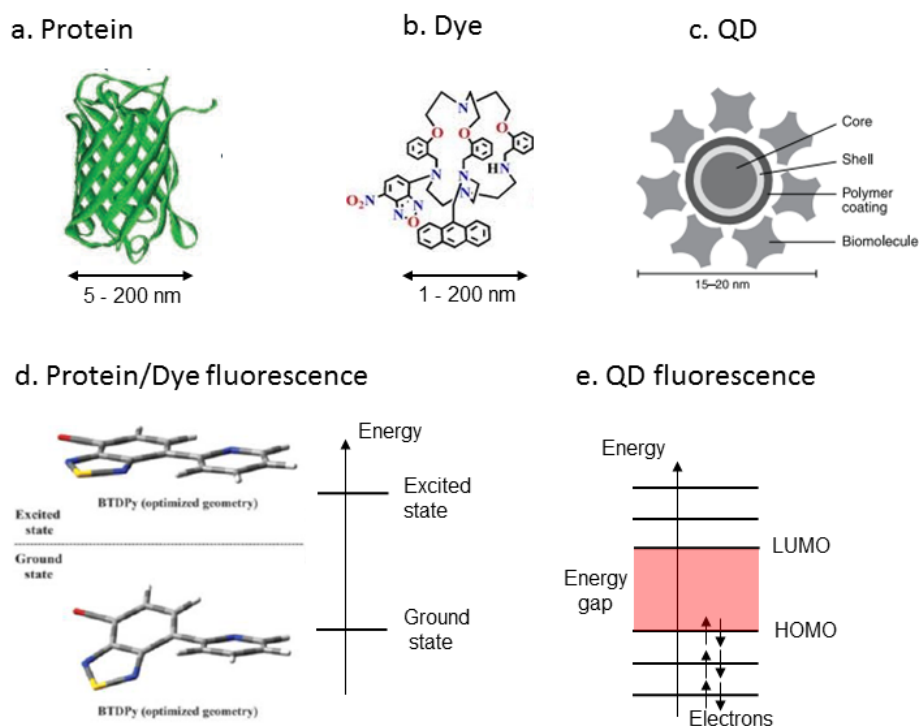


**Figure 1.17:** Fluorescent probe structures and fluorescence mechanism. Upper panel shows the structure and size difference between fluorescent proteins (**a**, long chain of polypeptides), fluorescent dyes (**b**, organic groups), QDs (**c**, nonorganic atom-like nanoparticles). Lower panel indicates the fluorescence mechanism difference between protein/dyes (**d**, structure changes) and QDs (**e**, electron transition between energy gap) [63, 79–81].

One of the biggest advantages of fluorescent protein is that they are genetically encodable and are straightforward for specific cellular structural labelling, such as lysosomes, and mitochondria [66]. Nowadays, the fluorescent proteins family has been expanded to a wide range of derivative products, including non-fluorescent-switchable proteins such as GFP and RFP [84], and fluorescent-switchable proteins like CFP, Eos, Dronpa, mCherry [62, 85–87]. QY of GFP has been reported to be 79 % to 85 % [88]. Fluorescent proteins allow live cell imaging and have a very good specificity, however they can cause problems to protein function and problems associated with over expressions [89].

Fluorescent dyes have provided an alternative fluorescence labelling solution to proteins, in terms of the small structure, high QY (more than 90 % [63]) and good

stability in cellular environment [63]. Dyes are small organic molecules (generally aromatic molecules) with fluorescent group or chemical bounds, such as Fluorescein, Quinine, Rhodamine [79], which are usually 1-10 nm in diameter. Advanced functional fluorescent dyes include derivatives from green-color-emitting products such as Carboxyfluorescein [90], to orange-colour-emitting products such as ATTO532 [91], and even red/near IR-colour-emitting products such as Rhodamine B, Cy5, Cy7 [92, 93]. When compared to fluorescent proteins, dyes have higher quantum yield which results in brighter probes with higher numbers of photons per molecule. Moreover, immunostaining allows the visualisation of endogenous proteins. However, immunostaining requires fixed cells and can lead to non-specific binding.

QDs are light-emitting nanoparticles (normally 1 ~ 50 nm) that rely on the confinement of the charge carriers (electrons and holes) as the mechanism behind the light emission. Emergence of QDs as novel fluorescent probes has attracted much attention since their application on live cell imaging [94, 95] and correlative imaging [96] during the last twenty years. QY of QDs can be as high as 70 % [97].

The majority of fluorescent proteins and dyes show comparatively narrow absorption and emission spectrum that often mirror each other with a small Stokes shift (Figure 1.18d-f). The poor separation between absorption and emission spectra brings cross-talk between different probes (also known as the spectra bleed-through problem in fluorescence imaging). In addition, a specific excitation light source is needed for each dye because of the narrow absorption. This causes a lot of additional requirements to the illumination system in multi-colour imaging using several dyes. In comparison to proteins and dyes, QDs show the attractive property of a broad absorption while exhibiting narrow emission spectrum (Figure 1.18a-c). Emission spectrum peak position is tuneable by changing the QDs size (this is due to the quantum size effect which will be further discussed in section 1.6.3.1). Figure 1.18 shows the spectra of three types of QDs (CdSe, CdTe and InP) and chemical dyes (Cy3, Cy5, MegaStokes dyes and Nile Red dyes). From this point of view, QDs show high compatibility with multi-colour imaging.

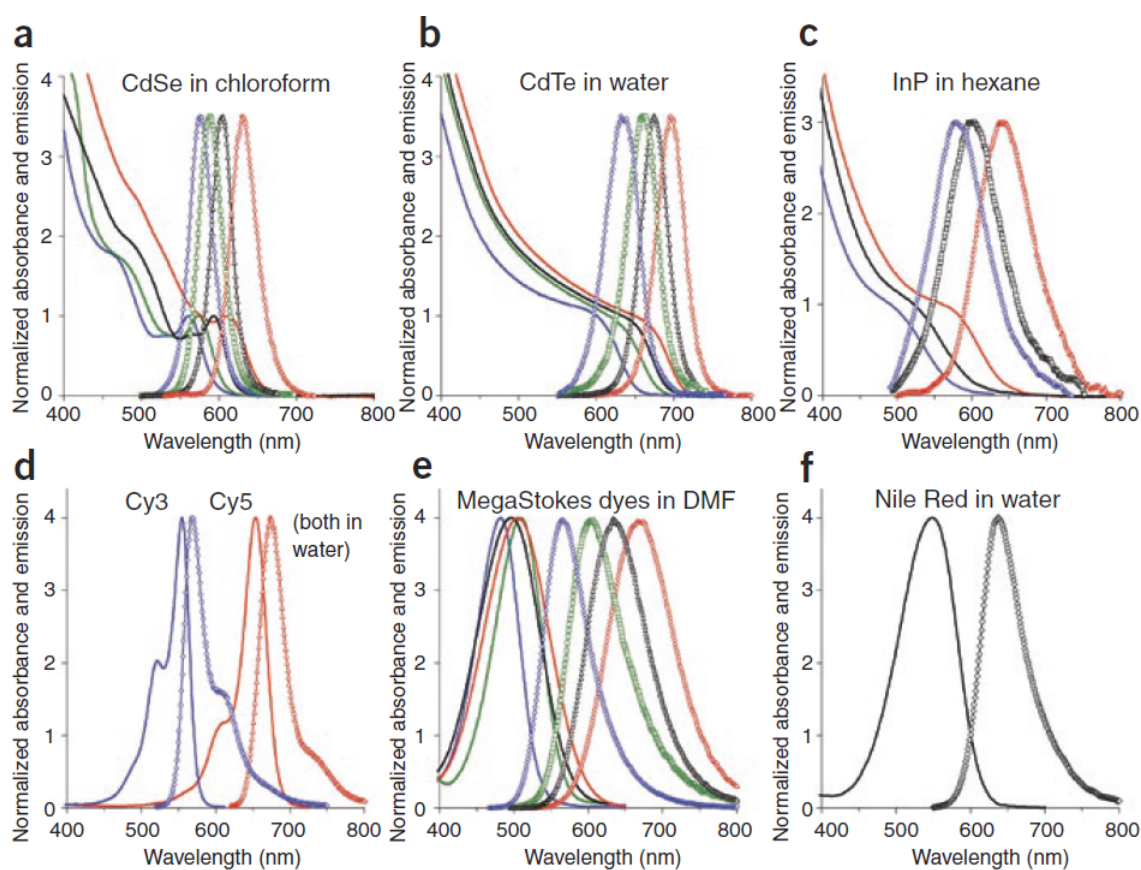


**Figure 1.18:** Excitation (lines) and emission (dot lines) spectrum of QDs (a - c) and chemical dyes (d - f). Colour were coded by molecule size (blue|green|black|red). MegStokes dyes were prepared for spectral multiplexing in dimethylformamide (DMF). Data reprinted from reference [97].

Another problem with dyes and proteins is photo-bleaching. In these systems the transition between a fluorescent and non-fluorescent state is due to structural changes. These multiple structural changes eventually result in weakening of the corresponding bonds and breakdown of a molecule. This causes the photo-bleaching phenomenon when the fluorescence intensity becomes weaker and weaker as a function of photo-switching/photo-activating repetition or illumination time. Photo-bleaching is often an important factor that limits the imaging of biological samples, particularly for long-term imaging. Bleaching behaviour can be exponential or non-exponential, depending on the chemical environment and structure (bound or free) of probes [98]. There are antiphotobleaching strategies, such as by reducing the amount of oxygen in the sample to prevent the bleaching to some extent, but most of them can be rather



**Table 1.1:** Optical properties comparison between proteins/dyes and QDs

Properties	Proteins/Dyes	QDs
Fluorescence mechanism	Structure change	Electron transition
Size	1-200 nm	1- 50 nm
Excitation	narrow	wide
Emission	narrow	narrow to wide*
QY( $\eta$ )	up to 95%	up to 70% [97]
Photobleaching	Yes	No
Biocompatibility	Good	Good

\* Depends on QDs size distribution

toxic for live cells.

In QDs, transitions between the excited and ground energy states are purely electronic and are completed without geometrical structural changes [81] which will be further illustrated in section 1.6.3.2. QDs are much more photo-stable than proteins and dyes and have been demonstrated to show negligible photo-bleaching [97, 99]. Examples are shown in Figure 1.19, in which QDs show no fluorescence decay even after 180 seconds while Alexa 488 dyes show almost no fluorescence signal. Table 1.1 lists the main differences between proteins/dyes and QDs.

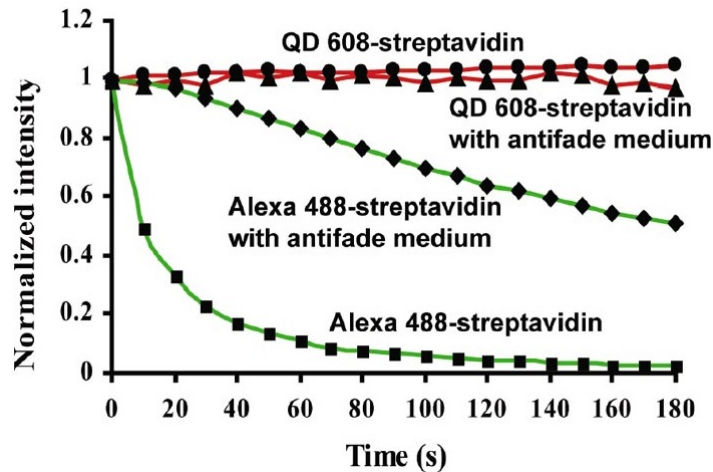


**Figure 1.19:** Photo-stability comparison between QDs and Alexa 488 dyes. QDs and dyes were labelled to nuclear antigens and microtubules respectively in one cell. Data reprinted from [100].

The emerging development of QDs with unique optical and chemical properties has been one of the most exciting advances in fluorescence imaging, to overcome spectra bleed-through and photo-bleaching problems and bring in additional benefits such as multi-colour imaging. However, it has been debated that QDs suffered from relatively low quantum yield and high cell toxicity, as well as very small number of commercially available choices. Efforts have been made to overcome these challenges to some extent by surface modifications and using biofriendly materials, such as germanium and silicon. The use of QDs is dramatically increasing, which in return also drives the improvements of QDs.

In the next section, a general description of QDs light emission mechanisms will be given.

### 1.6.2 Fluorescence mechanism

The fluorescence mechanism is depicted in a simplified Jablonski diagram<sup>5</sup> [101–103], as shown in Figure 1.20. The electronic singlet ground state,  $S_0$ , is described as a series of energy sublevels. Similarly, the first excited singlet state is described as  $S_1$ , the second as  $S_2$ . In the absence of radiation, these states are populated according to Fermi statistics. Ground state singlets are fully occupied by paired electrons (two opposite spin electrons) and the system has a minimum energy, and is therefore stable. The formation of the excited states is derived from the interactions of atoms.

Once a photon whose energy matches (or is greater than) the energy gap between an excited state and ground state is absorbed (indicated as Abs. in Figure 1.20), a carrier (electron) will transit to an excited state. The carrier quickly relaxes ( $\sim 10^{-12}$  s) to the lowest sublevel in the first excited state through vibrational relaxation (gray arrow) or internal conversion (ICo.). At this point, the carrier might relax back to

---

<sup>5</sup>Aleksander Jablonski was a Polish academic who devoted his life to the study of molecular absorbance and emission of light. He developed a theory that generally shows a portion of the possible consequences of applying photons from the visible spectrum of light to a particular molecule. These schematics are referred as Jablonski diagrams

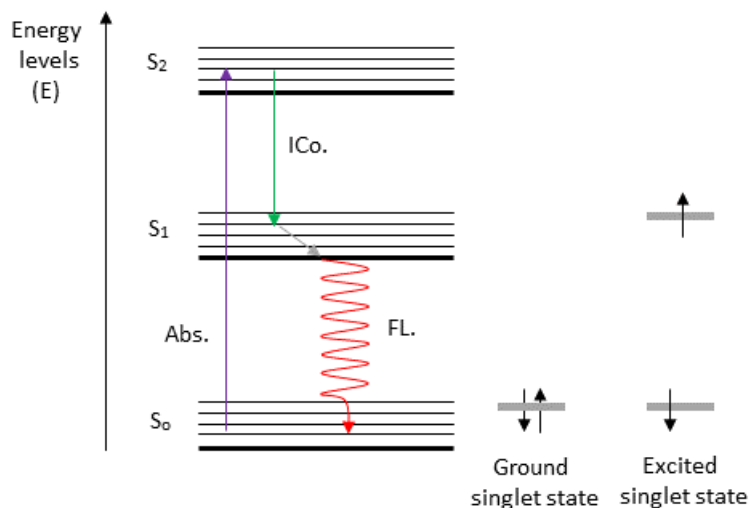


**Figure 1.20:** Jablonski diagram for fluorescent QDs.

the ground state by emitting fluorescence light (Fl.) in 1 - 10 ns. Also, electrons can transit back to the ground state through phosphorescence. The possibilities of each transition depend on their timescales. The faster the transition, the more likely it is to happen as determined by selection rules. Table 1.2 lists the timescales of the molecule transitions in the Jablonski diagram [101].

**Table 1.2:** Timescales of the basic radiative and non-radiative transitions involved in the Jablonski diagram.

Transition	Timescale (s)	Radiative process
Absorption	$10^{-15}$	Yes
Internal conversion	$10^{-14}$ - $10^{-11}$	No
Fluorescence	$10^{-9}$ - $10^{-7}$	Yes

In the next section, the discussion will focus on the QDs quantum mechanism underlying the light emission, their optical features, and particularly Ge QDs.

### 1.6.3 Quantum dots and bioimaging

Quantum dots are desirable for a wide range of medical studies and bioimaging applications, such as dynamic cellular imaging and medical diagnostics. For example, QDs labelling and imaging have revealed the complex workings of cell membrane receptors at high resolutions [104, 105]. Peptide-conjugated QDs have been used to examine the complex behaviour of nanoparticles in live cells [106]. Moreover, the unique optical properties of QDs can significantly enhance the sensitivity of bio-diagnostic assays such as in immunohistochemistry (IHC), fluorescence in situ hybridisation (FISH), flow cytometry and biochips [100, 107, 108]. Particularly, QDs are also providing benefits in the application of super-resolution cell imaging. Figure 1.21 summarises the main usage of QDs in medical and biological imaging.

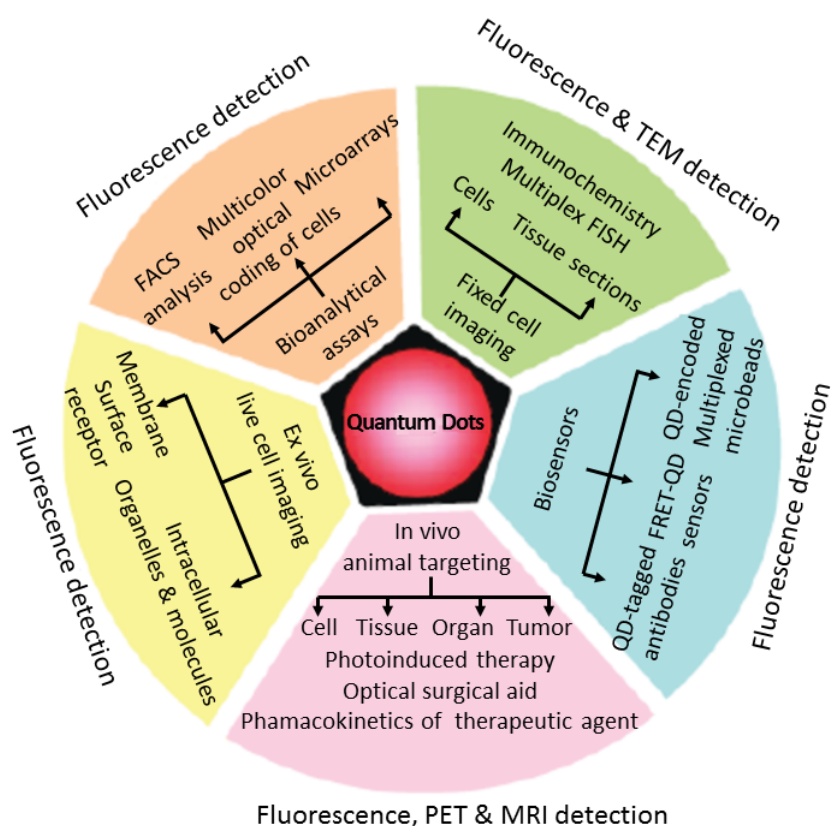


**Figure 1.21:** Current applications of quantum dots as fluorescent probes. Usage of QDs are wide and promising, particularly in fixed/live cell imaging, tissue targeting and tracking, bio-sensing and bioanalytical assays [109].

A schematic diagram of a typical bioimaging QD probe is shown in Figure 1.22. The core is the key component where the fluorescence originates from. It is typically made of II-VI, III-V materials (e.g CdSe, CdS, CdTe, PbS, InP). An external shell (e.g ZnS) plays an important role including improving the quantum yield, restricting the release of toxic core materials (Cd, In). Coatings (for example Polymers, Carboxyl) are generally introduced to improve functionality (stability, bioconjugation and specific targeting) [109].

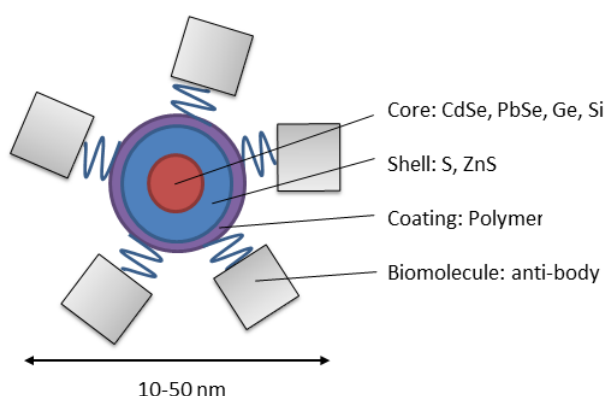


**Figure 1.22:** A typical core-shell type bioimaging quantum dot structure

Core-shell type QDs are most frequently used in biological fluorescence imaging. Meanwhile, core type QDs (QDs without a shell) also attract a lot of attention due to their small size [110], even though they may become less stable or there may be higher cell toxicity, such as core type CdS, CdSe QDs [111]. These problems can be solved or reduced by using biofriendly materials (e.g. C, Si, Ge) with an appropriate surface termination [112]. For example, core type Si QDs and core type Ge QDs have been reported to show better biocompatibility than CdSe based core-shell type of QDs at the same concentrations [112, 113]. This is why group IV QDs becomes a promising alternative to the traditional fluorescent probes and heavy metal QDs in the bioimaging applications.

In addition, Ge QDs are easy to synthesise using relatively simple routes such as colloidal methods. Colloidal methods have been regarded to be the most efficient way

considering the complexity and cost. Colloidal synthesis thus have been investigated and achieved by several following routes:

- Reduction of  $\text{GeCl}_4$  using organokali and alkali metal reagents in room temperature developed by Horst Weller in 1993 [114] and Susan M. Karuzlarich in 2005 [115].
- Metathesis reactions of Ge chloride and Zintl salts such as  $\text{KGe}$ ,  $\text{Mg}_2\text{Ge}$  developed by Susan M. Karuzlarich in 1998 [116].
- Hydride reactions of Ge salts such as  $\text{LiAlH}_4$  to reduce  $\text{GeCl}_4$  at room temperature that has been demonstrated by G. A. Samara in 2001 [117].

Simple colloidal synthesis methods to generate matrix-free Ge QDs in biocompatible solutions have been developed and widely used in the last ten years [112, 118–120]. Another reason that makes colloidal synthesis methods particularly attractive is that many of the colloidal synthesis can be achieved at room temperature. For example, ultra-small Ge QDs of size 2 - 4 nm with a light emission range of 350 - 700 nm [117], and of 3.2 - 6.4 nm with 900-1400 nm light emission [121] can be obtained by easily scalable bench top routes.

As to fluorescence performance, QDs show some unique optical properties as has been shown in the previous section. These remarkable properties are significantly determined by the physical size - this is usually described in terms of the quantum confinement effect (QCE) [122–124]. In the following subsections, we will firstly describe the physics underlying the QCE. Then the optical properties of QDs will be described in subsection 1.6.3.2. Furthermore, the advantage of using Ge QDs in biological imaging will be discussed.

### 1.6.3.1 Quantum confinement in semiconductor nanostructures

The concept of quantum confinement refers to the effects of reduced dimensionality on the electronic properties of materials. Generally, nanostructures can be subdivided in the following types according to their dimensionality: quantum wells/nano thin films (2D), quantum wires (1D) and quantum dots/nanoparticles (0D).

QDs are nanoparticles that consist of several to thousands of atoms. They are, on the size scale, larger than atoms but smaller than bulk, thus too big to behave like atoms and too small to act as bulk materials. From the point view of molecular orbital theory, electrons in an atom occupy atomic orbitals (quantized energy states). Interaction of atomic orbitals result in the formation of bounding orbitals (lower energy states) and anti-bounding orbitals (higher energy states). The overlapping of large number (typically on the order of  $10^{20}$  or greater [125]) of atomic orbitals gives raise to continuous electronic energy bands (Figure 1.23a): a filled band (the valence band) separated from an empty band (the conduction band) by a band gap of energy  $E_g$ .

In the case of reducing size from bulk materials, the total number of atoms becomes much smaller, for example on the order of  $10^3$ , the total number of orbitals is correspondingly smaller. Some of the large number of missing orbitals comes from near the top of the valence band or the bottom of the conduction band. This results in the continuous valence band and conduction band become discrete orbitals (Figure 1.23b) and increase in the value of the band gap energy (as we shall see later). The vertical arrow in Figure 1.23 denotes the band gap  $E_g$  for the bulk material, and the highest occupied molecular orbital - lowest unoccupied molecule orbital (HOMO-LUMO) energy gap in QDs.

For characterisation of the light emission in QDs, the charge carrier's behaviour must be taken into consideration. If an electron is being excited from the valance band, it results in absence of an electron in the original state; the electron absence can be

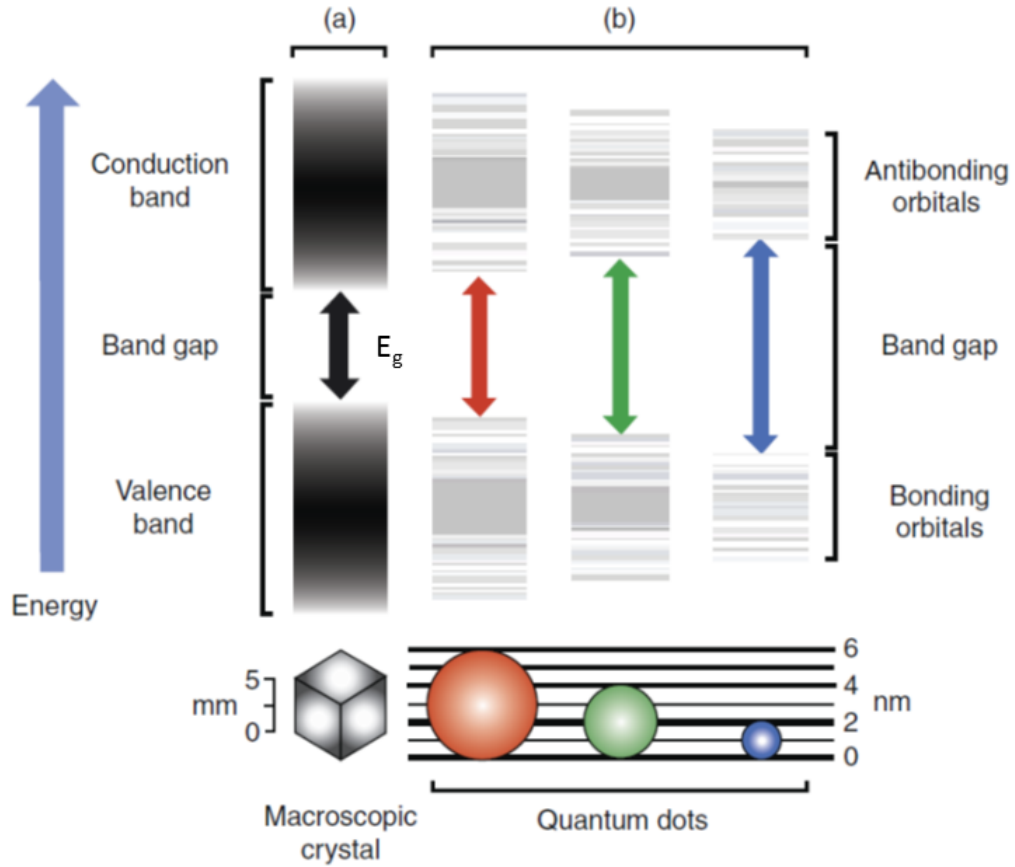


**Figure 1.23:** Energy level diagram of a bulk semiconductor and quantum dots. (a) In bulk materials, electrons are in bands. (b) As to the atom similar quantum particles, orbitals are too sparse to overlap. As a result, continuous valence band and conduction becomes discrete and band gap become larger. Figure reprinted from reference [81].

regarded as an elementary excitation - a hole. Electrons and holes form quasiparticles: electron-hole pairs named *excitons*. In a exciton, electron and hole interacts via Coulomb potential and thus can be described by the Bohr hydrogen model. The Bohr model was initially developed in 1913 to explain the hydrogen atom spectrum [126]. Bohr hydrogen atom model stated that the atom electron can only be in quantised orbitals of radius  $R_n$  with specific energies [127]:

$$R_n = na_B, \quad a_B = \frac{\hbar^2}{me^2} = 0.53\text{\AA} \quad (1.13)$$



where  $a_B$  is Bohr radius which is the orbital radius of the electron at minimum energy state,  $e$  is the electron charge,  $c$  is the light speed in vacuum.

Similar to the hydrogen atom, the electron-hole pairs can be characterised by an exciton Bohr radius (can be seen as a characteristic size of an exciton):

$$a_B^* = \frac{\varepsilon \hbar^2}{\mu e^2} = \varepsilon \frac{m_e}{\mu} \times 0.53 \text{Å} \quad (1.14)$$

where  $\varepsilon$  is the dielectric constant of the bulk material,  $\mu$  is the reduced mass of exciton defined by  $\mu = \frac{m_e^* m_h^*}{m_e^* + m_h^*}$  and  $m_e^*$  and  $m_h^*$  are the effective mass of the electron and hole respectively. Effective masses are used to take into account influence of interatomic potential on the motion of electrons and holes in a material. The exciton Bohr radius determines the range of sizes that QCE can be observed. When the size of the nanoparticles is comparable to the exciton Bohr radius, one expects to observe QCE. Application of the above model to Si and Ge result in Bohr radii of 5 nm and 18 nm respectively [128]. This suggest that QCE effect will be stronger in Ge for the same particle size. This indeed has been experimentally observed [129] (further discussions in section 1.6.3.3).

Under quantum confinement, carriers are trapped within a finite space and enclosed by, to an approximation, infinite potential barriers. This can be illustrated in one dimension by a ‘particle in a box’ model (Figure 1.24) [130]. The particle wave function amplitudes vanish at the potential barriers as they are spatially confined.

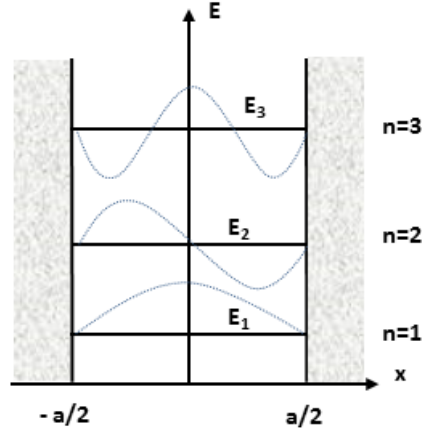


**Figure 1.24:** 1-D 'particle in a box' model. A quantum particle is restricted in potential well with infinite potential at  $|x| > \frac{a}{2}$  and zero potential in the box. The particle can only be at discrete energy states ( $E_1, E_2, E_3, \dots$ ) that obey  $E_n \approx n^2$ . There are infinite quantum states as indicated in dot dash lines ( $n = 1, 2, 3, \dots$ ). [130]

For a particle with effective mass of  $m^*$  confined in space of size  $a$ , it is characterised by a series of discrete quantum states with the energies:

$$E_n = \frac{\pi^2 \hbar^2}{2m^* a^2} n^2 \quad (n = 1, 2, 3, \dots) \quad (1.15)$$

Using this simple approach, Brus and Efros developed a model adequate for real semiconductor QDs, to relate the QDs size and the band gap energy [131, 132]:

$$E_g^* = E_g + \frac{\pi^2 \hbar^2}{2\mu R^2} - \frac{1.8e^2}{4\pi\epsilon} \propto \frac{1}{R^2} \quad (1.16)$$

where  $E_g^*$  is the excited energy states of excitons in QDs,  $E_g$  is the band gap energy of the corresponding bulk semiconductor,  $R$  is the radius of QD,  $\mu$  is the reduced mass of exciton,  $\hbar$  is the reduced Planck's constant. The middle term on the right hand side is a particle-in-a-box-like term for the exciton, and the third term accounts for the electron-hole Coulombic attraction.

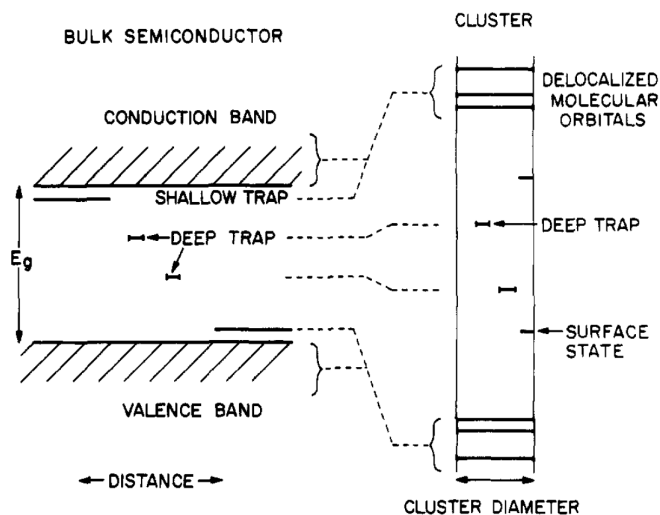


**Figure 1.25:** Correlation diagram relating bulk crystal states to quantum dots. Reprinted from reference[133]

It is shown in equation 1.16 that, as QDs size decrease, energy gap is expected to increase in value (Figure 1.25). This predicts blue shift of optical absorption and emission for smaller size of QDs [134–136]. This has indeed been observed in experimental investigations as can be seen from many reviews [137, 138].

In conclusion, QCE occurs at nanoscale when geometric size radically affects physical properties. It results from the physical confinement of exciton. The motion of electrons and holes is restricted along the confinement direction, giving rise to a series of discrete energy levels. This model predicts qualitatively electronic and optical properties: (i) the density of the energy states becomes discrete, (ii) the light emission is blue-shifted and size dependent. As a result, it is possible to tune the light emission from the QDs throughout the ultraviolet, visible, near-infrared and mid-infrared ranges. The featured optical properties of QDs will be described in the next subsection.

### 1.6.3.2 Optical properties of QDs, blinking

QDs can absorb light at a wide range of wavelengths with a threshold of band gap energy (Figure 1.26). Exciting an electron in QDs requires a photon of energy  $\hbar\nu \geq E_g^*$ . It is also possible for a photon that has higher energy than the band gap energy being absorbed, which allows QDs a wide absorption range [139].

Fluorescence light emission occurs due to the recombination of an excited electron-hole pair across the HOMO-LUMO gap. The emission spectra curve can be narrow or wide depending on the particle size distribution (Figure 1.26) [138, 140, 141]. The HOMO-LUMO gap, and therefore the related emission peak wavelength is also dependent on the QDs size due to the quantum confinement effect: the smaller size corresponds to the larger energy gap, hence the shorter emission wavelength [140].

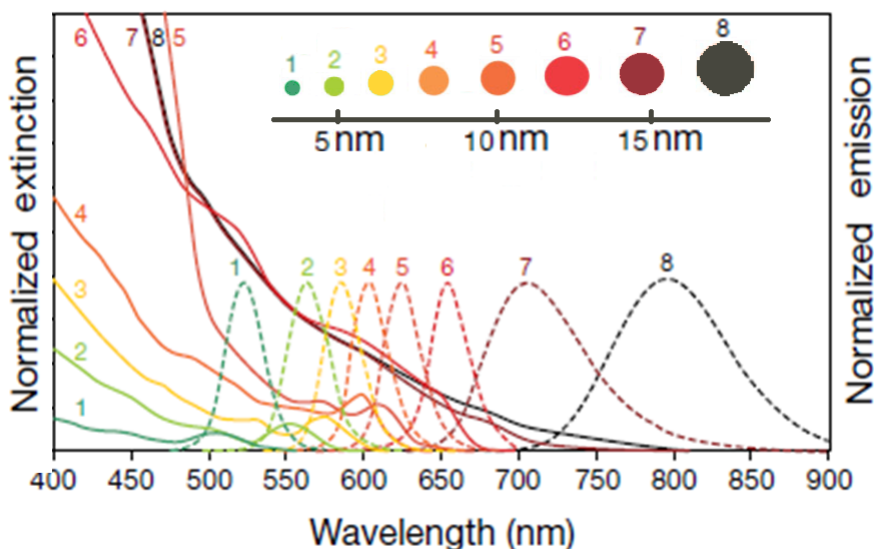


**Figure 1.26:** Size-dependent excitation and emission spectra of QDs. QDs have broad excitation spectra, and narrow and symmetrical emission spectrum. They are tunable depending on the diameter of the QDs and can reach to the near-infrared region. Information available from Invitrogen site [142].

The recombination of the photon excited electron-hole pairs is also affected by defects and surface states, all of which can cause the formation of trap states that trap carriers and thus reduce efficiency of the light emission.

Another phenomenon that has been associated with trap states is blinking. Blinking refers to the random fluorescence intermittency phenomenon that results in a stochastic blink ‘on’ and ‘off’ fluorescent state [99, 143]. Fluorescence intermittency phenomenon was firstly quantified on single QDs by investigating the fluorescence intensity versus time [144]. Even though many models have been put forward to interpret the intermittency mechanism, such as quantum jumps of trapped electrons [145] and Auger ionisation [144], it is still not fully understood. Studies on bioimaging applications of QDs focus on the usage of stochastic blinking events, rather than fully understanding the mechanism. It has been widely demonstrated that the distribution of individual QDs blinking on/off durations follow an inverse power law distribution [146]:

$$\mathbf{P}(t) \propto (t)^{-m} \tag{1.17}$$

$P(t)$  is the probability density of a QD on a certain state (blink ON or OFF) that lasts  $t$  long.  $m$  is the inverse power law index, normally at a value between 1 to 2 for most QDs at room temperature. The inverse power law distribution gives the following information related to bioimaging: (i) QDs fluorescence intermittency durations (stochastic blink off) are not specifically selectable, and it randomly varies from 200  $\mu\text{s}$  to hundreds of seconds, which enable any data collection speed up to 200  $\mu\text{s}$  per frame in stochastic reconstruction microscopy [143]; (ii) short fluorescence intermittency durations occur more frequently than long durations and the distribution follows inverse power law.

In brief, stable fluorescent emission, stochastic blinking, broad excitation and narrow emission make QDs a promising hybrid fluorescent label for biological applications. Within the currently existing QDs products, despite the wide use and relatively high QY of QDs such as CdSe, they are typically still rather large ( $\sim 20$  nm) and exhibit significant levels toxicity in live cell imaging [140]. Thus, introducing novel systems such as germanium QDs could even further raise the significance and widen the acceptance of QDs in cell imaging. Focused descriptions on Ge QDs properties will be illustrated in the next subsection.

### 1.6.3.3 Germanium quantum dots

In bulk Ge, the light yield is very low (QY < 1 % [147]). This is also true for its much wider studied structural counterpart Si (QY < 0.1 % [148]). They also both compare unfavourably with other semiconductors in terms of band gap values that are located in IR range (Table 1.3).

**Table 1.3:** Band gap energy and the corresponding wavelength of some bulk semiconductor materials that are commonly used for making quantum dots.

Bulk material	Band gap energy $E_g$ (eV)	Corresponding wavelength (nm)
Ge	0.64	1937
Si	1.17	1059
CdSe	1.84	673
ZnSe	2.8	442
CuBr	3.1	400

The reason for low QY is due to the electronic band structure: these are indirect-band gap materials. As shown in Figure 1.27, direct band gap materials (e.g. CdSe, GaAs, InP) refers to those where the bottom of conduction band (CB) are in the same momentum (wavevector) position as the top of the valance band (VB) (Figure 1.27a). Indirect band gap materials are those where there is a difference in momentum between the top of the valence and the bottom of the conduction bands ( $\Delta k \neq 0$ ) (Figure 1.27b) and include Si, Ge. In an indirect band gap material, an excited electron must also undergo a significant momentum change ( $\Delta k$ ) for a photon of energy  $E_g$  for the electron-hole recombination to occur. This requires the electrons not only to release energy in the form of a photon, but also interact with a lattice vibrations (phonons) in order to either gain or lose momentum. This is to say, that such transition must include energy transfer to a phonon and as a result, fluorescence QY is significantly reduced. Thus, indirect band gap materials therefore are not usually efficient light emitters.

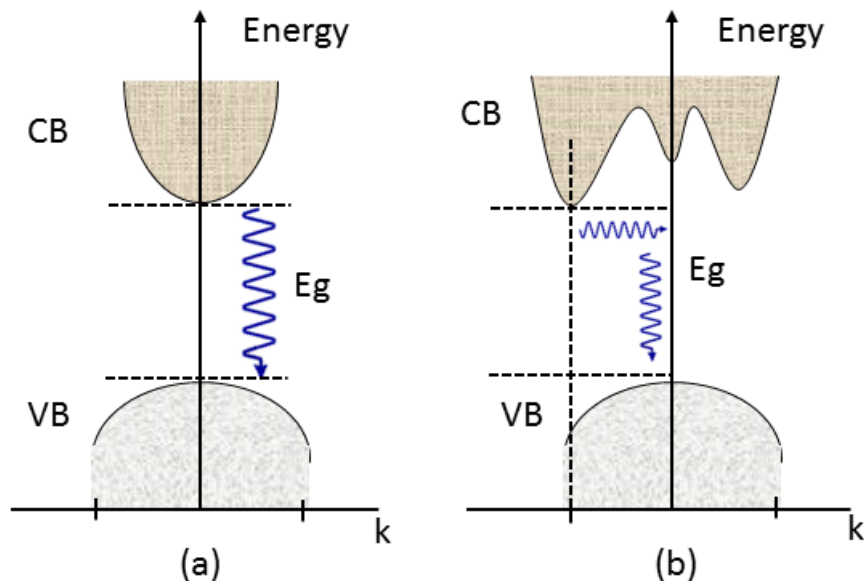


**Figure 1.27:** Direct band gap (a) and indirect band gap (b) in semiconductor materials. Direct band gap materials are which the bottom of CB and top of VB are shown in the same  $k$  point ( $k = 0$ ). Electron transitions can transit between CB and CB directly without momentum changes. As to indirect band gap materials, electrons transit from the bottom CB to the top VB indirectly as there are both energy state and momentum change [149].

However, this problem is lifted significantly in QDs which are too small to be treated as periodic crystal structures. The lack of periodicity leads to the dispersion curve formalism described above no longer being applicable. Instead, the density of electron states is considered, while in practice this means that fluorescence emission probability would increase. For example, Ge QDs have been reported fluorescent and with QY of as high as 8 % [121, 138, 150]. Fluorescent Si QDs have been reported to show QY of 60 % [151].

As far as the emission wavelength is concerned, this is affected by particle size (QCE), as discussed earlier. It has been demonstrated [129] that in order to cover the visible and NIR range ((1.0 - 2.5 eV of  $E_g^*$  correspondingly) which is commonly used for biological imaging, Ge particles must be between 1.5 nm and 3.5 nm (Figure 1.28). It also shows that Ge QDs have certain advantages over Si QDs since the band gap energy varies much faster and it's possible to obtain a wide wavelength

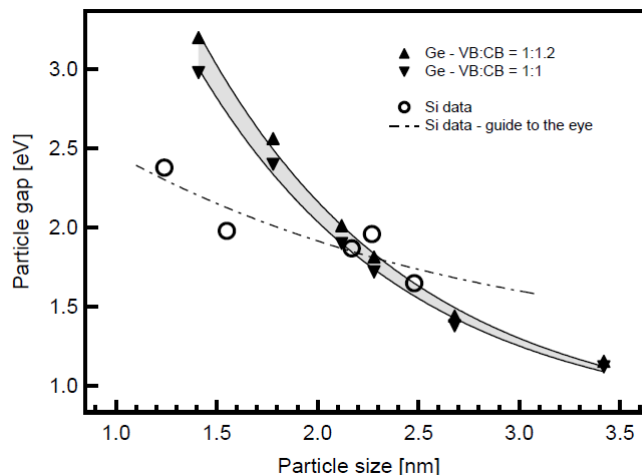


**Figure 1.28:** Germanium and Silicon QDs band gap energy changes as a function of particle size. VB and CB refer to valence band and conduction band. Figure reprinted from reference [129]

range over smaller size dispersion [128, 136]. Moreover, in single molecule localisation super-resolution imaging applications, the benefits of using Ge QDs also result from the small size (less than 4 nm in diameter for visible light emission Ge QDs). Thus, Ge QDs have a potential to improve the resolution limit to below 10 nm.

In the next section we will discuss the working principles of fluorescence and confocal microscopes used in super-resolution imaging.

## 1.7 Microscopes: fluorescence and confocal microscopes

In this section, fluorescence and confocal microscopes will be introduced, including the key optical elements, the working principle, and the advantages and disadvantages in cell imaging applications.



### 1.7.1 Fluorescence microscopy

The term *fluorescence* was introduced by Geroge Gabriel Stokes in 1852 when he witnessed the ultraviolet absorption and visible light emission from some fluid materials [152]. As the fluorescence microscope makes use of fluorescent probes, thus it has to be constructed in a way that allows fluorescence excitation, as well as the ability to separate the relatively weak emission light from strong excitation light. In physical configurations, almost without exception, epi-illuminators are used for fluorescence imaging because of their high efficiency. A sketch of the optical path of a standard epi-fluorescence microscope is shown in Figure 1.29. Filters are essential in fluorescence microscopes to enable their ability to separate fluorescence light and emission light. In this regard, filter cube is commonly used. It contains an excitation filter that allows only the wavelength of light necessary for excitation to the sample, a dichroic beam splitter that separates the excitation light from fluorescence light by reflecting light of a specific range of wavelength, while transmitting others, and an emission filter to extract useful fluorescence signals from any background.

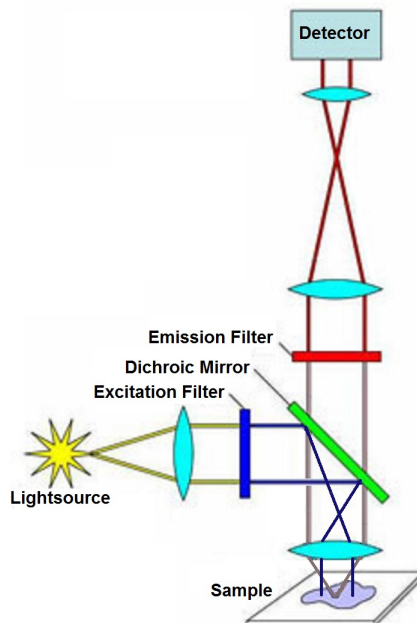


**Figure 1.29:** Schematic diagram of the optical path of an epi-fluorescence microscope. Fluorescence excitation light source, excitation/emission filters are equipped. This type of microscope enable fluorescence studies of live cells with good contrast.

In brief, due to the use of fluorescent probes, fluorescence microscope requires several critical components in the illumination and optical beam path. The fluorescence excitation needs a specific light source and, the emission signal is detected by advanced electronic devices.

The value of fluorescence microscopy lies in the high contrast and visibility in multicolour imaging. Unlike other optical microscopy techniques such as bright field and phase-contrast microscopies which rely on the macroscopic object features (for example, phase gradients and birefringence), fluorescence microscopy relies on the specified and sensitive fluorescent probes that cells or tissues have been stained with [153, 154]. Fluorescence microscopies have gained a wide usage, including fixed cell and live cell fluorescence imaging, immunofluorescence for molecule tracking and clinical diagnosis, and super-resolution imaging by localising single fluorescent molecules [22].

**Table 1.4:** Advantages and disadvantages of fluorescence imaging.

Advantages	Disadvantages	Tips
High sensitivity, even one probe can result in significant signal	Blurring	Use optical sectioning or deconvolution to minimise blurring. Use minimal illumination
High selectivity, capable to label specific structures with specific probes at the same time	Probe photo-bleaching	and anti-fade methods to decrease probe bleaching. Use proper combination of illumination lasers and filters to reduce
Good contrast, objects are self-luminous against a dark background	probe fluorescence bleed-through	bleedthrough.
Spectrum selectable, illumination spectrum and emission spectrum can be separated using filters	Sample autofluorescence	

In spite of numerous advantages and applications, fluorescence microscopy is naturally limited by the fluorescent probes and fluorescence detection. Table 1.4 summarises the main advantages and limits of fluorescence microscopy, as well as the improvements to address the disadvantages.

In the following section principles of confocal microscopy are described and the usage of combined fluorescence confocal imaging will be introduced.

## 1.7.2 Confocal microscopy

### 1.7.2.1 Confocal principles

The confocal microscope is a milestone in the development of classical microscopes [21]. In a conventional wide-field microscope (Figure 1.30a), an object is illuminated and imaged at the same time, which results in the image including the unfocused

background. The solution to this problem in confocal microscope (Figure 1.30b) is to put a pinhole in the back focal plane of the microscope to exclude the out-of-focus lights. In this way, only the light from the conjugation point on the sample is allowed to pass through and is being detected [155, 156]. Therefore, to visualise an area of interest of the sample, the image must be build point-by-point (usually be means of moving sample or excitation beam scanning) using a suitable detector. One of the drawbacks of using the confocal pinhole is that fewer photons can be collected at any given instant. Thus, it requires longer exposure time in order to get enough light to form a good contrast image. A popular modern solution is to utilise a high intensity light source - laser light.

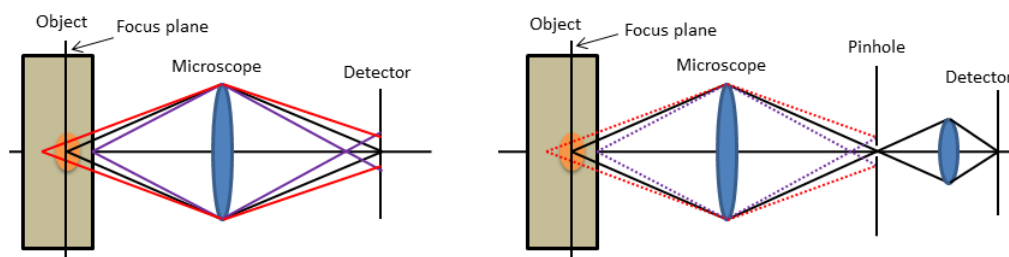


**Figure 1.30:** Principle of out-of-focus light rejection in confocal microscopy. (a) In wide-field microscopy, out-of-focus lights (blue and red) contribute to the detection and cause background noise. (b) In confocal microscopy, a pinhole is pre-set on the back focal plane of the objective lens, and majority out-of-focus lights (blue and red) are excluded.

Confocal microscope are generally combined with fluorescence microscope in cell imaging. Optical setups of conventional fluorescence microscopes and confocal fluorescence microscopes are different, as shown in figure 1.31. In conventional wide-field fluorescence microscopes, large area imaging (round orange circle area on the sample in figure 1.31a) is directly recorded by a CCD detector. However, in confocal fluorescence microscope (Figure 1.31b), large area images are constructed point-by-point by scanning the sample because of the use of pinhole. Temporal resolution of conventional fluorescence microscope is limited by the frame transfer rate of the CCD detector which is about milliseconds per frame. In confocal fluorescence microscope, it is limited by the point-by-point scanning speed, which is normally microseconds per

point, resulting in the final imaging temporal resolution of several seconds per frame. As to the spatial resolution improvements, it is important to understand that the optical advantages of a confocal microscope mainly derive from the pinhole's ability to reject out-of-focus light (Figure 1.32). Theoretically, the pinhole is able to reduce the effective PSF size to smaller than Airy disk which is related to the resolution limit (equation 1.7). For example,  $1.5\times$  resolution improvement compared to non-confocal can be expected with the pinhole size of smaller than 0.25 unit of Airy disk [157, 158]. However, shrinking the pinhole leads to a reduction of the signal light intensity, thus worsen the image contrast. Microscopist normally use Airy disk as the pinhole size in order to receive enough signals. Nowadays, the typical resolution for laser scanning confocal microscopy is  $\sim 200$  nm laterally and  $\sim 600$  nm axially.

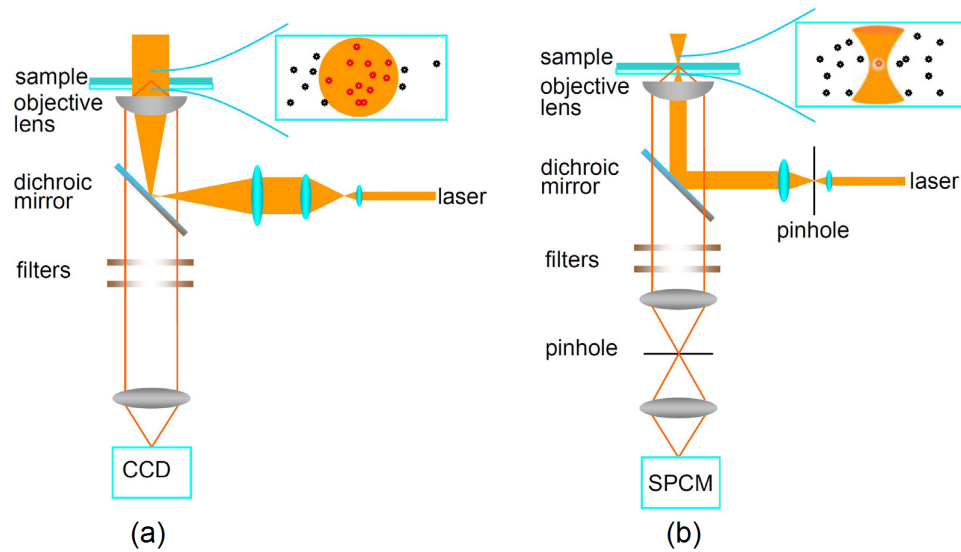


**Figure 1.31:** Optic path of conventional wide-field fluorescence microscope (a) and confocal fluorescence microscope (b). Figure modified from reference [159]

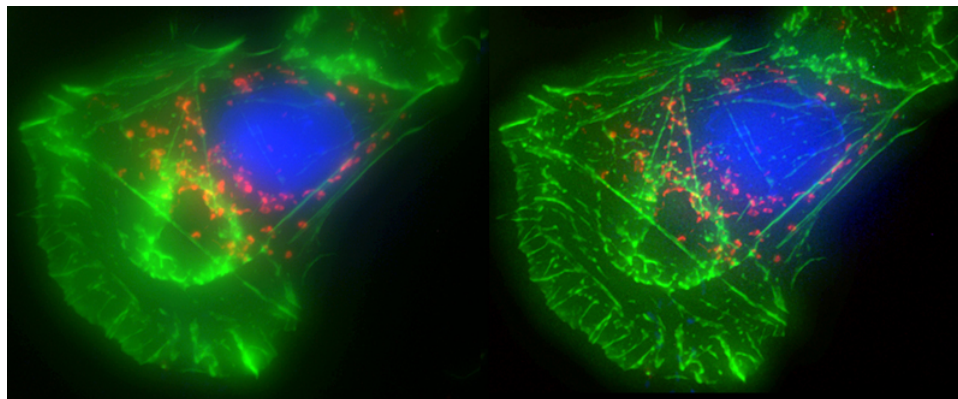


**Figure 1.32:** Conventional wide-field fluorescence image (**Left**) versus confocal fluorescence image (**Right**). Figure reprinted from reference [160].

In the following section we will introduce major types of confocal microscopes.

### 1.7.2.2 Types of confocal microscope

In practice, there is more than one way to achieve the confocal effect, as long as the out-of-focus light can be filtered and the 'point-by-point' imaging can be achieved. For example, laser scanning confocal, which uses lasers and pinholes, and digital confocal, which uses advanced CCD and software to perform the deconvolution process to the images in real time [161]. We will focus on laser scanning confocal microscopes in the following discussion, because they are now much more widely used in biological imaging. Classified by sample scanning methods, these are single beam and multi beam laser scanning confocal microscopes.

The single beam scanning confocal microscope is an archetype in the confocal family. It utilises both a laser and pinhole to obtain a single point-like light illumination of the object. Scanning of the object specimen is achieved by either using a precise stage control to move the sample (Figure 1.33a), or using a galvanometer that consists of two scanning mirrors for X-Y directions to move the laser beam (Figure 1.33b) [162]. The latest microscope products can employ an additional resonant scanning system to improve the scanning speed.

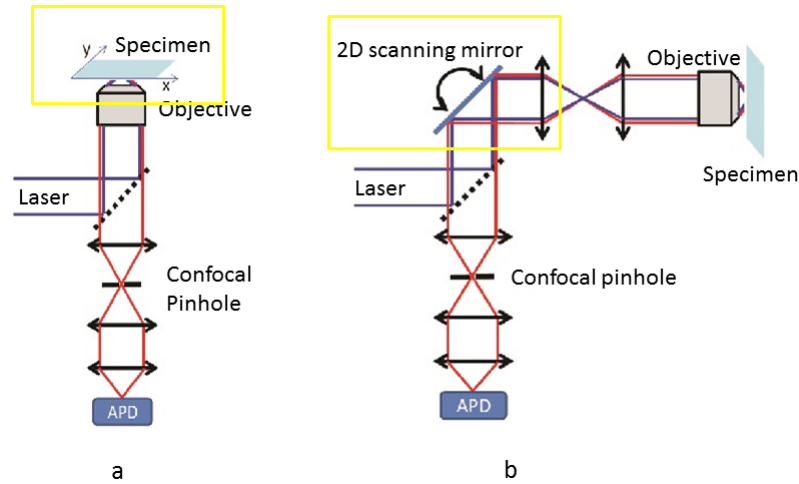


**Figure 1.33:** Optical path of single beam scanning confocal microscopes. Scanning of the specimen can be realised by either (a) moving the specimen stage or (b) using scanning mirrors [162].

Spinning disk confocal microscope (Nipkow Disk system [163]) is a multi-beam scanning method [164]. In this method, a spinning dual disk system with micro lenses and pinholes is installed between the light source and specimen (Figure 1.34). The disk typically has about 20, 000 pinholes that can spin at up to 10, 000 rpm [165]. The excitation laser beam passes through the pinholes to illuminate the sample field every millisecond. This is able to create real-time videos of up to 200 frames per second, which is suitable for observing some cellular processes that occur in milliseconds. Instead of using PMTs or APDs, the disk scanning system uses a CCD camera as a detector.

As illustrated in Figure 1.34, the spinning disk confocal microscope allows simultaneous plane scanning while maintaining both a stationary stage and light beam. It collects multiple points simultaneously, rather than a single point at a time. As a result, this technology gains fast scanning speed and lower excitation laser intensity is needed. In other words, the main advantage of the disk scanning system is its high scanning speed. The pinhole size on the spinning disk is fixed and generally can be 0.25  $\mu\text{m}$  to 2.5  $\mu\text{m}$  (0.8 to 4 Airy unit depending on the exact pinhole size and laser wavelength) in radius depending on the models and manufactures. Because

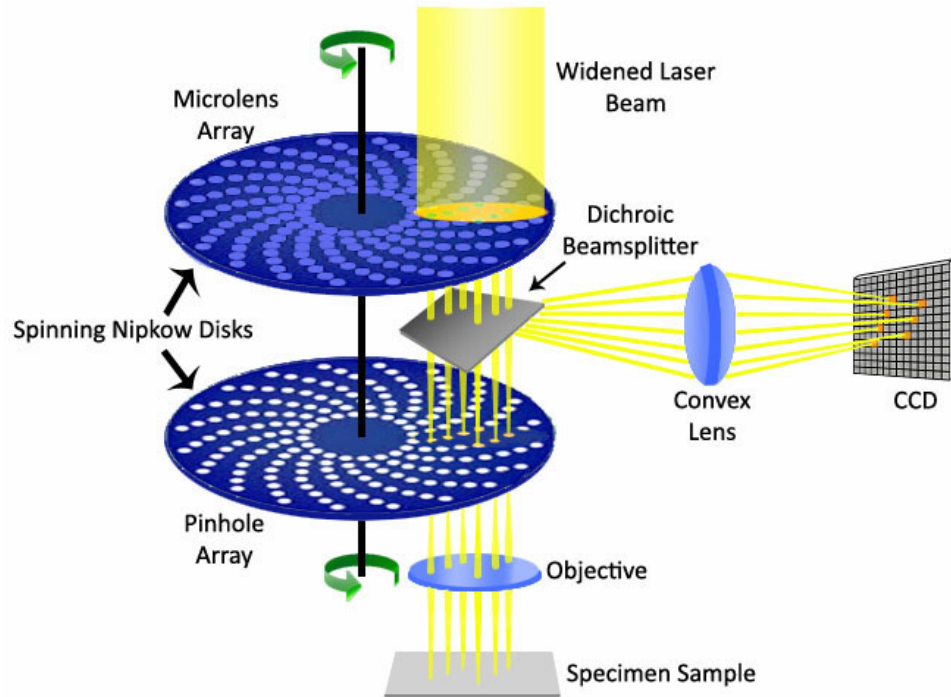


**Figure 1.34:** The optical path of a spinning disk imaging system. It consists of a pair of rotating disks with thousands of micro lenses and pinholes respectively. As light passes the pinholes array and excites the sample, fluorescent light from the sample returns along the same path and is reflected by the Dichroic Beamsplitter and heads to the CCD detector. Figure reprinted from reference [166].

of the fixed pinhole size, the spinning disk has comparable resolution to single point confocal method under a suitable objective, while has worse resolution when using lower power objectives for which the pinholes are oversized [167]. Compared to single point confocal method, the use of microscope lens and pinhole arrays in spinning disk improves the light transmission efficiency by about 50-fold, which allows 40 % of the illuminating light to go through [168]. However, when compared to the wide field configuration, the spinning disk can cause up to 50 % loss of photons [169]. Another disadvantage of the disk scanning system is its relatively poor image quality due to pinhole cross-talk problems [170], and its limitations on specimen thickness. If sequential detecting has to be used for multi-channels, the high-speed advantage of the system is lost.



There are also other types of laser scanning confocal microscopes that achieve different improvements, such as uni-directional scanning for overcoming image aliasing [171], endoscopic fast scanning for real-time imaging, spectral scanning for multi-colour imaging [172] and multi-photon confocal microscope for sample protection [155]. How they are used by the majority of scientist, as well as the limitations of confocal microscopes, will be discussed in the next subsection.

### 1.7.2.3 Usage and limits of confocal microscopes

The range of applications of a confocal microscope is now enormously diverse, as can be seen by scanning the pages of any leading journals of biology, chemistry and the life science fields. In particular, it has become a very important tool for biological research and clinical diagnosis. Confocal microscopes are entirely compatible with a wide range of most of the conventional and advanced light microscopy techniques. In many ways, confocal design is becoming a fundamental element of the new generation of advanced microscopes.

Fluorescence laser scanning confocal microscopes are extremely sensitive and can provide quantitative information in live cell and high resolution cellular research. This is an invaluable feature for examining the proteins or specific cells in a sample, for example, in co-localisation analysis to determine whether several different molecules reside at the same physical positions in a biosample. Owing to the rejection ability of out-of-focus light, confocal microscopes also have a strong ‘optical sectioning’ ability, which can be used to form 3D images. Additionally, fluorescence confocal can be used in spectra imaging because of the natural spectra capabilities of point-scanning. This enables the precise separation of fluorescence signals of strongly overlapping emission spectra by recording the spectral components in each of the scanned points. Commercially, Zeiss and Nikon have utilised PMTs for such detection, while Olympus and Leica have used monochromators and barrier filters [172]. More recently, several advanced super-resolution image methods using fluorescence confocal microscopies

through PSF modification, modulated illumination and single molecule localisations have been proposed, as has been mentioned in section 1.5.

Confocal is not a perfect microscopy solution and practical problems do exist. Firstly, the use of pinholes reduces the light intensity, therefore high intensity light sources are required and most commonly a laser, mercury lamp, or halogen lamp is used. This high intensity light is harmful to living cells, tissues and even fluorescent probes. Point-scanning limits the image construction speed. Besides, confocal multi-laser microscope systems are generally more expensive than non-confocal microscopes [173].

In conclusion, a discussion of the two important contrast and resolution enhancing methods - fluorescence and confocal - was described in this section. Both individual methods and their combination are still limited by the light diffraction, as indicated by the equation 1.7. Based on these diffraction limited methods, two single molecule localisation super-resolution imaging strategies that use QDs, will be demonstrated in the result and discussion chapter.

# Chapter 2

## Materials and methods

### 2.1 Tissue culture

#### 2.1.1 Cell culture

Hela cells<sup>1</sup> were grown in a medium that was made from a mixture of 89% high glucose DMEM (10569077, Life Technologies, USA), 10% Foetal Calf Serum and 1% Penicillin Streptomycin (Life Technologies, USA) in a 25 mL or 75 mL cell culture flask (T25 or T75, Corning Life science, USA) or in a 12-well plate (Corning Life science, USA). During normal cultivation, such as changing medium or splitting cells, the following materials were used: Typsin (12605-010, Life Technologies, USA), phosphate buffered saline (PBS, Life Technologies, USA), 1 mL and 15 mL sample tube (Eppendoff, Belgium) and Micropipette (2  $\mu$ L, 20  $\mu$ L, 2 mL, 10 mL, Sigma-Aldrich, USA). In addition, 70% ethanol was used to clean the experimental stage and sterilise the tools.

Under normal cultivation conditions, growth medium was refreshed every two to three days, depending on the density and speed of growth of the cells. These cells

---

<sup>1</sup>A type of human cervical carcinoma cells.

were split between 70% and 100% confluence by using the following protocol. First of all, PBS (sterile), growth medium, and Trypsin were put in a water bath for 15 minutes to warm up. Following this, the hood platform was cleaned by using 70% ethanol, before the cell flask was transferred to the hood. The cells were then washed once with sterile PBS (the same volume of growth medium the cells were growing in) and Trypsin (3 mL for a T25 flask, 5 mL for a T75 flask) was added to the cells. Next, the cells in the flask were put back for incubation in the tissue culture incubator (37 °C, with 5% CO<sub>2</sub>). After 5 minutes, the cells in the flask were checked through a microscope to see if they had all detached from the tissue culture flask. Once all cells had detached from the flask, the growth medium (using same volume as Trypsin) was added. Following this, the cell suspension was transferred to a 15 mL tube and spun down in centrifuge for 5 minutes at 1000 rpm. Then, the medium was aspirated by using a pipette, leaving a cell pellet on the bottom of the tube. The pellet was re-suspended in 10 mL growth medium. Then, 1 mL or 2 mL cells suspension was loaded to a new flask, along with 9 mL or 8 mL new growth medium. Finally, the flask was labelled (name, date, passage number) and put back into the incubator.

Cell counting was carried out during the quantitative cell culture experiments. This was accomplished by using a haemocytometer (abCAM, UK), plus a cover slip. The haemocytometer was observed under the bright field model of a phase-contrast microscope (TE2000-s, Nikon), using a 20× objective. The number of cells for each chamber on the haemocytometer was counted as  $N_1$ ,  $N_2$ , and the cell density was calculated by:  $(N_1+N_2)/2$  cells per  $\mu\text{L}$ .

### **2.1.2 Cell fixation, permeabilisation and staining**

Cell fixation is the first step in preparing cell samples so that the sample does not decay. Cell samples for further fluorescence staining, such as DAPI staining, or for microscope observations should be fixed. Materials used for cell fixation and fluorescence staining included 0.1% Triton (Sigma-Aldrich, USA), 4% Paraformaldehyde

(PFA, Agar Scientific, UK) and 1:10000 DAPI<sup>2</sup> (D9542, Sigma-Aldrich, USA). In addition, round cover slips of 0.15 mm thickness (Thermo Fisher, USA) were used to cover the samples on glass microscope slides and mowiol (Sigma-Aldrich, USA) was used as a mounting medium for samples. Cell fixation, permeabilisation and DAPI staining were conducted following standard protocols [174]. Furthermore, three types of fluorescent proteins and dyes were used for the photo-stability comparison with QDs: Dronpa, mEos, AlexaFluor 647 (Invitrogen Life Technology, UK). They were then labelled on the mitochondria, actin structure in the lamellipodia and Connexin vesicles respectively [61], by cell transfection. HeLa cells were transfected one day after plating using jetPRIME<sup>TM</sup> (Polyplus transfection, France) according to the manufacturer's protocol with either 1  $\mu$ g Eos-actin, or Dronpa-Mito DNA. AlexaFluor 647 was stained by incubating cells with anti-mouse Fab fragments AlexaFluor 647 secondary antibodies. The cell transfection work was done by laboratory technicians.

### 2.1.3 Cell viability assay

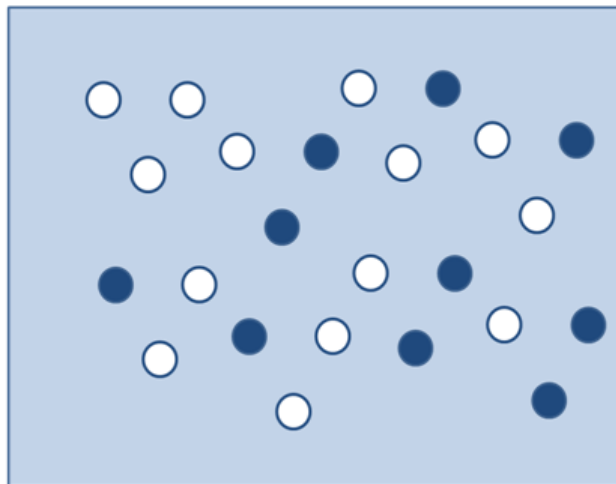
Cell viability assays were carried out during QDs biocompatibility test. Both qualitative and quantitative measurements were undertaken through a Trypan blue (Life Technologies, USA) and Muse (Millipore, USA) test respectively.

#### 2.1.3.1 Trypan blue qualitative test method

Trypan blue is a qualitative dye exclusion test that is used to examine the dead cells that are present in cell suspension after cultivating with QDs. It is based on the principle that live cells possess intact cell membranes that exclude trypan blue molecules, whereas dead cells take up these molecules and visually present as blue in colour [175]. Figure 2.1 shows the schematic diagram of how dead cells are being distinguished from live cells under the microscope.

---

<sup>2</sup>A blue fluorescent DNA label.

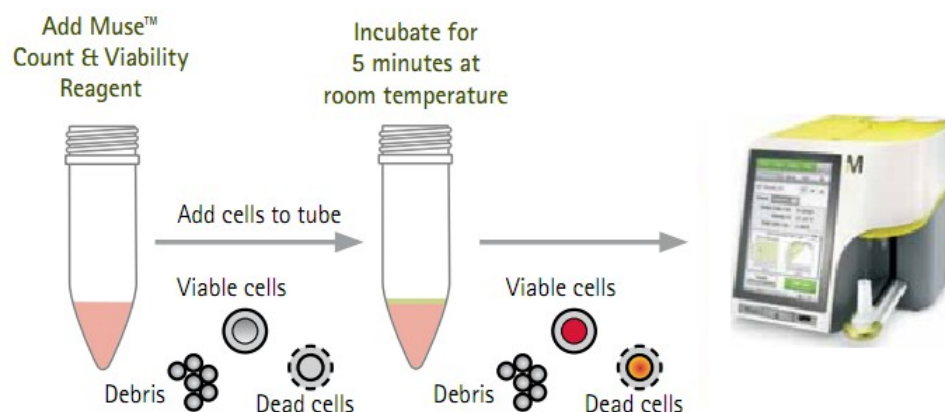


**Figure 2.1:** Observation of cell suspension after Trypan blue staining. Viable cells appear colourless, whereas dead cells take up the dye and appear dark blue. Figure reprinted from reference [175].





In the experiments, Trypan blue test was performed on Hela cells to check cell availability after they were grown with Invitrogen Qdot625 on a 12-well plate. The Qdot625 sample kit was originally supplied as 8  $\mu\text{M}$  QDs in the 250  $\mu\text{L}$  solution and were diluted into four concentrations for the Trypan blue test: 1 nM, 10 nM, 50 nM and 100 nM. After 24 hours of the QDs being loaded, cells were added with 0.4% Trypan blue test solutions. The 12-well plate was directly observed on a phase contrast microscopy (Nikon TE2000-s) under a 20 $\times$  air lens after Trypan blue staining.

### 2.1.3.2 Muse quantitative method

The Muse<sup>TM</sup> cell count and viability kit (Millipore, USA) is a compact instrument for fluorescence-based quantitative measurements of cell viability (Figure 2.2). The experimental protocol is shown in Figure 2.2.



**Figure 2.2:** The Muse for quantitative cell viability test. Figure reprinted from reference [176].

Anticipated Staining Pattern and Cell Size Index				
				
Cell Size Index	Low	High	Med to High	High
Nucleated Cell Stain	Neg	High	High	High
Viability Stain	Neg	Neg	Med	High

**Figure 2.3:** Principles of judging cell viability by cell fluorescence. Figure reprinted from reference [176].

Cell viability analysis was completed with the use of a mixture of two reagents: a membrane permeable DNA staining dye (MCH600103, Millipore) and a DNA binding dye (MCH100102, Millipore). The first DNA staining dye is cell membrane permeable and stains all the cells in the nucleus, which is called nucleated stain. The second DNA binding dye is not membrane permeable, so it only stains cells whose membranes have been compromised (dying or dead cells). It is therefore called viability staining. In principle, the cell solution flows through a micro-tube so that cells pass through the tube one by one. Excitation laser light illuminates the tube from the side. The fluorescence emission of each cell was then detected and used to judge the viability of cells (Figure 2.3).

### 2.1.4 Medium-term observation of live cells

The Incucyte Imaging System (Essen BioScience, USA) (Figure 2.4) was used to monitor long-term cell growth with QDs.

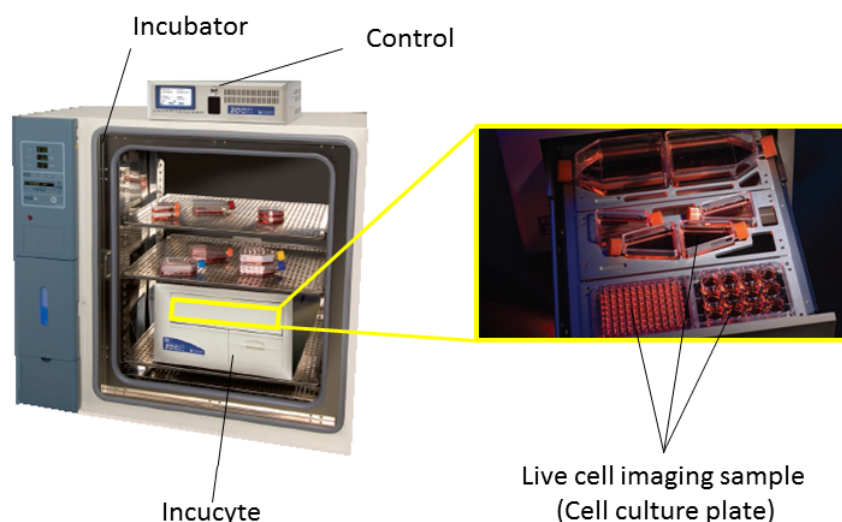


**Figure 2.4:** Incucyte imaging system in a cell culture incubator. Incucyte microscopy is located inside the cell culture incubator. Imaging samples are placed on a sample holder that is operated like a drawer (yellow squared). The microscope is inverted so that the lens is located under the sample holder and facing up. Imaging settings are controlled by the external control box, as well as a computer. Imaging model (fluorescence/phase contrast) and excitation laser light, auto-imaging acquisition setups are adjustable at any time through the control terminals.

Cells were cultured on a 12-well plate using a standard cell culture protocol as stated in section 2.1.1. Two initial cell densities were prepared (5000 cells/mL, 15000 cells/mL) and QDs were added to the wells as designed. Initially, cell solutions were loaded to plate wells (1 mL cell/well) (Table 2.1). The wells were labelled and left for a whole night in the incubator. Afterwards, cells were treated with different QDs as shown in Table 2.2.



**Table 2.1:** Cell preparation for Incucyte medium-term imaging. All labelled wells contained 1 mL cell solutions each.

1A (5000 cells)	2A ( 5000 cells)	3A (5000 cells)
1B (15000 cells)	2B (15000 cells)	3B (15000 cells)

**Table 2.2:** Different QDs or materials were added to the cells so that different growth conditions were generated for the cells. All added materials were in a 0.5 mL solution. GM, growth medium.

1A (GM)	2A (50 nM Ge QDs)	3A (50 nM Qdot625)
1B (GM)	2B (50 nM Ge QDs)	3B (50 nM Qdot625)

Finally, the plate was continuously imaged by the Incucyte mini microscope in the incubator and the images were stored through the external control terminal.

## 2.2 Ge and Invitrogen quantum dots

Synthesis of the Ge QDs started from the original materials  $\text{GeCl}_4$ , ethylene glycol and 2 mL of sodium borohydride solution in triethylene glycol dimethyl (Sigma-Aldrich, USA), following an optimised bench top-colloidal synthesis route (Figure 2.5) [118]. Changing Ge QDs sizes was achieved by changing the initial  $\text{GeCl}_4$  concentration [118, 177]. The synthesis of Ge QDs was carried out by my colleague Dr. Ali Karatutlu and Mr. Osman Ersoy.

In order to suspend Ge QDs into different liquid medium, Ge QDs products in colloidal chemical solution was centrifuged at 10000 rpm and the up layer chemical solution was then removed. Deposited QDs were then dried with Ar gas and weighted before being re-suspended in a certain amount of water or cell growth medium (usually 10 mg QDs in 1 mL water). Sterilisation was completed by putting the QDs vial under

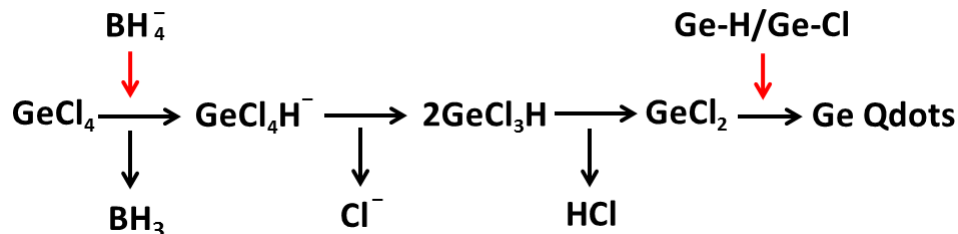


**Figure 2.5:** Chemical reactions in colloidal synthesis of our ultra-small Ge QDs.  $\text{GeCl}_4$  solution is initially hydrophilic attacked by  $\text{NaBH}_4$  as a source of hydride ion, which results in the formation of  $\text{GeCl}_3\text{H}$ . Following the removal of  $\text{HCl}$  from  $\text{GeCl}_3\text{H}$ , it could generate reactive Ge species such as  $\text{GeCl}_2$  which could be inserted Ge-H or Ge-Cl bonds as intermediates to generate H-terminated Ge nanoparticles (Ge QDs).

UV light ( $150\text{mJ}/\text{CM}^2$ , UV CrossLinker) for 15 minutes. After being stored in a fridge at  $4\text{ }^\circ\text{C}$  for a few days, Ge QDs may deposit at the bottom of the vial. In this case, QDs could be dispersed by putting the sample into a sonicator for 12-15 minutes. All QDs were not conjugated to any specific binding anti-bodies.

Apart from the Ge QDs, Invitrogen quantum dots Qdot625 carboxyl QDs (A10200, Invitrogen Life Technologies, USA) and the 6 Qdot sample kit (Q10151MP, Invitrogen Life Technologies, USA) have also been used in this project. Qdot625 is CdSe/ZnS core/shell QD and coated by carboxylate, which is provided as  $8\text{ }\mu\text{M}$  in  $125\text{ }\mu\text{L}$  solutions. It has broad excitation spectra from 300 nm to 550 nm and a narrow emission spectra of 625/15 nm. The 6 Qdot sample kit contains 6 streptavidin conjugated QDs of emission maxima of  $\sim 525\text{ nm}$ ,  $\sim 565\text{ nm}$ ,  $\sim 585\text{ nm}$ ,  $\sim 605\text{ nm}$ ,  $\sim 655\text{ nm}$  and  $\sim 705\text{ nm}$  respectively. Each of the 6 samples is supplied as  $1\text{ }\mu\text{M}$  in  $50\text{ }\mu\text{L}$  solution. All Invitrogen QDs were stored in refrigerator ( $2 - 8\text{ }^\circ\text{C}$ ).

QDs have been characterised through absorption and emission spectra measurements to characterise the optical properties, and electron microscopy observations to characterise their size. This will be described in the following sections.

## 2.3 Characterisation methods

The fluorescence emission measurements were carried out through the following steps. A 10  $\mu\text{L}$  QDs sample was prepared in an Eppendoff tube by using a micropipette. Samples were then excited by the 442 nm emission of a He-Cd laser (IK552R-F, Kimmon), with the laser power kept at 40 mW. The sample was loaded into a quartz cuvette and the fluorescence signal was collected by using an optical fibre coupled to the Andor Shamrock SR-163 spectrometer equipped with an Andor iDus 420 CCD detector. Analysis of the data was then performed on OriginLab software (OriginPro 2015, OriginLab Corporation).

Absorption spectra measurements were performed using U-3000 spectrophotometer (Hitachi, Japan). It has a twin monochromator that allows one to record measurements simultaneously with a reference sample. Then, in measurements, 1 mL Ge QDs suspended in water or ethanol was loaded into a quartz tube (Agar Scientific, UK). Pure water or ethanol in another quartz tube was recorded as a reference. The reference data was also recorded so that it could be subtracted from the QDs data.

The microscopy methods of cell imaging related experiments are described in the following section.

## 2.4 Microscopy

### 2.4.1 Fluorescence microscopes

For the microscopy experiments, the following instruments were used: a ZEISS Inverted epi-fluorescence microscope, a Leica fluorescence microscope and a Nikon ECLIPSE phase contrast/fluorescence microscope (Table 2.3). The Incucyte<sup>TM</sup> Kinetic Imaging

System was used to perform medium-term live cell imaging (Table 2.3). As for super-resolution imaging, a spinning disk confocal microscopy system and a laser scanning microscopy LSM 710 (ZEISS, UK) system were used (Table 2.3). The super-resolution imaging systems will be further described in sections 2.4.2 and 2.4.3.

**Table 2.3:** Light microscopes used in the experiments.

Microscope	Function	Configuration features	Manufacture details
ZEISS Inverted epi-fluorescence microscope	Timelapse long term imaging for live cells with QDs	Multichannel filters; Capped with a large environmental control chamber	17705808, ZEISS (microscope); QImaging EXi Blue (camera)
Leica epi-fluorescence microscope	Examining fluorescence performance of fluorescent probe	Four channel filters; Easy operation	DM4000B, Leica (microscope); IMAGING QClick (camera)
Nikon phase contrast/fluorescence microscope	Quick checking the fluorescence of a sample; Checking cells for tissue culture	Live-time image checking and storage control screen. Phase-contrast model	TE2000-s, Nikon (microscope); DS-Fil, Nikon (camera).
Incucyte <sup>TM</sup> Kinetic Imaging System	Long-term live cell imaging	The whole system is equipped in an incubator	Essen BioScience, USA
Spinning disk confocal microscope	Super-resolution imaging platform <sup>1</sup>	Spinning disk; Multiple lasers	ECLIPSE TE2000-s, Nikon (microscope); Yokogawa, Japan (spinning disk unit)
Spectra imaging confocal microscope	Super-resolution imaging platform <sup>2</sup>	Spectra imaging detector; Multiple lasers	LSM 710, ZEISS (microscope); QUASAR detector, ZEISS (detector)

1, A further description is found in section 2.4.2 and chapter 3.

2, 34 channels from 420 nm to 720 nm, 33 colour channels, 1 non-colour channel. Further description in section 2.4.3 and chapter 3.

Fluorescence microscopes were operated in the following way. The microscope

slide samples were prepared before any imaging experiments. The imaging experiments started with the switching of light source or lasers, control accessories, and the connected desktop. When an environment chamber was used, the proper temperature (32 °C) and CO<sub>2</sub> density (5%) were pre-set before the live cell imaging took place. The sample was then placed on the microscope stage. When a focus drive assistant device was connected and used, it was adjusted and calibrated by defining the initial (0,0,0) position. To focus on the sample, the Bright Field mode on the microscope was selected and the light path was selected to the eye piece. Focusing was achieved by tuning the position of the sample holder and observing through the eye piece. The bright field or phase contrast images were captured at this point by camera configurations. Then, an imaging model (either fluorescence channels or timelapse) was chosen and the fluorescent sample was more precisely focused by finely adjusting the sample holder's position. Image acquisition, excitation laser lights and intensity was changed from 0 mW to 50 mW, depending on the fluorescence emission intensity. Camera EM gain was typically set at 300 and the exposure time was typically set at 200 ms, 500 ms or 800 ms, depending on the image quality and the purpose of imaging. The fluorescence images were captured and then stored on an external hard drive.

## **2.4.2 Spinning disk confocal microscopy**

The fluorescence spinning disk confocal imaging system was used for the purpose of achieving super-resolution imaging using blinking QDs. The overall view of the system is shown in Figure 2.6, while schematic diagram is presented in Figure 2.7. The system is based on a Nikon TE 2000S confocal microscope and a YOKOGAWA CSU-x1 spinning disk unit. MFP is a multi-function port with lasers; EMCCD is a camera; FW refers to filter wheel; SD refers to spinning disk; ACL is the axial correction lens; PCF is piezo-controller with active feedback; OB is the objective; SRS is the super-resolution sample.

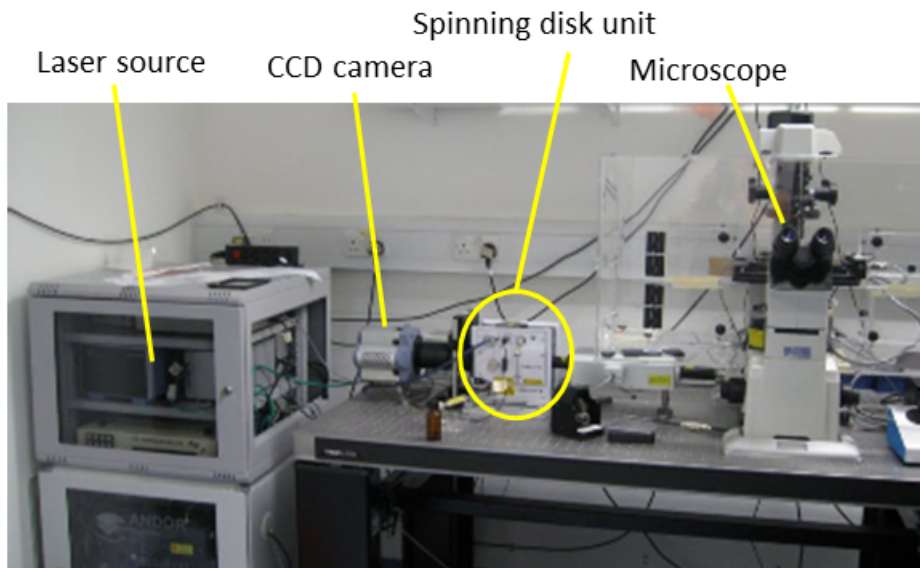


**Figure 2.6:** Outlook of our spinning disk confocal microscopy system.

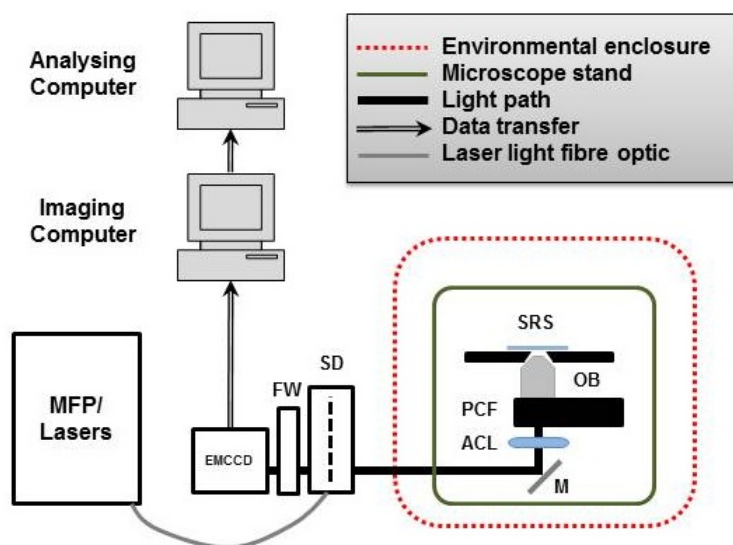


**Figure 2.7:** Components of our spinning disk confocal microscopy system [61].

The YOKOGAWA CSU-x1 spinning disk is able to spin at 1500 - 10000 revolutions per minute. A column of excitation light will pass through more than 1000 pinholes to image the entire field every millisecond. This microscope is able to create real-time videos at a rate of 30 fps at a full resolution. Additionally, the excitation light will also pass through another disk, which has thousands of micro-lenses. The

micro-lens disk and pinhole disk pair rotate identically on the same axis.

In order to achieve super-resolution imaging, we made a few modifications to our spinning disk setup. To prevent the environment disturbing the apparatus, such as environmental vibrations, the system was fitted on an anti-vibrational optical table in a quiet room. Furthermore, a transparent glass chamber with a temperature control unit was fitted over the specimen imaging parts to provide a suitable environment for live cell imaging. A focus drift compensation device was equipped (PI MicroMove Autofocusing device, Physik Instrumente, Germany). High power lasers were used: three laser lines with maximum power of 50 mW each, including 405 nm, 488 nm, 561 nm lasers and one 640 nm laser line with maximum power of 100 mW) to ensure sufficient light intensity on the sample, as the accuracy of super-resolution image quality is directly correlated to the number of photons detected (see equation 1.11). Lasers were coupled into Andor Laser Combiner (ALC, which provides milliseconds switching speed between different lasers). All super-resolution imaging was carried out through a 100 $\times$  (1.49 NA) Plan Apochromat objective (Nikon, UK). Images were collected on the iXon3 885 EMCCD camera (Andor Technology, UK). iXon3 885 camera has pixel unit size of 8  $\mu\text{m}$ , with 70 % quantum efficiency for detecting light in visible region. The key parameters of iXon3 885 are shown in Table 2.4. Imaging acquisition settings were controlled through the software IQ2 (Andor Tehnology, UK) on a desktop computer.

**Table 2.4:** iXon3 885 key parameters

Models	Pixel Format	Pixel Size	Max. Frame Rate
iXon3 885	1000 $\times$ 1000	8 $\mu\text{m}$	31 fps

A spectra confocal imaging system for super-resolution imaging will be described in the next subsection.

### 2.4.3 Spectroscopic confocal microscopy

A spectroscopic confocal microscopy system has been used for the purpose of achieving super-resolution using multi-size dispersion QDs. This method combines spectroscopy and imaging, which enable the spectroscopic separation of the fluorescence emission light components from the sample into several channels. It was achieved by using ZEISS LSM710 laser scanning confocal microscopy (Figure 2.8), which is capable of spectral signal separation. Spectra separation has been accomplished by using the 34-channel QUASAR detection unit (34 channels from 420 nm to 720 nm, including 33 colour channels and 1 non-colour channel, Figure 2.9). It was used on lambda scanning mode. In this mode, images were acquired by displaying the intensity of the fluorescent probe within a spectral bandwidth of 10 nm, called the  $\lambda$ -stack.

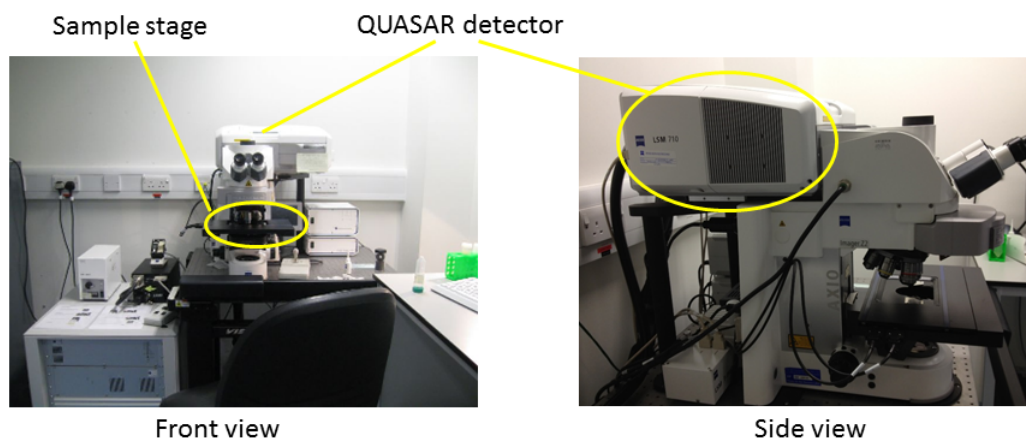


**Figure 2.8:** Outlook of LSM 710 confocal spectra imaging system

As shown in Figure 2.9, the optical path of the QUASAR detector is highlighted in the yellow ellipse area. The excitation light comes from the laser ports (1,2), typically at an intensity of 0.1 - 50 mW. The TwinGate beam splitter permits almost infinite wavelengths excitation combinations. Scan mirrors (7) control the laser beams to scan on the sample. The fluorescence signal from the sample come back through the beam splitter and then hit the pinhole (8), which allows one unit Airy disk size PSF (depending on the wavelength) to pass through. The spectral separation part consists of a diffraction grating, as well as reflecting and focusing optics, in order to split the



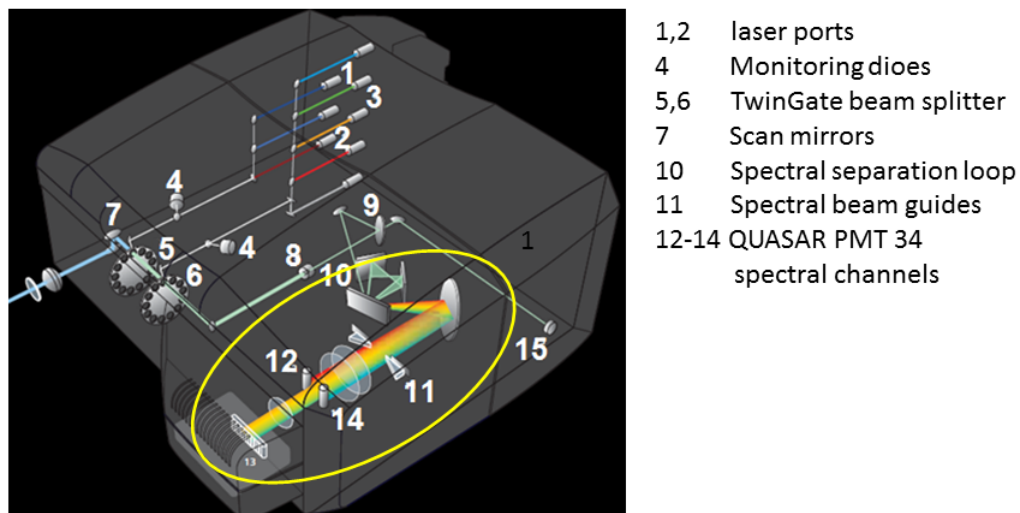


**Figure 2.9:** Optical path and spectroscopic separation principles of a QUASAR detector (inside the yellow circle). Figure reprinted from [178].

overall fluorescence signal by wavelength. Afterwards, the fluorescence signals were collected by a 34-PMTs array detector, in which 33 PMTs detected spectra signals from 420 to 720 nm with a 10 nm bandwidth each, and the other PMT to generate a bright field image. Figure 2.10 illustrates the quantum efficiency of the PMTs in responding to a different wavelength.

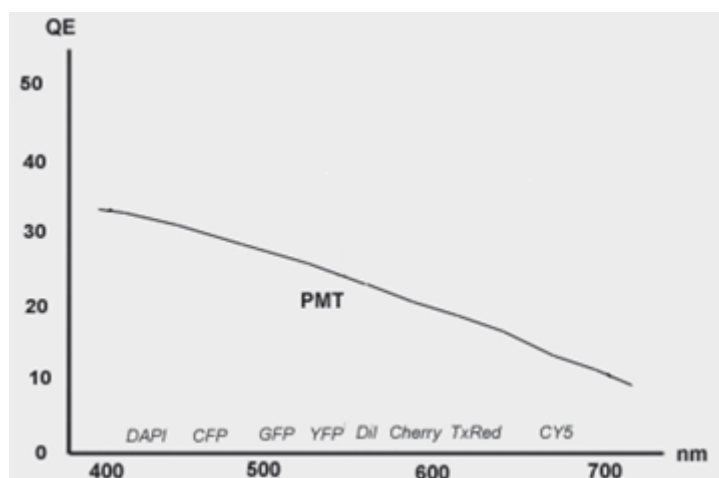


**Figure 2.10:** QE of the PMT unit in the spectral array detector[178]

ZEISS's ZEN software was used for data acquisition. In this software, the laser scanning area size on the sample can be defined and the scanning speed is adjustable.

Excitation lasers and PMT detection sensitivities are both changeable in real time. The auto contrast model was selected so that the software can intelligently change the PMT sensitivity and offset the gains to obtain a good contrast image.

The lasers involved in the experiments were a 405 nm diode laser, a 488 nm Argon laser, and a 633 Helium/Neon laser. Spectroscopic super-resolution data was collected through a 100 $\times$  oil lens (NA=1.45). The pinhole was set at one Airy unit. The scanning area was adjusted via the changing ‘optical zoom’ so that a pixel size of 70 nm was achieved. Scanning speed was set at 3.15  $\mu$ s per pixel. The largest background for most samples initially appeared either at the sample itself, such as too weak a fluorescence emission or too strong auto-fluorescence, or at the detector noise. Therefore, the render images averaged from 4 frames in order to minimise the background.

Under the excitation of a 5 mW 488 laser light, a complete spectroscopic image stack of 33 channels (which was used to reconstruct a super-resolution image) took from several hundred milliseconds to a few seconds to acquire. It was not too difficult to achieve a good stability of the microscope over such timescales. The whole system was settled in a quiet room and the microscope itself was placed on an anti-vibrational optical table, which meant sample drifting within seconds on such platform was negligible. On the other hand, the sample was fixed cells with QDs, which had been well-prepared and mounted with Mowiol. Samples drifting within seconds was not a significant impact on the images. This will be further demonstrated in chapter 3.

#### **2.4.4 Electron microscopy**

Transmission and scanning electron microscopies (TEM and SEM respectively) were used to assess the QDs sizes and extended correlative imaging. They provided direct high resolution observation capacity to QDs. The QDs used in this project were

semi-conductive and thus should be directly usable for EM. Two types of electron microscopes (Figure 2.11) were used: the scanning electron microscope (SEM, Quanta 3D, FEI), which detects the scattered electron beams from the object to form an image, and the transmission electron microscope (TEM, JEOL 2010), which detects the transmission beam through an ultra-thin sample [179]. Table 2.5 lists the advantages the these microscopes have over one another.

**Table 2.5:** Comparison of SEM and TEM

Advantages of TEMs over SEMs	Advantage of SEMs over TEMs
Higher magnification and greater resolution	SEMs produce three-dimensional (3D) images, while TEMs only produce flat (2D) images

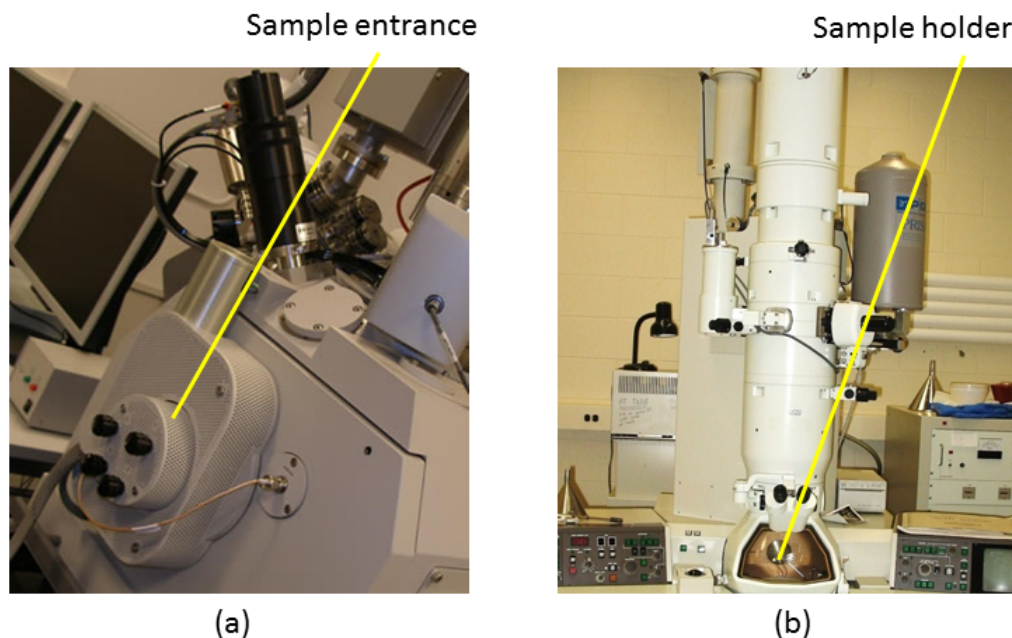


**Figure 2.11:** SEM(a) and TEM(b) systems

Protocols for SEM and TEM imaging are similar, including sample preparation and microscope operations. In preparing the imaging sample, QDs or fixed cell samples

were prepared on an Au TEM grid (S147A3H, Agar Scientific) or a polyester based SEM grid (260500, Agar Scientific). The samples were then dehydrated by rinsing the sample using 100 % ethanol for 15 minutes at room temperature. Coating of Au or Copper on samples was optional. It was used to enhance the contrast of the electron microscopy images. Once the sample was prepared, it was placed onto the SEM or TEM stage. The operation of SEM or TEM was done following the laboratory's technical guidance. The major settings included loading the sample and selecting 'Monitor' and 'Vacuum'. After about 5 minutes, all indicators should be at 'Ready' states. The sample's position was changed by aligning the small screw of the Goniometer. Zooming in to the sample was completed by increasing the electron beam voltage: a maximum of 50 KV was selected in our experiment. To shut down the system, the voltage needed to be reduced step by step over the course of two minutes, instead of being turned off rapidly. The platform was then cleaned after the experiments were completed.

## **2.5 Computational processing**

Computational processing to images and data were completed using by several types of software, including Microsoft Excel, ImageJ 1.46 (<http://imagej.nih.gov/ij/>), OriginPro Lab 9.0 (<http://www.originlab.com/>), Matlab2014 (<http://uk.mathworks.com/>). General data sorting, such as data display, plotting, and curve fitting were carried on OriginPro and Matlab. Imaging sorting and processing were performed on ImageJ. Coding and algorithm development were completed on Matlab2014.

### **2.5.1 Particle size measurements**

The average size and size distribution of Ge and Invitrogen QDs were determined from TEM images by using the following procedures. TEM images were loaded into ImageJ.

Size measurements were conducted using the default functions of ImageJ. Initially, the threshold of the images was ascertained by using the plug-in: ‘Image/Adjust/Threshold’. Then, the threshold values were adjusted to segment the image into particles (masked in red) and background. Moreover, despeckling could be performed if thresholding failed to completely separate the background from the particles. This action replaced each pixel with the median value in its 3×3 neighbourhood. To check the accuracy of the final threshold image, one could look at the overlay images by selecting Image/Overlay/Add Image. Afterwards, particle size measurement parameters were set through the ‘Analysis/Set measurements’ pop-up window. Selected parameters were: ‘Area’ (in square pixels or in calibrated square units), ‘Fit ellipse’ (which fitted an ellipse to the selection), ‘Feret’s diameter’ (the longest distance between any two points along the selection boundary, also known as the maximum caliper [180]) and ‘Limit to threshold’ (only thresholded pixels are included in the measurement). After these preparations were carried out, the ‘Analyse Particles’ function under the ‘Analyse’ menu was selected to complete the particle size analysis. Further data processes were undertaken on OriginLab software.

## 2.5.2 Statistical analysis

Statistical analysis for biocompatibility test data was carried out using the OriginPro Lab software package, version 9.0 2015. A  $p$ -value of  $< 0.05$  was considered significant. For cell viability test, data from three consecutive experiments were analysed. The data was presented as mean value of the three experiments. Unpaired student  $t$ -test was used to compare viability and percentage of control cells and QDs treated cells. One way ANOVA analysis was used to understand the cell viability trend along with time.

### 2.5.3 Point spread function Gaussian fitting

In order to calibrate the Point Spread Function (PSF) of each of the microscopy systems used, a 2D Gaussian distribution model was assumed as a standard PSF which has been widely accepted in the super-resolution imaging field [181].

Using this model, the PFSs in different channels of both Andor spinning disk confocal microscopy and Zeiss LSM710 spectroscopic microscopy were calibrated by a sample of 100nm (size) TetraSpeck beads (TetraSpeck Fluorescence Microspheres Sample Kit, Life Technologies, USA). This displayed four well-separated excitation/emission peaks - 360/430 nm (blue), 505/515 nm (green), 560/580 nm (orange) and 660/680 nm (dark red). Beads were supplied on a glass microscope slide and could be directly used on the microscopies. Single beads were then focused and scanned through different emission wavelengths. Beads were excited with selected laser during data acquisition (405 nm, 488 nm, 561 nm, 640 nm lasers respectively). PSFs were assumed as a 2D Gauss distribution. Collected data were then imported into OriginLab to subtract the background and fit with 2D Gaussian functions (equation 2.1).

$$z = z_0 + Ae^{\{-\frac{1}{2}(\frac{x-x_c}{w_1})-\frac{1}{2}(\frac{y-y_c}{w_1})\}} \quad (2.1)$$

Three parameters were of interest to us: centre position  $(x_c, y_c)$ ,  $x$  direction FWHM  $2.355w_1$ , and  $y$  direction FWHM  $2.355w_2$ .

### 2.5.4 Localisation algorithms

Several localisation algorithms were used in the super-resolution reconstruction in this research work. Table 2.6 lists some of the public algorithms that have been tested and discussed in this work. Further descriptions and test results will be shown in Chapter 3 section 3.2.5.1.

**Table 2.6:** Used algorithms

Algorithm names	Software codes	Reference
QuickPALM	ImageJ Plugin	[182]
SOFI	Matlab	[183]
DirectSTORM	C	[184]
DeconSTORM	Matlab	[185]
CSSTORM	Matlab	[186]
3B	Python/ ImageJ Plugin	[187]

Furthermore, two Matlab based localisation algorithms have been developed under the super-resolution imaging methodology using blinking QDs, and the spectroscopic super-resolution imaging methodology. They were developed on Matlab2014 using a 64-bit windows platform equipped with 2.1 GHz Intel Core i3 CPU. Blinking analysis super-resolution (BSA) utilised the Independent Component Analysis (ICA) and Gaussian fitting to register the QDs localisations. The spectroscopic super-resolution algorithm (SSA) employed Gaussian Mixed Model and Maximum likelihood estimation to register the localisations. In our case, we assembled and tailored the existing reliable mathematical models and made them suitable to process our own data. In BSA, users are free to directly modify parameters in the codes. In SSA, a Graphical User Interface (GUI, see Appendix G.1) has been developed to make it easier and handier to use. Further descriptions of these algorithms are found in the next chapter.

# Chapter 3

## Results and Discussion

### 3.1 Germanium quantum dots as bioimaging probes

In this section, optical characterisations, including absorption and emission spectra measurements of the colloidal Ge QD will be demonstrated. Then Ge QDs cell toxicity test and fluorescence imaging would be studied and compared to commercial QDs - Qdot625. Following this, long-term live cell behaviours would be investigated after being cultivated with QDs, including cell proliferation and nucleus shape changes.

#### 3.1.1 Ge quantum dots characterisation

##### 3.1.1.1 Optical characterisation

As-prepared Ge quantum dots and those re-suspended in ethanol are shown in Figure 3.1a. One can see significant changes in their visual appearance compared to bulk Ge (metallic greyish colour, Figure 3.1b), suggesting there were clear changes in the Ge band gap.





**Figure 3.1:** Ge QDs product (**a** left) in original chemical solution and in (**a** right) ethanol after being extracted from the original chemical solution. (**b**) Bulk Ge powder [188].

Optical characterisation has been carried out on Ge QDs, which have been re-suspended in water, via absorption and emission measurement. A sample of Ge QDs was prepared on a slide (one drop of QDs solution was used on each slide, with the QDs solution being made by 6 mg QDs suspended in 1 mL water). A quick test was carried out using a standard epi-fluorescence microscope equipped in 488/630+ nm excitation-emission filter configuration using a 50 $\times$  lens and a standard CCD camera (a webcam) to record an image. The results are shown in Figure 3.2a and indicate that Ge QDs can indeed be suitable for fluorescence imaging.

The absorption spectra (blue curve in Figure 3.2b) illustrates that Ge QDs have a broad UV-Vis absorption range. The increased absorption coefficient towards the UV was found to be similar to the findings in the previous report [189]. In such a case, stronger fluorescence emission can be expected from Ge QDs when they are excited by short wavelength lasers (for example  $\sim 400$  nm) rather than long wavelength lasers (for example  $> 600$  nm). From Figure 3.2b, we can see that in Ge QDs, absorption onset, as well as peak emission, are located in the visible range as predicted by QCE, this is also in agreement with previous work on colloidal Ge QDs prepared in a similar way [190]. This is indirect evidence of the QCE phenomenon in our Ge QDs, indicating a band gap energy change compared to bulk Ge ( $E_g = 0.64$  eV).

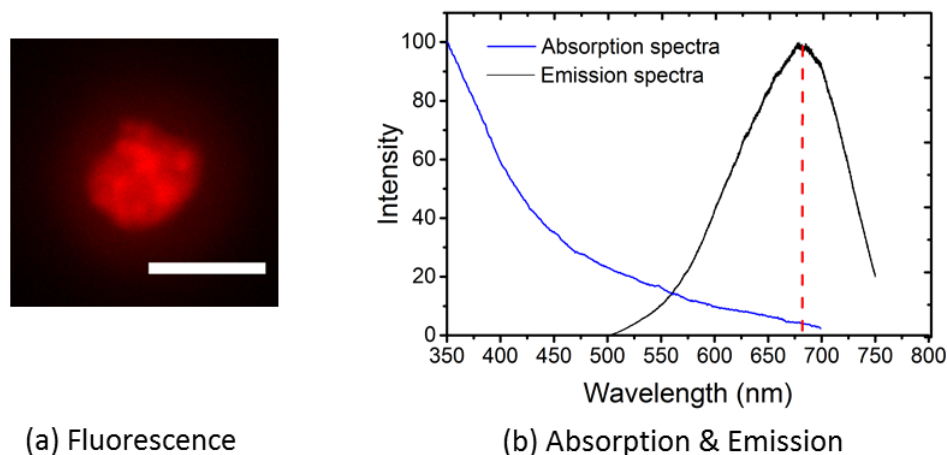


**Figure 3.2:** The optical characterisations of Ge QDs. **a** Fluorescence image of Ge QDs (in water) that have dropped on a microscope slide. Excitation light was filtered at band pass of  $488 \pm 10$  nm, and emission light was filtered at  $630+$  nm. **b** Ge QDs absorption and emission spectra in water. The emission spectra was measured under excitation of a 442 nm laser light. Scale bars, **(a)**  $20 \mu\text{m}$ .

Considering that the emission is due to QCE, the wide emission spectra of Ge QDs ( $\sim 150$  nm in FWHM) is due to particle size distribution. Thus, we further studied the average size and size distribution of Ge QDs by using TEM, which will be further demonstrated in the following subsection.

### 3.1.1.2 TEM characterisation

To observe the size and shape of Ge QDs, a TEM has been used. To prepare the sample, Ge QDs in water were dropped onto a TEM grid. The sample was then allowed to dry in a hood at room temperature for 24 hours. Next, it was transferred to the TEM. Magnification was set to  $50000\times$  and the maximum possible resolution was  $1.5 \text{ \AA}$ . Figure 3.3 shows a Ge QDs image under TEM and the distribution of sizes that have been calculated from this image. Sizes were calculated by using the imageJ default ‘Analyse Particles’ function which is described in section 2.5.1.

One can see that Ge QDs are nearly spherical in shape, with the size well below 10 nm (Figure 3.3a). Ge QDs sizes were found to be  $3.8 \pm 1.4$  nm (Figure 3.3b) from

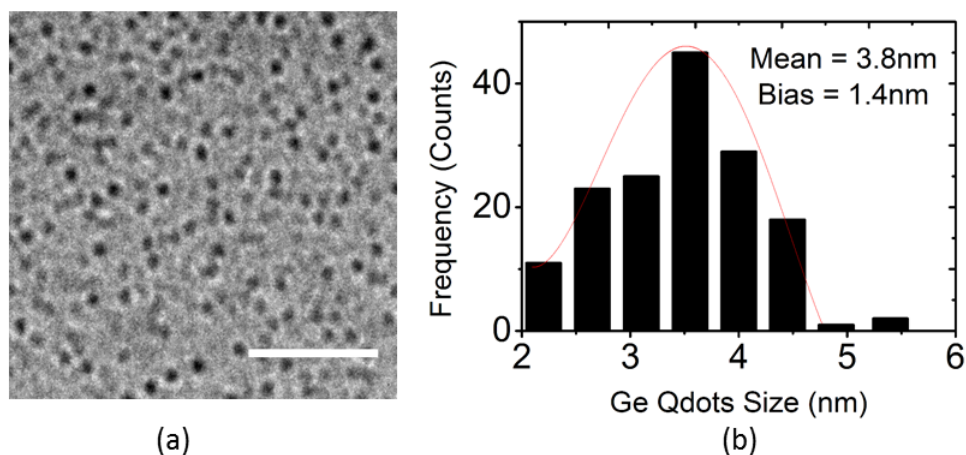


**Figure 3.3:** Ge QDs TEM image (a) and size characterisation (b) based on TEM image. Scale bar, 50 nm.

a statistic calculation of 150 QDs. However, the absorption spectrum (Figure 3.2b) suggests band gap of around 500 nm (2.5 eV) which in Figure 1.28 would correspond to particle size of around 2 nm rather than 3.8 nm. The observed discrepancy can be due to the structure and morphology of Ge QDs. Small particle size can lead to surface relaxation and result in the formation of an amorphous surface layer, leading to a core-shell-like structure in nanoparticles [191]. Indeed, our own structural measurements using a combination of x-ray and Raman methods ([192, 193]) support the core shell model. This could explain the discrepancies in the average particle sizes obtained by different techniques.

When both the size distribution trend line (red curve in Figure 3.3b) and PL emission curves (blue curve in Figure 3.2b) are compared, one can see the similarity that both curves are somewhat asymmetric to the left hand side. This correlation provides further indirect evidence of the dependence of the light emission spectra on particle size due to the QCE.

In conclusion, we have direct evidence that the Ge QDs we synthesised are 3.8 nm in size and have absorption and emission properties that are affected by size due to QCE. We also have an indirect evidence that broad emission spectra are due to the size distribution of the Ge QDs sample. Furthermore, Ge QDs have been found to

be potentially usable in bioimaging. We have therefore tested their biocompatibility, which will be introduced in the next section.

### **3.1.2 Biocompatibility tests**

Optical properties are not the only consideration when determining the suitability of quantum dots in cell imaging; biocompatibility (for example, interruptions to the cells' normal growth and activities) is also required in biological systems. In this investigation, the impact of Ge QDs and CdSe QDs on cells was studied and compared in the aspects of cell viability, cell proliferation and cell morphology. Ge QDs in water were sterilised under UV light before being loaded into cells for quantitative analysis. In the biology-related tests, Ge QDs were characterised in molar concentrations (nano mole per millilitre for example). The calculations are described in Appendix B. Commercial Invitrogen CdSe QDs - Qdot625 was tested as a reference.

Biocompatibility tests were carried out on Hela cells. The cell viability, which was defined by the number of viable cells, divided by the total number of cells was tested. In addition, we also tested cell proliferation and nucleus shape by confocal microscopy after DAPI staining.

#### **3.1.2.1 Cell viability tests**

In order to assess the effect of QDs on cell viability, an initial idea of relevant concentrations of QDs is required. Previous research on Invitrogen CdSe QDs suggested that concentrations of 10 - 50 nM/mL are suitable for live cell imaging [194, 195]. Hence, we tested concentrations in this range and then as a further test - at 100 nM/mL. This was completed through Trypan blue tests on Hela cells that had been cultivated with Qdot625. The Trypan blue staining would cause dead cells to appear dark blue in phase contrast images (Figure 3.5).

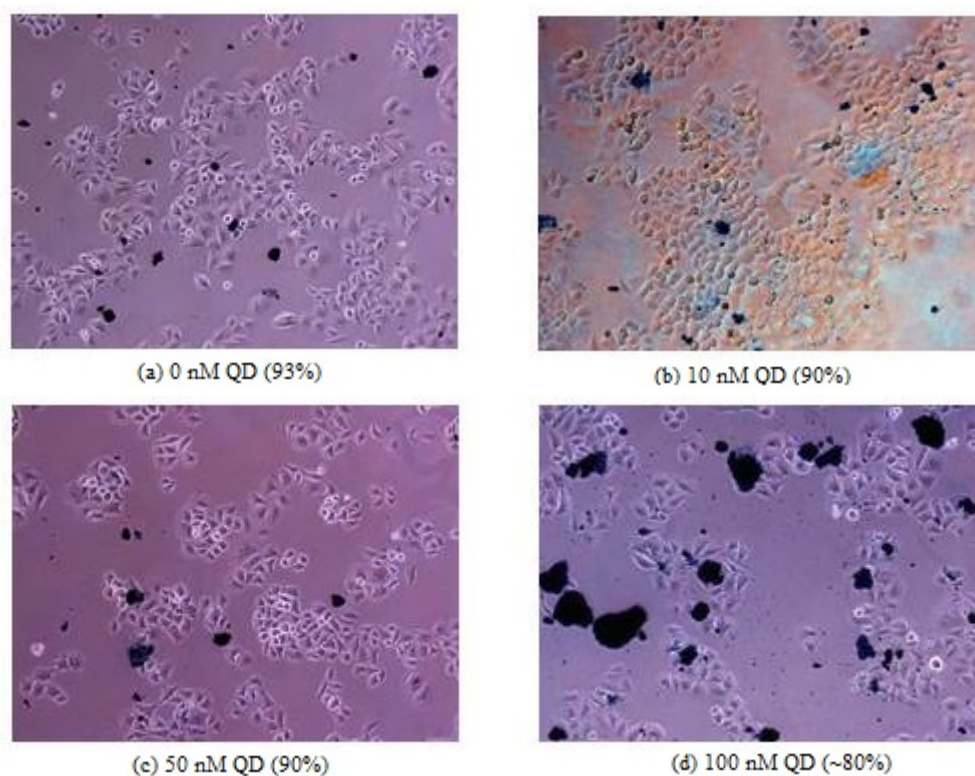


**Figure 3.4:** Phase contrast images of HeLa cells after Trypan blue staining. **a** to **d** are images of four cell samples that have been cultivated with 0 nM, 10 nM, 50 nM and 100 nM Qdot625 in 1 mL solution on a 12-well plate.

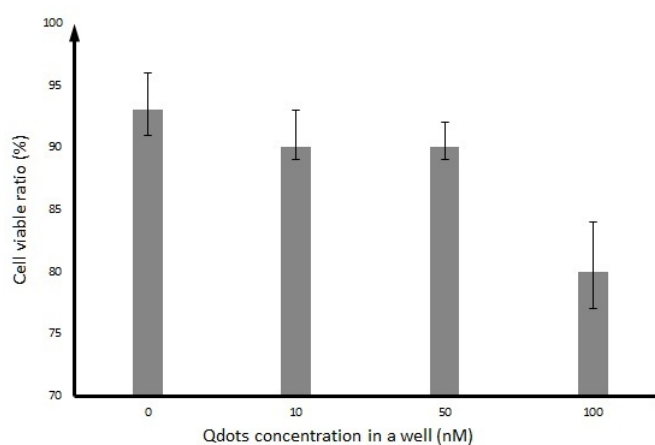


**Figure 3.5:** HeLa cells viability calculated from the Trypan Blue images in Figure 3.4.

Dark blue areas in Figure 3.5 indicate that there were dead cells in all four concentrations that were examined (0 nM/mL, 10 nM/mL, 50 nM/mL, 100 nM/mL),

but of different ratios. In order to estimate the ratios of dead cells, individual cells were recognised and counted manually. The number of dead cells within the large blue lumps was estimated by dividing the blue area by the average single dead cell area. Then, the ratios of dead cells were summarised and plotted (Figure 3.5). One can see that a high concentration (100 nM) of Qdot625 shows significant impact on cell viability ( $\sim 20\%$  cell death, Figure 3.4d). Low concentrations (10 and 50 nM) have shown a lower impact on cell viability ( $\sim 10\%$  cell death, Figure 3.4a, b), and thus they are potentially applicable for live cell imaging. This result is consistent with previous reports [194]. Having identified relevant QDs concentration range and tested against previous work, we carried out a quantitative viability assessment of Ge QDs and comparative tests on Invitrogen Qdot625 and Ge QDs by using the Muse test.

In preparation, fresh Ge QDs were produced and diluted into two concentrations: 25 nM/mL and 50 nM/mL Ge QDs. HeLa cells were prepared in dishes at an initial density of 30,000 cells/mL/dish. Ge QDs were then added to cells and tested on Muse at different time points. Table 3.1 shows the results averaged from three identical experiments (data presented as mean value). Unpaired student *t*-test was carried out between the results of Ge QDs treated cells and control cells in each time point. A *p*-value larger than 0.05 was considered non-significant. In order to find out if the Ge QDs caused any cell viability reduce, we performed the one way ANOVA test on the data of Ge QDs treated cells of three time points. *p* values of 0.68 and 0.09 were found out in 25 nM and 50 nM Ge QDs data respectively. This means that the Ge QDs haven't caused statistical significant (both *p* values are larger than 0.05) reduction on cell viability, even though 50 nM Ge QDs have showed higher probability of reducing cell viability than 25 nM ( $p = 0.09$  over  $p = 0.68$ ).

We can see that there is no significant difference of cell viability between the Ge QDs treated cells and control cells at all three time points (Table 3.1), just as in the case of Invitrogen Qdots. We then used the concentration of 25 nM/mL for a comparison between CdSe QDs and Ge QDs in medium-term Muse tests. For sample preparation, HeLa cells were cultivated on a 6-well plate with an initial concentration

**Table 3.1:** Cells viability with Ge QDs at different time points. \* stands for no significant statistical difference ( $p > 0.05$ ) of the cell viabilities between the Ge QDs treated cells and the control cells at the same time point.

Hela cells (1 mL)	24 h	48 h	72 h
Control cells	97.4%	98.5%	95.0%
Cells + 25 nM Ge QDs	86.1%*	82.9%*	83.9%*
Cells + 50 nM Ge QDs	87.4%*	82.5%*	82.1%*

of 5000 cells/well in 1 mL growth medium. Ge QDs and Qdot625 were then diluted into different concentrations before being seeded into each well. Cell viabilities were analysed at three time points (24, 48 and 72 hours) using Muse Analyser. The final results, as presented in Table 3.2 (data presented as mean value of three results) and Figure 3.6, are averaged from three individual experiments (attached in Appendix A). Similarly, unpaired  $t$ -test was performed on QDs treated cells viability data and control cells viability data. The comparisons with significant difference ( $p < 0.05$ ) between two data sets are labelled by  $\diamond$  symbol in Table 3.2 and Figure 3.6.

**Table 3.2:** Comparison of cell viability between Ge QDs and Qdot625.  $\diamond$  stands for significant statistical difference ( $p < 0.05$ ) of the cell viabilities between the QDs treated cells and the control cells at the same time point.

Hela cells (1 mL)	24 h	48 h	72 h
Control cells	93.6%	97.0%	92.8%
Cells (25 nM Ge QDs)	92.3%	87.8%	77.2% $\diamond$
Cells (25 nM Qdot625)	89.7%	81.1%	70.1% $\diamond$

Our results (Table 3.2 and Figure 3.6) suggest that as-prepared uncoated Ge QDs show comparable average biocompatibility with carboxyl coated commercial Invitrogen Qdots625 which was optimised for biocompatibility. Both two types of QDs have shown non-significant impact on cell viability at 24 hours and 48 hours time points. At 72 hours time point, both two types of QDs have shown some influence on cell viability (indicated as  $\diamond$  in Table 3.2 and Figure 3.6), however Ge QDs have shown significant better biocompatibility than Qdot625.

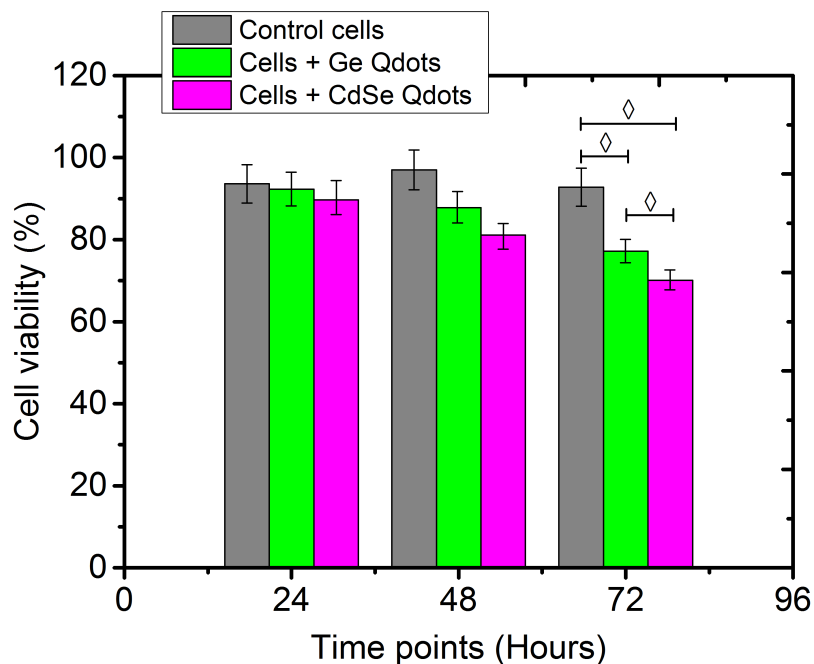


**Figure 3.6:** Comparison of cell viability between Ge QDs and Qdot625. Control cells (grey bar); cells cultivated with Ge QDs (green bar); cells cultivated with CdSe Qdots (magenta bar). Ge QDs and Qdot625 concentrations, 25 nM/mL. Chart plotted from data in Table 3.2.  $\diamond$  represents significant difference ( $p < 0.05$ ) between two data sets.

In summary, we found that as-prepared, uncoated Ge QDs show on average the same or better biocompatibility at concentrations below 50 nM/mL than carboxyl coated commercial Qdots625 optimised for bioapplications. In the following section, both Qdot625 and Ge QDs will be further studied for their impact on cell proliferation and cell morphology using medium-term live cell imaging.

### 3.1.2.2 Medium-term live cell imaging

As demonstrated in the previous subsection, the safe concentrations of QDs for live cell imaging were found to be  $\leq 50$  nM/mL. Based on these results, we further studied medium-term (up to 96 hours for Incucyte imaging) live cell imaging for cell proliferation, nanoparticle uptake and cell morphology (nucleus shape changes) study.



Initially, HeLa cells in 1 mL solution were prepared on a 12-well cell culture plate, of both low (5000 cells/mL) and high (15000 cells/mL) densities. Identical concentrations of Ge QDs and Qdot625 (50 nM/mL) were individually added to the cells. As a reference, control cells were set without adding any QDs. Images were taken on Incucyte with a 10× lens with the interval of 6 hours between two imaging. Both phase contrast and fluorescence modes (excitation 585 nm/ emission 635 nm) were used. Finally, merged Incucyte phase contrast and fluorescence images were obtained (Figure 3.7).

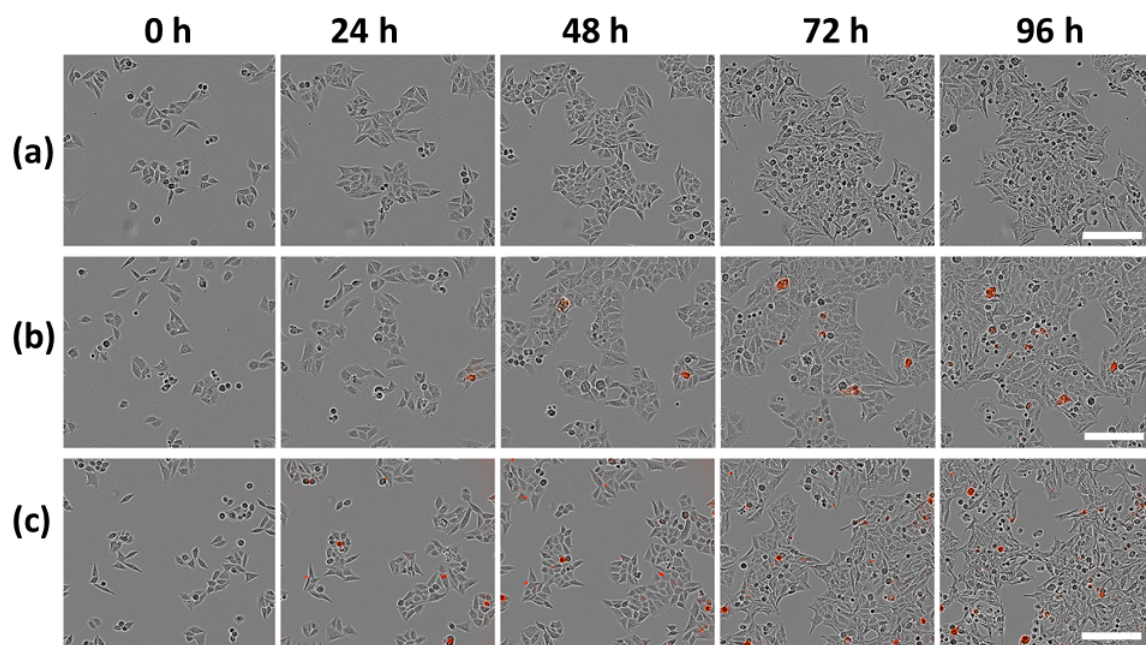


**Figure 3.7:** Merged phase contrast (grey) and fluorescence (red) Incucyte images of HeLa cells cultivated with Ge and Qdot625 QDs. HeLa cells were cultivated with (a) no QDs, (b) Ge QDs and (c) Qdot625 respectively. Scale bar, 100  $\mu\text{m}$ .

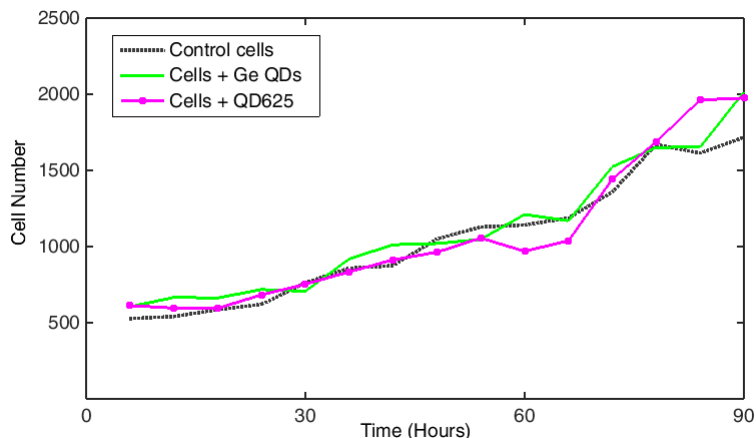


**Figure 3.8:** HeLa cells proliferation curve under different treatments. Grey dash line, green solid line and magenta dotted line show cell growing curve of control cells, cells with Ge QDs and Qdot625 respectively. The results were summarised from data shown in Figure 3.7.

Here we can see that the cells have taken up some QDs in the first 24 hours (Figure 3.7b, c) and showed increasing levels of fluorescence after 24 hours. Furthermore, the cell proliferation is an additional method for the assessment of impact of QDs on cell viability. The cell proliferation data obtained from these medium-term Incucyte measurements are shown in Figure 3.8. One can see that neither Invitrogen Qdots nor Ge QDs show an obvious impact on cell proliferation within 4 days at 50 nM/mL.

It's also well-known that QDs can cause DNA damage, which can affect the shape of the nucleus [196, 197]. Hence, the analysis of nucleus shape is another way to assess the impact of QDs on cell viability. In this study, HeLa cells were grown in the growth medium of 1 mL/well in a 12-well plate at a density of 5000 cells/mL. Following this, 25 nM growth medium, Ge QDs, Qdot625 solutions were added to the three wells respectively. Then, cells under different treatments were fixed and stained with DAPI. In order to examine the nucleus shape, cell samples were prepared on a microscope slide and checked on the Leica DM500 Epi-fluorescence microscopy using a 20 $\times$  lens. At three time points (24, 48, 72 hours), one sample was taken from each

treatment and was imaged. In each case, a random area was selected to be imaged in order to inspect the cell nucleus shapes. Figure 3.9 presents the merged cell outline images and DAPI staining fluorescence images.

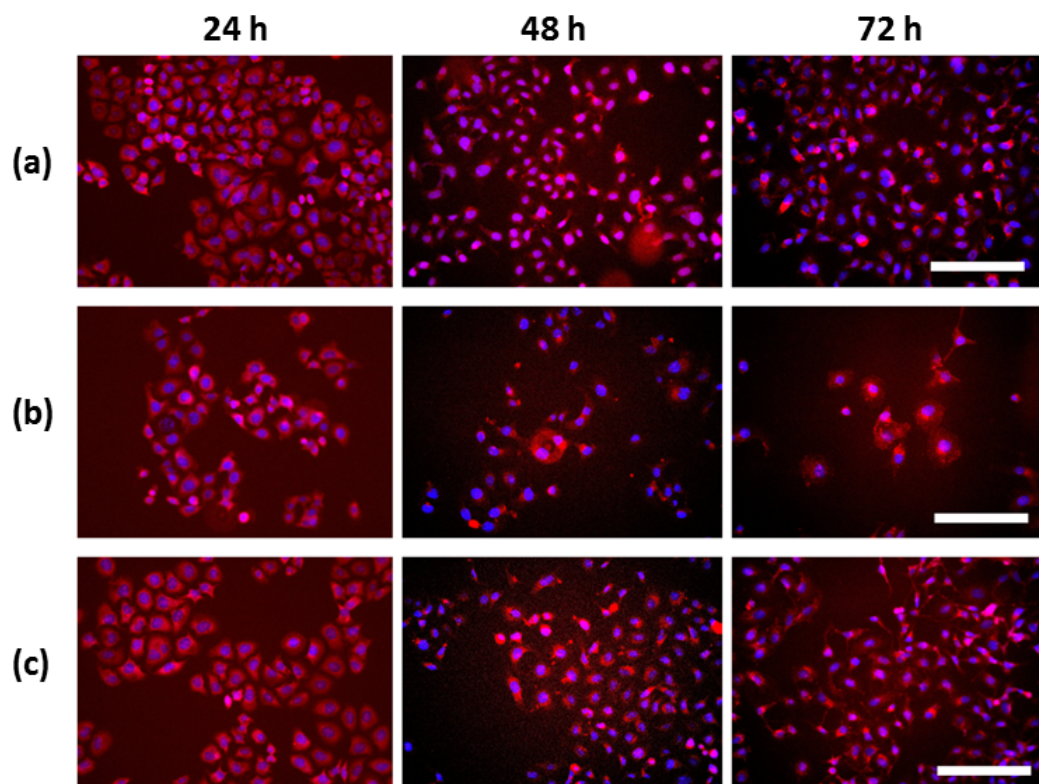


**Figure 3.9:** Cell and nucleus shape under different QDs treatments: (a) adding nothing, (b) adding 25 nM Ge QDs, (c) adding 25 nM Qdot625. Images were merged by cell outline images (red) and nucleus images (blue). Cell outlines were imaged through cell auto-fluorescence when excited with 400+ nm light. DAPI fluorescence images were collected with excitation light wavelength of band pass of 400/40 nm. Scale bars, 100  $\mu\text{m}$ .

Further quantitative measurements of the cell nucleus shape were performed. Both the nucleus size (measured as Feret's diameter [180]) and circularity (a value between 0 and 1 indicates the roundness of an object, 0 stands for not round at all and 1 stands for a perfect circle shape) of the cells were used to characterise the nucleus shapes. Figure 3.10 summarises both the cell nucleus size and circularity changes along with the time under different QDs treatments. For statistic analysis, unpaired *t*-test was performed between QDs treated cells data (numbered as 2 and 3

in Figure 3.10 for Ge QDs data and Qdot625 data respectively) and the control cells data (numbered as 1 in Figure 3.10).

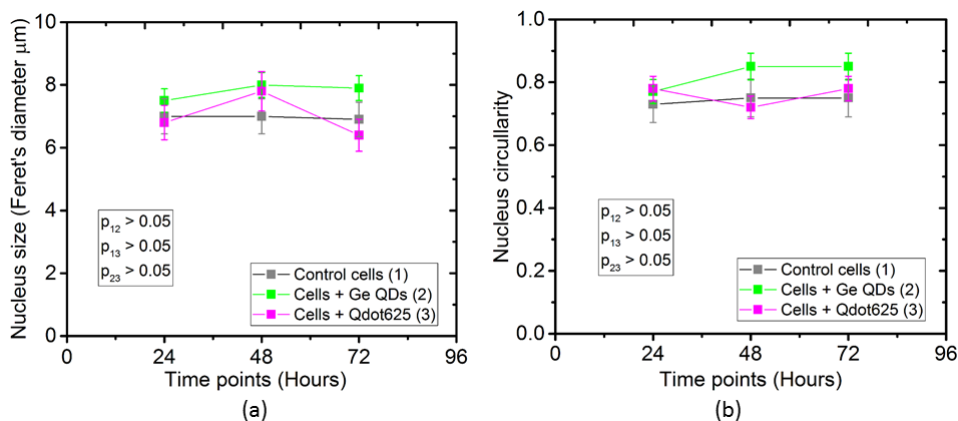


**Figure 3.10:** Summary of cell nucleus size(a) and shape (b) changes under QDs treatments. Results were analysed from the data shown in Figure 3.9. Results are presented as mean and standard deviation. A  $p$  value of larger than 0.05 ( $p > 0.05$ ) is considered non-significant statistical difference between the compared data sets.

All  $p$ -values in the  $t$ -tests were found out to be larger than 0.05 (Figure 3.10). This means that three different treatments have shown non-significant statistical differences in nucleus size and circularity. When compared with the control treatment, all QDs had very little impact on the shape and size of the cell nucleus. If anything, Ge QDs showed slightly better performance than Invitrogen Qdots625. This is consistent with the cell proliferation results (Figure 3.8) summarised from the Incucyte data.

To conclude,  $\leq 50$  nM/mL concentrations QDs were shown to have minimal side effects on cell proliferation within the first 96 hours, and unnoticeable impact on cell morphology, particularly nucleus shape. In the next section, we are going to load QDs into cells to undertake fluorescence imaging.

### 3.1.3 Fluorescence imaging

QDs of concentrations below 50 nM/mL are potentially suitable for live cells because they do not significantly reduce cell viability and proliferation, as has been demonstrated above. However, there have been no tests of Ge QDs to find out whether at these concentrations they show sufficient fluorescent signals to be useful for cell imaging. Thus, two imaging studies will be described in this subsection: (i) loading Ge QDs onto a microscope slide and testing imaging on a fluorescence microscope; (ii) loading Ge QDs to cells and carrying out fluorescence imaging.

#### 3.1.3.1 QDs test imaging

Ge QDs dissolved in water at 50 nM /mL were dropped onto a microscope slide and covered with a round cover slip, then sealed with clear nail polish. Next, fluorescence images (Figure 3.11) were taken on the spinning disk confocal microscopy using a 100 $\times$  1.49 NA oil objective lens. The sample was then excited with 488 nm and 561 nm lasers. The images were taken at an exposure time of 150 ms and EM gain of 300.

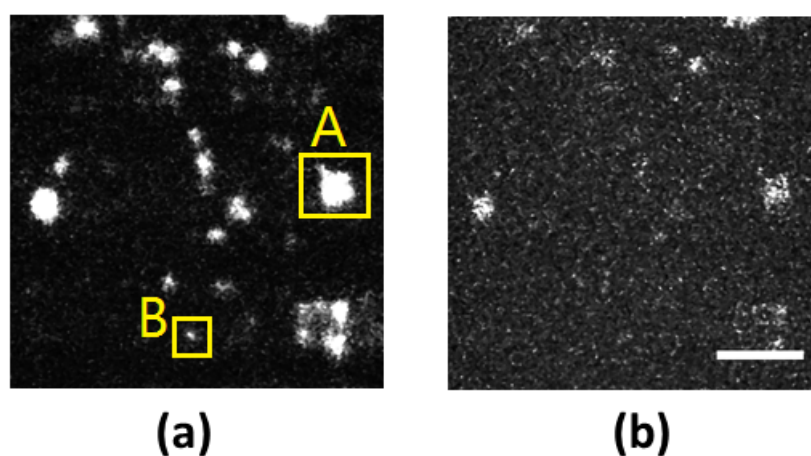


**Figure 3.11:** Ge QDs fluorescence images on a spinning disk microscopy with a 100 $\times$  lens, using same sample and imaging settings but different excitation laser lights: (a) 488 nm, (b) 561 nm. Lasers power: 8 % of the 50 mW full power. Scale bar, 5 $\mu$ m

Two excitation lasers under the same imaging settings have resulted in two images of different contrast. Ge QDs which were illuminated by a 488 nm laser (Figure 3.11a) showed stronger fluorescence emission than those excited by 561 nm lasers (Figure 3.11b). This is consistent with the Ge absorption curve (Figure 3.2), in which Ge QDs showed stronger absorption at nearly 488 nm than nearly 561 nm. It can also be seen in Figure 3.11a, that Ge QDs were possibly not uniform when distributed on the microscope slide and both a big cluster (yellow square A) and tiny dots (yellow square B) were observed.

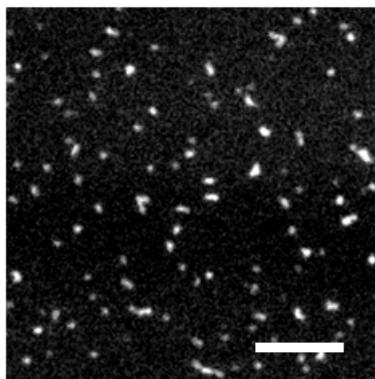


**Figure 3.12:** Qdot625 fluorescence images on spinning disk confocal microscopy with a  $100\times$  lens. Images were taken under the settings of EM gain of 300, with an exposure time of 100 ms. QDs concentration: 50 nM/mL. Scale bar,  $5\mu\text{m}$ .

Qdot625 in original solution was prepared at the same concentration on a microscope slide and then were observed on the spinning disk microscopy system as a reference. A 488 nm laser using at 8 % of the 50 mW full power was selected as the excitation. Invitrogen Qdot625 showed clear fluorescence brightness at the concentration of 50 nM/mL (Figure 3.12a).

Once we confirmed that Ge QDs can be clearly imaged under fluorescence microscope at a relatively low concentration, they were loaded into cells for imaging.

### 3.1.3.2 Cell imaging with Ge QDs

Fluorescence imaging of Ge QDs-labelled HeLa cells was carried out on the spinning disk system. HeLa cells were grown in a 12-well plate at a density of 5000 cells/mL/well. Ge QDs were seeded into HeLa cells at the concentration of 50 nM/mL/well for non-specific labelling. Cells were left to incubate for over 24 hours before being fixed and prepared for microscopy. During imaging, four laser wavelength that cover the Ge QDs absorption range were selected for excitation: 405 and 488, 561, 640 nm (Figure 3.13). As has been shown in Figure 3.11, the fluorescence emission of Ge QDs was rather weak when it was excited by lasers of wavelength longer than 488 nm. Here we used excitation lasers of 561 and 640 nm to further verify the results of the previous subsection. 405, 488, 561 nm lasers were set at 4 % of the 50 mW full power and the 640 nm laser was set at 2 % of the 100 mW full power. Exposure time was adjusted to 300 ms and the EM gain was 300.

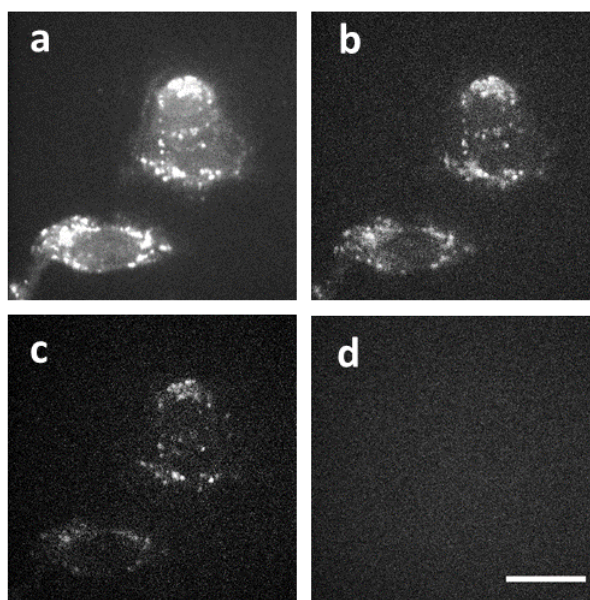


**Figure 3.13:** HeLa cells labelled with Ge QDs fluorescence images acquired under laser illumination of (a) 405 nm, (b) 488 nm, (c) 561 nm, (d) 640 nm. The exposure time was 300 ms. Scale bar, 20  $\mu\text{m}$ .

What can be clearly seen from Figure 3.13 is that Ge QDs in HeLa cells still have

a visibly stronger fluorescence emission when being excited by short wavelength lasers lights, such as 405 nm, 488 nm (Figure 3.13a, b), than long wavelength laser lights such as 561 nm, 640 nm (Figure 3.13c, d). In particular, nearly zero fluorescence was detected when the sample was excited by 640 nm lasers (Figure 3.13d). This could be predicted from the Ge QDs absorption curve (Figure 3.2) which indicated a strong absorption coefficient at around 400 nm and very little absorption at around 650 nm.

### 3.1.4 Conclusion

In conclusion, we have discovered that Ge QDs are suitable for in vitro cell imaging at concentrations of  $\leq 50$  nM/mL. They can provide good biocompatibility for live cells and sufficient fluorescence brightness when they are excited by proper laser lights. The small size of Ge QDs ( $\sim 3.8$  nm) also needs mention as this can potentially allow them to be used for imaging cellular locations with size restrictions, such as synapses, which could be an invaluable feature in cell imaging. In the next section, we are going to use the QDs to perform super-resolution imaging.



## **3.2 Stochastic super-resolution cell imaging using spinning disk confocal microscopy and blinking Ge QDs**

In this section, the stochastic super-resolution cell imaging, which is based on Ge QDs blinking statistics and uses Spinning Disk Statistical Imaging (SDSI) method [61], will be demonstrated. In practice, spinning disk laser scanning confocal microscopy was used to perform the experiments. This enables hundreds of images to be acquired in a few seconds. Cell culture related work was carried out in a standard tissue culture lab. In this section, the characterisations of our SDSI system will be described. Blinking events of Ge QDs will be analysed. Then, the photo-stability of QDs on the timescale of several minutes will be assessed and compared with dyes and proteins. Following this, the super-resolution imaging data collections and results will be detailed. To facilitate the reconstruction analysis, an efficient specific localisation algorithm has been developed.

### **3.2.1 Principles of stochastic super-resolution imaging using blinking QDs**

QDs blinking is not desired in fluorescence labelling because it results in a reduction of the level of integrated fluorescence signals. However, the stochastic blinking effect may offer an opportunity to distinguish individual QDs within a diffraction limited region, and thus it can be used for stochastic single molecule localisation super-resolution imaging (see section 1.5.2). The first demonstration of the principle of super-resolution imaging using blinking QDs was reported in 2005 by Keith A. Lidke and R. Heintzmann's group at King's College London [198], followed by contributions by several other groups [199, 200]. Here we studied the Ge QDs in order to

check whether they are suitable for the type of imaging based on blinking statistics.

The principle underlying this super-resolution imaging using blinking effect is to detect and separate the emission of single blinking QDs from within a group of QDs. The basic criteria in this method, which were proposed by Keith A. Lidke, include [201]: (i) the blinking of individual QDs to be resolved must be statistically independent; (ii) the probability distribution should be ideally non-Gaussian. Criterion (i) is to ensure that one blinking on QDs will not cause the neighbouring QDs within a diffraction limit region being blinking on and thus provides the possibility of single molecule imaging within one diffraction limit region. The blinking of individual QDs is a stochastic process and has been reported to be independent of neighbouring QDs [145, 146, 202] (as introduced in section 1.6.3.2) at concentrations relevant to this study and thus condition (i) is satisfied. As to the criterion (ii), a Gaussian probability distribution of QDs blinking means that majority of the QDs blinking off events happen at the same time window, therefore it is not easy to stochastically separate individual QDs and collect single molecule imaging as many as possible. For this reason, a non-Gaussian distribution is beneficial to the stochastic imaging. Hence, we have to understand the timescale and the probability distribution of the Ge QDs blinking events. With these considerations in mind, we carried out Ge blinking statistic measurements, stochastic cell imaging using blinking and single molecule localisation experiments to investigate if our Ge QDs were suitable for this super-resolution imaging.

As a stochastic single molecule localisation imaging method, this strategy makes the use of blinking effects and images of only a few blinking on QDs during one data acquisition period. In this way, thousands of images (an imaging time length of several minutes or even longer) should be acquired in order to identify as many QDs as possible. Then, a super-resolution image is obtained through single molecule localisation and reconstruction algorithms. In this type of methods, the resolution ability is determined by multiple factors, such as single molecule localisation precision and probe size. Other factors include the mechanical stability of the microscope

system and sample drift. Hence, we initially characterised the microscope system.

### 3.2.2 Microscope system characterisation

The mechanical stability of a microscope essentially influences the single molecule localisation resolution ability in many aspects. In order to understand and optimise our spinning disk confocal microscope system for the purpose of achieving single molecule localisation super-resolution imaging, we characterised its single molecule localisation capabilities, background noise and the PSF dependence on excitation wavelengths. We also studied sample drift. These are the key parameters that determine the resolution in stochastic single molecule localisation super-resolution methods, as was discussed in section 1.5.2.

#### 3.2.2.1 Localisation precision

Single molecule localisation precision is determined by many factors such as the image's background, system PSF, and CCD sensitivity. A widely accepted formula was developed in 2002, which shows that localisation precision can be calculated by the mean-squared position error of a single molecule  $m$  [203]:

$$\left(\sigma_{x,y}^2\right)_m \approx \frac{s^2 + a^2/12}{N_m} + \frac{4\sqrt{\pi}s^3b_m^2}{aN_m^2} \quad (3.1)$$

where  $s$  is standard deviation of the fitting function of PSF (usually a Gaussian function),  $a$  stands for the pixel size in the image ( $a \approx d/M$ , where  $d$  is CCD pixel size and  $M$  is the magnification of the microscope),  $N_m$  is the total number of photons measured from molecule  $m$ , and  $b_m$  is the number of background photons. PSF is fitted by a Gaussian function and it is dependent on excitation wavelength, which will be further discussed in the next subsection. Consequently, to achieve a higher resolution, an imaging method should aim at designing the smallest possible PSF size (small  $s$ ), high collection efficiency (large  $N_m$ ) and reducing the background signal (small  $b_m$ ).

If the background (large  $b_m$ ) is very high or the blinks are not bright (small  $N_m$ ), it may not be possible to localise the molecules with sufficient accuracy (small  $\sigma$ ).

The background signal is affected by a variety of sources. For example, the ambient light, CCD detector's dark current noise and autofluorescence of the sample mounting media. For background measurements of the spinning disk confocal microscope, a background-calibration-sample slide without QDs or cells was used. This calibration slide was prepared with one drop of water and was then covered by a thin glass cover slip.

Background measurements were performed by using a  $100\times$  1.49 NA oil objective. A series of 1000 images of size  $512\times 512$  pixels were taken with the CCD EM gain of 300 and exposure time of 50 ms. Images were taken under the following conditions of excitation laser wavelength: 488 nm (10 - 20 % of the 50 mW power), 561 nm (10 - 20 % of the 50 mW power) and 640 nm (5 - 15 % of the 100 mW power). Background images were then loaded onto OriginPro software for post processing. An average of the background grey value of the pixels was calculated over time. They were  $380 \pm 42$ ,  $363 \pm 28$ ,  $365 \pm 39$  for 488 nm, 561 nm and 640 nm laser excitations respectively. These background values were used in the localisation precision estimation. Furthermore, the background signal level was also considered and subtracted from the raw images when super-resolution imaging and reconstruction was undertaken.

Amongst other things, the final image resolution will depend on localisation precision. This will in turn depend on the number of measured photons (see Equation 3.1). Hence, we conducted a series of experiments to gauge the number of frames that are required to optimise the localisation process. Several datasets of different number of frames were investigated and the corresponding localisation precision was calculated. Images were taken with Qdot625 immobilised on a glass microscope slide on the spinning disk confocal system using a  $100\times$  objective. A 488 nm laser at 15 % of its 50 mW full power was chosen as excitation light source. Eight datasets (500, 1000, 1500, 2000, 2500, 3000, 4000, 5000 image frames respectively) were acquired

**Table 3.3:** Position error( $\sigma$ ) for different imaging frames. Unit: nm.

Frames	500	1000	1500	2000	2500	3000	4000	5000
1 st Exp.	-	23	-	23	-	27	31	42
2 nd Exp.	42	39	38	38	37	36	38	38
3 rd Exp.	51	45	39	38	33	25	23	23

Note: three datasets in the first experiments were destroyed due to a storage issue.

with the same imaging settings: camera gain 14, EM gain 300, exposure time 100 ms. For each dataset, ten points were traced over time and the intensity of each point (cropped by a  $12 \times 12$  pixels squared region) was recorded. The intensity value was converted into photon numbers by an equation that is specific for iXon3-885 CCD. The conversion calculations can be found in Appendix C.

The pixel size of the final image was calibrated using a  $100 \times$  objective and a standard microscope scale slide. The calculated pixel size was found to be 70 nm. Furthermore, the PSF size ( $s$  in equation 3.1) was found to be 226 nm, which was obtained by Gaussian fitting performed in OriginLab. Once all of the parameters had been determined, position error  $\sigma$  was calculated in Microsoft Excel using equation 3.1. The experiments were repeated three times and three groups of data were obtained for comparison. Table 3.3 shows the summarised results.

In order to find out the position error trend along with collected image frames, we conducted  $t$ -test between any two neighbouring image frames data and calculated the corresponding  $p$  values based on the mean and standard deviation of three data sets. Consistent significant decreasing of the position error values from 500 frames to 2000 frames has been found ( $p < 0.05$ , see Figure 3.14). However, results for images frames of more than 2000 frames have no significant differences between each other ( $p > 0.05$ , see Figure 3.14).

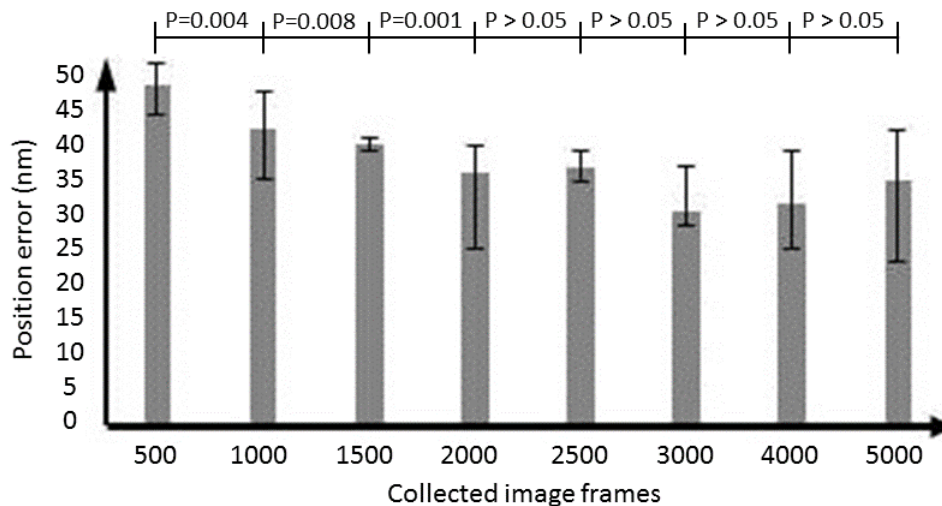


**Figure 3.14:** Position error ( $\sigma$ ) variations for different imaging frames. Data is presented as mean and standard deviations from three data sets mentioned in Table 3.3.  $p > 0.05$  is considered no significant statistic difference between the compared data sets.

In summary, position error ( $\sigma$ ) describes the localisation precision of single molecules. The results demonstrated in Table 3.3 and Figure 3.14 indicate that, with the spinning disk confocal system we are able to achieve a localisation precision of up to  $\sim 25$  nm in our imaging conditions. The localisation precision has a trend of improving as the frame numbers increase from 500 to 3000. Images with frame numbers of 3000 to 5000 show similar  $\sigma$  values of 20 - 40 nm. Therefore, collecting more than 3000 frames would not significantly increase the precision of single molecule localisation. In the next subsection, we will focus on the PSF size change with the excitation laser wavelength.

### 3.2.2.2 PSF dependence on excitation wavelength

The Point Spread Function (PSF) of the spinning disk confocal microscope was measured by using 100 nm Tetraspeck beads (Invitrogen, UK). The beads were stained with four different fluorophores. The four corresponding excitation/emission peaks were: 360/430 nm (blue); 505/515 nm (green); 560/580 nm (orange) and 660/680

nm (dark red). The beads were imaged by using a 100 $\times$  objective in X, Y, and Z directions (Z stacks). The PSFs were collected under four excitation conditions: 405, 488, 561 and 640 nm. The Z stack displayed by ImageJ reveals multiple views of the PSF in three directions (Figure 3.15).

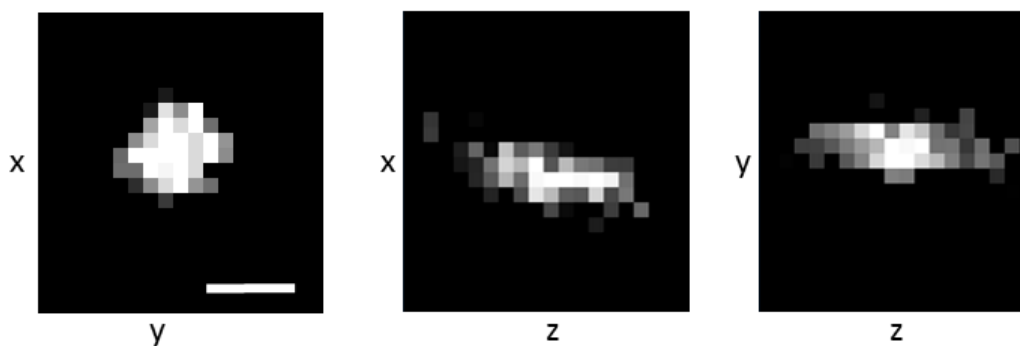


**Figure 3.15:** Multiple views of a PSF image in three directions, collected from standard beads excited by 561 nm laser on the spinning disk confocal microscopy. Scale bar, 500 nm.

Then, a PSF image in  $x - y$  direction (lateral plane) was plotted and fitted by the Gaussian function in OriginPro in order to study the PSF size changes with excitation wavelength. The fitting results are summarised in Table 3.4.

**Table 3.4:** PSF fitting results for four situations of excitation laser wavelength.  $s$  stands for the standard deviation of the PSF. The variances stand for the standard error of three groups of fittings.

Excitation laser wavelength (nm)	405	488	561	640
$s$ (nm)	184 $\pm$ 21	192 $\pm$ 21	230 $\pm$ 28	220 $\pm$ 19

The FWHM of the fitted Gaussian function has been adopted as the value of  $s$ , and this value increased with longer excitation wavelength. The results in Table 3.4 are consistent with what we expected for a diffraction-limited system. The PSF sizes are also important to the super-resolution reconstruction process, in which the segmented regions of interest (ROI) will be determined by the PSF sizes.

### 3.2.2.3 Sample drift

Drift refers to the continuous movement of the sample during imaging. In long-term cell imaging, for example several minutes or longer, drifts may become a significant problem. It is affected by many factors, such as the slippage of the focus mechanism, air flow, thermal gradients and platform vibrations. Drifts can be corrected or reduced by either hardware or software solutions. Our microscope system was equipped with a vibration isolation table to improve the instrument's stability. Lateral drift was further reduced by enclosing the sample stage and objective elements with an environmental chamber that maintained a stable temperature. It was pre-warmed for half a hour to 32°C prior to imaging. Axial drift of the focus mechanisms was corrected by using a capacitive feedback system (PI MicroMove Autofocusing device, Physik Instrumente, Germany).

In order to quantitatively characterise the sample drift in our spinning disk confocal microscope under these conditions, we measured the movements through a time-lapse image stack of a Tetraspeck slide (Invitrogen, UK) with 100 nm fluorescent microspheres. A 5000 frames image stack was acquired in 45 minutes by using a 100× oil objective lens. Then, ten objects in the images were traced by Metamorph software. The positions ( $X/Y$  coordinates) and time points were measured and recorded for each object. The sample drift (Figure 3.16) was revealed by averaging the ten objects' movements over time.

A clear sample drift in our system (Figure 3.16) was indicated by the monitoring of fluorescence signals of ten beads for a relatively long period (40 minutes). The drifts in both  $x, y$  directions varied from several nm to about 100 nm (Figure 3.16) in 40 minutes time. Following these measurements, we adopted a software-based drift correction similar to the method described in previous work, which used reference markers in the images and computational processing [204]. We chose several peak brightness areas as reference points.



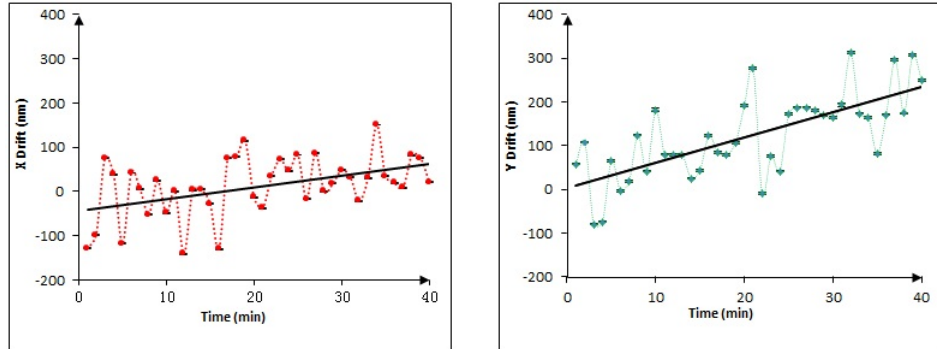


**Figure 3.16:** Qdot625 position drifts in X and Y directions on the spinning disk confocal microscope within 40 minutes.

In summary, it is clear from the demonstrations above that, the mechanical stability of a microscope has a significant influence on the resolving ability (effective resolution limit) of a stochastic imaging super-resolution microscopy. For example, the sample drift of a few tens of nm in 40 minutes (Figure 3.16) could lower the effective resolution which is otherwise determined by the localisation precision of around 25 nm (Table 3.3). Nevertheless, high localisation precision and a stable microscope do not directly translate into high imaging resolution if the overlapping fluorescence signals from QDs within the size of one PSF can not be well separated. In our method, this separation relies on the repetitive imaging of blinking Ge QDs, and the imaging takes several minutes. Hence, a clear characterisation of the blinking events of Ge QDs and understanding their photo-stability over several minutes is rather important. In the next subsection we will be assessing the blinking phenomena and photo-stability in Ge QDs using SDSI.

### 3.2.3 Ge QDs as SDSI probes

#### 3.2.3.1 Ge QDs blinking measurements

In order to check if our Ge QDs meet the criteria for blinking stochastic super-resolution imaging (see section 3.2.1), we characterised the blinking phenomenon of

Ge QDs. To ensure a sparse distribution for single QDs observation, Ge QDs dissolved in water in a vial were put in the sonicator for 12 minutes to disperse. They were further diluted to 1 pM/mL in water. Then, 2  $\mu\text{L}$  liquid was sucked and dropped onto a glass microscope slide, subsequently being mounted by a 22 mm square cover slip, resulting in typical surface densities of  $\sim 0.25$  QDs/ $\mu\text{m}^2$ . The average distance between two neighbouring Ge QDs was calculated to be  $\sim 500$  nm, which is larger than a PSF ( $\sim 200$  nm). The sample was observed under the spinning disk confocal microscopy using a  $100\times$  objective (NA=1.49). Ge QDs were excited by a 488 nm laser using of 10 % of the 50 mW full power. A time series image stack of 5000 frames was collected with an exposure time of 50 ms and the imaging interval set to 0. Image size was set as  $1024\times 1024$  pixels, with each pixel size of  $\sim 70$  nm. Potential single QDs were manually cropped by  $14\times 14$  pixel regions, and a single QD for blinking measurement was identified and selected through two criteria: spot size similar to a PSF ( $\sim 200$  nm); and the most stable brightness (minimum difference between the strongest brightness and average brightness). The single QD on the image stack was traced over time using ImageJ. Figure 3.17 presents a few selections of fluorescent QD images showing obvious fluorescence intensity change within 30 seconds.

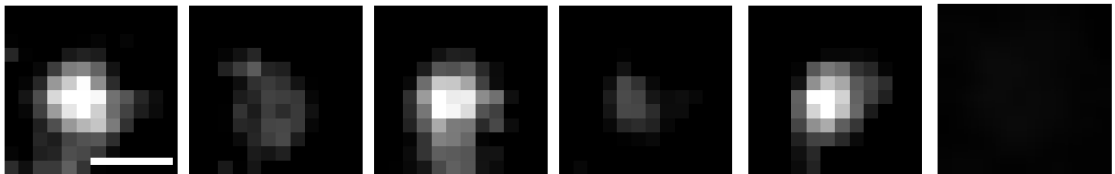


**Figure 3.17:** A few captures of single Ge QD fluorescence intensity changes (blinking) within 30 seconds, observed on spinning disk confocal microscopy. Scale bar: 400 nm

For the purpose of quantitative study, the duration of each fluorescence intermittency event was measured and plotted (Figure 3.18). Fluorescence intensity of a single QD was presented against to time. A 20% value of the brightest level was used to judge the fluorescence intermittency (blink ‘off’) according to the background measurements (maximum background image pixel grey values were less than 20 % of the brightest value). Any fluorescence intensity value beyond this level would be

regarded as non-fluorescence; thus, fluorescence intermittency was recognised and the duration was measured accordingly. All blinking ‘off’ events of a single Ge QD within 180 seconds were measured (see Figure 3.18 for 5 selections of Ge QD blinking events). Figure 3.19 summarises the statistics of all Ge QD blinking ‘off’ durations that were observed within 180 seconds. The durations distribution follows an inverse power law with an exponent of -1.6 (Figure 3.19).

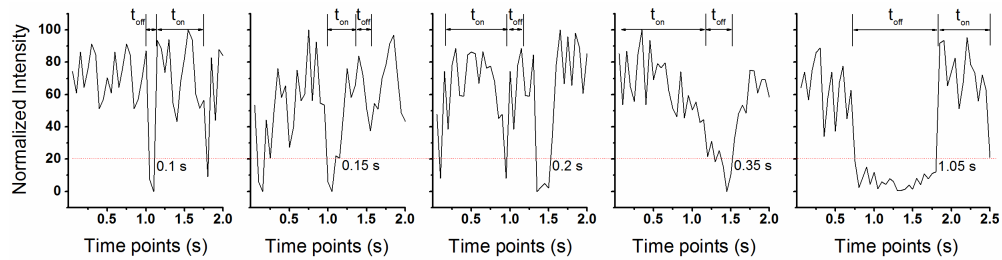


**Figure 3.18:** A few selections of the fluorescence intermittency durations of a single Ge QD.

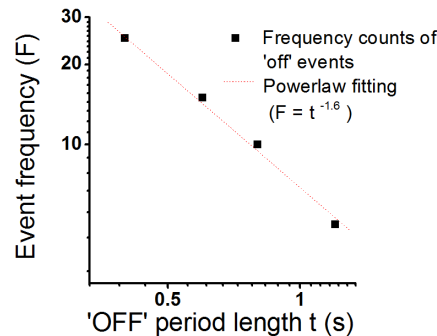


**Figure 3.19:** Inverse power law distribution of Ge QDs blinking ‘off’ event durations. Fitted power function index: -1.6.

The results in Figures 3.18 and 3.19 show that our Ge QDs were observed stochastic blinking under the spinning disk confocal microscopy. Blinking off durations vary from 0.1 s to more than 1 s with an inverse power distribution of the frequency. Typically the exponents of  $-1.6 \pm 0.2$  are also observed in CdSe QDs for off durations over as many as 6 orders of magnitude in time [205]. In the context of a model for blinking, in which the off-state occurs due to charged QD species (ionisation), one can explain the QDs blinking phenomenon [205]. However, there is still a lack of reliable

models to precisely predict the blinking events and control them. Furthermore, it has been experimentally demonstrated that the off-state exponents are independent of QDs number, size, composition and temperature [145, 206]. Considering the blinking stochastic super-resolution imaging criteria (ii) described in section 3.2.1, one can see that our Ge QDs meet the condition that the probability distribution of blinking is non-Gaussian (inverse power law with an index of -1.6). The power law distribution with index of -1.6 would be further used as a standard of Ge QDs to determine the number of QDs within a diffraction-limited region. This will be described in the super-resolution reconstruction section 3.2.5.2. The results in Figure 3.19 also suggest that exposure times below 0.5 seconds should be most suitable in imaging experiments due to much higher probability of the blinking events in that region.

In order to carry out stochastic super-resolution imaging based on blinking, imaging procedures should be repeated thousands of times in order to temporally distinguish as many QDs as possible. This can typically take several minutes. As a consequence, knowing the photo-stability of Ge QDs on the timescale of minutes is of great importance. In the next section, the optical stability of Ge QDs in cells was studied in terms of photo-bleaching measurements. This is achieved by comparing the photo-bleaching curve of several probes, as will be demonstrated below.

### **3.2.3.2 Photo-bleaching**

To investigate the photo-stability performance of Ge QDs in a cellular environment, several fluorescent probes (Ge QDs, CdSe/ZnS Qdots, Dronpa, mEos, AlexFluor 647) have been tested and compared on HeLa cells. In each case, these fluorescent probes were delivered to cells either by endocytosis, or through antibody conjugation labelling (see Materials and method section 2.1.2). Ge and CdSe QDs were delivered to cells with non-specific labelling. Dronpa, mEos and AlexFluor 647 were delivered to the mitochondria, the actin structure in the lamellipodia and Connexin vesicles

respectively [61], by cell transfection. They were imaged on the spinning disk confocal microscope working with a 100 $\times$ , NA 1.49 oil objective. Ge and CdSe QDs were illuminated continuously by a 488 nm laser using 10 % of 50 mW full power, and the imaging exposure time was set at 100 ms. mEos was imaged under excitation of a 561 nm laser at 20 % to 25 % of 50 mW full power. AlexFluor 640 was imaged using a 640 nm laser at variable power from 8 % - 16 % of 100 mW full power and a 405 nm 100 mW laser at 1 % to 5 % power [61]. A time-lapse (longer than 3 minutes) image stack of each sample was acquired. A square region of 10 $\times$ 10 pixels of relatively strong brightness was cropped in each dataset and traced over time. In this way, the fluorescence intensity of the cropped region was plotted. For quantitative comparison, ten 10 $\times$ 10 pixels square regions were analysed for each dataset, and an averaged fluorescence intensity change was calculated and normalised into the scale of 0 to 100.

Comparison of the fluorescence intensity for five datasets was carried out over 150 seconds time (Figure 3.20). Both CdSe and Ge QDs showed very little reduction in fluorescence intensity in 150 seconds, whereas three protein and dye probes (Dronpa, mEos and AlexFluor 647) lost more than 50 % fluorescence intensity in the same period. This photo-bleaching comparison among several probes confirms the good photo-stability of QDs in cell imaging. This is consistent with previous findings (Figure 1.19).

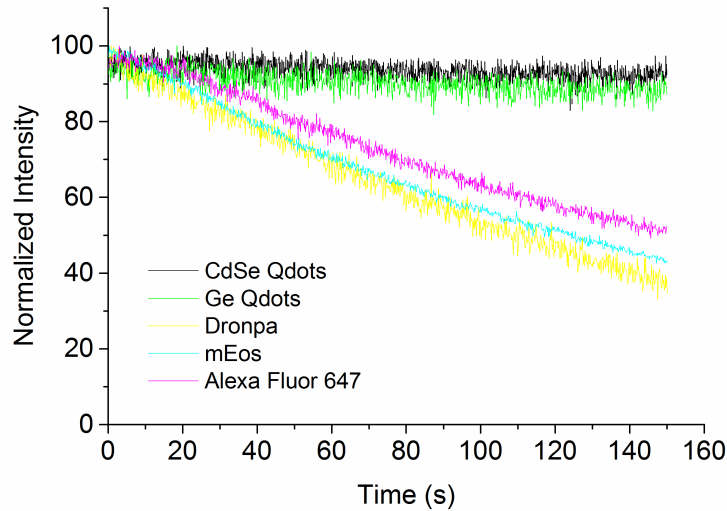


**Figure 3.20:** Probes photo-bleaching comparison. Black, green, magenta, light blue and yellow curves correspond to CdSe QDs, Ge QDs, Dronpa (a fluoresce protein), mEOS (a fluorescent protein) and AlexFluor 647 (a chemical dye) data respectively.

To summarise, we have confirmed the good photo-stability of QDs in cellular environment, thus making them suitable for the proposed imaging approach. In the next subsection, the stochastic imaging using the spinning disk confocal microscopy and Ge QDs will be demonstrated.

### 3.2.4 Stochastic cell imaging with QDs

Ge QDs non-specific labelled Hela cell sample was imaged using the spinning disk confocal microscopy. As a reference, we also studied the commercial CdSe QDs - Qdot625. For sample preparation, QDs at the concentration of 50 nM/mL suspended in water were added to Hela cells (5000 cells/mL on a 15 mm round cover slip in a cell culture plate) for cultivation over 24 hours. QDs were delivered to cells by endocytosis. Cover slips were then removed and transferred (cell side facing down) to a glass microscope slide mounted with Mowiol and sealed with clear nail polish. Raw images were collected with a 100 $\times$ , NA 1.49 oil objective. A 488 nm laser at 10 % of its 50 mW full power was selected as the excitation laser. Considering the

previous measurement on QDs blinking period distribution and exposure time impact on fluorescence intensity, we set the exposure time at 0.2 seconds/frame. CCD gain and EM gain were set as 15 and 300. Figure 3.21 and 3.22 presents the fluorescence images of 2000 frames of QDs labelled Hela Cells. It took less than 7 minutes to collect these 2000 frames.

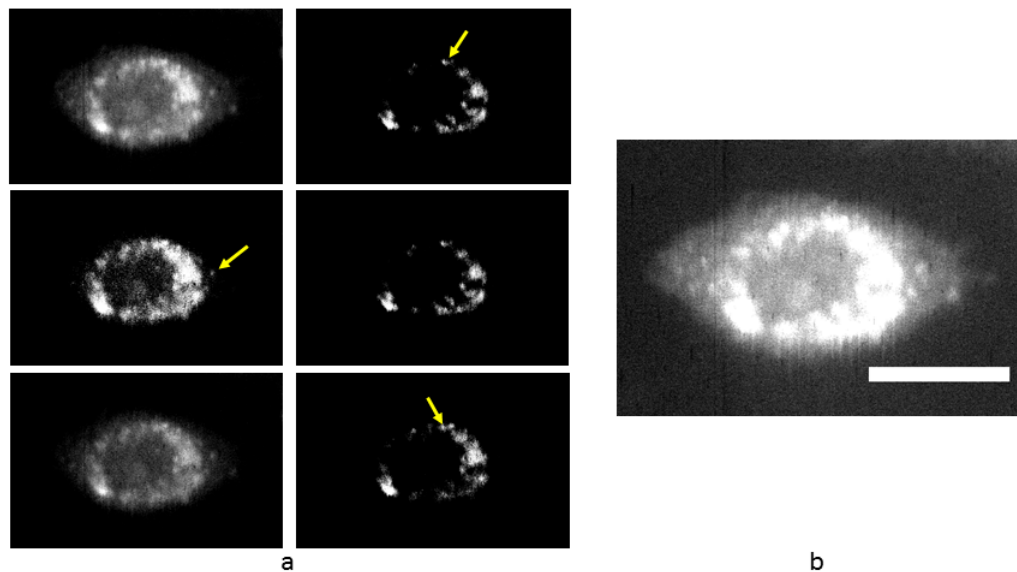


**Figure 3.21:** Fluorescence images of Ge QDs in Hela cells, imaged on the spinning disk confocal microscopy. **(a)** 6 selected frames. **(b)** Sum image of 2000 image frames. Scale bar, 10  $\mu\text{m}$ .

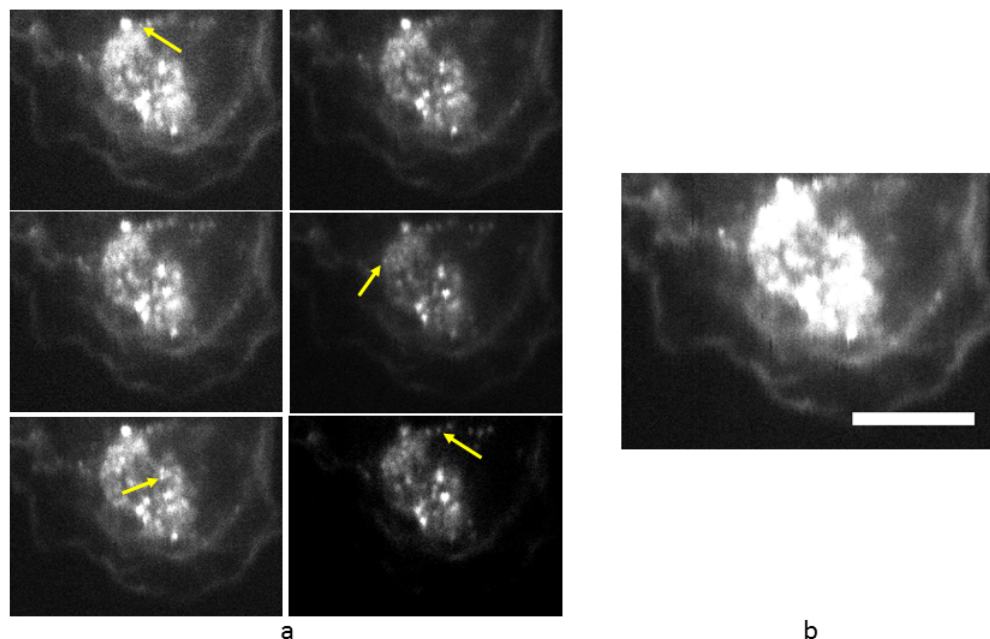


**Figure 3.22:** Fluorescence images of CdSe QDs in HeLa cells, imaged on the spinning disk confocal microscopy. **(a)** 6 selected frames. **(b)** Sum image of 2000 image frames. Scale bar, 10  $\mu\text{m}$ .

It is shown in Figure 3.21 and 3.22 that single molecule imaging has been achieved (see the yellow arrow indicated points presented in certain frames). However, large block of QDs are seen all frames. This could have been resulted from the exposure time being too long (200 ms exposure time is longer than blinking events of 50 ms) and too dense labelling. Even though this was not further studied and corrected in our proof-of-principle demonstration, the labelling efficiency issue will be a key point to deal with in the applications to solve real biological problems. The imaging speed can be compared with that of standard STORM/PALM methods where a similar size of data would require 8 minutes or longer [67]. Furthermore, one should keep in mind the capability of the SDSI method for Z-stacking, potentially leading to 3D images. Besides, Ge QDs offer good photo-stability for continuous stochastic imaging.

The aim of the stochastic imaging is to sequentially image sparse subsets of blinking QDs distributed over thousands of frames, and populate a high-density map



of QDs position. The raw image dataset requires single molecule statistical analysis localisation and reconstruction algorithms to distinguish and precisely localise individual QDs, and reconstruct a super-resolution image. This will be demonstrated in the next subsection.

### **3.2.5 Super-resolution reconstruction**

The fundamental principle of the stochastic reconstruction is to identify individual molecules and estimate their positions accurately. Several key steps are required to obtain a super-resolution image: (i) to identify individual molecules or separate single molecule signals from stochastically obtained overlapping signals; (ii) to localise single molecules with a sub-pixel refinement; (iii) to render the localisations to construct a high-resolution map of the molecule densities. To date, analysis algorithms for single molecule localisation (steps (i) and (ii)) have been divided into several categories which differ by specific mathematical procedures of localisation and reconstruction. Here, several commonly used algorithms have been used to understand their applicability to the case of blinking Ge QDs. These algorithms have been compared through analysis of the previous research, as well as dataset tests. As a result, a specific Matlab algorithm - the blinking analysis super-resolution algorithm (BSA) has been developed to analyse our spinning disk based blinking QDs data.

#### **3.2.5.1 Existing stochastic reconstruction algorithms and comparison**

Localisation algorithms vary from different image acquisition methods, probes, labelling densities and microscopes. Table 3.5 gives the descriptions of some of these algorithms, which have software or codes available for use, as well as their advantages and limitations. They are mainly divided into three groups according to the way in which they deal with diffraction spots: (i) using spatial information to localise molecules (see the methods in Table 3.5) by searching the centroid of peak

regions (QuickPALM [182]), laterally fitting the individual Gaussian-like PSF [207], or estimating the densities of overlapping PSFs such as DeconSTORM [185], DirectSTORM [184], CSSTORM [186, 208]; (ii) using temporal fluctuation information (see the methods in Table 3.5) to localise molecules with specific stochastic models, or using fluctuation analysis to shrink the possible position area of molecules beyond diffraction limit such as 3B [187] and SOFI [183, 209, 210]; (iii) using both spatial information and temporal fluctuation to localise molecules, in which temporal fluctuations are usually used to determine the number of independent molecule signals and to isolate each signal, after which spatial information is used to localise molecules such as QDB3 [200] and BaLM [211], [212]. However, these comparisons are based on each of the algorithms being applied to the corresponding very specific datasets. Therefore, we carried out a series of experiments using simulated data [61] and Ge QDs (using SDSI method, Table 3.6) to obtain a meaningful experimental assessment of these algorithms for our purpose. The experimental dataset was collected using a HeLa cell sample non-specifically labelled by Ge QDs (50 nM/mL), on spinning disk confocal microscopy with a 100 $\times$ , 1.49 NA objective. Imaging settings: excitation laser wavelength 488 nm; exposure time 200 ms/frame; EM Gain 300. Demonstrated algorithms were optimised on processing parameters to match our data (see the notes below Table 3.6).

One can see that the QuickPALM gives clear single molecule localisation output with a fast processing speed (3 minutes for 10000 frames) (Table 3.6); however, the reconstructed image seem to have lost much information about the sample. SOFI seem to have gained slight improvements in the image contrast, instead of obvious resolution improvements. Due to lengthy durations of the process, a small dataset (yellow square in the raw image in Table 3.6) was cropped for the tests using DirectSTORM, DeconSTORM and CSSTORM. These three algorithms are either not able to reconstruct significant images at all, or take too long to process even a small dataset (more than 2.5 hours for a 64 $\times$ 64 $\times$ 100 pixels dataset for CSSTORM, Table 3.6). Therefore, the last three software were not further used to process our SDSI

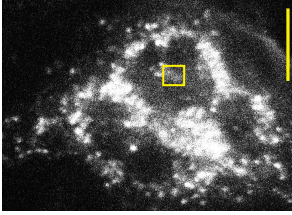
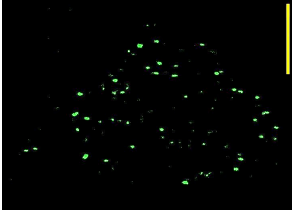
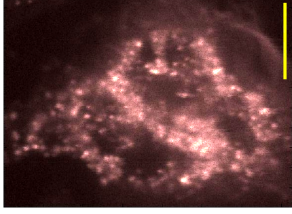
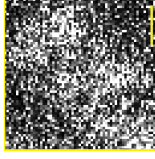
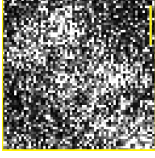
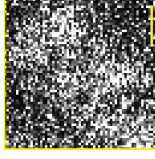
data.

It has been reported in a series of papers ([58, 182, 213]) that these algorithms can achieve remarkable super-resolution (as good as several nm [214]). This may be because they are only suitable for very specific datasets [215]. For example, the strategies in group (i) are able to achieve a high localisation precision with a well-characterised system (PSF size and distortion, camera counts and noise) and sparse signals. However, this could become less reliable when the information of the microscopy system is partly missing or the images contain fluorescence signals that are too dense (see QuickPALM result in Table 3.6). Moreover, they lack statistical single molecule detection analysis. Strategies used in group (ii) are fast in processing (seconds in SOFI), but with a limited resolution ( $\sim 60$  nm) or even no obvious resolution improvement (see SOFI result in Table 3.6). More importantly, they usually suffer from the molecule bleaching/blinking and mislocalisation problems [216], due to the loss of fluorescence intensity over time and the blinking phenomenon of the probes. Strategies in group (iii) are efficient in utilising information and could be relatively fast in processing (minutes) and able to achieve high resolution (less than 10 nm [200]), but there is no such software available for direct use. Even though some algorithms may be applied to a statistical analysis of blinking QDs, currently existing algorithms such as BaLM are only suitable for analysing dye or protein dataset from STORM/PALM type microscopies, as it also relies on the bleaching events which are not obviously seen in QDs data. Moreover, BaLM provides reasonable analysis on sparsely distributed molecule datasets, it may be unable to identify single molecules from a group of overlapping signals. Therefore, existing algorithms with software and codes that are available for use are not optimised for QDs blinking super-resolution reconstruction, as has been also pointed out by others [198, 213].

**Table 3.5:** Description of several existing stochastic super-resolution reconstruction algorithms

Algorithms	Methods	Advantages and limitations
QuickPALM [182]	<ol style="list-style-type: none"> <li>1. Threshold to assign nonoverlapping ROI</li> <li>2. Centroid analysis on ROIs</li> <li>3. Gausssian least-squares fit using the centroid coordinates as initial guess</li> <li>4. For 3D QPALM, define spot shape along the horizontal axes</li> </ol>	<p>Resolution: 40 nm</p> <p>Quick reconstruction and free software</p> <p>Limit: Discard overlapping molecules</p>
DeconSTORM [185]	<ol style="list-style-type: none"> <li>1. Initialize estimate by using statistic model (reduce noise)</li> <li>2. Calculate the correlations of the same pixels in different frames</li> <li>3. Iterative image nonlinear deconvolution directly for all frames</li> </ol>	<ol style="list-style-type: none"> <li>1. Localisation free (estimate a SR image without localizing emitters)</li> <li>2. Allow high densities of activated fluorophores</li> </ol>
DirectSTORM [184]	<ol style="list-style-type: none"> <li>1. 2D Gaussian fitting for single molecule localisation</li> <li>2. Reconstruction after thousands of localisation</li> </ol>	<p>20 nm resolution</p> <p>Limit: Single molecule fitting</p>
CSSTORM [186]	<ol style="list-style-type: none"> <li>1. Divide the image into a set of small images patches</li> <li>2. Create an oversample grid for each small patch</li> <li>3. L1-norm minimization by compressed sensing obtaining the optimisation molecule distribution X for each small patch</li> <li>4. Add all the X together to form the result of the full image</li> </ol>	<p>High molecule density</p> <p>Limit: Restricted isometry principle(RIP) in compressed sensing requires a complete RIP analysis</p>
3B [187]	<ol style="list-style-type: none"> <li>1. Select initial spot position for a model</li> <li>2. Optimise model using hybrid MCMC</li> <li>3. Compute free energy, add a new fluorophore randomly and re-compute free energy</li> <li>4. Repeat 2-3 steps</li> </ol>	<p>Resolution: 50 nm on 4-s timescale</p> <p>Allow many overlapping fluorophores</p> <p>Limit: software applicability</p>
SOFI [183]	<ol style="list-style-type: none"> <li>1. Obtain a frames series</li> <li>2. Calculate the n-order cumulant of each original pixel</li> <li>3. Plot the value of n-order cumulant for any given set of time lags</li> </ol>	<p>Achieve background-free, contrast-enhanced super-resolution images</p> <p>Limit: brightness scaling, max resolution: pixel size.</p>
QDB3 [200]	<ol style="list-style-type: none"> <li>1. Identify blinking QDs by subtracting adjacent images frames in both backward and forward direction</li> <li>2. 2D Gaussian fitting to localise identified QDs</li> <li>3D recovery of all localisations</li> </ol>	<ol style="list-style-type: none"> <li>1. Make use of blinking information</li> <li>2. Useful for big area data</li> </ol> <p>Limits: Not reliable with high density QDs data</p> <p>Require no sample drifting</p>

**Table 3.6:** Performance of several available public algorithms testing on our spinning disk microscopy based blinking QDs in HeLa cells dataset

Algorithms	Original Data	QuickPALM	SOFI	DirectSTORM	DeconSTORM	CSSTORM	3B
Software codes		ImageJ Plugin	Matlab	C	Matlab	Matlab	C++/ Python/ ImagingJ plugin
Size (pixel)	529×727	529×727	529×727	64×64	64×64	64×64	No assessment available
Processed frames number		10000	5000	100	100	100	
Processing time		4 mins	7 mins	3 mins	10 mins	2.5 hours	
							
Scale bars		10 $\mu$ m				1 $\mu$ m	

QuickPALM settings, Maximum FWHM 6 pixels, image pixel size 70 nm, minimum symmetry 0, minimum SNR 0.1, render pixel size 30 nm. SOFI settings, 2nd order cumulant. DirectSTORM settings, ROI 6 pixels, confidence 95 %, render pixel size 30 nm. CSSTORM setting, dividing 4 times, optimisation chi square value 1.5, baseline offset 100. DeconSTORM settings, noise model Gaussian, iterations 1000.

Recently, a few algorithms specifically dealing with blinking QDs data have been proposed; for example, combined Independent Component Analysis (ICA) and Maximum Likelihood Estimation algorithm for statistic blinking QDs data [198], and QDB3 3D super-resolution algorithm [200]. These algorithms have claimed to use stochastic blinking events to identify single QDs within a diffraction limited region. 8 - 17 nm resolution in  $x - y$  plane as well as 58 nm resolution in  $z$  plane have been realised using QDB3, as stated in [200]. These QDs blinking specified algorithms are not publicly available, but they are still apt for guiding further algorithm development. Therefore, we developed a code, named blinking analysis super-resolution algorithm (BSA), using the mathematical models that have been proposed and tested in [198] and [200]. The models are the Independent Component Analysis model proposed by Keith A. Lidke [198] and the Gaussian fitting model for each QDs that has been widely tested and used in other existing algorithms [198, 213, 217]. A full description of how BSA has been built is given in the next subsection and the relevant MATLAB codes is found in Appendix F.

### 3.2.5.2 BSA description

BSA was developed in MATLAB2014 and was designed to be easily adjusted to incorporate extra functionality through porting of additional image processing modules available in Matlab (or supplied by a user). In this algorithm, blinking QDs time series image data were utilised. Independent component analysis (ICA) was initially performed to identify the number of QDs in the segmented regions of interest(ROI), then Gaussian fitting was applied on each QD component in which the centre of the fitted Gaussian was registered as a localisation. Reconstruction was finally realised by redrawing all localisations in a new image.

Modelling of BSA was firstly constructed on the ICA analysis. ICA is a computational method for separating a multivariate signal into additive components. The basic assumption behind this model is that the components are non-Gaussian signals.

This is true for QDs because blinking events have been shown following an inverse power law (Figure 3.19), instead of Gaussian distribution. Hence, the ICA model based algorithm can be applied to decompose the images into a set of non-Gaussian probability distribution components with spatial information.

Considering the general mathematical framework of ICA, our work can be formulated as follows. An image stack is represented by the matrix  $I$  of size  $m \times n \times j$ , with  $m$  rows,  $n$  columns and  $j$  frames. The raw images can be represented by a vector:

$$I = [I_1, I_2, \dots, I_j] \quad (3.2)$$

The components of the super-resolution image can be written as a random vector:

$$S = [S_1, S_2, \dots, S_j] \quad (3.3)$$

In an ICA model, it is assumed that each mixture  $I_j$ , as well as each independent component  $S_j$  is a random variable, thus a vector-matrix  $A$  can be generated that satisfies:

$$I_j = A \times S_j \quad (3.4)$$

The statistic model in Equation 3.4 is called the ICA model. It describes how the raw image data is constructed by a process of mixing the components  $S_j$ . ICA is able to discover a suitable matrix  $A$  based on the assumption of the independence of all components in  $S$ . After estimating the matrix  $A$ , we can calculate its inverse  $W = A^{-1}$  and obtain the independent components simply by:

$$S = W \times I \quad (3.5)$$

The ICA requires the number of the component to be given in advance. However, the real number of components (QDs) is unknown before processing. Thus, we estimate the maximum possible number of components on the image (for example,

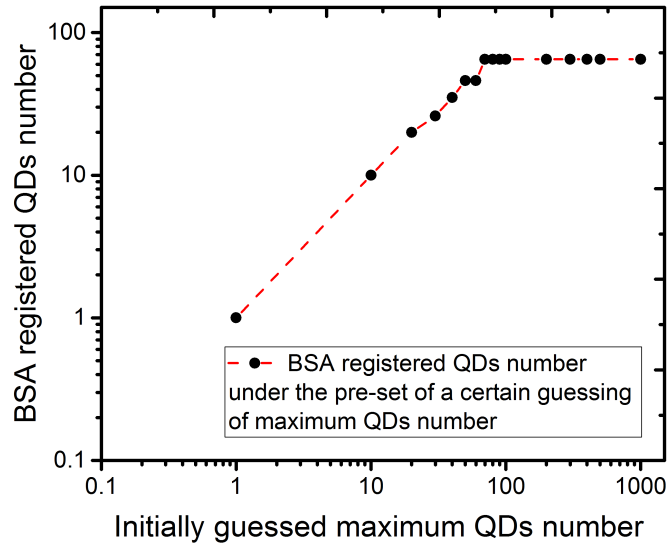


**Figure 3.23:** Plot of BSA localised QDs number changes along with the initial guess for maximum number of QDs. Test was performed on a 2000 frames of  $18 \times 18$  pixels image stack of Ge QDs labelled Hela cell sample. The guess of maximum QDs number was set as 1, 10, 20, 30, 40, 50, 60, 70, 80, 90, 100, 200, 300, 400, 500, 1000.

using the image area divided by a single QD area). The algorithm then performs ICA to each condition of the component from 0 to the maximum number. The condition in which the objective component's frequency distribution is closest to the standard power-law distribution (with index of -1.6 for our Ge QDs data) is regarded to have revealed the right number of components in  $S$ . Mathematically, Kullback–Leibler divergence [218] has been used to calculate the difference between the components' (QDs) frequency distribution and the power-law distribution. Finally, the components  $S$  are then further fitted by a 2-D Gaussian function (refer to equation 2.1). Central points of the fitted Gaussian functions are regarded as the localisations of QDs. In order to better understand how sensitivity the BSA analysis to the guess of maximum QDs number and optimise the initial guessing, we conducted a series of BSA analysis on one data set but different initial guess of the maximum number. The tested data set was a 2000 frames of  $18 \times 18$  pixels image stack of Ge QDs labelled Hela cell sample (will be further demonstrated in the Figure 3.24b<sub>1</sub>). Figure 3.23 plots out the output of BSA localised QDs number and the guess for the maximum number.



It is clear that the BSA localised QDs number increases linearly with the increasing of initial guess number from 1 to 70, but the BSA consistently localises 65 QDs after the guess number becoming larger than 70 to even 1000. This is reasonable because when the guess number is too small, the BSA localisation is limited by this hard constraint. When the guess number is large enough (70 in the case of the example), the BSA will find out the most reasonable QDs number, in spite of the increase of guess number. This is also expected for any reliable algorithm to return the localisations depending on the data, instead of the guess number.

The realisations of the BSA processes are described in flow chart [3.7](#). Full codes can be found in Appendix [F](#).

**Table 3.7:** Flow chart of ICA based BSA algorithm

---

**Algorithm**  $ICA(I)$

---

**Input:**

$I$ : Input image (.tif format)

**Output:** Localisations  $L_i$ ; Number of components  $C$ .

**Main:**

**Initiate** dataset  $XTIF = M \times N \times J$ .

Evaluate noise level, set up the threshold.

Initiate maximum ROIs (segmentation) number ' $maxPeaks$ '.

**For** each number  $t = 1$  to  $maxPeaks$

**While** segmentations  $< t$

Initial pixels:  $iXgmm = ones(M, N)$ .

Do threshold, update  $iXgmm$ .

Crop the segmented ROIs:  $sData = Xaverage \times (ones(M, N) - iFgmm)$ .

Calculate QDs brightness:  $totalQDbrightness = sum(sum(sData))$ .

**End while**

Set up ICA parameters: components  $i$ , search region ( $low$  to  $high$ ).

**For**  $i = low$  to  $high$

Perform ICA.

Compare resulted ICAs frequency distribution to standard inverse power law:

$[value, sICs] = min(dhigh)$ .

**End for**

Select the ICA distribution result (with components number  $C$ ) with the smallest 'value' to standard inverse power law

**Foreach** component  $i = 1$  to  $C$

Fit Gaussian distribution  $gData$  to  $sData$

Return localisations  $L_i$

**End for**

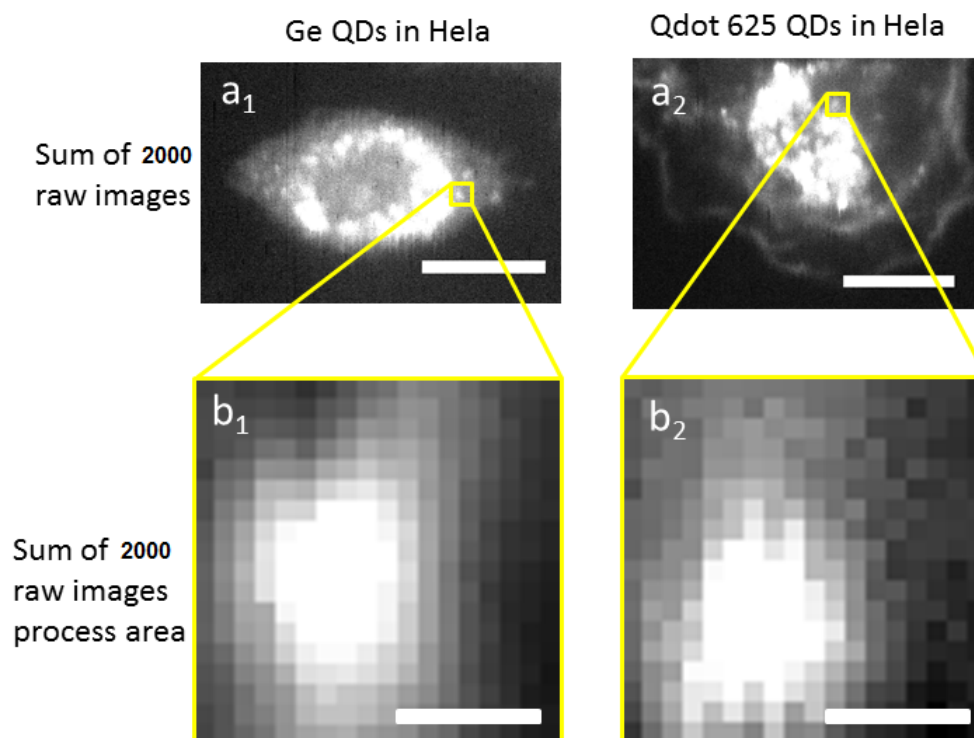
**Return**  $L_i, C$ . **Plot**  $L_i$

---

In the following subsection, the single molecule localisation and super-resolution reconstruction of our experimental data using BSA will be shown. For comparison, the same data processed by BSA have also been processed by QuickPALM and SOFI as a reference.

### 3.2.5.3 BSA reconstruction

BSA combines well-documented and well-tested mathematical models to generate an easier way of using MATLAB software to process blinking QDs super-resolution imaging data. The localisation process has been applied to the data shown in Figure 3.21 and 3.22. For demonstration, a small area (the yellow square in Figure 3.24<sub>a<sub>1</sub></sub>, <sub>a<sub>2</sub></sub>, <sub>b<sub>1</sub></sub>, <sub>b<sub>2</sub></sub>) was selected to perform localisation algorithms.



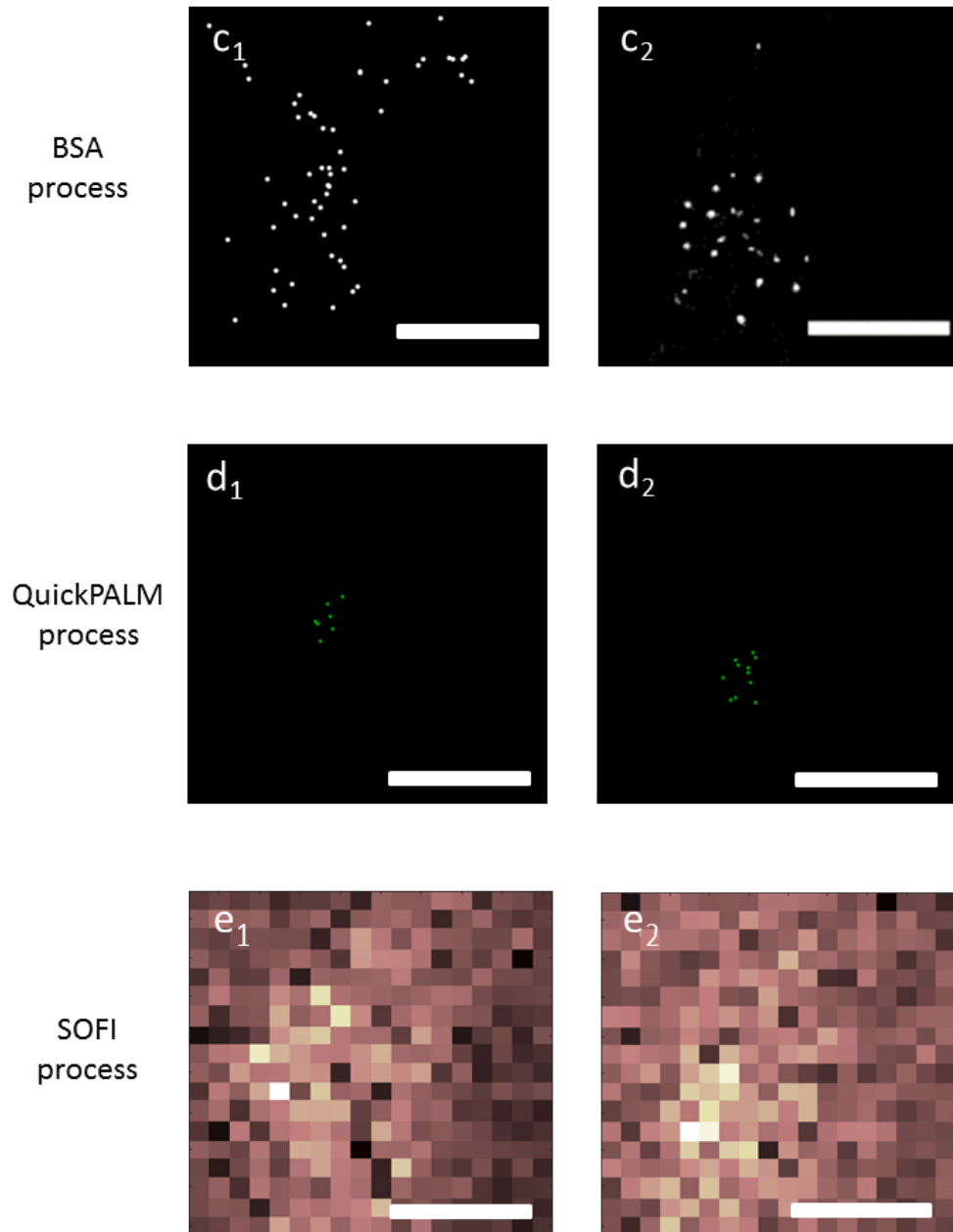


**Figure 3.24:** Super-resolution reconstruction using BSA ( $c_1$ ,  $c_2$ ), QuickPALM ( $d_1$ ,  $d_2$ ) and SOFI ( $e_1$ ,  $e_2$ ). Yellow arrows point out the nearest two localised QDs. Scale bars,  $a_1$  and  $a_2$   $10\ \mu\text{m}$ ;  $b_1$  to  $e_2$   $500\ \text{nm}$ .

The data was firstly processed by BSA (Figure 3.24 $c_1$ ,  $c_2$ ). During BSA processing, localised (reconstruction) image pixel size was set as 5 nm for Ge QDs data, and 15 nm for Qdot 625 data, in accordance with their physical sizes (3.8 nm and 14 nm respectively). Gaussian fitting confidence was set as 90 % to determine the

localisation point sizes. The fitting confidence represents how well the fitted Gaussian function matches the raw image. Obviously, this also determines the localisation error. For example, a localisation with fitting confidence of 90 % means the algorithm is 90 % sure that the real QDs is located within the given point area. In this way, 65 Ge QDs and 28 CdSe QDs (white dots in Figure 3.24  $\mathbf{c}_1, \mathbf{c}_2$ ) have been recognised within this  $1.44 \mu\text{m}^2$  area. By comparing the raw images ( $\mathbf{b}_1, \mathbf{b}_2$ ) to the BSA processed images ( $\mathbf{c}_1, \mathbf{c}_2$ ), one can see that the BSA localisations match the brightest region of the raw image. In other words, the profile of the localisation distribution ( $\mathbf{c}_1, \mathbf{c}_2$ ) seems similar to the geometric profile of the sample in the raw image ( $\mathbf{b}_1, \mathbf{b}_2$ ).

Additionally, as QuickPALM and SOFI have shown (Table 3.6) to be able to process a large stochastic imaging dataset with a relatively fast speed (within a few minutes for thousands of image frames), they were used here as a reference. Even though they are not specifically designed for blinking analysis, we still used them for the sake of qualitative comparison. QuickPALM registers localisations by simply finding the centroid of each ROI; thus, only QDs at the brightest region will be more likely to be registered. We found that less than 15 QDs were registered in both cases (green dots in Figure 3.24  $\mathbf{d}_1, \mathbf{d}_2$ ). Moreover, the localisations are not seemed to match the geometric profile of the raw image very well, because all the registered QDs are located in the central area of the brightest pixels. In this sense, BSA has interpreted more useful information (more QDs) than QuickPALM. SOFI analysis was based on a cumulant calculation for pixels, instead of single molecule localisation, consequently returning a super-resolved image (Figure 3.24  $\mathbf{e}_1, \mathbf{e}_2$ ) instead of localisations. It is hard to define the resolution and number of QDs in SOFI results, because the processing does not seem to have resulted in super-resolution images (Figure 3.24  $\mathbf{e}_1, \mathbf{e}_2$ ).

In order to assess the true resolution of our approach we attempted to conduct correlative light and electron microscopy (CLEM) imaging using confocal microscopy and TEM and SEM (Appendix E). However these were not successful. CLEM is not technically easy and there were outstanding difficulties with sample preparation and avoiding sample damage problems (see Appendix E). Other methods can also

be used to assess the resolution. For example, priori cellular structures information, such as proteins, microtubules and DNA rulers [66, 184] are very helpful for testing super-resolution methods. In the case that such priori structure information are not available, the simulation methods such as Fourier Ring Correlations (FRC) [219] can be carried out. FRC determines the resolution threshold by evaluating the similarity of two independent reconstructions of the same dataset when both reconstructions are consistent. It is a fast computational method and does not require calibration standard or priori structure information about the sample, thus are said to be widely applicable to any single molecule localisation super-resolution microscopy.

### 3.2.6 Conclusion

Here, the blinking phenomenon of Ge QDs has been studied and utilised in stochastic super-resolution imaging. This study introduced a new type of QDs probe (Ge QDs) and combined a fast surface scanning confocal microscopy (instead of point scanning).

Colloidal fluorescent Ge QDs were found out to be suitable for stochastic super-resolution imaging. They presented a stochastic fluorescence blinking phenomenon in which the durations of blinking off events have been found following an inverse power law with the exponent of -1.6, which is similar to those commonly found in widely used CdSe/ZNS Qdots. Our Ge QDs were observed to have statistic blinking off durations from 0.1 s to  $\sim 1.5$  s.

Ge QDs were further tested in stochastic reconstruction super-resolution microscopy. Exposure times of 0.2 seconds/frame was found to be suitable for such imaging. This is a promising outcome and is due to the fact that the repetitive imaging required for this method relies on natural blinking of QDs (on millisecond timescale see Figure 3.18). In turn, the medium timescale repetitive imaging is possible due to strong photo-stability of Ge QDs (see Figure 3.20). Thus, stochastic super-resolution imaging can potentially be further pushed to a higher speed (milliseconds per frame).

Coupled with the small particle size ( $\sim 4$  nm, Figure 3.3) this should also provide further improvement in spatial resolution.

The blinking super-resolution algorithm has been developed for our super-resolution strategy. BSA takes into consideration Ge QDs blinking exponent in a cellular environment, and microscope PSF shape, to determine the number of QDs and achieve accurate localisations. This will greatly rely on the blinking characterisation of used QDs and the PSF characterisation of the microscopy system. This algorithm has shown the ability of identifying more QDs and revealing more accurate information of the raw image than QuickPALM and SOFI. This proof-of-concept experiments indicate that our approach can thus be used in super-resolution imaging.

This super-resolution imaging strategy is indeed elegant on principle. However, the stochastic imaging procedures greatly rely on the imaging of only one statistically blinking ‘on’ QDs, which is separated only if surrounding QDs within the diffraction limited region are just luckily blinking ‘off’. This is somewhat time-consuming. Moreover, it is impossible to acquire all blinks. Some QDs may blink more than once while some may never blink. This could become problematic in biological applications; for example, a single QDs may appear as a cluster of localisations due to variable intervals of blinking [57]. One previous solution to this problem was proposed based on improving the algorithm calculations, so as to identify different QDs by analysing the discrete on-off blinking events, rather than only QDs intensity fluctuations [220]. In our method, this problem has been reduced by accurately determining the number of QDs before performing the localisation process.

In the next section, a new super-resolution imaging strategy based on spectroscopic separation (instead of stochastic imaging), which utilises the size-dependent emission of QDs to separate overlapping fluorescence signals by spectra, has been proposed.

### **3.3 Spectroscopic super-resolution fluorescence cell imaging using Ge quantum dots**

In this section, the super-resolution imaging approach based on spectroscopic (rather than temporal) separation microscopy using Ge QDs will be described and demonstrated. In this strategy, we take advantage of QDs size dependent emission spectra (as described in sections 1.6.3 and 3.1.1.1) to address the time constraints in temporal separation and physical size limit, and this is particularly suited for live cell imaging. This approach was initially tested using off-the-shelf CdSe/ZnS Qdots and then using Ge QDs. This super-resolution microscopy approach is further complemented by a specially developed reconstruction algorithm.

#### **3.3.1 Spectroscopic super-resolution imaging strategy using quantum dots**

As has been illustrated in Figure 1.15 in chapter 1, in single molecule localisation super-resolution imaging strategies, the central point of achieving super-resolution relies on the separation of two overlapping fluorescent probes into individual images. In STORM/PALM methods, this is achieved by temporal separation, which images only one probe within a diffract region at any instant. However, if the fluorescent probes have different emission wavelengths, they can be spectrally separated. The concept of achieving super-resolution by spectroscopic separation was first demonstrated by C. Cremer in 2008 using fluorescent proteins [60]. Experimental realisation was never easy, until the use of quantum dots in super-resolution applications, because mixing too many classical dyes or fluorescent proteins will introduce other problems such as the need for too many excitation light sources and spectra bleed-through, as well as photo-bleaching problems to the dyes and proteins (see Figure 3.20). Since excitation



spectra of QDs are broad and the emission depends on particle size, we can use one laser source for excitation and identify individual QDs by emission spectra.

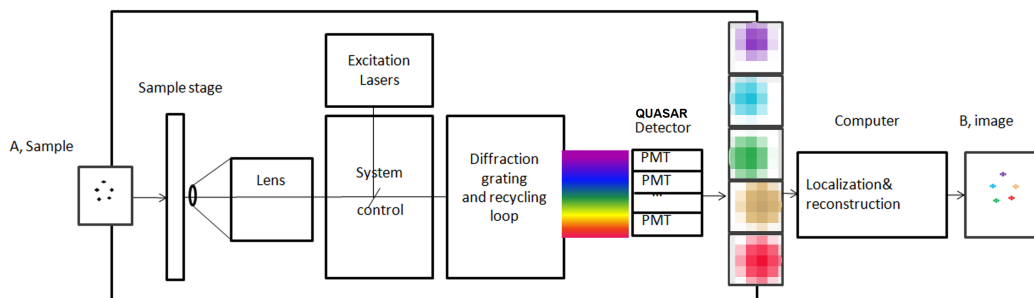


**Figure 3.25:** Schematic sketch of spectroscopic imaging and the super-resolution strategy.

The spectroscopic imaging method we implemented is schematically shown in Figure 3.25. A cell sample (‘A’) which is labelled with different sizes of QDs is imaged by the microscope. The sample is point-by-point scanned (with the timescale of a few hundreds of milliseconds per image) and imaged using a high numerical aperture (NA) lens, while being excited by a laser source. Fluorescence signals are transferred to the microscope. Light is harvested and spectrally separated using a spectral detector (in our case, a diffraction grating). This separates the fluorescence signals into different spatial positions by wavelength. A PMT array detector is pre-set to collect these separated fluorescence signals with 10 nm spectra resolution (see Materials and Methods section 2.4.3).

Spectroscopic super-resolution can be further achieved by localising fluorescent probes below the Abbe diffraction limit in the spectrally separated channels (Figure 3.26), instead of temporally (as done in STORM/PALM). Spectroscopic super-resolution microscopy (SSRM) is essentially a ‘spectrally assigned localisation’ microscopy [60] that spectrally isolate individual QDs in a diffraction region (Figure 3.26). Using this methodology, any conventional single point laser scanning confocal microscope equipped with a spectral detector could be used.

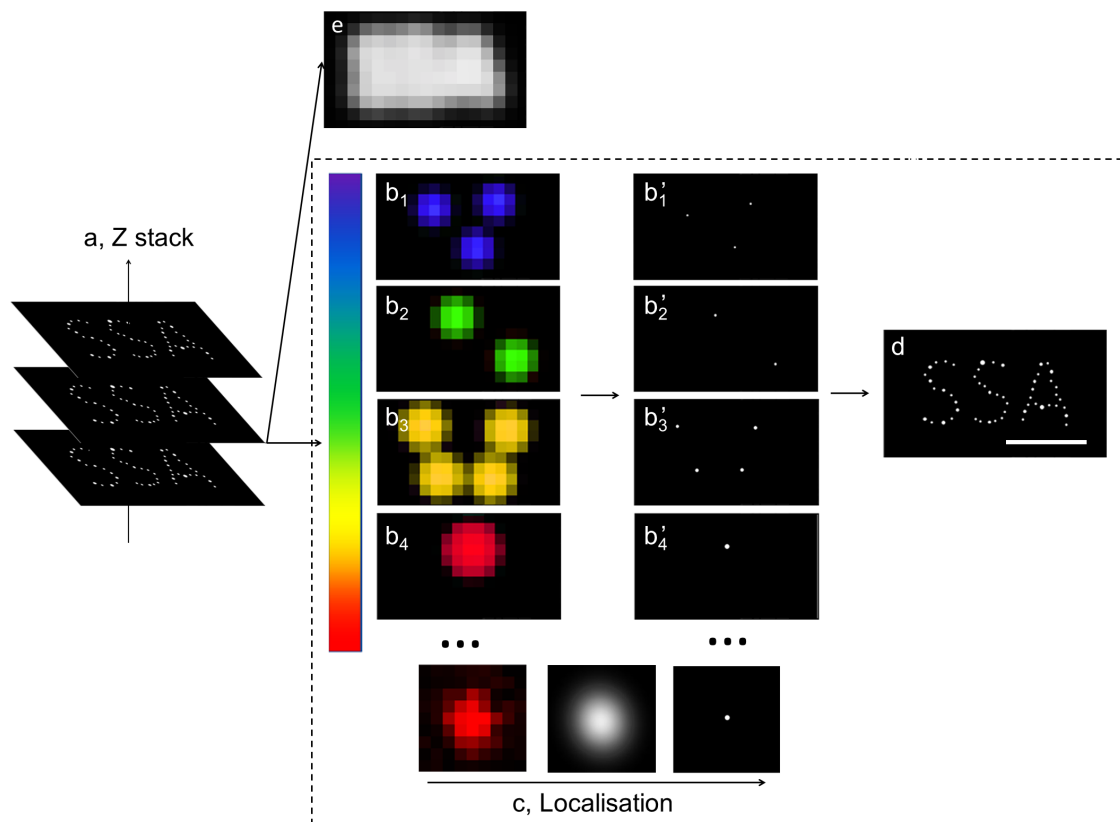


**Figure 3.26:** Principle of spectroscopic super-resolution reconstruction. (a) 2D sections of a 3D QDs labelled biosample, also known as Z stack during microscopy imaging. Each of the 2D sections was spectroscopically separated imaged ( $b_1 - b_4$ ) at the same time, then localised with a high resolution ( $b'_1 - b'_4$ ) using localisation algorithms (c). (d) Super-resolution image is obtained and then 3D structure is able to be created from the Z stacks. However, fluorescence image without spectroscopic separation is shown as optical diffraction blurry (e). Scale bar, 400 nm.

In the present research, ZEISS LSM 710 microscopy system was used in spectral imaging mode (in this mode, the 34 channel spectra detector - QUASAR detector was selected to record images). Images were taken using alpha Plan-Fluar 100 $\times$ , NA 1.45 oil objective. A 488 nm Argon laser was utilised for imaging and was used at 5 - 30 % of the 50 mW full power. QUASAR detector master gain and digital gain were set as 600 and 2 respectively. Exposure time was set as 'Auto', which means that the imaging software Zen automatically determines the appropriate exposure time for generating a good contrast image. Following this, the system characterisation of point spread

function (PSF) for different spectra channels of LSM 710 will be demonstrated. Then, the size-dependent fluorescence emission of both commercial QDs (Invitrogen CdSe QDs) and Ge QDs will be described. Furthermore, the spectroscopic cell imaging using QDs as fluorescent probes will be described. Finally, super-resolution reconstruction using an in-house developed algorithm - SSA will be demonstrated.

### 3.3.2 Microscope PSF characterisation

The LSM710 microscope system is capable of collecting fluorescence images by wavelengths, via spectroscopic separation. The PMTs array in the QUASAR detector introduces the concept of ‘channels’. Each channel corresponds to a PMT detector, and records fluorescence signals of a specific wavelength range of 10 nm width. PSF is determined by the light wavelength, therefore the channels’ effect on PSF size should be taken into consideration. Here, in order to collect the PSFs, a standard 100 nm TetraSpeck fluorescence beads sample (T7284, Invitrogen Life Technology) was tested and excited by a 488 nm laser using at 10% of the 50 mW full power. PSFs images were collected and fitted by 2D Gaussian function (see Materials and Methods section 2.5.3). Figure 3.27 shows the procedure of fitting a PSF image by Gaussian function performed on Matlab2014.

Similar to the example of 585 nm channel PSF, PSFs of several other wavelength channels were collected and fitted by Gaussian in the same way. The FWHM of the fitted Gaussian function has been taken as the size of PSF. A summary of all channels’ PSF sizes in  $x - y$  direction are given in Figure 3.28. The variation of PSF sizes is between  $\sim 180$  nm and 340 nm, and short wavelengths correspond to small PSF sizes, which is consistent with what the resolution limit equation 1.7 indicates. It can be seen (Figure 3.28) that the microscope PSFs are not perfectly symmetrical on the  $x - y$  plane, particularly at the wavelength range between 500 and 650 nm in which sizes of PSF on  $x$  direction are larger than that on  $y$  direction.

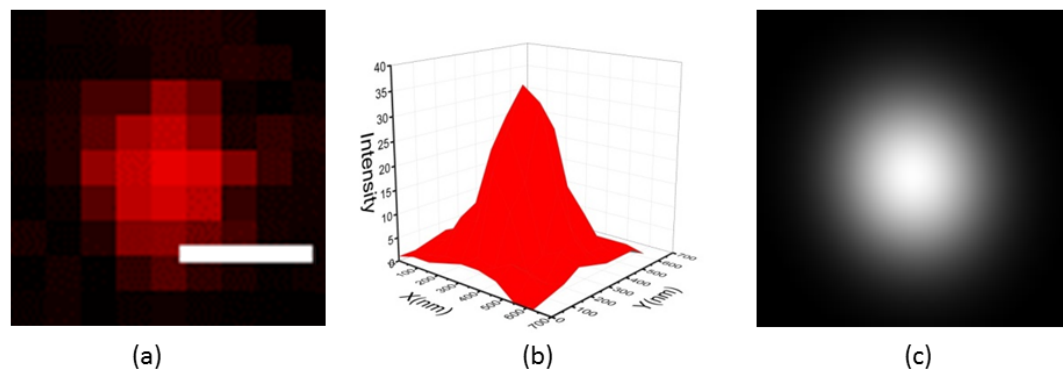


**Figure 3.27:** Point spread function (PSF) characterisation on Zeiss LSM 710. (a) 585 nm channel image of 100 nm TetraSpeck™ beads being excited by a 488 nm laser on LSM 710 confocal microscopy in spectral mode. (b) Surface plot of Tetraspedk bead (at 585 nm channel). (c) 2D Gaussian fitting pattern of images a and b. Sale bar, 300 nm.

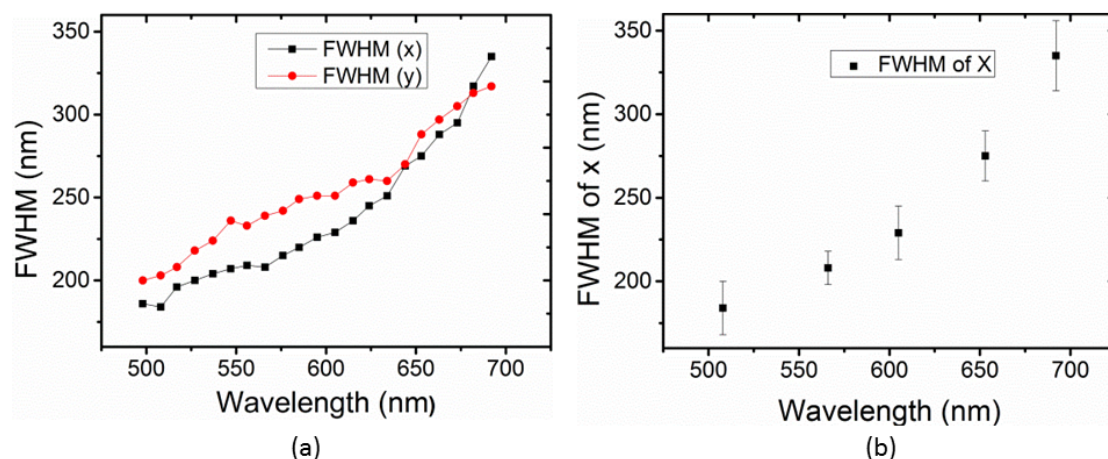


**Figure 3.28:** Gaussian fitted PSF sizes variation with wavelength. (a) FWHM of x,y variation along with wavelength. In each channel, 10 beads were analysed and averaged as the representation of PSF to this channel. In the short wavelength range ( $<650$  nm), PSF in x direction shows a slightly larger spread than that in the y direction. In the longer wavelength range, they tend to be similar. (b) An error bar included FWHM variation in x direction. These results were used during the localisation analysis.

The significance of knowing the lateral PSF sizes emerges at the localisation for single QDs where the individual PSFs of QDs are to be identified. Although it is true that real objects are three dimensional and the microscopes have considerably more aberration axially than laterally, as discussed in the introductory section 1.4, the axial

correction for our QUASAR detector was not carried out as we didn't perform 3D imaging.

In the next section, the size-dependent fluorescence emission of quantum dots will be demonstrated.

### 3.3.3 QDs size dependent emission spectra

Three types of Invitrogen QDs (Qdot525, Qdot605, Qdot705) were analysed to visually confirm the size-dependence of the emission spectra. In order to measure the QDs' size using TEM, one drop ( $< 10 \mu\text{L}$ ) of each type of Invitrogen QDs diluted in water (50 nM/mL) was prepared onto a Au TEM grid. It was then allowed to dry in a hood at room temperature for 24 hours. Next, the sample was transferred to the TEM. Magnification was set to  $50000\times$  and the maximum possible resolution was  $1.5 \text{ \AA}$ . Average size calculations of QDs were carried out using TEM images (Figure 3.29). Figure 3.30 illustrates how this was carried out, step by step.

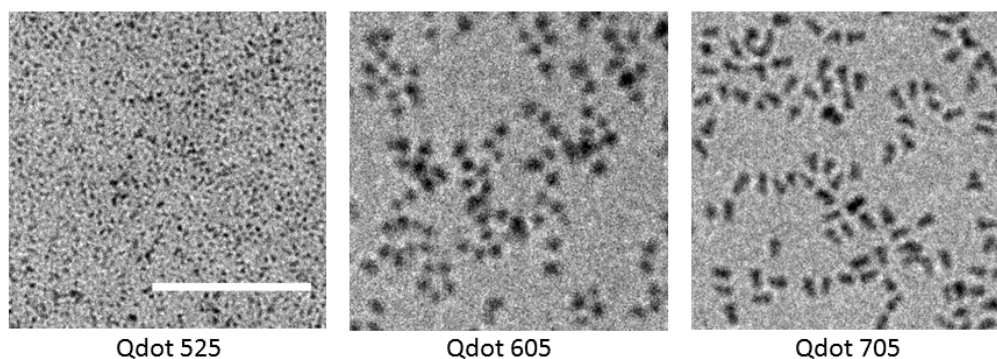


**Figure 3.29:** Transmission electron microscopy (TEM) images of Qdot525, Qdot605 and Qdot705 on carbon film grids. Magnification:  $50000\times$ . These images were used for QDs size calculation. Scale bar, 100 nm.

A summary of measurements of all QDs is given in Table 3.8. It was found that Qdot525, Qdot605 and Qdot705 have diameters of 5.8 nm, 10.5 nm and 15.3 nm respectively. Size distributions of Qdot525, Qdot605 are narrower (1.1 nm and 1.3 nm of the FWHM respectively) than that of Qdot705 (2.3 nm of FWHM).

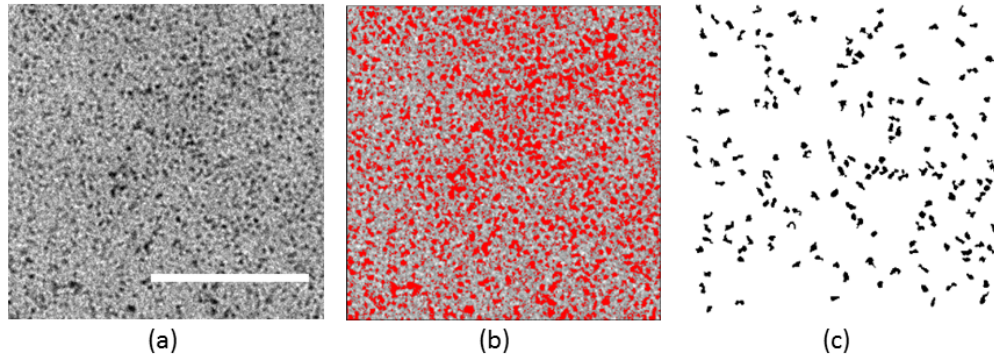


**Figure 3.30:** An example of Qdots size calculation based on TEM images. (a) A TEM image of Qdot525. (b) Image processing to select individual QD (refer to method section 2.5.1). (c) Count mask of analysed particles from image b. QDs sizes were analysed based on the count mask, using ImageJ default ‘Particle Analysis’ function. Scale bar, 100 nm.

**Table 3.8:** Quantum dots size calculation summarisation

QDs	Number of Particles	Average Area (nm <sup>2</sup> )	Average Size (nm)	FWHM of size distribution (nm)
Qdot525	232	12.7	5.8	1.1
Qdot605	274	54.4	10.5	1.3
Qdot705	281	90.3	15.3	2.3

Contrastingly, QDs emission spectra were measured and the curves were fitted with Gaussian function (Figure 3.31). Peak emissions of Qdot525, Qdot605 and Qdot 705 were found out to be 522 nm, 606 nm and 699 nm. From the grey and blue curves in Figure 3.31, one can see that Qdot525 and Qdot605 have narrower emission spectra (30 nm and 31 nm of FWHM respectively) than that of Qdot705 (63 nm of FWHM). This agrees with the size distribution results (Table 3.30) and is consistent with what we expect of QCE in QDs (see section 1.6.3.1).

TEM and fluorescence emission measurements have shown the differences between the three QDs samples (Qdot525, Qdot605, Qdot705) in size and fluorescence emission properties. These results have confirm the size-dependent emission of the QCE effect in small QDs (Table 3.8, Figure 3.31 and Figure 3.32a). Hence, a random mixture (emission spectra see Figure 3.32a) of Qdot525, Qdot605, and Qdot705 can be used for spectroscopic signal separation.

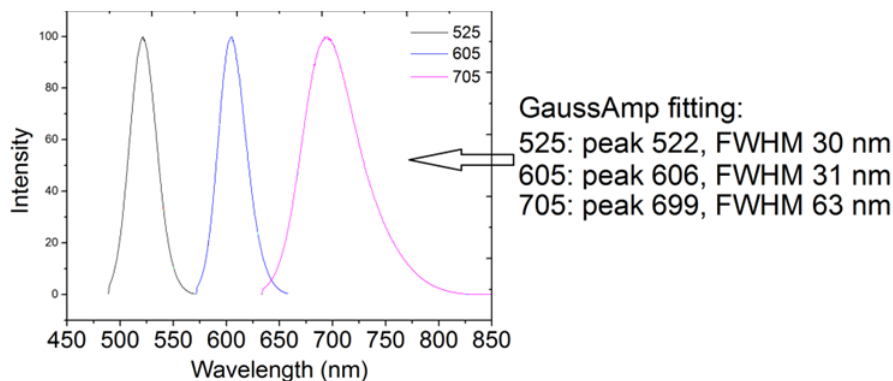


**Figure 3.31:** Calibration of emission spectra of 3 Qdot samples (product labelled emission peaks are 525 nm, 606 nm, 699 nm). Samples were excited under a Helium/Cadmium 442 nm laser. Gaussian fitting parameters (peak position and FWHM) are stated in the figure.

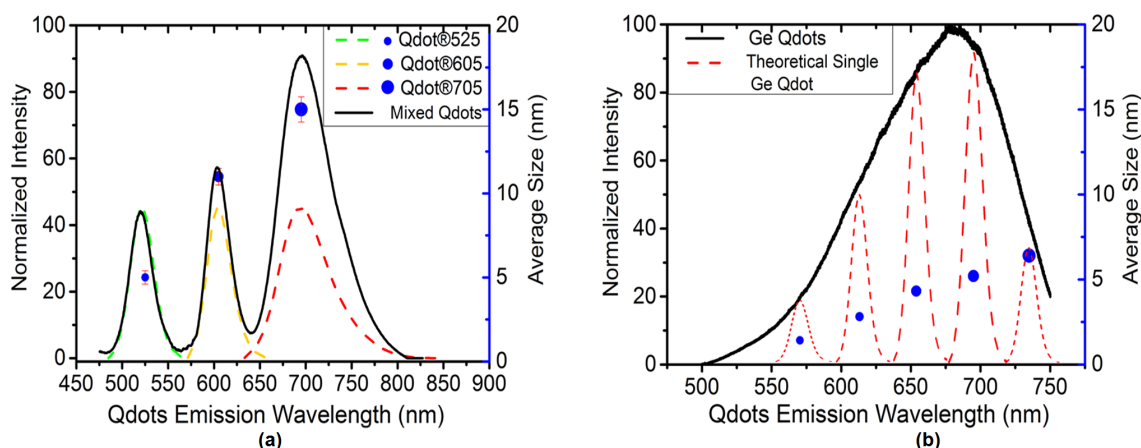


**Figure 3.32:** Emission-size analysis for CdSe/ZnS Qdots and Ge QDs. (a) Emission spectra of three CdSe/ZnS Qdots (green, yellow, red dash lines) and their physical size (blue markers) measured from TEM images. Black full line is the emission spectrum of an equally mixed sample of these three QDs. Mixed sample shows a 3-peaks emission spectra (black full line) contributed by 3 QDs components. (b) A broad emission spectrum of as-prepared Ge QDs sample with particle sizes from 2.6 to 5.2 nm (as previously shown in Chapter 3). It is assumed that broad emission is due to variation in particle sizes: red dash lines and blue markers indicate the emission spectral of several different size Ge QDs, which is expected considering the quantum confinement effects.

Since the emission of QDs depends on particle size, we can use the emission profile (Figure 3.32a) in a mixture for the localisation of individual QDs. Here, along

with the standard Invitrogen Qdot systems, Ge QDs were also used. Taking into account the previously demonstrated size-dependent emission analysis, the emission spectra of the mixture of Ge QDs ( $\sim 150$  nm FWHM, black full line in Figure 3.32b) may indicate a broader particle size distribution than that found in Invitrogen Qdots. However, our analysis of the size distribution in Ge QDs (see Figure 3.3) suggests that it's not dissimilar to that found in Invitrogen Qdots. This contradiction is resolved if we recollect that the Ge QDs of small size used here ( $\sim 3.8$  nm) are in strong QCE regime (see subsection 1.6.3.3), where the dependence of the band gap (and hence of the peak emission) on particle size is very strong (see Figure 1.28). Furthermore, using Ge QDs allowed us to reduce the probe size to below 5 nm.

In the following sections, SSRM cell imaging will be described and demonstrated.

### 3.3.4 Spectroscopic cell imaging using QDs

In this subsection, as a proof-of-principle demonstration of the SSRM method, experiments were carried out using both off-the-shelf CdSe Qdot and the Ge QDs. QDs labelled Hela cells were imaged under the LSM 710 spectra imaging model. Individual QDs were then localised using the in-house developed algorithm, spectroscopic super-resolution algorithm.

In order to realise spectroscopic cell imaging using Qdot and Ge QDs, Hela cells in cell culture dish (5000 cells/mL/dish) were labelled with 50 nM/mL mixed Qdots described above (see section 3.3.3). Images were taken using a 100 $\times$ , NA 1.45 oil objective. A 488 nm laser at 15 % of the 50 mW power was utilised for sample excitation. QUASAR detector master gain and digital gain were set as 600 and 2 respectively. Auto exposure time was selected. It took 1.6 seconds to acquire an image stack. Images recorded for a number of emission channels (33 channels  $\lambda$ -stack from 498 nm to 721 nm) with a single excitation wavelength (488 nm) are shown in Figure 3.33. The total fluorescence emission sum image is presented in the inset



in Figure 3.34a. A small area of interest (Figure 3.34b, marked as a yellow square corresponding to a  $1.5 \times 1.5 \mu\text{m}^2$  area) was selected. For more data about the  $\lambda$ -stack frames of different QDs, please see Appendix D.1.

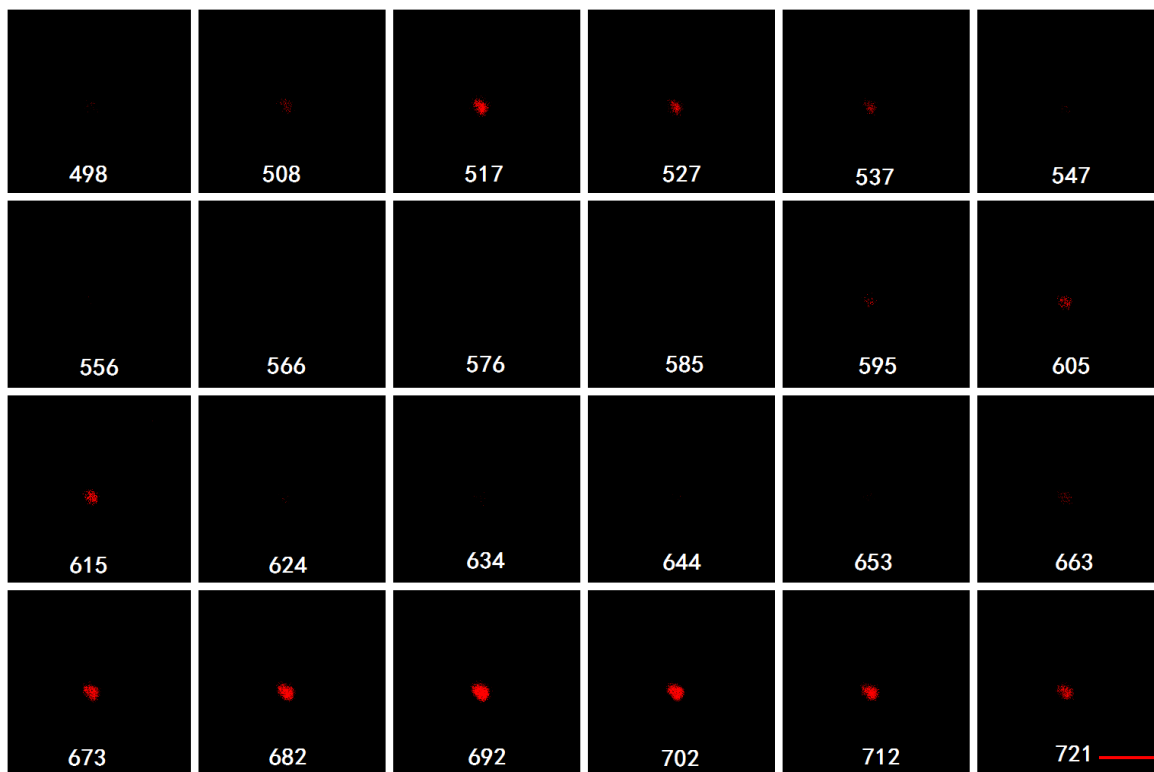


**Figure 3.33:** Fluorescence spectra channels of the mixed CdSe Qdots sample. These  $\lambda$ -stack frames contain of specific unique fluorescence information from each of the 10 nm spectral width channel. Channel window wavelengths are labelled at the bottom of each frame. The excitation laser is a 488 nm laser using at 8% of the 50 mW full power. Auto exposure time mode was used. Scale bar,  $3 \mu\text{m}$ .

Three channels (shown in green, magenta, and yellow in Figure 3.34c) corresponding to the emission peaks of Qdots are selected to run the localisation algorithms. Each frame only contains fluorescence signals from specific Qdots thus generating a unique fluorescence image.

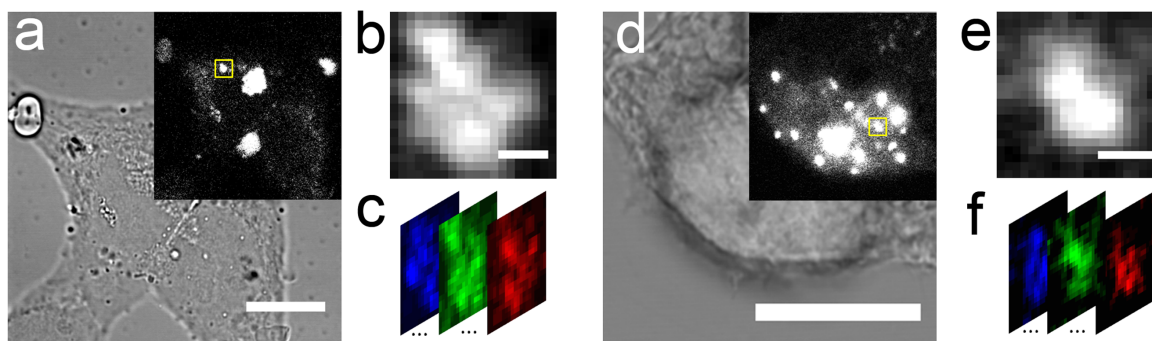


**Figure 3.34:** Spectroscopic super-resolution microscopy images. (a) HeLa cell cultivated with mixed three CdSe/ZnS Qdots and sum fluorescence image (insert a). (b) zoom-in of the yellow square area in the fluorescence image (insert a) and the spectroscopic separated image frames – lambda stack (c) collected in this microscopy. Three channels (517 nm, 605 nm, 702 nm) where three Qdots emission peaks occur were selected and presented (green, magenta and yellow). Subsequently, Ge QDs labelled HeLa cell (d) was demonstrated on this microscopy. Ge QDs shows a strong fluorescence emission in cells. (e) zoom-in details of the yellow square in the fluorescence image (insert a) and f indicates the spectroscopic separated images frames. Three channels (595 nm, 644 nm, 692 nm) were selected to present the different spectroscopic images. Scale bars, (a) 10  $\mu\text{m}$ , (d) 5  $\mu\text{m}$ , (b, e) 500 nm.

A similar approach was used for spectroscopic imaging on HeLa cells which were labelled with Ge QDs at the concentration of 50 nM/mL. Initially,  $\lambda$ -stack image of Ge QDs was recorded (Appendix D.2). HeLa cells were cultivated with Ge QDs for 24 hours and the fluorescence image of all spectroscopic channels is shown in the inset in Figure 3.34d. A small area of interest (Figure 3.34e, f, marked as the yellow square in Figure 3.34d) was selected to test spectroscopic localisation algorithms. In order to demonstrate the SSRM, three channels with  $\sim 50$  nm apart were selected from 33 channels  $\lambda$ -stack for further processing. Differences between the selected colour (wavelength) channels became apparent even before the processing stage of both Qdot cell data (Figure 3.34c) and Ge cell data (Figure 3.34f). These data were then used for the single molecule localisation process and super-resolution reconstruction.

Need to mention, an important issue associated with these spectroscopic separation imaging is the spectra overlap of similar size quantum dots. With multiple

QDs, close spectral bands (for example 10 nm width in our case) are often not possible to fully isolate signals from a single QD. Thus the individual spectral channels usually contain fluorescence light originating from several QDs, which have to be separated by computational methods called 'spectral unmixing' or 'emission fingerprinting' [221]. In this technique, the fluorescence contributions of different molecules at a given pixel are calculated based on the spectral information of fluorescence molecules. In mathematical realisation, this is done by the inversion of a linear equation combining the fluorescence molecule concentration, the fluorescence signal intensity and a coefficient term revealing the emission spectra properties of the molecules [222]. In principle, optimised resolution could be expected through spectra unmixing even under presence of a relatively high noise level [221, 223]. However, spectral unmixing was not carried in our demonstration because the distance between the selected three channels are much further than a single QD emission spectral (FWHM 0.45 nm [224]).

In the next subsection, the in-house single molecule localisation algorithm SSA will be introduced and used for super-resolution reconstruction.

### 3.3.5 Super-resolution reconstruction

As has been discussed in section 3.2.5.1 and by other authors [215], single molecule localisation algorithms should make a tradeoff between single molecule localisation precision and processing efficiency (speed). Consequently, it is necessary to strike the balance between raw data processing (as few computational process as possible) and high precision of localisation (considering as many factors as possible, which normally leads to more computational process steps and longer processing time). Current ready-to-use algorithms are designed for specific types of super-resolution imaging methods or datasets, either based on image spatial or temporal information for reconstruction. For our data, each spectroscopic image frame contains unique and definite information, thus statistic analysis is not applicable. Additionally, PSFs in different frames are different because of the different wavelength components (as has

been characterised in section 3.3.2). Therefore particular attention should be paid to the variation of PSFs in different channels, which demands individual processing of each frame. Due to the lack of software or codes to process our dataset, a Matlab software code SSA was developed to handle our SSRM data.

### 3.3.5.1 SSA description

The SSA includes three parts: de-noising, segmentation, and maximum likelihood estimation (MLE). The de-noising step employed a Gaussian de-noise model and Poisson de-noise model (one should choose the appropriate model based on the detector specification). For our PMT detected image data, the Gaussian de-noise model was used. The de-noising is achieved through a convolution process. The degree of de-noise is determined by the standard deviation of the Gaussian distribution of the noise [225], where larger standard deviation Gaussians require larger convolution kernels. The centre value of a pixel ( $v_{xy}$ ) is replaced by a weighted average of its neighbourhood ( $x, y$ ) ( $v$ ), as shown in equation 3.6.

$$v = \frac{1}{2\pi\sigma^2} e^{-\frac{x^2+y^2}{2\sigma^2}} v_{xy} \quad (3.6)$$

where  $\sigma$  stands for the standard deviation of Gaussian distribution of the noise.

The segmentation step is to partition the original image into multiple segments, which satisfies the hard constraints of the possible sizes of PSF. Firstly, the grey value to each pixel is acquired and the pixel with a largest grey value is identified. The area around this pixel (called regions of interest (ROIs)) is selected based on expected PSF size. Then, a pixel with the next largest grey value is selected and procedure is repeated until the whole image is segmented. The resulting segments collectively cover the entire image and each of them includes a brightest point and its neighbourhood pixels in the constrained region.

Maximum likelihood estimation (MLE) [226] was implemented to achieve the Gaussian fitting for PSF in the ROIs. Then the mean and variance of the Gaussian functions can be estimated with MLE. Mathematically, this is achieved by treating the mean and variance as variables and finding particular parametric values that maximize the likelihood function (making the observed results the most probable). For a dataset  $D$ , the likelihood for how  $D$  matches the Gaussian distribution  $N(\mu, \sigma^2)$  is judged using equation 3.7:

$$f(D | \mu, \sigma) = \frac{1}{\sqrt{2\pi}\sigma} e^{-\sum_{i=1}^n (d_i - \mu)} \quad (3.7)$$

There are two parameters  $(\mu, \sigma)$  to be determined. Hence, we maximise the likelihood  $f(D | \mu, \sigma)$  over both parameters simultaneously. Since the logarithm  $\log f(D | \mu, \sigma)$  is a continuous strictly increasing function over the range of the likelihood, let  $\frac{\partial f(D | \mu, \sigma)}{\partial \mu} = 0$  and  $\frac{\partial f(D | \mu, \sigma)}{\partial \sigma} = 0$ , we have:

$$\mu = \frac{\sum_{i=1}^n d_i}{n}$$
$$\sigma = \frac{\sum_{i=1}^n (d_i - \mu)^2}{n}$$

where  $\mu$  determines the localisation position and  $\sigma$  accounts for the error and localisation confidence.

Once the localisations have been determined, the output figure is then reconstructed. Molecule positions are printed with standard plot function in Matlab2014 with default black colour. The positions of the points are elicited from the mean values from fitted Gaussians (line 50, SSA codes, Appendix G). The render point sizes are set as the default value, and users also can adjust the circle size online. The final multi-frame results are saved in a separate *.mat* file, which could be used for further analysis. Following this, there is a flow chart of the SSA algorithm given in Table 3.9. Full code of each module is found in Appendix G.

**Table 3.9:** Flow chart of SSA algorithm**Algorithm**  $SSA(D, K, \lambda, P)$ **Input:** $D$ : Input image (.tif format) $K$ : The maximum possible molecules in each frame. $\lambda$ : Corresponding wavelength for each frame. $g$ : Gaussian de-noise parameter.**Output:** Localisations  $L_{ik'}$  in each frame  $D_i$ .**Main:****For** each frame  $D_i \in D (i = 1, 2, \dots, N)$ .Calculate the PSF half width at half maximum (HWHM),  $h_i = f(\lambda_i)$ .Gaussian den-oise this frame  $D_{i'} = im.filter(D_i, g)$ .**For**  $k = 1$  to  $K$ Initialize the fitted Gaussian distribution sets  $G_k = \Phi$ .**While** length ( $L_k$ )  $< k$  or ( $D_{i'}$  is not blank)Find the brightest point (peak)  $P_b$  in  $D_{i'}$ .Copy all the points  $P_s$  in  $D_{i'}$  satisfying  $dis_{Euclidian}(P_s, P_b) < h_i$  into a temporal set  $S_b$ .Fit a Gaussian distribution  $G_b$  to  $S_b$ . $G_k = \{G_k, S_b\}$ Remove the points  $S_b$  in  $D_{i'}$ ,  $D_{i'} = D_{i'} - S_b$ .**End While**Fit the Gaussian Mixture Model (GMM) with centres and covariance matrices in  $G_k$  to original data  $D_i$ .Calculate the log-likelihood  $ll_k$  of the fitted GMM.**End for** $k' = \operatorname{argmax}_k ll_k$ .Get the localisation set  $L_{ik'}$  from  $G_{k'}$  (elicit all the mean values of  $G_{k'}$ ).**End for**Return  $\{L_{ik}\}_{i=1}^N$

In the next subsection, the single molecule localisation and super-resolution reconstruction processing to our SSRM data using SSA will be demonstrated.

### 3.3.5.2 SSA reconstruction

The single molecule localisation and super-resolution reconstruction was carried out using SSA. As a reference, a similar algorithm named CSSTORM [186] that had been developed to handle STORM data was applied to our data.

In the SSA reconstruction, individual ROI size was tailored according to the changes of PSFs with wavelength (the default fitting region size was set as 3 times the PSF size in each channel) and the default value of 3 was used in this processing. The maximum possible number of QDs in each frame was set at 1000 according to an initial guessing by looking at the raw image. It took less than one second for SSA to process each frame. In the CSSTORM reconstruction, the processing parameters were set as default (optimisation chi square value of 1.5 and the baseline offset of the camera at 100). Processing time in CSSTORM was about 10 seconds for each frame.

Figure 3.35 shows the results of analysis of Qdot data (left side) and of Ge QDs data (right side). Selected image frames and the sum images in Figure 3.34 are used here (Figure 3.35a-d). CSSTORM-processed results can be seen in e to j, and the final reconstructed image (g, j) is obtained by merging frames in f, i. SSA-processed results are represented in k to n. A comparison was then carried out between the localisation precision (which primarily depends on how users set the reconstructed image size and the fitting confidence region according to the data), localisation resolution (which stands for the minimum distance of any two separated signals) and confidence (which stands for a percentage of how well the fitting describes the raw data, obtained from the maximum likelihood). Qdot data and results of analysis are used as a reference for Ge QDs.

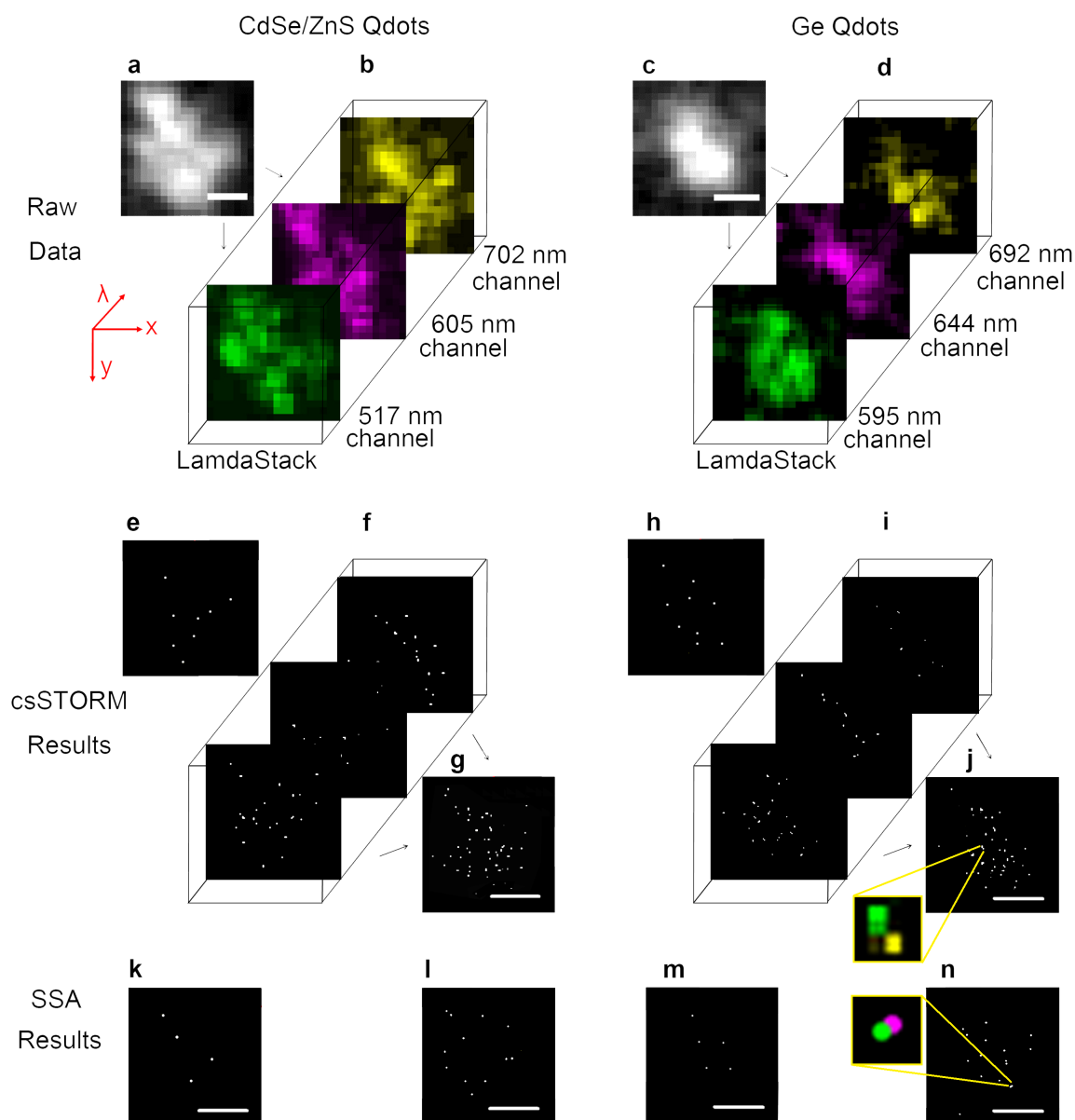


**Figure 3.35:** Spectroscopic super-resolution localisation and reconstruction. Left column are CdSe/ZnS Qdots super-resolution data and results. (a, b) selected three spectroscopic separated frames (595 nm, 644 nm, 692 nm) and sum of all spectroscopic separated frames. (e, f) CSSTORM localized results of (a) and (b) respectively; (g) final merged CSSTORM results of images from (f). (k, l) localisation and reconstruction of (a, b) frames using our SSA algorithm, revealing the potential Qdots distribution behind the fluorescence signals (a). Right column are Ge QDs data and results. (c, d) fluorescence and sum images. (h-j) CSSTORM process results, a final CSSTORM final result (j). (m, n) SSA result of (c, d) represents the final super-resolution image in SSRM. Scale bars, 500 nm.



The SSA localisations are filtered by a hard constraint that the Gaussian fitting confidence of larger than 95 %. This parameter is not seen in csSTORM as it doesn't give any localisation confidence. SSA reconstruction spots size was set as 12 nm for Ge QDs data and 40 nm for CdSe QDs data (twice the size of the physical size of QDs). One can see that the SSA meets the constraint of 95 % fitting confidence at the cost of localising fewer QDs than csSTORM (49 QDs in **g** while only 12 QDs in **i**, 42 QDs in **j** while only 16 QDs in **n**). Comparing **e** to **g**, **h** to **j**, **k** to **i** and **m** to **n**, one can see that the spectroscopic separation does result in more QDs being localised. For clearer, two closely located QDs (the yellow zoom-in square in **i** and **n**) are localised through spectroscopic separation and reconstruction.

Considering the real QDs distribution and the effective resolution of the super-resolution images, we can imagine that several identical QDs may be located too close to each other (less than 12 nm for Ge QDs for example), this could increase the inaccuracy of single molecule localisation because these QDs would be regarded as one QD. This means that the localisations could be further supplemented with a standard fitting error (typically from 10 to 30 nm in FWHM [227]). Furthermore, the registered QDs number will also be influenced by the maximum possible number which is user determined (see Figure 3.23). As to an as-prepared sample, it is nearly impossible to find out the real QDs distribution unless undertaking CLEM imaging and directly visualise them under electron microscope. Take a step back, Fourier Ring Correlations has been widely accepted to measure the effective resolution even though it is only based on computational analysis. Alternatively, experimental methods such as DNA rulers and proteins imaging should also benefit the examining of the effective resolution of a super-resolution imaging method.

As to the initial guess of the maximum number of QDs, it is easier to set this number in SSA compared to the BSA in stochastic imaging method, because there is only one frame to localise one QD. Considering the hard constraint of single molecule imaging within one diffraction limit region, the SSA is only suitable for those images with sparse distributed QDs. This requires a suitable sample preparation to control

the labelling density. To any existing data, the maximum number could be estimated by using the total intensity grey value divided by the intensity one single QDs, for example, 100 Ge QDs (intensity grey of 600 for single QD) in an region with total intensity grey value of 60000. Higher density of QDs than this number will lead to the SSA algorithm not suitable to the data any more. In this context, future work for our algorithm improvement can be developed to make a proper balance between the QDs labelling density and the effective resolution.

### 3.3.6 Conclusion

In this section, it has been shown that a combination of spectroscopic image acquisition and a suitable localisation algorithm is capable of delivering nearly a three-fold improvement in the number of localised QDs (see Figure 3.35l) compared to non-spectroscopic image (see Figure 3.35k). With the addition of advanced ultra-small Ge probes, the number can be improved even further, giving at least 1.5 times improvement when compared to standard Invitrogen Qdots (see Figure 3.35k and n). Some of these improvements are, no-doubt, due to the small size of Ge Qdots ( $\sim 2 - 5$  nm) compared to Invitrogen ( $5 - 15$  nm). It can also be seen from Figure 3.35 (g, l and j, n) that improvement the localisation number and precision comes in part from SSA algorithm, which delivers better values than csSTORM. This algorithm reduces the unnecessary processing of raw data and pays greater attention to extracting useful information in a single frame, instead of increasing the speed for multi-frames processing. This algorithm is easily modifiable in Matlab. Researchers are able to insert any modules into the current framework in order to achieve extra functions.

Compared to temporal separation in stochastically reconstructed super-resolution microscopy, spectroscopic separation super-resolution microscopy greatly reduces the demands of system drifting correction and environmental influence compensation due

to the short data acquisition time (1.6 seconds in our case, see section 3.3.4). Improved temporal resolution should result in this method being suitable for life cell imaging. It is also of great significance in applying this method to live cell bioimaging.

One of the key points of this method in biological application is the labelling density control and good sample preparation. In order to obtain adequately separated fluorescence signal, randomly mixed multi-size QDs and a uniformly labelled sample are desirable, which is usually not practically easy as has been discussed in previous reports [194, 214]. Besides, a microscopy system needs to be characterised before imaging. At the very least, background and PSF spots in all channels should be characterised and considered in localisation in order to improve precision.

In summary, this super-resolution microscopy approach could achieve the separation of two closely located QDs on the image while simultaneously keeping a high temporal resolution (1.6 seconds per frame, section 3.3.4). Future extensions of this methodology could include the specific labelling of cellular structures, live cell super-resolution imaging, and 3D imaging.

As a novel fluorescent probe, ultra-small core type QDs are revolutionising biofluorescence imaging, by overcoming the narrow excitation and emission spectra problems of using conventional fluorescent proteins, and particularly large size problem in using core-shell type of II-VI, III-V QDs. In SSRM, using small Ge QDs can improve localisation down to  $\sim 5$  nm due to their small size, thus providing a promising future for their application in biological super-resolution imaging.

# Chapter 4

## Conclusion and future work

### 4.1 Conclusion

In this thesis, in-house colloidal fluorescence germanium QDs were used as a novel fluorescent probe for single molecule localisation super-resolution cell imaging. In the first place, some fundamental characterisations and studies were carried out to evaluate the suitability of the Ge QDs for cell imaging. Ge QDs were characterised using both a fluorescence microscope and an electron microscope. Light emission was observed in the visible range (550 - 750 nm) with a peak at near 670 nm (see section 3.1.1.1). The physical size of Ge QDs was calculated as 3.8 ( $\pm$  1.4) nm in diameter based on TEM images (see section 3.1.1.2). Ge QDs' biocompatibility was tested on HeLa cells using both qualitative assays such as Trypan blue and quantitative assays such as Muse and Incucyte. They have shown lower cell toxicity to live cells compared to commercially available Invitrogen carboxyl-coated CdSe QDs (see section 3.1.2). Hence, Ge QDs were considered to be suitable for cell imaging. Ge QDs were found to have sufficient fluorescence emission in both fixed and live cells for microscope imaging (see section 3.1.3). Following this, single molecule localisation super-resolution cell imaging has been studied using Ge QDs, with CdSe QDs as a reference. Confocal fluorescence microscopes - a spinning disk confocal microscope and a spectra imaging

laser scanning confocal microscope were utilised as the main experimental platforms. Two modes were utilised for super-resolution imaging: one based on QD blinking and another mode was based on spectral signal separation.

Ge QDs showed blinking phenomenon and blinking events were studied using the spinning disk confocal microscope under the exposure time of 50 ms. The stochastic blinking off duration probability distribution was found to follow an inverse power law with exponent of - 1.6 (see section 3.2.3.1). In this case, Ge QDs were regarded as suitable for stochastic reconstruction super-resolution imaging. The time-trace and measurements of blinking events used in this study not only provide a clear confirmation of the statistical blinking phenomenon of Ge QDs, but could also inspire new insights into electron excitation inside QDs. Such QDs blinking analysis can also be a visual tool to characterise and compare different types of QDs, such as other fluorescent molecules like single conjugated polymer molecules [228].

Stochastic super-resolution imaging using blinking Ge QDs has been demonstrated on non-specific labelled Hela cells. This has been done through the combination of a spinning disk confocal microscopy system for imaging and a computational image post-process for localisation and reconstruction. Localising single molecules has been demonstrated and super-revolved images have been reconstructed (see section 3.2.5.3). One should pay attention to the effective resolution in the final image (even though the measurements of the resolution has not been shown in the thesis) as it will also be a crucial aspect in real biological applications.

Current ready-to-use single molecule localisation algorithms were either taking too long to process a small amount of data, or were unable to analyse the blinking statistics. By contrast, our algorithm, blinking super-resolution algorithm (BSA) developed on Matlab (see section 3.2.5.2), was able to identify single QDs with a precision of 20 nm at the confidence of 95 % (see section 3.2.5.3), based on the statistical analysis of blinking events.

Size-dependent light emission of QDs was confirmed using Invitrogen CdSe QDs

(see section 3.3.3). For Ge QDs, this hasn't been directly proven in this project; however, there is considerable indirect evidence for it, such as band gap change and a clear similarity between photoluminescence curve and size distribution (see section 3.1.1). Based on this assumption (and clear evidence in case of Invitrogen QDs), spectroscopic super-resolution imaging was carried out (see section 3.3.4). Using this method, Two closely located (much closer than the diffraction limit distance) QDs were localised precisely (see Figure 3.35) and distinguished from a randomly mixed QDs (see section 3.3.5.2). Another remarkable advantage of this method is that it allows all image frames to be acquired at the same time. A short data collection time of 1.6 seconds has been achieved (see section 3.3.4). Compared to STORM/PALM stochastic super-resolution methods which normally take several minutes to collect the data, this method provides a significant improvement in temporal resolution, thus should lead to the extension of super-resolution imaging to live systems.

Similarly to the blinking analysis algorithm development, we also developed a Matlab based algorithm, SSA (see section 3.3.5), to process the SSRM data, due to the lack of available suitable algorithms. SSA has a fast processing speed (a few hundreds of milliseconds for one spectroscopic image frame, see section 3.3.5.2).

Above all, such proof-of-principle research has brought Ge QDs into the single molecule localisation super-resolution cell imaging application. Because of its blinking phenomenon and size-dependent light emission, using Ge QDs could break through the diffraction limit and achieve a localisation resolution of less than 20 nm on a light microscope. Furthermore the spectroscopic super-resolution strategy suggests the strong possibility of achieving imaging on live cells. In the next section, the outstanding questions and some imperative further work will be discussed.

## 4.2 Outstanding questions and future work

### 4.2.1 Ge QDs quantum yield study and functionalisation

As a new fluorescent probe, Ge QDs are not as well studied as traditional dyes and fluorescent proteins. The fluorescence emission quantum yield has not been quantitatively studied, even though sufficient fluorescence has been observed from Ge QDs under a confocal fluorescence microscope. Measuring the quantum yield (QY) is important as a guidance to the Ge QDs synthesis. Measuring the QY of QDs can be achieved through a standard method of comparing the optical absorption and emission of a reference sample, which can be carried out at room temperature [229–231]. Comprehensive work is required to link the QY with QDs structure and surface in order to optimise the utility of Ge QDs in bioimaging through further functionalisation.

There are some important biological application questions that need to be addressed, such as the QDs' stability, especially in different cellular environments. In fact, cellular environments can significantly impact on the fluorescence performance of QDs in live cell imaging. For example, the pH can influence the quantum yield of QDs, thus impacting the fluorescence brightness. In order to improve the stability of Ge QDs in different cellular environments, recent research has proposed some chemical approaches, such as surface passivation [232–234] and hydrogen termination [235]. With respect to such research, we expect in the future to carry out the surface modification on Ge QDs. The surface modifications can also be used to improve the stability, quantum yield and functionalities, such as anti-body conjugation for specific cell structure labelling. Surface modification and organic group conjugation techniques should connect the QDs and specific labelling cell imaging. One should also remember that if the conjugated groups to the surface are larger than Ge QDs itself, the advantage of Ge QDs being ultra-small would be lost. So far, there are still limited reports describing the biocompatible surface modifications of Ge QDs.

Therefore, there are many possibilities to explore in this area.

Furthermore, other materials in Group IV are also worth studying, such as Carbon and Silicon QDs. Future systematic research could extend to a wider comparative study of using Ge, C and Si QDs in bioimaging.

### **4.2.2 Improving the super-resolution imaging methods**

With regards to the super-resolution cell imaging methods that have been demonstrated in this thesis, there is a lot of further research to be done to turn them into practically useful tools in cell imaging. Improvements in imaging speed and analysis speed should be further expanded through integration with each other. For example, the SDSI method could be further developed through multiple CCD detection to enable the simultaneous multicolour imaging and improve the temporal resolution. The SSRM could be further enhanced through line/surface scanning and optical sectioning [236, 237], allowing for faster imaging of thicker samples. Further examination of the effective image resolution (experimental methods such as on microtubules or proteins [66, 184], or simulated calculations such as FRC can be carried out in real biological applications. Furthermore, developing a useful and efficient correlative light and electron microscopy (CLEM) method for our super-resolution imaging will be the most direct way to compare the real sample structure and the super-resolved image. Our previous attempts on the CLEM method (Appendix E) indicates that implementing such a method is not technically easy. There is a lot of future work worth to do to solving the problems with sample preparation and avoiding sample damage in the electron microscopy.

It is imperative to apply our super-resolution imaging strategies on live cells systems, as well as 3D imaging. Live cell imaging proposes additional challenges to the single molecule imaging using Ge QDs because of the highly dynamic nature of cellular activities in live samples. Not only a good stability of Ge QDs in cellular environment,



but also a high imaging speed have to be ensured for live cell imaging. As regards 3D imaging, several methods have been proposed by other authors to encode the axial information of probes into their observable 2D lateral profile. For example, there are: astigmatism approaches which use a cylindrical lens into the optical detection path to translate the axial position information into lateral PSF elongation [238]; double-helix approaches which use a spatial light modulator to accurately translate the molecule axial position information into the angle information of visible PSF lobes laterally [239]; and biplane approaches that use two detection planes to image the sample at slightly different axial positions simultaneously, from which the molecule axial coordinates are retrieved by analysing the changes to their PSF profile within the two planes [240]. Even though, this thesis has not solved any real biological problems using our super-resolution imaging methods, we have in principle proven the feasibility of these methods. The thesis thus provides straight forward guidance for further applications to live cell imaging, in order to solve real biological problems in 3D.

### **4.2.3 Algorithm tests and improvements**

Much more testing and comparison work of our localisation algorithms alongside other existing algorithms still needs to be done from different aspects. For example, localisation precision comparison using the root mean square error, imaging quality evaluation using signal-to-noise ratio criterion, computation speed and algorithm usability (accessibility, open source, maintenance) [215]. There is no doubt that faster processing and more reliable computational frame works to our algorithms are essentially required to meet the large demands of image processing in the super-resolution cell imaging field.

Another important issue while handling real biological applications is the balance between the cellular target labelling and effective resolution. For example, QDs must firstly be conjugated to a carrier molecule for specific labelling, and in many cases

the number of QDs involved is questionable [241]. This increases the uncertainty of the targets position despite a high localisation precision on QDs. This should be taken into account in the algorithm. Moreover, the labelling density should be not too sparse in order to meet the Nyquist criterion (see section 1.5.2), and not too dense in order to obtain temporal/spectroscopic separation for single molecule localisation. For example, to determine the resolution of a long, highly folded microtubule in a cell, or a similar polymer, meeting the Nyquist criterion is crucial. In some other cases, to determine to what extent a point object A (such as a short DNA sequence) is adjacent to another point object B (such as a short DNA sequence, or a protein), too dense labelling should be avoided in order to determine the accurate distance. Future work can be done to test the reconstruction resolution of our algorithms as a function of the labelling density in different biological applications, as has been mentioned in section 3.3.5.2.

To conclude, super-resolution cell imaging has been a comprehensive field of study among physicists, chemists and biologists. Future developments will, as before, rely on new optical methods, more suitable fluorescent probes and a better understanding of biology at the nanoscale. It will also benefit from more efficient computational algorithms. Certainly, the use of more photo-stable and controllable semiconductor quantum dots will lead to greater advancements in super-resolution imaging. The emergence of new quantum dots will not replace the traditional fluorescent proteins and dyes, but will complete them as diversiform applications of light microscopy. In the future, new developments will enable more user-friendly multi-colour 3D live cell imaging to disclose more biological secrets that are still hidden from humanity today.

# Appendix A

## Supplementary Muse test data

**Table A.1:** Comparison of cell viability with Ge QDs and Qdot625 on Muse test

Experiment 1			
Hela cells (1 mL)	24 h	48 h	72 h
Control cells	95.7%	98.2%	94.1%
Cells (25 nM Ge QDs)	94.9%	89.3%	80.6%
Cells (25 nM Qdot625)	90.3%	84.1%	71.6%

Experiment 2			
Hela cells (1 mL)	24 h	48 h	72 h
Control cells	94.1%	95.7%	93.6%
Cells (25 nM Ge QDs)	91.4%	86.5%	75.9%
Cells (25 nM Qdot625)	87.0%	80.5%	68.4%

Experiment 3			
Hela cells (1 mL)	24 h	48 h	72 h
Control cells	91.0%	96.9%	90.7%
Cells (25 nM Ge QDs)	90.6%	87.6%	75.1%
Cells (25 nM Qdot625)	91.8%	78.1%	70.3%

# Appendix B

## Calculation of molar concentration of Ge QDs

The calculation method was adopted from reference [242, 243]. It assumes that the QDs have a spherical shape. The calculation equation is:

$$C = \frac{N_T}{NVN_A} \quad (\text{B.1})$$

where  $C$  = molar concentration of QDs solution,  $N_T$  = Total number of Ge atoms in the sample (determined by the total sample mass and the atomic mass),  $N$  = number of atoms per QD ( $N \approx 400$  at the QD diameter of 3 nm [191]),  $V$  = volume of the solution in liter,  $N_A$  = Avogadro's constant.

For example, 1 mg Ge QDs dry powder in 1 mL water will results in a molar concentration of 35 nM per mL.

# Appendix C

## iXon3 photon number calculation

iXon3 photon number calculation information was found in the manufacture guide book [244]. It is illustrated in the following equation:

$$\begin{aligned} \textit{Photonnumber} &= \frac{\textit{Electrons/EMGain}}{\textit{QE}} \\ \textit{Electrons} &= \frac{\textit{Counts - Background}}{\textit{CCDsensitivity}} \end{aligned}$$

where EMGain is an user controlled parameter during imaging; counts and background refer to the pixels gray value of any given signal and back ground; QE refers to quantum efficiency of the the iXon3 camera which is  $\sim 0.7$  at visible light wavelength range; CCD sensitivity corresponds to electrons per count, which is 1.25 in our case (available from the camera specification book).

# Appendix D

## Supplementary $\lambda$ -stack data in SSR

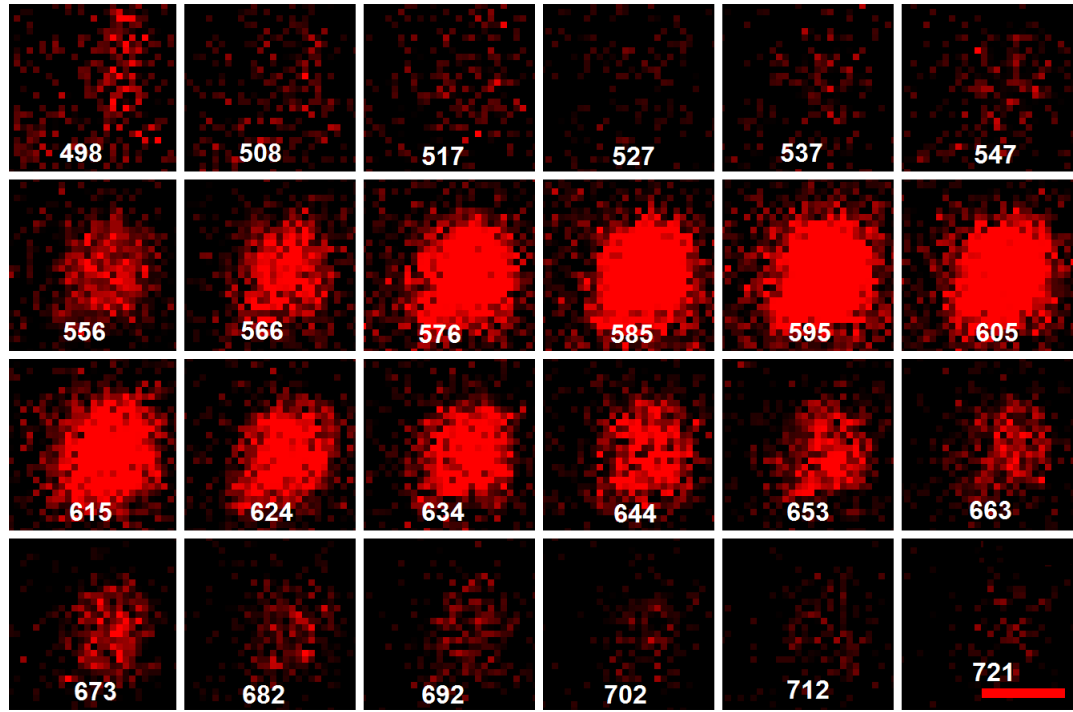
### D.1 Supplementary data 1: 6-Qdots

Table D.1: Individual Invitrogen QDs  $\lambda$ -stack images from LSM710 microscope

Samples	Channels(nm)																									
	498	508	517	527	537	547	556	566	576	585	595	605	615	624	634	644	653	663	673	683	692	702	712	721		
Qdot 525																										
Qdot 565																										
Qdot 585																										
Qdot 605																										
Qdot 655																										
Qdot 705																										

Note: Objective,  $100\times$  oil lens. Excitation light source, 488 nm laser. Frame size,  $2\ \mu\text{m} \times 2\ \mu\text{m}$ .

## D.2 Supplementary data 2: Ge QDs



**Figure D.1:** Fluorescence spectra channels of Ge QDs sample. Ge QDs were diluted in water. The excitation laser was of 488 nm wavelength. Channel window wavelengths are labelled at the bottom of each frame. Scale bar, 1  $\mu\text{m}$



# Appendix E

## Correlative imaging

Correlative imaging, in this investigation, refers to correlative light and electron microscopy (CLEM) imaging method on the same sample. It combines the ability of multi-colour imaging of fluorescence microscopy that can do large area live-cell imaging, and electron microscopy that is of super high resolution. The significance of studying the performance of QDs application in correlative imaging come at two aspects: (i) find out if QDs can be used as a correlative imaging probe which is suitable for both fluorescence imaging and electron microscopy; (ii) obtain super high resolution electron microscopy images for QDs labelled biological sample fluorescence images.

In experimental realisation, correlative imaging is divided into two parts, the optical imaging, and the electron microscopy imaging (Figure E.1). Optical imaging is carried out on a fluorescence microscopy, either with a live cell sample or a fixed cell sample. Electronic imaging can be accomplished on a transmission electron microscope with ultra-thin cryosections [245] or on a scanning electron microscope to image the sample surface. To date, for many researchers the solution is to make a proper combination of achieving strong fluorescence intensity and enough electron density during the correlative sample preparation, such as using nanogold and platinum on nickel finder grid [246], green dye and Au on Cu finder grid [247], gold and carbon

nano-particles on grid glass cover slips [248].

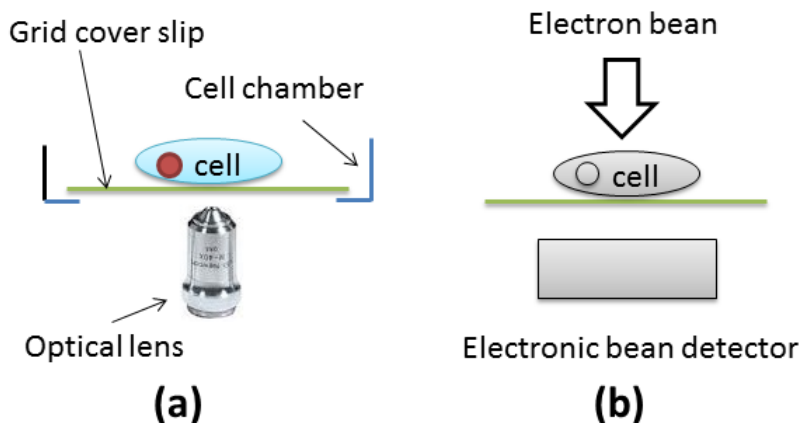


**Figure E.1:** Correlative imaging experimental steps: (a) fluorescence labelling and imaging, (b) electronic microscopy labelling and imaging.

CLEM have been carried out as illustrated in figure E.1. Initially, cells were imaged on a fluorescence microscope. It was started from cell culture on an electron microscopy grid (suitable for cell culture), then the cell fixation and fluorescence staining steps were completed. The grid with cells was then mounted onto glass slides, additionally covered by a 0.15 mm thickness glass cover slip. It was then sealed with clear nail polish. Then, the sample was imaged using fluorescence microscopy. Moreover, the acquisition of Z-plane images for 3D reconstruction could also be carried out on the fluorescence microscope at this point using this sample.

Then the sample was re-prepared for electron microscopy imaging. The grid was taken out of the microscope slide carefully. This needs extra care to avoid damaging the sample. Nanogold coating or post cell fixation in  $\text{OsO}_4$  could be included to enhance the image contrast. Then, the sample was dehydrated using 100% ethanol. The normal electron microscope imaging procedures were then taken to the sample.

In this sense, correlative imaging is limited by the complexity of experimental protocols that are time consuming and laborious. A suitable biological labelling probe which is directly usable for both fluorescence microscopy and electron microscopy will greatly reduce the complexity of sample preparations for correlative imaging. QDs

are fluorescence, and electron conductive, thus are expected to be a suitable probe for CLEM. Therefore, both Ge QDs and CdSe QDs were studied in CLEM in this project.

In practise, a laser scanning confocal microscopy system was utilized for fluorescence imaging. A scanning electron microscopy (SEM) and a transmission electron microscopy (TEM) system were used for electronic imaging. And discussions are divided into two sections: confocal and SEM correlative imaging, confocal and TEM correlative imaging.

## E.1 Confocal and SEM correlative imaging

In this route, a mixed CdSe QDs sample of Qdot525, Qdot605, Qdot705 was deposited on a conductive polyester based correlative microscopy cover slip. Before undertaking correlative imaging, the QDs were examined on the SEM and it turned out to be directly observable under SEM (Figure E.2). However, QDs that were additionally coated with gold (10 nm thickness, Figure E.2a) gained an obviously better contrast than QDs without coating (Figure E.2b).

Then, correlative imaging was studied. As the first step, confocal imaging was carried out on the LSM 710 laser scanning confocal microscopy. Afterwards, electron imaging was performed on the scanning electron microscopy. Figure E.3 represent the correlative imaging results at low magnification ( $100\times$ ). This not only gives us a clear view of how the correlative images looks like, but also guide us a practical doable route of how to do correlative imaging under similar situations.

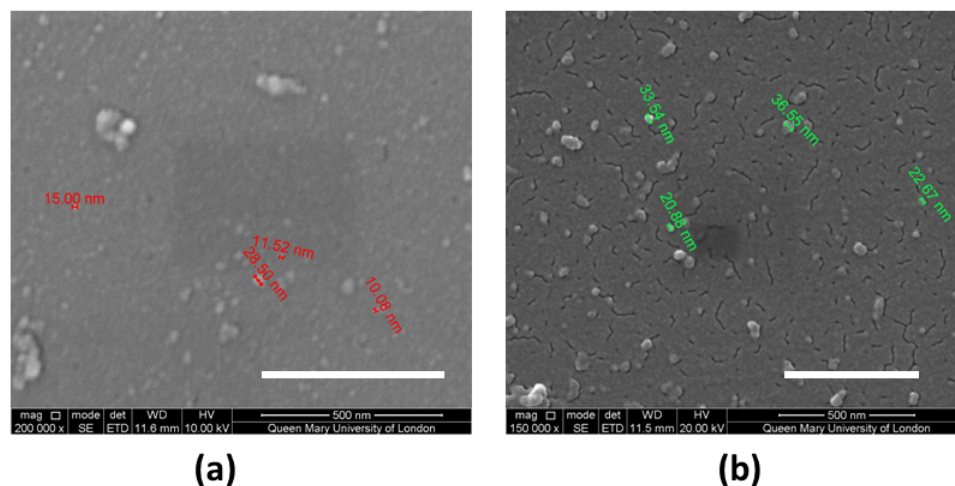


**Figure E.2:** SEM images of CdSe QDs. (a) Sample without extra coating was not very clear beyond 500 nm scale, (b) Sample with additional coating of gold of 10 nm thickness was clearly seen at the same scale. Scale bars: 500 nm.

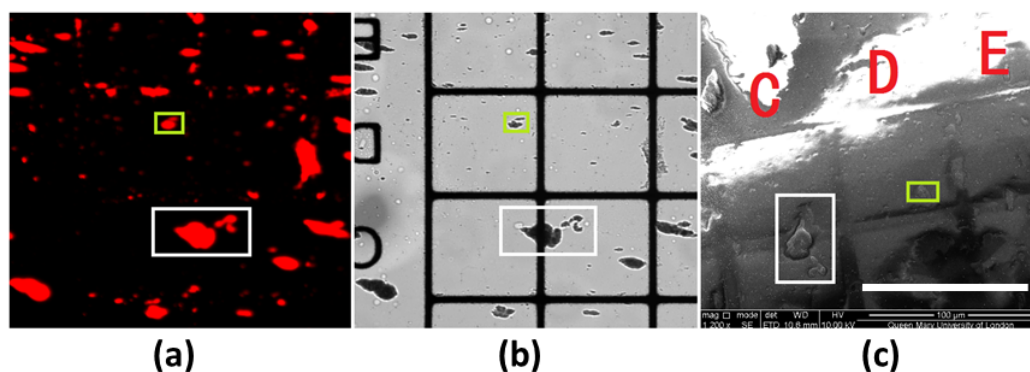


**Figure E.3:** Correlative imaging of QDs via confocal light microscopy and SEM at low magnification ( $100\times$ ). (a), (b) fluorescence and bright field images under light microscopy, (c) SEM image in which the sample was additionally coated with gold. White boxes and yellow boxes are two identified correlated areas. Scale bar:  $10\ \mu\text{m}$

Sample damage problem was caused when the magnification in SEM was increased to  $2,000\times$ . That was due to the electronic beam power increasing. As shown in figure E.4, yellow area indicates a correlated area observed by both confocal light microscopy and SEM at  $2,00\times$  magnification. After being focused for 5 seconds in SEM, sample was damaged (damage spot indicated in yellow rectangle in Figure

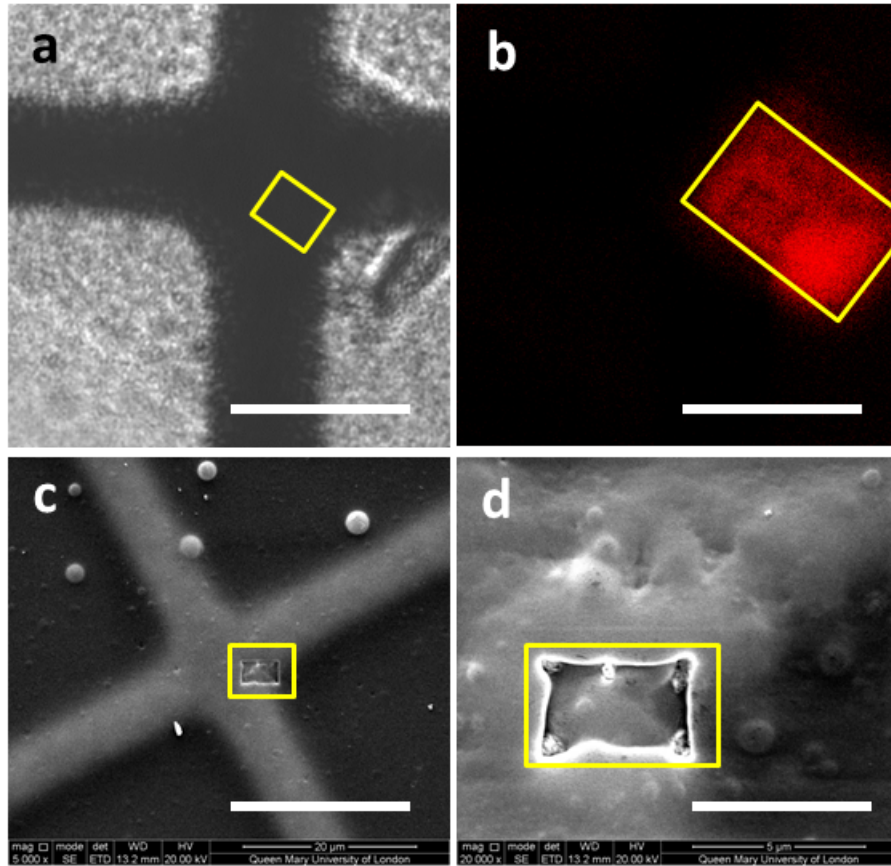


**Figure E.4:** Correlative imaging of QDs via confocal light microscopy and SEM at high magnification ( $2,000\times$ ). (a), (b) Bright field and fluorescence images under light microscopy, (c), (d) SEM images in which the sample was additionally coated with gold. Yellow box is an identified correlative area. Scale bars, a c  $20\ \mu\text{m}$ , b d  $5\ \mu\text{m}$ .

E.4c, d). This was deduced resulting from the strong electron beam damage to the polyester cover slip. As a result, sample within the damage area was not possible to be observed any more.

In the followed subsection, another CLEM method - correlative imaging between confocal and TEM will be described.

## E.2 Confocal and TEM correlative imaging

In this route, the same mixed CdSe QDs sample of Qdot525, Qdot605, Qdot705 was used and deposited onto a Holey/Carbon film TEM grid. Similar to the previous route, sample was firstly imaged on LSM 710 microscopy. Then sample was naturally dried for 24 hours, followed by imaging on TEM. The CLEM results are shown in figure E.2. From Figure E.2 (a) to (e), TEM imaging started from focusing on a big area, then zooming into a smaller region which is high lighted in red boxes. At the scale beyond 100 nm (e), individual QDs were visible. While the same area of (d) was not resolvable any more by confocal fluorescence microscopy (f) at the scale.

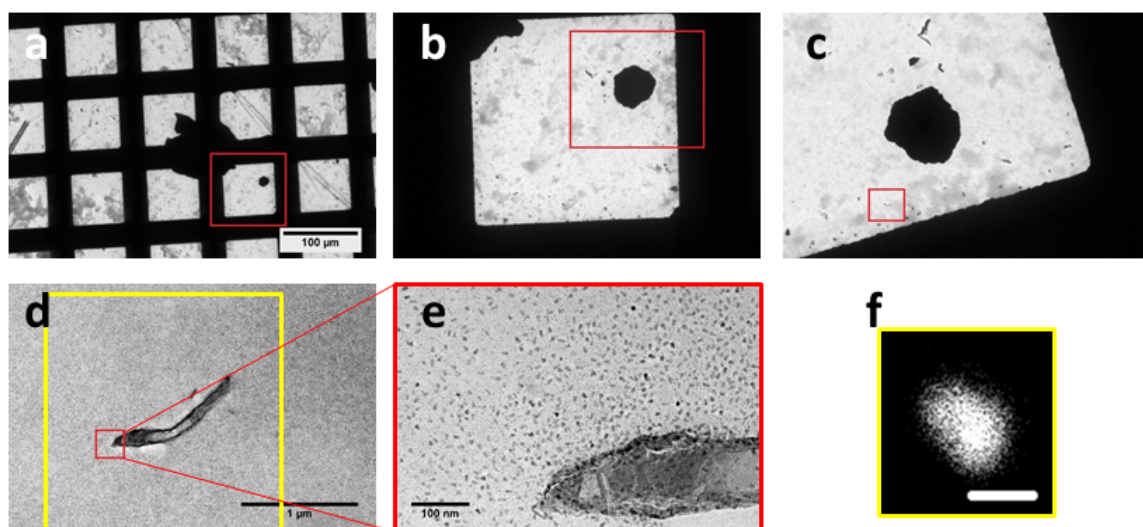


**Figure E.5:** Correlative imaging of QDs via confocal light microscopy and TEM. From **a** to **e**, TEM imaging steps for a small area through several magnifications. Red box represents the same area of the followed image. By looking through **a** to **e**, people can see how the identification and localisation of individual QDs was realised step by step in electron microscopy. **f** Fluorescence image of the yellow box area showed in **d**. More details of QDs in the fluorescence image (**f**) have been revealed by electron microscopy images (**a** - **e**). Scale bars: **a** 100  $\mu\text{m}$ , **d** 1  $\mu\text{m}$ , **e**, **f** 100 nm.

In summary, correlative imaging strategies using SEM and TEM were studied. We studied these two routes with Invitrogen CdSe QDs, but haven't moved to the Ge QDs and cell samples due to the lack of experimental conditions.

# Appendix F

## BSA codes

As has been described in section 3.2.5.2, the flame work of BSA consists of three main processing parts: (i) data segmentation to find the regions of interest (ROI) that might contain any QDs; (ii) ICA analysis on the ROIs. In this step, ICA analysis are iterated from 0 to the maximum possible number of QDs. For each analysis, the frequency of the blinking events of all QDs are plotted and compared to the standard QDs blinking distribution, in our case, an inverse power law with index of  $-1.6$  is applied to Ge QDs data. (iii) The number of QDs is determined when its ICA process gives the minimum value of average distance to the standard blinking distribution function. Then maximum likelihood estimation of Gassiuian fitting is performed to find the centre point of each QD. Finally, reconstruction is completed by redraw all localisations on a new image. The scripts were written using MATLAB2014, contributed by Dr. Yun Zhou and Mr. Yongxin Yang in School of Electronic Engineering and Computer Science, Queen Mary University of London.

### Module 1. Initialise parameters

---

```
XTIF      = readTIF('raw data file name');
Xtmp      = XTIF{1,1};
Xsum      = zeros(size(Xtmp,1),size(Xtmp,2));
for f = 1:size(XTIF,1)
    Xsum   = Xsum + XTIF{f,1};
end
```



## Appendix F. *BSA codes*

---

```
Xaverage = Xsum/size(XTIF,1);
figure;
subplot(1,2,1)
colormap gray;
imagesc(Xaverage);
title('Pics Average')
subplot(1,2,2)
colormap gray;
imagesc(Xtmp);
title('First Pic')
maxPeaks = 1;
z = cell(1,maxPeaks);
threshold = 3;
singleQDbrightness = [];
totalQDbrightness = [];
```

---

### Module 2. Segmentation to find the ROIs (ceiling points)

---

```
for t = 1:maxPeaks
[M,N] = size(Xaverage);
iX = ones(M,N);
iX2 = zeros(M,N);
whilebreak = 0;
while sum(sum(iX2)) < t
[~,ind] = max(Xaverage(:));
[m,n] = ind2sub(size(Xaverage),ind);
iX2(m,n) = 1;
iXgmm = ones(M,N);
for ii = 1:M
for j = 1:N
if pdist([ii,j;m,n]) < threshold
iX(ii,j) = 0;
iXgmm(ii,j) = 0;
end
end
end
sData = Xaverage.*(ones(M,N)-iXgmm);
totalQDbrightness = sum(sum(sData));
[z$_t$,DIM,rows,cols] = data$_{preprocess}$(sData,XTIF);
%DIM: MVG dimension
%ICs: number of independent components (IC) to decompose into
Xaverage = Xaverage.$\times$iX;
%Last line is used to avoid the exception that the image is fully selected
if sum(sum(Xaverage))==0
break;
```

## Appendix F. BSA codes

---

```
whilebreak = 1;
end
end % End while
if (sum(sData(:))/25) < 10* min(XTIF{1,1}(:))
break;
end
end % End for each peak
```

---

### Module 3. Iterative search to find the best ICA analysis

---

```
ratio = 1.2;
low = fix(totalQDbrightness/(singleQDbrightness*ratio)); % - ratio scale
high = fix((ratio*totalQDbrightness)/singleQDbrightness); % + ratio scale
dhigh = zeros(1,(high-low)+1);
tstart = clock;
for i = 1:(high-low)+1
[~,~,~,~,dhigh(i)] = performICA(cell2mat(z),i+(low-1),XTIF);
sprintf('The current ICs is: %d, the average K-L divergence is: %0.3f',
i+(low-1), dhigh(i))
end
tend = clock;
total = etime(tend,tstart);
plot(low:high,dhigh)
[value, sICs] = min(dhigh);
sprintf('The selected ICs is: %d, with smallest average K-L divergence is:
%0.3f', sICs+(low-1), value)
sprintf('The running time is: %0.3f s', total)
```

---

### Module 4. Reconstruction of all localisations from previously obtained ICAs results.

---

```
[z$_{ic}$, A, T, mean$_z$, aveDis] = performICA(cell2mat(z),sICs+(low-1),XTIF);
afterIC = A'*z$_{ic}$*z$_{ic}$'; %25X64
allfoundICs = zeros((sICs+(low-1)),2);
allfoundOrigin = zeros((sICs+(low-1)),2);
for i = 1:size(afterIC,2)
tmpcol = afterIC(:,i);
tmp = tmpcol - min(tmpcol);
tmp = reshape(tmp,[5 5]);
% From now, it is Gaussian fitting (Maximum Likelihood Estimation)
gData = tmp;
M = 5;
N = 5;
A = repmat(1:N, [M 1]);
B = repmat((1:M)', [1 N]);
```

## Appendix F. *BSA codes*

---

```
C      = [B(:) A(:)];
b      = ceil(gData(:)');
a      = 1:length(b);
c      = rude(b,a);
gData2 = C(c,:);
options= statset('Display','iter','MaxIter',1000);
gm     =
fitgmdist(gData2,1,'Options',options,'CovType','diagonal','Regularize',0.01);
allfoundICs(i,:) = gm.mu;
allfoundOrigin(i,:) = gm.mu + [(m-2) (n-2)];
end
figure;
subplot(1,2,1)
colormap gray;
imagesc(Xaverage((m-2):(m+2),(n-2):(n+2)));
subplot(1,2,2)
for i = 1:size(afterIC,2)
h = scatter(allfoundICs(i,1),allfoundICs(i,2),10,'MarkerEdgeColor','k',...
'MarkerFaceColor','k',...
'LineWidth',0.5);
hold on
end
```

---

# Appendix G

## SSA codes

The SSA was build up on a standard MATLAB Gaussian Mixed Model (GMM) with a Graphical User Interface (GUI) frame work (Figure [G.1](#)). The SSA starts with a de-noise processing to the raw image data. Then, segmentation is applied to pick up the ROIs. ROIs are then fitted by mixed Gaussian functions, in which the maximum likelihood estimation are used. Localisations are registered when the maximum likelihood estimation has been completed. The scripts were written using MATLAB2014, contributed by Dr. Yun Zhou and Mr. Yongxin Yang in School of Electronic Engineering and Computer Science, Queen Mary University of London.

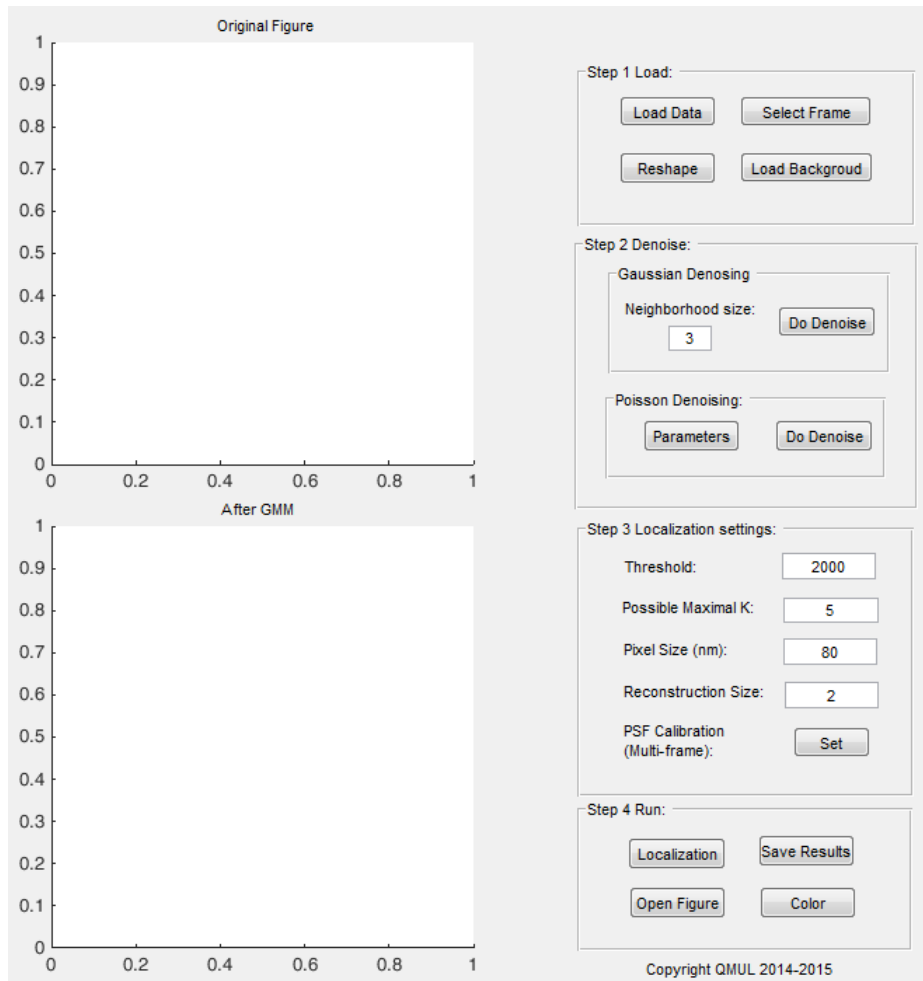


Figure G.1: GUI of SSA algorithm

Module 1. GMM-GUI frame for the data processing

```
function varargout = gmm_gui(varargin)
% This is a standard GMM_GUI MATLAB code for gmm_gui.fig
% GMM_GUI, by itself, creates a new GMM_GUI or raises the existing
% singleton*.%
% H = GMM_GUI returns the handle to a new GMM_GUI or the handle to
% the existing singleton*.%
% GMM_GUI('CALLBACK',hObject,eventData,handles,...) calls the local
% function named CALLBACK in GMM_GUI.M with the given input arguments.%
% GMM_GUI('Property','Value',...) creates a new GMM_GUI or raises the
% existing singleton*. Starting from the left, property value pairs are
% applied to the GUI before gmm_gui_OpeningFcn gets called. An
% unrecognized property name or invalid value makes property application
% stop. All inputs are passed to gmm_gui_OpeningFcn via varargin.%
% *See GUI Options on GUIDE's Tools menu. Choose "GUI allows only one
```

## Appendix G. *SSA codes*

---

```
%      instance to run (singleton)".
%% See also: GUIDE, GUIDATA, GUIHANDLES
% Edit the above text to modify the response to help gmm_gui
```

---

Initialization of the GUI codes, normally this doesn't need to be changed.

---

```
gui_Singleton = 1;
gui_State = struct('gui_Name',       mfilename, ...
                  'gui_Singleton',   gui_Singleton, ...
                  'gui_OpeningFcn',  @gmm_gui_OpeningFcn, ...
                  'gui_OutputFcn',  @gmm_gui_OutputFcn, ...
                  'gui_LayoutFcn',   [], ...
                  'gui_Callback',    []);
if nargin && ischar(varargin{1})
    gui_State.gui_Callback = str2func(varargin{1});
end
if nargout
    [varargout{1:nargout}] = gui_mainfcn(gui_State, varargin{:});
else
    gui_mainfcn(gui_State, varargin{:});
end
% --- Executes just before gmm_gui is made visible.
function gmm_gui_OpeningFcn(hObject, eventdata, handles, varargin)
% This function has no output args, see OutputFcn.
% hObject    handle to figure
% eventdata  reserved - to be defined in a future version of MATLAB
% handles    structure with handles and user data (see GUIDATA)
% varargin   command line arguments to gmm_gui (see VARARGIN)
```

---

Module 2. GUI for users to input default values, including raw image pixel size, possible maximum number of QDs within a ROI or an image, localisation points size.

---

```
handles.threshold = 2000; % The threshold of non-noise signal
% handles.k       = 5;
handles.output    = hObject;
handles.gdm       = 3;
handles.gdn       = 3;
handles.iter      = 0;
handles.iterdata  = cell(0);
\begin{lstlisting}
handles.k        = str2num(get(handles.edit_k,'String')); %Possible maximal QDs
handles.pSize    = str2num(get(handles.edit8,'String'));  %Output localisation point size
handles.dpSize   = str2num(get(handles.edit7,'String'));  %Raw image pixel size
handles.center=  [];                                     %Center points saved
```

## Appendix G. *SSA codes*

---

```
% Update handles structure
guidata(hObject, handles);
```

---

During the users inputting the initialize parameters, the GUI is made to a state waiting for users' responds. Return the initialized parameters to the command line in the main command window.

---

```
% UIWAIT makes gmm_gui wait for user response (see UIRESUME)
% uiwait(handles.figure1);
setappdata(0, 'hMainGui', gcf);
setappdata(gcf, 'xleft', 1); %the left of x axes range
setappdata(gcf, 'xright', 50); %the right of x axes range
setappdata(gcf, 'ybot', 1); %the bottom of y axes range
setappdata(gcf, 'ytop', 50); %the top of y axes range
setappdata(gcf, 'fhUpdateAxes', @updateAxes1);
setappdata(gcf, 'fhUpdateframe', @updateAxesfromFrame);
setappdata(gcf, 'hMainAxes1', handles.axes1);
setappdata(gcf, 'hMainAxes2', handles.axes2);
setappdata(gcf, 'color', 'k');
% --- Outputs from this function are returned to the command line.
function varargout = gmm_gui_OutputFcn(hObject, eventdata, handles)
% varargout cell array for returning output args (see VARARGOUT);
% hObject handle to figure
% eventdata reserved - to be defined in a future version of MATLAB
% handles structure with handles and user data (see GUIDATA)

% Get default command line output from handles structure
varargout{1} = handles.output;
```

---

Module 3. Load data by pressing the 'Load data' bottom in the GUI. This module is made to allow users to browse local files and load it into the algorithm. Also, it allows users to assign any specific area of the image to be processed. For example, an  $10 \times 10$  pixels area at point (3, 4) will segment the small area of coordinates (3, 4) as a separate image for further processing.

---

```
% --- Executes on button press in pushbutton_load_data.
function pushbutton_load_data_Callback(hObject, eventdata, handles)
% hObject handle to pushbutton_load_data (see GCBO)
% eventdata reserved - to be defined in a future version of MATLAB
% handles structure with handles and user data (see GUIDATA)
[filename] = uigetfile({'*.tif'}, 'File Selector');
```

## Appendix G. SSA codes

---

```
hMainGui = getappdata(0, 'hMainGui');
XTIF     = readTIF(filename);
X        = XTIF{1,1};

setappdata(hMainGui, 'maxFrame'    ,size(XTIF,1));
setappdata(hMainGui, 'currFrame'   ,1);
setappdata(hMainGui, 'xleft'       ,1);           %the left of x axes range
setappdata(hMainGui, 'xright'      ,size(X,1));  %the right of x axes range
setappdata(hMainGui, 'ybot'        ,1);           %the bottom of y axes range
setappdata(hMainGui, 'ytop'        ,size(X,2));  %the top of y axes range
setappdata(hMainGui, 'originalData',XTIF);
setappdata(hMainGui, 'fileName'    ,filename);
setappdata(hMainGui, 'plotData'    ,X);
setappdata(hMainGui, 'reshape'     ,0);
setappdata(hMainGui, 'pixelSizes'  ,handles.dpSize);
updateAxes1

function updateAxes1
hMainGui = getappdata(0, 'hMainGui');
sX       = getappdata(hMainGui, 'plotData');
hAxes    = getappdata(hMainGui, 'hMainAxes1');

axes(hAxes);
colormap gray;
imagesc(sX);

function updateAxesfromFrame
hMainGui = getappdata(0, 'hMainGui');
currFrame = getappdata(hMainGui, 'currFrame');
XTIF      = getappdata(hMainGui, 'originalData');
xl        = getappdata(hMainGui, 'xleft');
xr        = getappdata(hMainGui, 'xright');
yb        = getappdata(hMainGui, 'ybot');
yt        = getappdata(hMainGui, 'ytop');
hAxes     = getappdata(hMainGui, 'hMainAxes1');

X = XTIF{currFrame,1};
sX = X(xl:xr,yb:yt);
axes(hAxes);
colormap gray;
imagesc(sX);

function updateAxesduringRun
hMainGui = getappdata(0, 'hMainGui');
currFrame = getappdata(hMainGui, 'currFrame');
```



## Appendix G. SSA codes

---

```
XTIFt      = getappdata(hMainGui, 'taylorfullData');
XTIFo      = getappdata(hMainGui, 'originalData');
hAxes      = getappdata(hMainGui, 'hMainAxes1');
reshape    = getappdata(hMainGui, 'reshape');

if reshape == 1
    XTIF = XTIFt;
else
    XTIF = XTIFo;
end

X = XTIF{currFrame,1};
axes(hAxes);
colormap gray;
imagesc(X);

function plotLearnedCenter(handles)
hMainGui = getappdata(0, 'hMainGui');
xl       = getappdata(hMainGui, 'xleft');
xr       = getappdata(hMainGui, 'xright');
yb       = getappdata(hMainGui, 'ybot');
yt       = getappdata(hMainGui, 'ytop');
hAxes    = getappdata(hMainGui, 'hMainAxes2');
color    = getappdata(hMainGui, 'color');
axes(hAxes);
cla(hAxes);
center   = handles.center;
for o = 1:size(center,2)
    h = scatter(center(2,o),center(1,o),'MarkerEdgeColor',color,...
                'MarkerFaceColor',color,...
                'LineWidth',0.5);
    hChildren = get(h, 'Children');
    set(hChildren, 'Markersize', handles.pSize)
    hold on
    axis([xl xr yb yt]);
    set(gca,'YDir','reverse');
end
```

---

Module 4. Allow the algorithm to perform Mixed Gaussian Model fitting to the data when user press the 'Do GMM' bottom.

---

```
% --- Executes on button press in pushbutton_do_gmm.
function pushbutton_do_gmm_Callback(hObject, eventdata, handles)
% hObject    handle to pushbutton_do_gmm (see GCBO)
```

## Appendix G. *SSA codes*

---

```
% eventdata reserved - to be defined in a future version of MATLAB
% handles structure with handles and user data (see GUIDATA)
rng(0)
K = handles.k;
options = statset('Display','iter','MaxIter',1000);

hMainGui = getappdata(0, 'hMainGui');
taylData = getappdata(hMainGui, 'tayloredfullData');
origData = getappdata(hMainGui, 'originalData');
xl = getappdata(hMainGui, 'xleft');
xr = getappdata(hMainGui, 'xright');
yb = getappdata(hMainGui, 'ybot');
yt = getappdata(hMainGui, 'ytop');
hAxes = getappdata(hMainGui, 'hMainAxes2');
res = getappdata(hMainGui, 'reshape');

if res == 1
    sXfull = taylData;
else
    sXfull = origData;
end

gmfull = cell(size(sXfull,1),1);
for i = 1:size(sXfull,1)
    updateAxesduringRun;
    if i < size(sXfull,1)
        currFrame = i + 1;
        setappdata(hMainGui, 'currFrame', currFrame);
    end
    sX = sXfull{i,1};
    [M,N] = size(sX);
    maxPeaks = K;
    threshold = handles.dpSize/(2*11.4);
    sigma = 1;
    axes(hAxes);
    cla(hAxes);
    likelihood = zeros(1,maxPeaks);
    A = repmat(1:N, [M 1]);
    B = repmat((1:M)', [1 N]);
    C = [B(:) A(:)];
    b = sX(:)';
    a = 1:length(b);
    c = rude(b,a);
    Datalikeli = C(c,:);
    allmodel = cell(1,maxPeaks);
```

## Appendix G. *SSA codes*

---

```
for t = 1:maxPeaks
    model.mu      = zeros(2,t);
    model.sigma   = zeros(2,2,t);
    model.weight  = zeros(1,t);
```

---

Module 5. De-noise to the raw image and do segmentation. This code is executed after the user pressing ‘Do GMM’. The de-noise parameters are changeable according to user’s data.

---

```
kernelSize = [2,2]; % This is changeable according to your own data.
For example, [1,1] will lead to non-smooth, i.e., no filter applies
X           = imfilter(sX,fspecial('gaussian',kernelSize,sigma),'replicate');
iX          = ones(M,N);
iX2         = zeros(M,N);
whilebreak = 0;
while sum(sum(iX2)) < t
    [~,ind] = max(X(:));
    [m,n] = ind2sub(size(X),ind);
    iX2(m,n) = 1;
    iXgmm    = ones(M,N);

% Segmentation
for ii = 1:M
    for j = 1:N
        if pdist([ii,j;m,n]) < threshold
            iX(ii,j) = 0;
            iXgmm(ii,j) = 0;
        end
    end
end
end
```

---

Module 6. Following the de-noise process, Gaussian fitting is applied to the ROIs using the Maximum Likelihood Estimation. Output localisations are plotted in a new image.

---

```
gData = sX.*(ones(M,N)-iXgmm);
A      = repmat(1:N, [M 1]);
B      = repmat((1:M)', [1 N]);
C      = [B(:) A(:)];
b      = gData(:)';
a      = 1:length(b);
c      = rude(b,a);
```

## Appendix G. SSA codes

---

```
gData2 = C(c,:);
gm = fitgmdist(gData2,1,'Options',options,'CovType','diagonal','Regularize',0.01);

index          = sum(sum(iX2));
model.mu(1,index) = gm.mu(1,1);
  model.mu(2,index) = gm.mu(1,2);
tmp            = zeros(2,2);
tmp(1,1)      = gm.Sigma(1);
tmp(2,2)      = gm.Sigma(2);
model.sigma(:,:,index) = tmp;
model.weight(index) = sum(gData(:));
X = X.*iX;
% To avoid situation that the image is fully selected during segmentation.
The following codes are used.
if sum(sum(X))==0
  break;
whilebreak = 1;
  end
end % End while
  if whilebreak == 1
    likelihood(t) = -Inf;
  else
    model.weight = model.weight/sum(model.weight);
    [R, likelihood(t)] = Estep(Datalikeli', model);
  end
  allmodel{1,t} = model;
end % End for each K
likelihood = likelihood - 0.5*[1:maxPeaks];
[maxLikeli, mIndex] = max(likelihood);
bestmodel          = allmodel{1,mIndex}
save('results.mat','bestmodel');
%Output
maxLikeli
center = bestmodel.mu;
handles.center = center; %save center information for re-plot usage.
for o = 1:size(center,2)
  h = scatter(center(2,o),center(1,o),'MarkerEdgeColor','k',...
    'MarkerFaceColor','k',...
    'LineWidth',0.5);
  hChildren = get(h, 'Children');
  set(hChildren, 'Markersize', handles.pSize)
  hold on
  axis([xl xr yb yt]);
  set(gca,'YDir','reverse');
end
```

## Appendix G. *SSA codes*

---

```
%legend(['GMMEst points, log-likelihood: ', sprintf('%10.2f',maxLikeli)], ...
%'Location','Best');
end
setappdata(hMainGui, 'gmmResults', gmfull);
saveFig = figure;
copyobj(hAxes, saveFig);
set(gca,'xtick',[])
set(gca,'xticklabel',[])
set(gca,'ytick',[])
set(gca,'yticklabel',[])
set(gca,'LooseInset',get(gca,'TightInset'))
box on
hgsave(saveFig, 'outputFigure.fig');
close(saveFig);
guidata(hObject, handles);
uiwait(msgbox('Localisation Finished','Success','modal'));
```

---

\* Modules for the use of functional bottoms in the GUI.

---

```
function edit_threshold_Callback(hObject, eventdata, handles)
% hObject    handle to edit_threshold (see GCBO)
% eventdata  reserved - to be defined in a future version of MATLAB
% handles    structure with handles and user data (see GUIDATA)
handles.threshold = str2double(get(hObject,'String'));
guidata(hObject, handles);
% Hints: get(hObject,'String') returns contents of edit_threshold as text
% str2double(get(hObject,'String')) returns contents of edit_threshold as a double

% --- Executes during object creation, after setting all parameters.
function edit_threshold_CreateFcn(hObject, eventdata, handles)
% hObject    handle to edit_threshold (see GCBO)
% eventdata  reserved - to be defined in a future version of MATLAB
% handles    empty - handles not created until after all CreateFcns called
% Hint: edit controls usually have a white background on Windows.
if ispc && isequal(get(hObject,'BackgroundColor'),
    get(0,'defaultUicontrolBackgroundColor'))
    set(hObject,'BackgroundColor','white');
end

% --- Executes on button press in pushbutton_save_results.
function pushbutton_save_results_Callback(hObject, eventdata, handles)
% hObject    handle to pushbutton_save_results (see GCBO)
% eventdata  reserved - to be defined in a future version of MATLAB
% handles    structure with handles and user data (see GUIDATA)
hMainGui = getappdata(0, 'hMainGui');
```

## Appendix G. *SSA codes*

---

```
pX          = getappdata(hMainGui, 'plotData');
gmfull     = getappdata(hMainGui, 'gmmResults');
save('results.mat','pX');
save('results.mat','gmfull');

% --- Executes on button press in pushbutton_open_figure.
function pushbutton_open_figure_Callback(hObject, eventdata, handles)
% hObject    handle to pushbutton_open_figure (see GCBO)
% eventdata  reserved - to be defined in a future version of MATLAB
% handles    structure with handles and user data (see GUIDATA)
openfig('outputFigure.fig');

function edit_x_Callback(hObject, eventdata, handles)
% hObject    handle to edit_x (see GCBO)
% eventdata  reserved - to be defined in a future version of MATLAB
% handles    structure with handles and user data (see GUIDATA)
handles.x = str2double(get(hObject,'String'));
guidata(hObject, handles);
% Hints: get(hObject,'String') returns contents of edit_x as text
%        str2double(get(hObject,'String')) returns contents of edit_x as a double

% --- Executes during object creation, after setting all properties.
function edit_x_CreateFcn(hObject, eventdata, handles)
% hObject    handle to edit_x (see GCBO)
% eventdata  reserved - to be defined in a future version of MATLAB
% handles    empty - handles not created until after all CreateFcns called

% Hint: edit controls usually have a white background on Windows.
%       See ISPC and COMPUTER.
if ispc && isequal(get(hObject,'BackgroundColor'),
    get(0,'defaultUicontrolBackgroundColor'))
    set(hObject,'BackgroundColor','white');
end

function edit_y_Callback(hObject, eventdata, handles)
% hObject    handle to edit_y (see GCBO)
% eventdata  reserved - to be defined in a future version of MATLAB
% handles    structure with handles and user data (see GUIDATA)
handles.y = str2double(get(hObject,'String'));
guidata(hObject, handles);
% Hints: get(hObject,'String') returns contents of edit_y as text
%        str2double(get(hObject,'String')) returns contents of edit_y as a double

% --- Executes during object creation, after setting all paramters.
function edit_y_CreateFcn(hObject, eventdata, handles)
```

## Appendix G. *SSA codes*

---

```
% hObject    handle to edit_y (see GCBO)
% eventdata  reserved - to be defined in a future version of MATLAB
% handles    empty - handles not created until after all CreateFcns called

% Hint: edit controls usually have a white background on Windows.
%         See ISPC and COMPUTER.
if ispc && isequal(get(hObject,'BackgroundColor'),
    get(0,'defaultUicontrolBackgroundColor'))
    set(hObject,'BackgroundColor','white');
end

function edit_k_Callback(hObject, eventdata, handles)
% hObject    handle to edit_k (see GCBO)
% eventdata  reserved - to be defined in a future version of MATLAB
% handles    structure with handles and user data (see GUIDATA)
handles.k = str2double(get(hObject,'String'));
guidata(hObject, handles);
% Hints: get(hObject,'String') returns contents of edit_k as text
%         str2double(get(hObject,'String')) returns contents of edit_k as a double

% --- Executes during object creation, after setting all parameters.
function edit_k_CreateFcn(hObject, eventdata, handles)
% hObject    handle to edit_k (see GCBO)
% eventdata  reserved - to be defined in a future version of MATLAB
% handles    empty - handles not created until after all CreateFcns called

% Hint: edit controls usually have a white background on Windows.
%         See ISPC and COMPUTER.
if ispc && isequal(get(hObject,'BackgroundColor'),
    get(0,'defaultUicontrolBackgroundColor'))
    set(hObject,'BackgroundColor','white');
end

% --- Executes on button press in pushbutton_options.
function pushbutton_options_Callback(hObject, eventdata, handles)
% hObject    handle to pushbutton_options (see GCBO)
% eventdata  reserved - to be defined in a future version of MATLAB
% handles    structure with handles and user data (see GUIDATA)
% SupResPosits = evalin('base','SupResPosits');
% SupResParams = evalin('base','SupResParams');
% myFrame = evalin('base','myFrame');

%Run the Reviewer m-file.
axes_setting;
```

## Appendix G. *SSA codes*

---

```
function edit_gaussian_n_Callback(hObject, eventdata, handles)
% hObject    handle to edit_gaussian_n (see GCBO)
% eventdata  reserved - to be defined in a future version of MATLAB
% handles    structure with handles and user data (see GUIDATA)

% Hints: get(hObject,'String') returns contents of edit_gaussian_n as text
%        str2double(get(hObject,'String')) returns contents of edit_gaussian_n as a double
handles.gdn = str2double(get(hObject,'String'));
handles.gdm = handles.gdn
guidata(hObject, handles);

% --- Executes during object creation, after setting all parameters.
function edit_gaussian_n_CreateFcn(hObject, eventdata, handles)
% hObject    handle to edit_gaussian_n (see GCBO)
% eventdata  reserved - to be defined in a future version of MATLAB
% handles    empty - handles not created until after all CreateFcns called

% Hint: edit controls usually have a white background on Windows.
%       See ISPC and COMPUTER.
if ispc && isequal(get(hObject,'BackgroundColor'),
    get(0,'defaultUiControlBackgroundColor'))
    set(hObject,'BackgroundColor','white');
end

% --- Executes on button press in pushbutton_do_gaussian_denosie.
function pushbutton_do_gaussian_denosie_Callback(hObject, eventdata, handles)
hMainGui = getappdata(0, 'hMainGui');
taylData = getappdata(hMainGui, 'tayloredfullData');
origData = getappdata(hMainGui, 'originalData');
currFrame = getappdata(hMainGui, 'currFrame');
reshape = getappdata(hMainGui, 'reshape');

if reshape == 1
    testdata = taylData;
else
    testdata = origData;
end

gdData = cell(size(testdata,1),1);
for i = 1:size(testdata,1)
    tmp = testdata{i,1};
    gdData{i,1} = wiener2(tmp,[handles.gdm handles.gdn]);
end

pData = gdData{currFrame,1};
```



## Appendix G. SSA codes

---

```
%update the original data with the gaussian denoised one
setappdata(hMainGui, 'tayloredfullData', gdData);
setappdata(hMainGui, 'plotData'          , pData);
updateAxes1;
uiwait(msgbox('Denosie Completed','Success','modal'));

% hObject    handle to pushbutton_do_gaussian_denosie (see GCBO)
% eventdata  reserved - to be defined in a future version of MATLAB
% handles    structure with handles and user data (see GUIDATA)

% --- Executes on button press in pushbutton_do_poisson_denoise.
function pushbutton_do_poisson_denoise_Callback(hObject, eventdata, handles)
% hObject    handle to pushbutton_do_poisson_denoise (see GCBO)
% eventdata  reserved - to be defined in a future version of MATLAB
% handles    structure with handles and user data (see GUIDATA)
hMainGui = getappdata(0          , 'hMainGui');
taylData = getappdata(hMainGui, 'tayloredfullData');
currFrame = getappdata(hMainGui , 'currFrame');
mx        = getappdata(hMainGui, 'mx');
mn        = getappdata(hMainGui, 'mn');
J         = getappdata(hMainGui, 'J');
let_id    = getappdata(hMainGui, 'let_id');
nSpin     = getappdata(hMainGui, 'nSpin');

pdData    = cell(size(taylData,1),1);
for i = 1:size(taylData,1)
    [z,im] = poisson_count(taylData{i,1}, mn, mx );
    try
        pdData{i,1} = cspin_purelet(z, let_id,J,nSpin);
        break;
    catch err
        msgbox('The cropped figure is too small! Poisson denoise failed!');
        break;
    end
end

pData     = pdData{currFrame,1};
%update the original data with the gaussian denoised one
setappdata(hMainGui, 'tayloredfullData', pData);
setappdata(hMainGui, 'plotData'          , pData);
updateAxes1;
uiwait(msgbox('Denosie Completed','Success','modal'));

% --- Executes on button press in pushbutton_poisson_para.
function pushbutton_poisson_para_Callback(hObject, eventdata, handles)
```

## Appendix G. *SSA codes*

---

```
% hObject    handle to pushbutton_poisson_para (see GCBO)
% eventdata  reserved - to be defined in a future version of MATLAB
% handles    structure with handles and user data (see GUIDATA)
poisson_setting;

% --- Executes on button press in pushbutton_select_frame.
function pushbutton_select_frame_Callback(hObject, eventdata, handles)
% hObject    handle to pushbutton_select_frame (see GCBO)
% eventdata  reserved - to be defined in a future version of MATLAB
% handles    structure with handles and user data (see GUIDATA)
select_frame;

% --- Executes on button press in pushbutton12.
function pushbutton12_Callback(hObject, eventdata, handles)
% hObject    handle to pushbutton12 (see GCBO)
% eventdata  reserved - to be defined in a future version of MATLAB
% handles    structure with handles and user data (see GUIDATA)
hMainGui = getappdata(0, 'hMainGui');
color    = getappdata(hMainGui, 'color');
if isequal(color,'k')
    color = 'r';
else
    color = 'k';
end
setappdata(hMainGui, 'color', color);
plotLearnedCenter(handles)

function edit7_Callback(hObject, eventdata, handles)
% hObject    handle to edit7 (see GCBO)
% eventdata  reserved - to be defined in a future version of MATLAB
% handles    structure with handles and user data (see GUIDATA)
handles.dpSize = str2double(get(hObject,'String'));
guidata(hObject, handles);
% Hints: get(hObject,'String') returns contents of edit7 as text
%       str2double(get(hObject,'String')) returns contents of edit7 as a double

% --- Executes during object creation, after setting all properties.
function edit7_CreateFcn(hObject, eventdata, handles)
% hObject    handle to edit7 (see GCBO)
% eventdata  reserved - to be defined in a future version of MATLAB
% handles    empty - handles not created until after all CreateFcns called

% Hint: edit controls usually have a white background on Windows.
%       See ISPC and COMPUTER.
if ispc && isequal(get(hObject,'BackgroundColor'),
```

## Appendix G. *SSA codes*

---

```
    get(0,'defaultUicontrolBackgroundColor'))
    set(hObject,'BackgroundColor','white');
end

function edit_iter_Callback(hObject, eventdata, handles)
% hObject    handle to edit_iter (see GCBO)
% eventdata  reserved - to be defined in a future version of MATLAB
% handles    structure with handles and user data (see GUIDATA)

% Hints: get(hObject,'String') returns contents of edit_iter as text
%        str2double(get(hObject,'String')) returns contents of edit_iter as a double

% --- Executes during object creation, after setting all properties.
function edit_iter_CreateFcn(hObject, eventdata, handles)
% hObject    handle to edit_iter (see GCBO)
% eventdata  reserved - to be defined in a future version of MATLAB
% handles    empty - handles not created until after all CreateFcns called

% Hint: edit controls usually have a white background on Windows.
%       See ISPC and COMPUTER.
if ispc && isequal(get(hObject,'BackgroundColor'),
    get(0,'defaultUicontrolBackgroundColor'))
    set(hObject,'BackgroundColor','white');
end

% --- Executes on button press in pushbutton_load_background.
function pushbutton_load_background_Callback(hObject, eventdata, handles)
% hObject    handle to pushbutton_load_background (see GCBO)
% eventdata  reserved - to be defined in a future version of MATLAB
% handles    structure with handles and user data (see GUIDATA)
[filename] = uigetfile({'*.tif'},'File Selector');
XTIF      = readTIF(filename);
background = XTIF{1,1};
handles.threshold = mean(background(:));
set(handles.edit_threshold,'String',mat2str(handles.threshold,2))
guidata(hObject, handles);

function edit8_Callback(hObject, eventdata, handles)
% hObject    handle to edit8 (see GCBO)
% eventdata  reserved - to be defined in a future version of MATLAB
% handles    structure with handles and user data (see GUIDATA)
handles.pSize = str2double(get(hObject,'String'));
if isempty(handles.center)
    % do nothing
else
```

```
        plotLearnedCenter(handles);
end
guidata(hObject, handles);
% Hints: get(hObject,'String') returns contents of edit8 as text
%        str2double(get(hObject,'String')) returns contents of edit8 as a double

% --- Executes during object creation, after setting all parameters.
function edit8_CreateFcn(hObject, eventdata, handles)
% hObject    handle to edit8 (see GCBO)
% eventdata  reserved - to be defined in a future version of MATLAB
% handles    empty - handles not created until after all CreateFcns called

% Hint: edit controls usually have a white background on Windows.
%        See ISPC and COMPUTER.
if ispc && isequal(get(hObject,'BackgroundColor'),
    get(0,'defaultUicontrolBackgroundColor'))
    set(hObject,'BackgroundColor','white');
end

% --- Executes on button press in pushbutton_set.
function pushbutton_set_Callback(hObject, eventdata, handles)
% hObject    handle to pushbutton_set (see GCBO)
% eventdata  reserved - to be defined in a future version of MATLAB
% handles    structure with handles and user data (see GUIDATA)
set_pixel_sizes;
```

---

# Bibliography

- [1] J. Pawley. *Handbook of biological confocal microscopy*. Number v. 236 in Handbook of biological confocal microscopy. Springer, 2006.
- [2] D. Whitehouse. *Renaissance genius: Galileo Galilei & his legacy to modern science*. Sterling, 2009.
- [3] Barry R Masters. History of the optical microscope in cell biology and medicine. In *eLS*. 2008.
- [4] C. Dobell and A. van Leeuwenhoek. *Antony Van Leeuwenhoek and His "Little Animals": Being Some Account of the Father of Protozoology and Bacteriology and His Multifarious Discoveries in These Disciplines; Collected, Translated, and Edited, from His Printed Works, Unpublished Manuscripts, and Contemporary Records*. Brace, 1932.
- [5] History of-the microscope.org. The curious observer. events of the first half of van leeuwenhoek's life. <http://lensonleeuwenhoek.net/>, 2009. [Online; accessed 20-April-2015].
- [6] Christoph Cremer and Barry R. Masters. Resolution enhancement techniques in microscopy. *The European Physical Journal H*, 38:281–344, 2013.
- [7] Nikon Corporation. Instruments products. <http://www.nikon.com/products/instruments/lineup/bioscience/confocal/singlephoton/a1/a1r.htm>, 2015. [Online; accessed 04-May-2015].

- [8] AmScope Company. Professional infinity kohler binocular compound microscope. <http://www.amscope.com/40x-1500x-professional-infinity-kohler-binocular-compound-microscope.html>, 2014. [Online; accessed 04-May-2015].
- [9] Barry R. Masters. Ernst Abbe and the foundation of scientific microscopes, 2007.
- [10] Lord Rayleigh. On the theory of optical images, with special reference to the microscope. *Journal of the Royal Microscopical Society*, 23(4):447–473, 1903.
- [11] Carl Zeiss. Highlights from the history of immersion objectives Carl Zeiss, in memory of Ernst Abbe. *The magazine from Carl Zeiss: Innovation*, page 84, 2005.
- [12] Martin L. Scott. Innovations in light microscopy. <https://www.microscopyu.com/articles/general/innovations.html>, 2013. [Online; accessed 18-May-2015].
- [13] History of-the microscope.org. Hans and zacharias jansen: A complete microscope history. <http://www.history-of-the-microscope.org/hans-and-zacharias-jansen-microscope-history.php>, 2010. [Online; accessed 20-April-2015].
- [14] Nicole Howard. Robert Hooke: tercentennial studies, 2007.
- [15] Michael W. Davidson. Configuration a microscope for Kohler illumination. <http://zeiss-campus.magnet.fsu.edu/articles/basics/kohler.html>, 2015. [Online; accessed 30-April-2015].
- [16] Berkeley University of California. Optical paths for condensers yielding Critical and Köhler Illumination. <http://microscopy.berkeley.edu/courses/tlm/condenser/optics.html>, 2015. [Online; accessed 25-May-2015].

- [17] F Zernike. Diffraction theory of the knife-edge test and its improved form, the phase-contrast method. *Monthly Notices of the Royal Astronomical Society*, 1(2):87–94, 2002.
- [18] R D Allen, G B David, and G Nomarski. The zeiss-Nomarski differential interference equipment for transmitted-light microscopy. *Zeitschrift fur wissenschaftliche Mikroskopie und mikroskopische Technik*, 69:193–221, 1969.
- [19] G. G. Stokes. On the change of refrangibility of light. *Philosophical transactions of the Royal Society of London*, 142:463–562, January 1852.
- [20] John Condeelis and Ralph Weissleder. In vivo imaging in cancer. *Cold Spring Harbor perspectives in biology*, 2(12):a003848, December 2010.
- [21] Marvin Minsky. Memoir on inventing the confocal scanning microscope. *Scanning*, 10:128–138, 1988.
- [22] Sarah M Wilson and Antony Bacic. Preparation of plant cells for transmission electron microscopy to optimize immunogold labeling of carbohydrate and protein epitopes. *Nature Protocols*, 7:1716–1727, 2012.
- [23] Michael W. Davidson Rudi Rottenfusser, Erin E. Wilson. Enhancing contrast in optical microscopy. <http://zeiss-campus.magnet.fsu.edu/articles/basics/contrast.html>, 2015. [Online; accessed 10-April-2015].
- [24] W. Kecs. *The convolution product and some applications*. Mathematics and its applications (D. Reidel Publishing Company): East European series. Editura Academiei, 1982.
- [25] R N Bracewell. *The fourier transform and its applications*, volume 42. 1986.
- [26] J.W. Goodman. *Introduction to Fourier Optics*. McGraw-Hill physical and quantum electronics series. Roberts & Company, 2005.
- [27] Stephan Roth, Colin Jr Sheppard, Kai Wicker, and Rainer Heintzmann. Optical photon reassignment microscopy (OPRA). *Optical Nanoscopy*, 2:5, 2013.

- [28] E Abbe. Beiträge zur Theorie des Mikroskops und der mikroskopischen Wahrnehmung, 1873.
- [29] Abbe Ernst. On the theory of the microscope. *Proceedings of the Bristol Naturalists's Society*, 1:200–261, 1874.
- [30] J. W. Stephenson. Observations on professor abbe's experiments illustrating his theory of microscopic vision. *The Monthly Microscopical Journal*, 17(2):82–88, 1877.
- [31] B. Richards and E. Wolf. Electromagnetic diffraction in optical systems. II. structure of the image field in an aplanatic system, 1959.
- [32] S F Gibson and F Lanni. Experimental test of an analytical model of aberration in an oil-immersion objective lens used in three-dimensional light microscopy. *Journal of the optical society of America*, 9:154–166, 1992.
- [33] Raimund J Ober, Sripad Ram, and E Sally Ward. Localization accuracy in single-molecule microscopy. *Biophysical Journal*, 86:1185–1200, 2004.
- [34] Ulrich Kubitscheck. *Fluorescence microscopy: from principles to biological applications*. 2013.
- [35] Bonnie O Leung and Keng C Chou. Review of super-resolution fluorescence microscopy for biology. *Applied spectroscopy*, 65(9):967–80, October 2011.
- [36] François Aguet, Dimitri Van De Ville, and Michael Unser. An accurate PSF model with few parameters for axially shift-variant deconvolution. *2008 5th IEEE International Symposium on Biomedical Imaging: From Nano to Macro, Proceedings, ISBI*, pages 157–160, 2008.
- [37] H. Kirshner, F. Aguet, D. Sage, and M. Unser. 3-D PSF fitting for fluorescence microscopy: Implementation and localization application. *Journal of Microscopy*, 249(0):13–25, 2013.



- [38] Sjoerd Stallinga and Bernd Rieger. Accuracy of the gaussian point spread function model in 2D localization microscopy. *Optics express*, 18:24461–24476, 2010.
- [39] M M Freundlich. Origin of the electron microscope. *Science*, 142(3589):185–188, 1963.
- [40] W. Neumann. Electron microscopy – principles and fundamentals, 1999.
- [41] J.P. Heath. *Dictionary of microscopy*. Microscopy and analysis. John Wiley & Sons, 2005.
- [42] Stanley L. Flegler, John W. Heckman, and Karen L. Klomparens. *Scanning and transmission electron microscopy: an introduction*. W.H. Freeman and Company, New York, 1 edition, 1993.
- [43] E. H. Synge. A suggested method for extending microscopic resolution into the ultra-microscopic region. *Philosophical Magazine Series 7*, 6:356–362, 1928.
- [44] Schrader M and S W Hell. 4Pi confocal images with axial superresolution. *Journal of Microscopy*, 183(August):189–195, 1996.
- [45] M. G L Gustafsson, D. a. Agard, and J. W. Sedat. I5M: 3D widefield light microscopy with better than 100 nm axial resolution. *Journal of Microscopy*, 195(July):10–16, 1999.
- [46] J. Bewersdorf, R. Schmidt, and S. W. Hell. Comparison of I5M and 4Pi-microscopy. *Journal of Microscopy*, 222(December 2004):105–117, 2006.
- [47] S W Hell and J Wichmann. Breaking the diffraction resolution limit by stimulated emission: stimulated-emission-depletion fluorescence microscopy. *Optics Letters*, 19(11):780–782, June 1994.
- [48] Benjamin Harke, Jan Keller, Chaitanya K Ullal, Volker Westphal, Andreas Schönle, and Stefan W Hell. Resolution scaling in STED microscopy. *Optics Express*, 16(6):4154–4162, 2008.

- [49] U Valentin Nägerl and Tobias Bonhoeffer. Imaging living synapses at the nanoscale by STED microscopy. *The Journal of Neuroscience*, 30(28):9341–9346, 2010.
- [50] Super-resolution fluorescence microscopy. *Annual Review of Biochemistry*, 78:993–1016, January 2009.
- [51] M.G.L. Gustafsson, J.W. Sedat, and D.A. Agard. Method and apparatus for three-dimensional microscopy with enhanced resolution, November 11 1997. US Patent RE38,307.
- [52] M.A.A. Neil, R. Juškaitis, and T. Wilson. Real time 3D fluorescence microscopy by two beam interference illumination, 1998.
- [53] Lothar Schermelleh, Peter M Carlton, Sebastian Haase, Lin Shao, Lukman Winoto, Peter Kner, Brian Burke, M Cristina Cardoso, David a Agard, Mats G L Gustafsson, Heinrich Leonhardt, and John W Sedat. Subdiffraction multicolor imaging of the nuclear periphery with 3D structured illumination microscopy. *Science*, 320(June):1332–1336, 2008.
- [54] M G Gustafsson. Surpassing the lateral resolution limit by a factor of two using structured illumination microscopy. *Journal of Microscopy*, 198(January):82–87, 2000.
- [55] Mats G L Gustafsson. Nonlinear structured-illumination microscopy: wide-field fluorescence imaging with theoretically unlimited resolution. *Proceedings of the National Academy of Sciences of the United States of America*, 102(37):13081–13086, September 2005.
- [56] Sébastien Herbert, Helena Soares, Christophe Zimmer, and Ricardo Henriques. Single-molecule localization super-resolution microscopy: deeper and faster. *Microscopy and Microanalysis*, (July 2015):1–11, 2012.

- [57] Dylan M. Owen, Markus Sauer, and Katharina Gaus. Fluorescence localization microscopy: the transition from concept to biological research tool. *Communicative and Integrative Biology*, 5(08):345–349, 2012.
- [58] Michael J Rust, Mark Bates, and Xiaowei Zhuang. Sub-diffraction-limit imaging by stochastic optical reconstruction microscopy ( STORM ). *Nature Methods*, 3(10):793–795, 2006.
- [59] Eric Betzig, George H Patterson, Rachid Sougrat, O Wolf Lindwasser, Scott Olenych, Juan S Bonifacino, Michael W Davidson, Jennifer Lippincott-Schwartz, and Harald F Hess. Imaging intracellular fluorescent proteins at nanometer resolution. *Science*, 313(5793):1642–5, September 2006.
- [60] P. Lemmer, M. Gunkel, D. Baddeley, R. Kaufmann, a. Urich, Y. Weiland, J. Reymann, P. Müller, M. Hausmann, and C. Cremer. SPDM: light microscopy with single-molecule resolution at the nanoscale, September 2008.
- [61] Neveen a Hosny, Mingying Song, John T Connelly, Simon Ameer-Beg, Martin M Knight, and Ann P Wheeler. Super-resolution imaging strategies for cell biologists using a spinning disk microscope. *PloS one*, 8(10):e74604, January 2013.
- [62] Fedor V Subach, George H Patterson, Suliana Manley, Jennifer M Gillette, Jennifer Lippincott-Schwartz, and Vladislav V Verkhusha. Photoactivatable mCherry for high-resolution two-color fluorescence microscopy. *Nature Methods*, 6:153–159, 2009.
- [63] Marta Fernández-Suárez and Alice Y Ting. Fluorescent probes for super-resolution imaging in living cells. *Nature Reviews*, 9(12):929–43, December 2008.
- [64] W. E. Moerner and L Kador. Optical detection and spectroscopy of single molecules in a solid. *Phys. Rev. Lett*, 62:2535–2538, 1989.

- [65] M. Orrit and J. Bernard. Single pentacene molecules detected by fluorescence excitation in a *p*-terphenyl crystal. *Phys. Rev. Lett.*, 65:2716–2719, Nov 1990.
- [66] Eric Betzig, George H Patterson, Rachid Sougrat, O Wolf Lindwasser, Scott Olenych, Juan S Bonifacino, Michael W Davidson, Jennifer Lippincott-Schwartz, and Harald F Hess. Imaging intracellular fluorescent proteins at nanometer resolution. *Science*, 313(5793):1642–5, September 2006.
- [67] Samuel T Hess, Thanu P K Girirajan, and Michael D Mason. Ultra-high resolution imaging by fluorescence photoactivation localization microscopy. *Biophysical journal*, 91(11):4258–72, December 2006.
- [68] Alexa L Mattheyses, Sanford M Simon, and Joshua Z Rappoport. Imaging with total internal reflection fluorescence microscopy for the cell biologist. *Journal of cell science*, 123:3621–3628, 2010.
- [69] Alexa L Mattheyses, Sanford M Simon, and Joshua Z Rappoport. Imaging with total internal reflection fluorescence microscopy for the cell biologist. *Journal of cell science*, 123:3621–3628, 2010.
- [70] Marcel van 't Hoff, Vincent de Sars, and Martin Oheim. A programmable light engine for quantitative single molecule TIRF and HILO imaging. *Optics express*, 16:18495–18504, 2008.
- [71] Thomas F. Coleman and Zhang Yin. *Optimization toolbox user guide 2015*. The Mathworks Inc, Natick, MA, version 7. edition, 2015.
- [72] Raimund J Ober, Sripad Ram, and E Sally Ward. Localization accuracy in single-molecule microscopy. *Biophysical Journal*, 86(February):1185–1200, 2004.
- [73] Tingwei Quan, Shaoqun Zeng, and Zhen-Li Huang. Localization capability and limitation of electron-multiplying charge-coupled, scientific complementary metal-oxide semiconductor, and charge-coupled devices for superresolution imaging. *Journal of Biomedical Optics*, 15(December):066005, 2010.

- [74] A.D. Wyner and S. Shamai. Communication in the presence of noise. *Proceedings of the IEEE*, 86(2), 1998.
- [75] Hari Shroff, Catherine G Galbraith, James A Galbraith, and Eric Betzig. Live-cell photoactivated localization microscopy of nanoscale adhesion dynamics. *Nature Methods*, 5(5):417–423, 2008.
- [76] Bo Huang, Mark Bates, and Xiaowei Zhuang. Super resolution fluorescence microscopy. *Annual Review of Biochemistry*, 78:993–1016, 2010.
- [77] Xin X. Zhou and Michael Z. Lin. Photoswitchable fluorescent proteins: Ten years of colorful chemistry and exciting applications, 2013.
- [78] T. Vo-Dinh. *Biomedical Photonics Handbook, Second Edition: Therapeutics and Advanced Biophotonics*. Biomedical Photonics Handbook: Biomedical Diagnostics. Taylor & Francis, 2014.
- [79] Joseph R. Lakowicz. *Principles of fluorescence spectroscopy*. Baltimore, USA, third edit edition, 2006.
- [80] Brenno A D Neto, Pedro H P R Carvalho, Diego C B D Santos, Bruna C Guido, Claudia C Gatto, Heibbe C B De Oliveira, and Marcos N Eberlin. Selective and efficient mitochondrial staining with designed 2,1,3-benzothiadiazole derivatives as live cell fluorescence imaging probes. *Journal of the Brazilian Chemical Society*, 23(4):770–781, 2012.
- [81] Dimitris Ioannou and Darren K Griffin. Nanotechnology and molecular cytogenetics: the future has not yet arrived. *Nano Reviews*, 1:1–14, January 2010.
- [82] Harold P Erickson. Size and shape of protein molecules at the nanometer level determined by sedimentation, gel filtration, and electron microscopy. *Biological Procedures Online*, 11(1):32–51, January 2009.
- [83] R Y Tsien. The green fluorescent protein. *Annual review of biochemistry*, 67:509–544, 1998.

- [84] Vladislav V. Verkhusha and Alexander Sorkin. Conversion of the monomeric red fluorescent protein into a photoactivatable probe. *Chemistry and Biology*, 12:279–285, 2005.
- [85] Nadya G Gurskaya, Vladislav V Verkhusha, Alexander S Shcheglov, Dmitry B Staroverov, Tatyana V Chepurnykh, Arkady F Fradkov, Sergey Lukyanov, and Konstantin A Lukyanov. Engineering of a monomeric green-to-red photoactivatable fluorescent protein induced by blue light. *Nature Biotechnology*, 24:461–465, 2006.
- [86] Jörg Wiedenmann, Sergey Ivanchenko, Franz Oswald, Florian Schmitt, Carlheinz Röcker, Anya Salih, Klaus-Dieter Spindler, and G Ulrich Nienhaus. EosFP, a fluorescent marker protein with UV-inducible green-to-red fluorescence conversion. *Proceedings of the National Academy of Sciences of the United States of America*, 101:15905–15910, 2004.
- [87] Martin Andresen, Andre C Stiel, Jonas Fölling, Dirk Wenzel, Andreas Schönle, Alexander Egner, Christian Eggeling, Stefan W Hell, and Stefan Jakobs. Photoswitchable fluorescent proteins enable monochromatic multilabel imaging and dual color fluorescence nanoscopy. *Nature Biotechnology*, 26:1035–1040, 2008.
- [88] Vladislav V Verkhusha, Konstantin A Lukyanov, Dmitry M Chudakov, and Sergey Lukyanov. Photoactivatable fluorescent proteins. *Nature Reviews Molecular Cell Biology*, 6:885–890, 2005.
- [89] S Dhandayuthapani, L E Via, C A Thomas, P M Horowitz, D Deretic, and V Deretic. Green fluorescent protein as a marker for gene expression and cell biology of mycobacterial interactions with macrophages. *Molecular Microbiology*, 17:901–912, 1995.
- [90] J.A. Theriot K. Gee A. Mallavarapu T.J. Mitchison, K.E. Sawin. Caged fluorescent probes. *Methods in Enzymology*, 1998.

- [91] Gerald Donnert, Jan Keller, Christian A, Silvio O Rizzoli, Volker Westphal, Andreas Schönle, Reinhard Jahn, Stefan Jakobs, Christian Eggeling, and Stefan W. Hell. Two-color far-field fluorescence nanoscopy. *Biophysical Journal*, 92:L67—9, 2007.
- [92] J. Fölling, V. Belov, R. Kunetsky, R. Medda, A. Schönle, A. Egner, C. Eggeling, M. Bossi, and S. W. Hell. Photochromic rhodamines provide nanoscopy with optical sectioning. *Angewandte Chemie International Edition*, 46:6266–6270, 2007.
- [93] Mark Bates, Bo Huang, Graham T Dempsey, and Xiaowei Zhuang. Multi-color super-resolution imaging with photo-switchable fluorescent probes. *Science*, 317:1749–1753, 2007.
- [94] Jyoti K Jaiswal, Ellen R Goldman, Hedi Mattoussi, and Sanford M Simon. Use of quantum dots for live cell imaging. *Nature Methods*, 1:73–78, 2004.
- [95] X Michalet, F F Pinaud, L a Bentolila, J M Tsay, S Doose, J J Li, G Sundaresan, a M Wu, S S Gambhir, and S Weiss. Quantum dots for live cells, in vivo imaging, and diagnostics. *Science*, 307(5709):538–544, January 2005.
- [96] Ben N G Giepmans, Thomas J Deerinck, Benjamin L Smarr, Ying Z Jones, and Mark H Ellisman. Correlated light and electron microscopic imaging of multiple endogenous proteins using Quantum dots. *Nature Methods*, 2(10):743–749, 2005.
- [97] Ute Resch-genger, Markus Grabolle, Sara Cavaliere-jaricot, Roland Nitschke, and Thomas Nann. Quantum dots versus organic dyes as fluorescent labels. *Nature methods*, 5(9):763–775, 2008.
- [98] Loling Song, E. J. Hennink, I. Ted Young, and Hans J. Tanke. Photobleaching kinetics of fluorescein in quantitative fluorescence microscopy. *Biophysical Society*, 68(6):2588–2600, 1995.

- [99] Eva Arnsfang Christensen, Pasad Kulatunga, and B Christoffer Lagerholm. A single molecule investigation of the photostability of quantum dots. *PloS one*, 7(8):e44355, January 2012.
- [100] Xingyong Wu, Hongjian Liu, Jianquan Liu, Kari N Haley, Joseph A Treadway, J Peter Larson, Nianfeng Ge, Frank Peale, and Marcel P Bruchez. Immunofluorescent labeling of cancer marker Her2 and other cellular targets with semiconductor quantum dots. *Nature Biotechnology*, 21:41–46, 2003.
- [101] E. B Priestley and A. Haug. Phosphorescence spectrum of pure crystalline naphthalene. *The Journal of Chemical Physics*, 49:622–629, 1968.
- [102] Michael Kasha. From Jablonski to femtoseconds. Evolution of molecular photophysics. *Acta Physica Polonica A*, 95:15–36, 1999.
- [103] H. H. Jaffe and Albert L. Miller. The fates of electronic excitation energy. *Journal of Chemical Education*, 43:469, 1966.
- [104] Diane S Lidke, Peter Nagy, Rainer Heintzmann, Donna J Arndt-Jovin, Janine N Post, Hernan E Grecco, Elizabeth A Jares-Erijman, and Thomas M Jovin. Quantum dot ligands provide new insights into erbB/HER receptor-mediated signal transduction. *Nature Biotechnology*, 22:198–203, 2004.
- [105] M Dahan, S Levi, C Luccardini, P Rostaing, B Riveau, and A Triller. Diffusion dynamics of glycine receptors revealed by single quantum dot tracking. *Science*, 302:442–445, 2003.
- [106] Gang Ruan, Amit Agrawal, Adam I. Marcus, and Shuming Nie. Imaging and tracking of Tat peptide-conjugated quantum dots in living cells: New insights into nanoparticle uptake, intracellular transport, and vesicle shedding. *Journal of the American Chemical Society*, 129:14759–14766, 2007.
- [107] Yun Xing, Qaiser Chaudry, Christopher Shen, Koon Yin Kong, Haiyen E Zhau, Leland W Chung, John A Petros, Ruth M O’Regan, Maksym V Yezhelyev,



- Jonathan W Simons, May D Wang, and Shuming Nie. Bioconjugated quantum dots for multiplexed and quantitative immunohistochemistry. *Nature Protocols*, 2:1152–1165, 2007.
- [108] Sungjee Kim, Yong Taik Lim, Edward G Soltesz, Alec M De Grand, Jaihyoung Lee, Akira Nakayama, J Anthony Parker, Tomislav Mihaljevic, Rita G Laurence, Delphine M Dor, Lawrence H Cohn, Mounqi G Bawendi, and John V Frangioni. Near-infrared fluorescent type II quantum dots for sentinel lymph node mapping. *Nature Biotechnology*, 22:93–97, 2004.
- [109] Maureen a Walling, Jennifer a Novak, and Jason R E Shepard. Quantum dots for live cell and in vivo imaging. *International Journal of Molecular Sciences*, 10(2):441–91, February 2009.
- [110] Sigma-Aldrich. 3-D nano and micro structures. *Material Matters*, 3(1):1–25, 2014.
- [111] Sigma-Aldrich Co. LLC. Core type quantum dots. <http://www.sigmaaldrich.com/materials-science/material-science-products.html>, 2014. [Online; accessed 02-April-2015].
- [112] Jiyang Fan and Paul K Chu. Group IV nanoparticles: synthesis, properties, and biological applications. *Small*, 6(19):2080–2098, October 2010.
- [113] W C Chan and S Nie. Quantum dot bioconjugates for ultrasensitive nonisotopic detection. *Science*, 281:2016–2018, 1998.
- [114] Andreas Kornowski, Michael Giersig, Ralf Vogel, Abdelkarim Chemseddine, and Horst Weller. Nanometer-sized colloidal germanium particles: Wet-chemical synthesis, laser-induced crystallization and particle growth. *Advanced Materials*, 5(9):634–636, 1993.
- [115] Hsiang Wei Chiu, Christopher N Chervin, and Susan M Kauzlarich. Phase changes in Ge nanoparticles. *Chemistry of Materials*, 95616(19):4858–4864, 2005.

- [116] Boyd R Taylor, Susan M Kauzlarich, Howard W H Lee, and Gildardo R Delgado. Solution Synthesis of Germanium Nanocrystals Demonstrating Quantum Confinement. *Chemistry of Materials*, 10(1):22–24, 1998.
- [117] J. Wilcoxon, P. Provencio, and G. Samara. Synthesis and optical properties of colloidal germanium nanocrystals. *Physical Review B*, 64(3):035417, June 2001.
- [118] Nam Hawn Chou, Karl D Oyler, Nathan E Motl, and Raymond E Schaak. Colloidal synthesis of germanium nanocrystals using room temperature benchtop chemistry. *Chemistry of Materials*, 21(18):4105–4107, September 2009.
- [119] H P Wu, J F Liu, Y W Wang, Y W Zeng, and J Z Jiang. Preparation of Ge nanocrystals via ultrasonic solution reduction. *Materials Letters*, 60(7):986–989, 2006.
- [120] Jamie H Warner and Richard D Tilley. Synthesis of water-soluble photoluminescent germanium nanocrystals. *Nanotechnology*, 17(15):3745–3749, August 2006.
- [121] Doh C Lee, Jeffrey M Pietryga, Istvan Robel, Donald J Werder, Richard D Schaller, and Victor I Klimov. Colloidal synthesis of infrared-emitting germanium nanocrystals. *Journal of the American Chemical Society*, 131(10):3436–3437, March 2009.
- [122] A. P. Alivisatos, A. L. Harris, N. J. Levinos, M. L. Steigerwald, and L. E. Brus. Electronic states of semiconductor clusters: Homogeneous and inhomogeneous broadening of the optical spectrum. *The Journal of Chemical Physics*, 89:4001–4011, 1988.
- [123] L E Brus. A simple model for the ionization potential, electron affinity, and aqueous redox potentials of small semiconductor crystallites. *The Journal of Chemical Physics*, 79(May 2015):5566, 1983.

- [124] V. Colvin, A. Alivisatos, and J. Tobin. Valence-band photoemission from a quantum-dot system, 1991.
- [125] C. C J Roothaan. New developments in molecular orbital theory. *Reviews of Modern Physics*, 23:69–89, 1951.
- [126] Akhlesh Lakhtakia. *Models and modelers of hydrogen*, volume 65. 1997.
- [127] Wei Dan. *Solid state physics (Chinese)*. Materials Science and Engineering. Tsinghua University Press(China), Beijing, China, 2003.
- [128] Heqing Yang, Xingjun Wang, Huazhong Shi, Fujian Wang, Xiaoxiao Gu, and Xi Yao. Sol-gel preparation of Ge nanocrystals embedded in SiO<sub>2</sub> glasses. *Journal of Crystal Growth*, 236:371–375, 2002.
- [129] Christoph Bostedt. *Electronic Structure of Germanium Nanocrystal Films Probed with Synchrotron Radiation*. PhD thesis, 2002.
- [130] G Hernandez, R Jones, C Wykes, K G Ibbs, R M Osgood, P N Butcher, D Cotter, P D Townsend, P J Chandler, L Zhang, and D Suter. *Optical properties of semiconductor nanocrystals*. Cambridge, UK, 1998.
- [131] L E Brus. Electron–electron and electron-hole interactions in small semiconductor crystallites: The size dependence of the lowest excited electronic state. *The Journal of Chemical Physics*, 80(January):4403, 1984.
- [132] J M Nedeljković, R C Patel, P Kaufman, C Joyce-Pruden, and N O’Leary. Synthesis and optical properties of quantum-size metal sulfide particles in aqueous solution. *Journal of Chemical Education*, 70:342–345, 1993.
- [133] Louis Brus. Electronic wave functions in semiconductor clusters: experiment and theory. *The Journal of Physical Chemistry*, 90(2):2555–2560, 1986.
- [134] W. S. Li, Z. X. Shen, H. Y. Li, D. Z. Shen, and X. W. Fan. Blue shift of Raman peak from coated TiO<sub>2</sub> nanoparticles. *Journal of Raman Spectroscopy*, 32:862–865, 2001.

- [135] D.B. Murphy. *Fundamentals of light microscopy and electronic imaging*. Wiley, 2002.
- [136] Y. M. Niquet, G. Allan, C. Delerue, and M. Lannoo. Quantum confinement in germanium nanocrystals. *Applied Physics Letters*, 77:1182, 2000.
- [137] Jing Shi, S. Gider, K. Babcock, and D.D. Awschalom. Semiconductor clusters, nanocrystals, and quantum dots. *Science*, 271:933–937, 1996.
- [138] Al. L Efros and M Rosen. The electronic structure of semiconductor nanocrystals. *Annual Review of Materials Science*, 30:475–521, 2000.
- [139] Ephrem O. Chukwuocha. Theoretical studies on the effect of confinement on quantum dots using the Brus equation, 2012.
- [140] E Tholouli, E Sweeney, E Barrow, V Clay, J A Hoyland, and R J Byers. Quantum dots light up pathology. *Journal of Pathology*, 216:275–285, 2008.
- [141] Scott E. Irvine, Thorsten Staudt, Eva Rittweger, Johann Engelhardt, and Stefan W. Hell. Direct light-driven modulation of luminescence from Mn-doped ZnSe quantum dots. *Angewandte Chemie International Edition*, 47:2685–2688, 2008.
- [142] Invitrogen company. Absorption and emission profiles of Qdot® nanocrystals. <http://www.lifetechnologies.com/>, 2013. [Online; accessed 26-April-2015].
- [143] M. Kuno, D. P. Fromm, H. F. Hamann, a. Gallagher, and D. J. Nesbitt. Nonexponential “blinking” kinetics of single CdSe quantum dots: A universal power law behavior. *The Journal of Chemical Physics*, 112(7):3117, 2000.
- [144] M. Nirmal, B. O. Dabbousi, M. G. Bawendi, J. J. Macklin, J. K. Trautman, T. D. Harris, and L. E. Brus. Fluorescence intermittency in single CdSe nanocrystals. *Nature*, 383:802 – 804, 1996.
- [145] Fernando D Stefani, Jacob P Hoogenboom, and Eli Barkai. Beyond quantum jumps: blinking nano - scale light emitters. *Physics Today*, 1(1):34–39, 2009.

- [146] Masaru Kuno, David P Fromm, Alan Gallagher, David J Nesbitt, Olga I Micic, and Arthur J Nozik. Fluorescence intermittency in single InP quantum dots. *Nano letters*, 1(10):557–564, 2001.
- [147] Shayan Saeidi and Hassan Kaatuzian. Theoretical estimation to improve optical characteristics of germanium lasers for integrated silicon photonics application. *International journal of optics and applications*, 5(3):65–70, 2015.
- [148] K.D. Sattler. *Handbook of nanophysics: nanoelectronics and nanophotonics*. Handbook of Nanophysics. Taylor & Francis, 2010.
- [149] Charles Kittel. *Introduction to solid state physics*. John Wiley & Sons, Inc, Hoboken, United States of America, 8th edition, 2004.
- [150] Shinji Takeoka. Size-dependent near-infrared photoluminescence from Ge nanocrystals embedded in SiO<sub>2</sub> matrices. *Physical Review B*, 58(12):7921–7925, 1998.
- [151] David Jurbergs, Elena Rogojina, Lorenzo Mangolini, and Uwe Kortshagen. Silicon nanocrystals with ensemble quantum yields exceeding 60%. *Applied Physics Letters*, 88(2006):60–63, 2006.
- [152] Royal Society (London). *Giving some accounts of the present undertakings, studies, and labours, of the ingenious, in many considerable parts of the world*. Number 142 in Philosophical transactions of the Royal Society of London. 1852.
- [153] Gert-Jan Kremers, Sarah G Gilbert, Paula J Cranfill, Michael W Davidson, and David W Piston. Fluorescent proteins at a glance. *Journal of Cell Science*, 124:157–160, 2011.
- [154] Yingxiao Wang, John Y-J Shyy, and Shu Chien. Fluorescence proteins, live-cell imaging, and mechanobiology: seeing is believing. *Annual Review of Biomedical Engineering*, 10:1–38, 2008.

- [155] Denis Semwogerere and Eric R Weeks. Confocal microscopy. Technical report, 2005.
- [156] Nathan S Claxton, Thomas J Fellers, and Michael W Davidson. Laser scanning confocal microscopy. *Confocal Microscopy*, 1979(21), 1979.
- [157] Colin Sheppard and David Shotton. Confocal laser scanning microscopy: principles. *Carl Zeiss*, page 37, 1998.
- [158] Florent Battistella, Steven Berger, and Andrew Mackintosh. Scanning optical microscopy. *Journal of Electron Microscopy Technique*, 6(4):377–384, 1987.
- [159] Ruiyun Chen, Ruixiang Wu, Guofeng Zhang, Yan Gao, Liantuan Xiao, and Suotang Jia. Electron transfer-based single molecule fluorescence as a probe for nano-environment dynamics. *Sensors*, 14:2449–2467, 2014.
- [160] Image Buddy. Fluorescence microscopy vs confocal microscopy. <http://imgbuddy.com/fluorescence-microscopy-vs-confocal-microscopy.asp>, 2015. [Online; accessed 25-May-2015].
- [161] Alexandre S. Goy and Demetri Psaltis. Digital confocal microscope, 2012.
- [162] T Wilson. *Confocal microscopy*. Acad. Press, 1990.
- [163] T. Tanaami and K. Mikuriya. Nipkow disk for confocal optical scanner, October 15 1997. EP Patent 0,539,691.
- [164] Akihiko Nakano. Spinning disk confocal microscopy: a cutting-edge tool for imaging of membrane traffic need for a rapid confocal scanning system. *Cell Structure and Function*, 27:349–355, 2002.
- [165] Rui Lima, Shigeo Wada, Ken-ichi Tsubota, and Takami Yamaguchi. Confocal micro-PIV measurements of three-dimensional profiles of cell suspension flow in a square microchannel, 2006.

- [166] Australia University of New South Wales. Beam path of a confocal spinning disk microscope. <http://php.med.unsw.edu.au/cellbiology/index.php>, 2010. [Online; accessed 08-June-2015].
- [167] E. Wang, C. M. Babbey, and Kenneth W. Dunn. Performance comparison between the high-speed Yokogawa spinning disc confocal system and single-point scanning confocal systems. *Journal of Microscopy*, 218:148–159, 2005.
- [168] Takeo Tanaami, Shinya Otsuki, Nobuhiro Tomosada, Yasuhito Kosugi, Mizuho Shimizu, and Hideyuki Ishida. High-speed 1-frame/ms scanning confocal microscope with a microlens and Nipkow disks. *Applied Optics*, 41:4704–4708, 2002.
- [169] John M. Murray, Paul L. Appleton, Jason R. Swedlow, and Jennifer C. Waters. Evaluating performance in three-dimensional fluorescence microscopy. *Journal of Microscopy*, 228:390–405, 2007.
- [170] Chris H Rycroft, Grigory Isaakovich Barenblatt, Kazuo Yamagata, Takefumi Kondo, Shigeo Hayashi, Atsunori Shitamukai, Daijiro Konno, Fumio Matsuzaki, Shuichi Onami, Hiroshi Nakayama, Yasuhito Kosugi, Tomonobu M Watanabe, Katsumasa Fujita, Yuko Mimori, Morphogenetic Signaling, Cell Asymmetry, Jun Takayama, M Tomonobu, and Yuko Mimori-kiyosue. Improving spinning disk confocal microscopy by preventing pinhole cross-talk for intravital imaging. *Proceedings of the National Academy of Sciences*, 110(50):6240–6240, 2013.
- [171] Peng Xi, Yujia Liu, and Qiushi Ren. Scanning and image reconstruction techniques in confocal laser scanning microscopy. In Chau-Chang Wang, editor, *Laser Scanning , Theory and Application*, chapter 27, pages 523 – 542. InTech, Shanghai, 2011.
- [172] Claudette M St Croix, Stuart H Shand, and Simon C Watkins. Confocal microscopy: comparisons, applications, and problems. *BioTechniques*, 39(6):S2–5, December 2005.

- [173] Adaobi Nwaneshiudu, Christiane Kuschal, Fernanda H Sakamoto, R Rox Anderson, Kathryn Schwarzenberger, and Roger C Young. Introduction to confocal microscopy. *The Journal of Investigative Dermatology*, 132:e3, 2012.
- [174] Inc Molecular probes. DAPI nucleic acid stain. Technical report, 2006.
- [175] Warren Strober. Trypan blue exclusion test of cell viability. *Current Protocols in Immunology*, 3, 2001.
- [176] Inc. Millipore Corporation. *Muse count and viability kit user guide*. Millipore Corporation, Hayward, U.S.A., first edit edition, 2012.
- [177] Ali Karatutlu. *Structural Origin of Light Emission in Germanium Quantum Dots*. PhD thesis, Queen Mary University of London, September 2014.
- [178] Carl Zeiss MicroImaging GmbH. LSM 710, LSM 780 operating manual. Technical report, GmbH, Carl Zeiss MicroImaging, Jena, Germany, 2010.
- [179] Ruska Ernst. The development of the electron microscope and electron microscopy. Technical report, Berlin, Germany, 1986.
- [180] Dune Sciences. Particle size analysis SOP, 2011.
- [181] Bo Zhang, Josiane Zerubia, and Jean-Christophe Olivo-Marin. Gaussian approximations of fluorescence microscope point-spread function models. *Applied Optics*, 46:1819–1829, 2007.
- [182] Ricardo Henriques, Mickael Lelek, Eugenio F Fornasiero, Flavia Valtorta, Christophe Zimmer, and Musa M Mhlanga. QuickPALM: 3D real-time photoactivation nanoscopy image processing in ImageJ. *Nature methods*, 7(5):339–40, May 2010.
- [183] T Dertinger, R Colyer, G Iyer, S Weiss, and J Enderlein. Fast, background-free, 3D super-resolution optical fluctuation imaging ( SOFI ). *Proceedings of the National Academy of Sciences of the United States of America*, 106(52):22287–22292, 2009.



- [184] Mike Heilemann, Sebastian Van De Linde, Mark Schüttpelz, Robert Kasper, Britta Seefeldt, Anindita Mukherjee, Philip Tinnefeld, and Markus Sauer. Subdiffraction-resolution fluorescence imaging with conventional fluorescent probes. *Angewandte Chemie - International Edition*, 47:6172–6176, 2008.
- [185] Eran a Mukamel, Hazen Babcock, and Xiaowei Zhuang. Statistical deconvolution for superresolution fluorescence microscopy. *Biophysical Journal*, 102(10):2391–400, May 2012.
- [186] Lei Zhu, Wei Zhang, Daniel Elnatan, and Bo Huang. Faster STORM using compressed sensing. *Nature Methods*, 9(7):721–723, April 2012.
- [187] Susan Cox, Edward Rosten, James Monypenny, Tijana Jovanovic-Talisman, Dylan T Burnette, Jennifer Lippincott-Schwartz, Gareth E Jones, and Rainer Heintzmann. Bayesian localization microscopy reveals nanoscale podosome dynamics. *Nature Methods*, 9(2):195–200, February 2012.
- [188] DFNano Technology. What’s Germanium. <http://www.what-is-nanotechnology.com/13germanium-oxide-grain-GeO2-powders.htm>, 2013. [Online; accessed 09-July-2015].
- [189] Henry Gerung, Scott D Bunge, Timothy J Boyle, C Jeffrey Brinker, and Sang M Han. Anhydrous solution synthesis of germanium nanocrystals from the germanium(II) precursor  $\text{Ge}[\text{N}(\text{SiMe}_3)_2]_2$ . *Chemical Communications*, (111):1914–1916, 2005.
- [190] Daniel a Ruddy, Justin C Johnson, E Ryan Smith, and Nathan R Neale. Size and bandgap control in the solution-phase synthesis of near-infrared-emitting germanium nanocrystals. *ACS Nano*, 4(12):7459–7466, 2010.
- [191] Laurent Pizzagalli, Giulia Galli, John E. Klepeis, and François Gygi. Structure and stability of germanium nanoparticles. *Phys. Rev. B*, 63:165324, Apr 2001.

- [192] Ali Karatutlu, Mingying Song, Ann P. Wheeler, Osman Ersoy, William R. Little, Yuanpeng Zhang, Pascal Puech, Filippo S. Boi, Zofia Luklinska, and Andrei V. Sapelkin. Synthesis and structure of colloidally stable free-standing Germanium quantum dots and their application in live cell imaging. *Submitted to Journal of Particle & Particles Systems Characterization*, 5:20566–20573, 2015.
- [193] Yuanpeng Zhang, Ali Karatutlu, Osman Ersoy, William Little, Giannantonio Cibin, Andy Dent, and Andrei Sapelkin. Structure and effects of annealing in colloidal matrix-free Ge quantum dots. *Journal of Synchrotron Radiation*, 22:105–112, 2015.
- [194] Wolfgang J Parak, Teresa Pellegrino, and Christian Plank. Labelling of cells with quantum dots. *Nanotechnology*, 16(2):9–25, February 2005.
- [195] Helen Rawsthorne, Trevor G. Phister, and Lee Ann Jaykus. Development of a fluorescent in situ method for visualization of enteric viruses. *Applied and Environmental Microbiology*, 75(24):7822–7827, 2009.
- [196] W Robert J Funnell and Dusica Maysinger. Three-dimensional reconstruction of cell nuclei, internalized quantum dots and sites of lipid peroxidation. *Journal of Nanobiotechnology*, 4:10, 2006.
- [197] Huize Chen, Yan Gong, and Rong Han. Cadmium Telluride Quantum Dots (CdTe-QDs) and Enhanced Ultraviolet-B (UV-B) Radiation Trigger Antioxidant Enzyme Metabolism and Programmed Cell Death in Wheat Seedlings. *PLoS ONE*, 9(10):e110400, 2014.
- [198] Keith A Lidke, Bernd Rieger, Thomas M Jovin, and Rainer Heintzmann. Super-resolution by localization of quantum dots using blinking statistics. 13(18):1599–1609, 2005.
- [199] Fan-Ching Chien, Chiung Wen Kuo, and Peilin Chen. Localization imaging using blinking quantum dots. *The Analyst*, 136(8):1608–13, April 2011.

- [200] Yong Wang, Gilbert Fruhwirth, En Cai, Tony Ng, and Paul R Selvin. 3D super-resolution imaging with blinking quantum dots. *Nano Letters*, 13:5233–5241, 2013.
- [201] Keith A Lidke, Bernd Rieger, Thomas M Jovin, and Rainer Heintzmann. Superresolution by localization of quantum dots using blinking statistics. *Optics Express*, 13(18):1599–1609, 2005.
- [202] Sungchul Hohng and Taekjip Ha. Near-complete suppression of quantum dot blinking in ambient conditions. *Journal of the American Chemical Society*, 126:1324–1325, 2004.
- [203] Russell E Thompson, Daniel R Larson, and Watt W Webb. Precise nanometer localization analysis for individual fluorescent probes. *Biophysical Journal*, 82(5):2775–83, May 2002.
- [204] Marko Kreft, Matjaz Stenovec, and Robert Zorec. Focus-drift correction in time-lapse confocal imaging. *Annals of the New York Academy of Sciences*, 1048:321–30, June 2005.
- [205] Jeffrey J. Peterson and David J. Nesbitt. Modified power law behavior in quantum dot blinking: A novel role for biexcitons and Auger ionization. *Nano Letters*, 9:338–345, 2009.
- [206] Jie Yao, Daniel R Larson, Harshad D Vishwasrao, Warren R Zipfel, and Watt W Webb. Blinking and nonradiant dark fraction of water-soluble quantum dots in aqueous solution. *Proceedings of the National Academy of Sciences of the United States of America*, 102(40):14284–9, October 2005.
- [207] Fang Huang, Samantha L Schwartz, Jason M Byars, and Keith a Lidke. Simultaneous multiple-emitter fitting for single molecule super-resolution imaging. *Biomedical optics express*, 2(5):1377–93, January 2011.

- [208] Seamus J Holden, Stephan Uphoff, and Achillefs N Kapanidis. DAOSTORM: an algorithm for high- density super-resolution microscopy., 2011.
- [209] Rainer Heintzmann, Herrmann Münch, and Christoph Cremer. High-precision distance measurements in epifluorescent microscopy - simulation and experiment. *Cell vision*, 4:252 – 253, 1997.
- [210] Edward Rosten, Gareth E Jones, and Susan Cox. ImageJ plug-in for Bayesian analysis of blinking and bleaching. *Nature Methods*, 10(2):97–8, February 2013.
- [211] Dylan T Burnette, Prabuddha Sengupta, Yuhai Dai, Jennifer Lippincott-Schwartz, and Bechara Kachar. Bleaching/blinking assisted localization microscopy for superresolution imaging using standard fluorescent molecules. *Proceedings of the National Academy of Sciences of the United States of America*, 108(52):21081–6, December 2011.
- [212] Anthony Barsic and Rafael Piestun. Super-resolution of dense nanoscale emitters beyond the diffraction limit using spatial and temporal information. *Applied Physics Letters*, 102(23):231103, 2013.
- [213] Alex Small and Shane Stahlheber. Fluorophore localization algorithms for super-resolution microscopy. *Nature Methods*, 11(3):267–279, February 2014.
- [214] Beth L Haas, Jyl S Matson, Victor J DiRita, and Julie S Biteen. Imaging live cells at the nanometer-scale with single-molecule microscopy: obstacles and achievements in experiment optimization for microbiology. *Molecules*, 19:12116–12149, 2014.
- [215] Daniel Sage, Hagai Kirshner, Thomas Pengo, Nico Stuurman, Junhong Min, Sulliana Manley, and Michael Unser. Quantitative evaluation of software packages for single-molecule localization microscopy. *Nature Methods*, (08):1–12, 2015.
- [216] Sebastian van de Linde, Steve Wolter, Mike Heilemann, and Markus Sauer. The effect of photoswitching kinetics and labeling densities on super-resolution fluorescence imaging. *Journal of Biotechnology*, 149:260–266, 2010.

- [217] Anthony Barsic and Rafael Piestun. Super-resolution of dense nanoscale emitters beyond the diffraction limit using spatial and temporal information. *Applied Physics Letters*, 102(23):231103, 2013.
- [218] Fernando Pérez-Cruz. Kullback-leibler divergence estimation of continuous distributions. In *IEEE International Symposium on Information Theory - Proceedings*, pages 1666–1670, 2008.
- [219] Niccolò Banterle, Khanh Huy Bui, Edward a. Lemke, and Martin Beck. Fourier ring correlation as a resolution criterion for super-resolution microscopy. *Journal of Structural Biology*, 183:363–367, 2013.
- [220] B Christoffer Lagerholm, Laurel Averett, Gabriel E Weinreb, Ken Jacobson, and Nancy L Thompson. Analysis method for measuring submicroscopic distances with blinking quantum dots. *Biophysical Journal*, 91(8):3050–3060, 2006.
- [221] Max-planck-institut Chemie and D Göttingen. Optimizing imaging parameters for the separation of multiple. *Journal of Microscopy*, 213(April 2003):46–62, 2004.
- [222] Timo Zimmermann, Jens Rietdorf, and Rainer Pepperkok. Spectral imaging and its applications in live cell microscopy, 2003.
- [223] Yuval Garini, Ian T Young, and George Mcnamara. Spectral imaging: principles and applications. *International Society for Analytical cytology*, 747:735–747, 2006.
- [224] Ilya Sychugov, Robert Juhasz, Jan Valenta, and Jan Linnros. Narrow luminescence linewidth of a silicon quantum dot. *Physical Review Letters*, 94, 2005.
- [225] A. Buades, B. Coll, and J. M. Morel. A review of image denoising algorithms, 2005.
- [226] KP Murphy. *Machine learning: a probabilistic perspective*. MIT Press, Cambridge, USA, 1 edition, 2012.

- [227] Paul D Simonson, Eli Rothenberg, and Paul R Selvin. Single-molecule-based super-resolution images in the presence of multiple fluorophores. *Nano Letters*, 11(11):5090–6, November 2011.
- [228] D. a. Bout. Discrete intensity jumps and intramolecular electronic energy transfer in the spectroscopy of single conjugated polymer molecules. *Science*, 277(August):1074–1077, 1997.
- [229] Julien Laverdant, Willy Daney de Marcillac, Carlos Barthou, Vu Duc Chinh, Catherine Schwob, Laurent Coolen, Paul Benalloul, Pham Thu Nga, and Agnès Maitre. Experimental determination of the fluorescence quantum yield of semiconductor nanocrystals. *Materials*, 4:1182–1193, 2011.
- [230] John-Christopher Boyer and Frank C. J. M. van Veggel. Absolute quantum yield measurements of colloidal  $\text{NaYF}_4:\text{Er}^{3+}, \text{Yb}^{3+}$  upconverting nanoparticles. *Nanoscale*, 2:1417–1419, 2010.
- [231] T J Russin, E I Altinoglu, J H Adair, and P C Eklund. Measuring the fluorescent quantum efficiency of indocyanine green encapsulated in nanocomposite particulates. *Journal of Physics: Condensed Matter*, 22(33):334217, 2010.
- [232] Hui Peng, Lijuan Zhang, Christian Soeller, and Jadranka Travas-Sejdic. Preparation of water-soluble CdTe/CdS core/shell quantum dots with enhanced photostability. *Journal of Luminescence*, 127:721–726, 2007.
- [233] Dimitri D Vaughn and Raymond E Schaak. Synthesis, properties and applications of colloidal germanium and germanium-based nanomaterials. *Chemical Society Reviews*, 42(7):2861–79, April 2013.
- [234] Paul W Loscutoff and Stacey F Bent. Reactivity of the germanium surface: Chemical passivation and functionalization. *Annual Review of Physical Chemistry*, 57:467–495, 2006.

- [235] Dunwei Wang, Ying Lan Chang, Zhuang Liu, and Hongjie Dai. Oxidation resistant germanium nanowires: Bulk synthesis, long chain alkanethiol functionalization, and Langmuir-Blodgett assembly. *Journal of the American Chemical Society*, 127:11871–11875, 2005.
- [236] Shinya Inoué. Foundations of confocal scanned imaging in light microscopy. In *Handbook of Biological Confocal Microscopy: Third Edition*, pages 1–19. 2006.
- [237] Patrick J Cutler, Michael D Malik, Sheng Liu, Jason M Byars, Diane S Lidke, and Keith a Lidke. Multi-color quantum dot tracking using a high-speed hyperspectral line-scanning microscope. *PloS One*, 8(5):e64320, January 2013.
- [238] Bo Huang, Sara A Jones, Boerries Brandenburg, and Xiaowei Zhuang. Whole-cell 3D STORM reveals interactions between cellular structures with nanometer-scale resolution. *Nature Methods*, 5:1047–1052, 2008.
- [239] Sri Rama Prasanna Pavani, Michael A Thompson, Julie S Biteen, Samuel J Lord, Na Liu, Robert J Twieg, Rafael Piestun, and W E Moerner. Three-dimensional, single-molecule fluorescence imaging beyond the diffraction limit by using a double-helix point spread function. *Proceedings of the National Academy of Sciences of the United States of America*, 106:2995–2999, 2009.
- [240] Manuel F Juetten, Travis J Gould, Mark D Lessard, Michael J Mlodzianoski, Bhupendra S Nagpure, Brian T Bennett, Samuel T Hess, and Joerg Bewersdorff. Three-dimensional sub-100 nm resolution fluorescence microscopy of thick samples. *Nature Methods*, 5:527–529, 2008.
- [241] Hari Shroff, Catherine G Galbraith, James A Galbraith, Helen White, Jennifer Gillette, Scott Olenych, Michael W Davidson, and Eric Betzig. Dual-color superresolution imaging of genetically expressed probes within individual adhesion complexes. *Proceedings of the National Academy of Sciences of the United States of America*, 104(51):20308–20313, 2007.

- [242] a. J. Williamson, C. Bostedt, T. Van Buuren, T. M. Willey, L. J. Terminello, G. Galli, and L. Pizzagalli. Probing the electronic density of states of germanium nanoparticles: A method for determining atomic structure. *Nano Letters*, 4:1041–1045, 2004.
- [243] Xiong Liu, Mark Atwater, Jinhai Wang, and Qun Huo. Extinction coefficient of gold nanoparticles with different sizes and different capping ligands. *Colloids and Surfaces B: Biointerfaces*, 58:3–7, 2007.
- [244] Andor Technology. iXon3 software guide. Technical Report June, 2011.
- [245] Katia Cortese, Alberto Diaspro, and Carlo Tacchetti. Advanced correlative light/electron microscopy: current methods and new developments using Tokuyasu cryosections. *The Journal of Histochemistry and Cytochemistry*, 57(12):1103–12, December 2009.
- [246] Kristina Jahn, Deborah Barton, and Filip Braet. *Correlative fluorescence and scanning, transmission electron microscopy for biomolecular investigation*, volume 1. 2007.
- [247] Dh Powell and Kj Czymmek. A low cost correlative technique for cell imaging via confocal and scanning electron microscopy. *Microscopy and Microanalysis*, 15(S2):940, July 2009.
- [248] Shigeki Watanabe, Jackson Richards, Gunther Hollopeter, Robert J Hobson, Wayne M Davis, and Erik M Jorgensen. Nano-fEM: protein localization using photo-activated localization microscopy and electron microscopy. *Journal of Visualized Experiments*, (70):e3995, January 2012.